Label-Free Multiphoton Microscopy of Lipid Droplets in Oocytes, Eggs and Early Embryos

Josephine Bradley

Thesis submitted for the degree of Doctor of Philosophy (Ph.D.)

2016
CARDIFF UNIVERSITY

Author's Declaration

I declare that the work comprising this thesis was carried out only through my own investigation, and the views expressed are my own. No portion of this work has been submitted or is currently in canditature for any other degree or award at this, or any other university or place of learning.

ICSI was carried out by Dr. Randa Sanusi. Initial imaging of embryo stages was performed using fixed embryos provided by Dr. Judith Eckert. All other experimental work was performed by myself.

Josephine Bradley

July 2016

“Anything’s possible, if you’ve got enough nerve” – J.K. Rowling

For Milly,

without your unyielding strength and courage, I could not have completed this thesis.

Acknowledgements

Thank you to my supervisors, Karl and Paola, who have given me invaluable support, kindness and guidance throughout my project. Two utterly brilliant brains that I have had the pleasure of working with. Thank you to Pete, for all of his support and motivational speeches! Thank you to Iestyn, without whom I would never have been able to complete this project or thesis. Thank you to Wolfgang and Francesco, for the use of your software. Thank you to Randa and Judith for your experimental help. Thank you to all of the friends I have made along the way in the lab, whose support and friendship will always be incredibly valued. A special mention to Mela, my fellow Enabler for making lab and office life 'tip-top'!

To my Sister Wives, my rocks, my army- thank you for your eternal love and support. We have all proven this year, more than any other, that we can get through the toughest of times and come out smiling. To Smiles, and my Ron and Harry (Chandler and Ross), your friendship is unlike any other, and you keep me sane by keeping insane. Never change.

To my wonderfully crazy and loving family- Mum, Dad, Tom, Leanne, thank you for simply everything. Everything I have achieved has been achieved with you by my side, and I simply cannot express how utterly grateful I am to you all.

Finally, to Simon- the overwhelming love, support and laughter you provide makes life a walk (dance) in the park.

Abstract

Successful development of mammalian oocytes, eggs and embryos relies on the production of ATP by their mitochondria, through metabolism of pyruvate and fatty acids. Imaging of lipid droplets in mammalian eggs has proven difficult due to the invasive, unspecific and unquantitative nature of fluorescent lipophilic stains. Here, we show that coherent anti-Stokes Raman scattering (CARS) microscopy can be used to image lipid droplets in live mouse oocytes and pre-implantation embryos, in a label-free, chemically-specific manner. CARS enables visualisation of lipid droplet distributions, and quantitation of droplet size, number and spatial distribution, notably whilst maintaining their developmental viability. CARS also allows examination of the type of lipids comprising lipid droplets, through means of hyperspectral imaging. It is shown that the chemical composition of these droplets differ in oocytes matured in media supplemented with saturated and unsaturated fatty acids. Correlation of CARS measurements with simultaneous two-photon fluorescence (TPF) microscopy of conventionally used lipid dyes demonstrates only partial correlation, and shows their lack of specificity and unpredictable staining patterns. Dynamic monitoring of lipid metabolism in eggs allows determination of the extent of fatty acid oxidation occurring in mouse oocytes and embryos. Investigation into how inhibition of fatty acid metabolism affects the mitochondrial redox state, membrane potential and ATP level allows further understanding of why fatty acid metabolism is significant for egg and pre-implantation embryo development. Starvation and fatty acid-feeding of oocytes shows that the lipid droplet distribution reflects their level of lipid metabolism, while the detrimental effects of palmitic acid are shown to involve its action at the endoplasmic reticulum SERCA pumps.

Contents

List of Figures and Tables

CHAPTER 1.

Abbreviations

3D	Three-dimensional
ACAC	Acetyl coA carboxylase
ART	Assisted Reproduction Techniques
ADP	Adenosine diphosphate
ATP	Adenosine triphosphate
BMI	Body mass index
BSA	Bovine albumin serum
C. elegans	Caenorhabditis elegans
Ca^{2+}	Calcium
CARS	Coherent anti-Stokes Raman Scattering
CCD	Charge-coupled device
CH_3	Carboxyl group
C=O	Carbonyl group
CI	ETC Complex I (NADH reductase)
CII	ETC Complex II (Succinate dehydrogenase)
CIII	ETC Complex III (Cytochrome b-c complex)
CIN	Cinnamate
CIV	ETC Complex IV (Cytochrome oxidase)
CN^-	Cyanide
CO_2	Carbon dioxide
CoA	Co-enzyme A (Pantothenic acid)
COC	Cumulus-oocyte complex
CPT	Carnitine palmitoyl transferase
DAG	Diacylglycerol
DIC	Differential interference contrast
DM	Dichroic Mirror

DNA	Deoxyribose nucleic acid
DNP	Dinitrophenol
e^-	Electron
ER	Endoplasmic Reticulum
ETC	Electron transfer chain
FAs	Fatty acids
FAD	Flavin adenine dinuceotide
FADH	Reduced flavin adenine dinuceotide
FAO	Fatty acid oxidation
FCCP	Carbonyl cyanide-*4*-(trifluoromethoxy)phenylhydrazone
FCS	Foetal calf serum
FFAs	Free fatty acids
Fs	Femtosecond
FSH	Follicle-stimulating hormone
Fsp27	Fat-specific protein (27kDa)
GnRH	Gonadotrophin-releasing hormone
GTO	Glycerol trioleate
GV	Germinal vesicle
GVBD	Germinal vesicle breakdown
H	Hydrogen
H^+	Proton
H_2O	Water
hCG	human chorionic gonadotrophin
HFEA	Human Fertilisation and Embryology Authority
HGM	Harmonic Generation Microscopy
HIA	Hyperspectral image analysis
HKSOM	Hepes-buffered potassium simplex optimised medium
hrs	Hours

IBMX	isobutyl-1-methylxanthine
ICM	Inner cell mass
ICSI	Intra-cytoplasmic sperm injection
IFD	Instantaneous frequency difference
IMM	Inner mitochondrial membrane
IP_3	Inositol triphosphate
IUI	Intra-uterine insemination
IVF	*in vitro* fertilisation
IVM	*in vitro* maturation
KCL	Potassium chloride
KSOM	Potassium simplex optimised medium
LD	Lipid droplet
LH	Luteinisng hormone
LipDH	Lipodehydrogenase
MAPK	Mitogen-activated protein kinase
MCT	Monocarboxylate transporter
MEM	Minimum essential medium
MII	Metaphase II
MitoGFP	Mitochondrial-targeted GFP
MMP	Mitochondrial membrane potential
MPF	Maturation-promoting factor
MtDNA	Mitchondrial DNA
MUFA	Mono-unsaturated fatty acid
NAD	Nicotinamide adenine dinucleotide
NADH	Reduced nicotinamide adenine dinucleotide
NaOH	Sodium hydroxide
NEFA	Non-esterified fatty acid
NHS	National Health Service

NIR	Near infrared
NSN	Chromosomes not surrounding nucleus
O_2	Oxygen
OA	Oleic acid
OGBD	Oregon green BAPTA-dextran
OMM	Outer mitochondrial membrane
PA	Palmitic acid
PB	Polar body
PBS	Phosphate-buffered saline
PCKK	Phase-corrected Kramers-Kronig
PDH	Pyruvate dehydrogenase
PFA	Paraformaldehyde
PFK	Phosphofructokinase
PGD	Pre-implantation genetic diagnosis
PGS	Pre-implantation genetic screening
PIP_2	Phosphoinositol 4,5 bisphosphate
PLCζ	Phospholipase C zeta
PMSG	Pregnant mare's serum gonadotrophin
PMT	Photomultiplier tube
PN	Pronuclei
PRKA	AMP-activated protein kinase (formerly AMPK)
Ps	Picosecond
PUFA	Poly-unsaturated fatty acids
PVA	Poly-vinyl alcohol
RColoc	Pearson's correlation coefficient
RNA	Ribose nucleic acid
ROI	Region of interest
ROS	Reactive oxygen species

Sec	Seconds
SERCA	Sarco/endoplasmic reticulum Ca^{2+} ATPase
SHG	Second Harmonic Generation
SN	Chromosomes surrounding nucelus
SNARE	Soluble N-ethylmaleimide-sensitive factor attachment receptor
SRS	Stimulated Raman scattering
SVD	Singular value decomposition
TAG	Triacylglycerol/Triglyceride
TCA	The Citric Acid/Tricarboxylic acid/Kreb's cycle
TEM	Transmission electron microscopy
THG	Third Harmonic Generation
ThPA	Three photon absorption
Ti:Sa	Titanium sapphire laser source
TMRE	Tetramethylrhodamine ethyl ester
TPF	Two-photon fluorescence
ZGA	Zygotic genome activation
ZP	Zona Pellucida

Chapter 1. Introduction

1.1. Oocyte, Egg and Embryo Development

Oocyte development and growth are crucial steps in foetal development, to create a reserve of eggs within the female reproductive organs for later fertility. Meiotic oocyte maturation and ovulation in response to hormonal stimuli at puberty begin a female's reproductive period. Development and release of an egg allows fertilisation by sperm, and subsequent embryonic development via mitotic cell divisions. Throughout this thesis, an 'oocyte' is understood to be an immature female gamete, whereas, an 'egg' refers to the cell in its mature stage.

1.1.1. Follicular Development and Oogenesis

Gamete development begins as proliferation of germ cell progenitor cells which migrate to the developing gonads within the first few weeks of human embryonic development and undergo a process known as gametogenesis. Oocytes are produced within the developing ovary, in accordance with the inherited XX chromosomes conferring female sex, or spermatozoa develop in the developing testes, as dictated by the male XY chromosomes. Somatic cells are diploid, with a double set of chromosomes, in order to produce two identical daughter cells at mitotic cell division. During the cell division of germ cells- known as meiosis- germ cells undergo two divisions, with a purpose to produce cells with half the number of somatic chromosomes, and half the original and normal amount of nuclear information. Thus, upon fusion of the oocyte and sperm at fertilisation, the usual diploid number and amount of genetic information (DNA- deoxyribose nucleic acid) can be restored before embryonic development begins. During embryonic development of the female foetus in the uterus, germ cell development begins in the 2nd week of pregnancy, whereas meiosis begins nearer the time of birth.

The stages of both meiotic divisions (I and II) are similar to that of mitosis. During interphase, the DNA in the nucleus is copied to produce two sets of identical chromosomes. In the following prophase, these chromosomes condense into recognisable X-shaped structures and each pair with their identical sister chromosome. The membrane around the nucleus then breaks down, entering meiotic metaphase, involving the alignment of chromosomes in their pairs along the meiotic spindle, created by microtubules assembling at the edge of the cytoplasm. In anaphase, organelles known as centrioles pull the pairs of chromosomes apart to the opposite ends of the cell. In Telophase, the chromosomes reach the opposite poles of the cell, and an asymmetric division yields a daughter cell and what is known as a polar body (PB) both surrounded by the outer protective zona pellucida (ZP), and both with a set of DNA. After the second meiotic division, there is one daughter cell with two extruded PBs within the perivitelline space, and half of the initial genetic information within its newly-formed nucleus due to the lack of a second DNA replication phase. Both PBs from the first and second meiotic division are of little importance and eventually degrade.

Flat epithelial cells known as granulosa cells derive from ovarian surface epithelium and surround each individual developing oocyte, separating the ovary into subunits called follicles. The developing oocytes within the foetal ovarian follicles undergo the very first stage of meiosis I in the later stages of foetal development. In most animals, they then become arrested at prophase I, with the nuclear membrane intact (Sadler, 2004). At this stage, the oocyte is known as an immature oocyte, or 'germinal vesicle' (GV) oocyte, as its nucleolus is contained within a visible vesicle. This GV arrest is maintained by a number of cell cycle inhibitors, preventing further cell development.

Within each individual follicle, the GV oocytes are each surrounded by nutritive cumulus cells, derived from the somatic granulosa cells of the follicle walls. Gap junctions connect the cells, extending from the cytoplasm through the ZP to the adjacent cumulus cell cytoplasm. Metabolic processes such as glycolysis occur in these cells, providing the developing oocyte with substrates e.g. pyruvate required for energy production and maintenance of cell viability (Sadler, 2004; Voronina and Wessel, 2003).

Prophase I arrest occurs near to the time of birth, and a female is born with her full ovarian complement of oocytes (~700,000-2million), all at GV stage. It isn't until puberty that changes start to occur, when only ~400,000 remain (Sadler, 2004).

1.1.2. Oocyte Maturation and Ovulation

In most mammals, sexual maturity and sexual cycles are governed by Gonadotrophin-releasing hormone (GnRH) secreted by the hypothalamus. Once puberty is initiated in humans, monthly release of follicle-stimulating hormone (FSH) and luteinising hormone (LH) from the anterior pituitary gland located in the brain stimulates the development of ovarian follicles, resumption of meiosis I and thus the exit of oocytes within the ovary from prophase I (see Fig. 1.1.2.1). Other mammals such as rodents, pigs, cows and sheep enter their oestrous phase several times a year, often affected by season, their cycles differing in length and the number of developing follicles differing with varied litter size. Each cycle, release of FSH from the anterior pituitary induces the growth of a number of follicles. Granulosa cells secrete oestrogen in order to induce proliferation of the endometrial lining of the uterus, and to reduce the amount of mucus surrounding the cervix, in order to allow sperm access. Granulosa cells and the oocyte both secrete glycoproteins to form the ZP, and fluid begins to fill the spaces between granulosa cells, the primary follicle now becoming the secondary follicle. The granulosa cells derive the cumulus cells, and the cumulus oocyte complex (COC) is formed, while stromal cells surrounding the follicle become secretory thecal cells. Of the several developing follicles, only one will reach full maturity, the others rendered useless and degenerating. When the secondary follicle reaches maturity, the release of LH ceases prophase I arrest, and meiosis I is completed (Sadler, 2004; Downs, 1989). Germinal vesicle breakdown (GVBD) occurs to allow for chromosome segregation, and an asymmetric division is achieved, where the secondary oocyte receives the majority of the cytoplasmic contents, the extruded PB receiving very little (Sadler, 2004; Voronina and Wessel, 2003). Once meiosis I is completed, the cell enters the second meiotic division. When the developing oocyte reaches metaphase of the second meiotic division (MII), it becomes arrested again, once again mediated by cell cycle

inhibitors. The timing of oocyte maturation differs greatly between mammalian species, from 6-7 hours in most rodents, to 15-20 hours in human, 16-24 hours in bovine species, 36-40 hours in porcine species, and as long as 40-48 hours in cats (Voronina and Wessel, 2003; Dominko and First, 1997; Sirard *et al.* 1989; Johnston *et al*. 1989; Hunter, 2000).

Spontaneous oocyte maturation may also occur in culture if the follicular cells are removed, suggesting a responsibility of granulosa cells to provide or maintain the cell cycle inhibitors in order to maintain prophase I arrest. The timing of spontaneous maturation however is longer than natural hormone-induction (Voronina and Wessel, 2003).

It is at the MII stage of development that the egg is ovulated from the ovary, a number of hours after undergoing arrest. Only ~400 eggs are ovulated in one human reproductive lifetime. The surge of LH also causes ovarian contractions which lead to ovulation of the mature egg within its cumulus mass from the ovary and into the fallopian tube. The egg is collected from the ovaries by finger-like projections at the end of the oviducts, called fimbriae, and then is able to move along the tubes, facilitated by cilia lining the epithelium. Once in the fallopian tubes, the egg is ‘wafted’ down the length of the tubes, where fertilisation by sperm is possible. The MII egg is not released from its arrest until egg is activated by fertilisation.

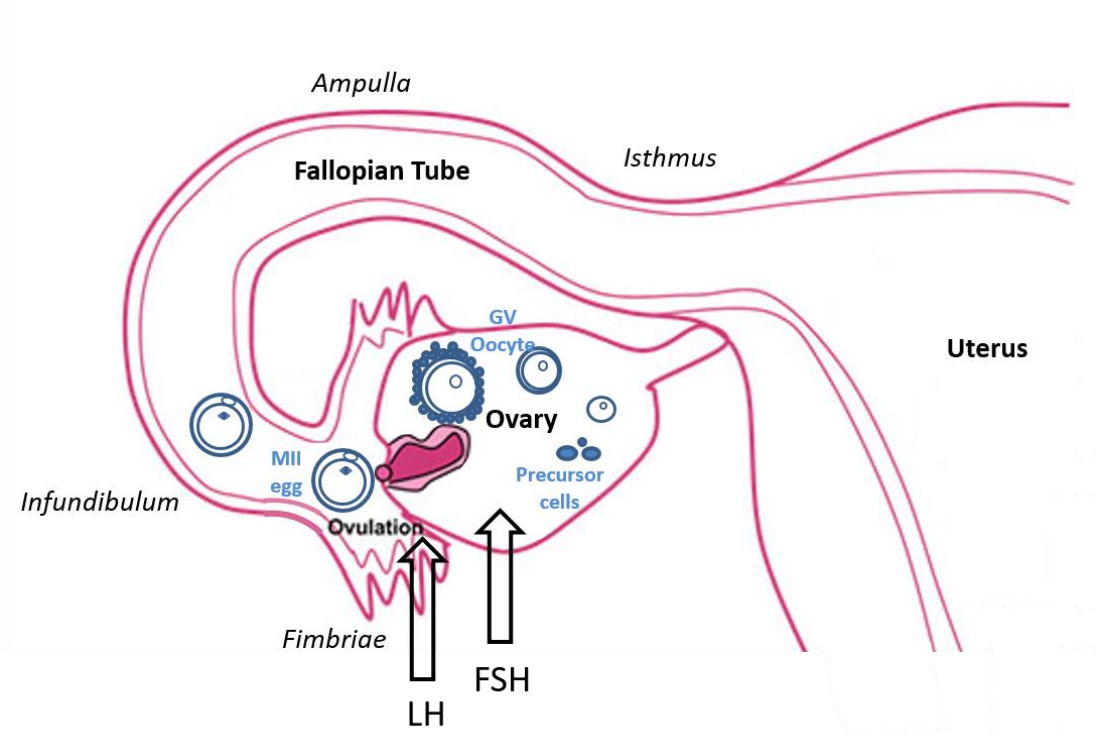

Fig.1.1.2.1. Oocyte Maturation within the Ovarian Follicle and Ovulation into the Fallopian Tubes

Immature oocytes develop from precursor cells within the ovarian follicles and become arrested at prophase I of the meiotic cell cycle, characterised by a nucleolus contained within a germinal vesicle (GV). At puberty, a surge of luteinising hormone (LH) initiates GV oocyte maturation to metaphase II (MII) of meiosis. Follicle rupture in response to LH causes ovulation of the mature MII egg into the fallopian tube.

1.1.3. Fertilisation

After the egg is ovulated into the oviducts, high levels of LH induce the change of the outer thecal cells into a structure called the corpus luteum, which produces progesterone in order to maintain the endometrium for later embryo implantation (Sadler, 2004).

Following intercourse, the most successful sperm reach the ampulla of the fallopian tubes, where they undergo a process called capacitation. Capacitation involves stripping the sperm head of its glycoprotein layer, so that it is able to penetrate the mass of cumulus cells surrounding the ovulated egg. Factors in the cumulus mass and interactions between the sperm and cumulus cells causes what is known as the

acrosome reaction: a number of chemical reactions which lead to the exposure of the cap-like acrosome on the sperm head (Sun *et al.* 2011; Chen *et al.* 2013). The acrosome reaction in mammals allows exposure of the sperm cell surface Izumo1 protein, which binds to the egg cell surface receptor Juno (Bianchi *et al.* 2014). After binding, enzymes within the sperm head acrosome are released, allowing sperm penetration of the ZP to reach the cytoplasmic membrane. This process also causes release of enzymes from cortical granules on the surface of the plasma membrane. These enzymes work to harden the ZP by changing the extracellular matrix conformation, in order to prevent any further sperm fusion and what is known as 'polyspermy'. Polyspermy is detrimental to the resulting zygote, as development will not continue due to presence of multiple copies of genetic information. The mitochondria and DNA contained within the sperm head are released into the egg cytoplasm, and the sperm mitochondria are quickly destroyed- by the 4Cell-8Cell transition in mice (Sutovsky *et al.* 1999; Cummins, 2000). Also within the sperm contents is the sperm factor Phospholipase C zeta (PLCζ) responsible for egg activation (Saunders *et al.* 2002). PLCζ binds to phosphatidylinositol 4,5 bisphosphate (PIP_2), hydrolysing it to release inositol triphosphate (IP_3). IP_3 acts upon the IP_3 receptors on the endoplasmic reticulum (ER) membrane, causing calcium (Ca^{2+}) release (Swann *et al.* 2004). A positive feedback mechanism mediates the transient increase in IP_3 and release of Ca^{2+}. The subsequent Ca2+ oscillations being responsible for egg activation and resumption of meiosis. Two major protein kinases, MPF (maturation-promoting factor) and mitogen-activated protein kinase (MAPK) are thought to be responsible for maintaining MII arrest. MPF maintains this arrest through the action of comprising proteins cdk1 and cyclin B and its destruction is brought about by the action of Ca^{2+}-activated upstream promoters. It has been shown that MAPK destruction cannot occur until activity of MPF is decreased (Gonzalez-Garcia *et al.* 2014). Once MAPK levels fall, meiosis II is completed, and the two sets of genetic information (both male and female) are packaged into what are known as pronuclei (PN). Pronuclear formation marks the end of meiosis, and the zygote can enter the somatic cell cycle in order to begin embryonic development.

If fertilisation does not occur, the ovulated egg usually degenerates within ~24hrs, absence of an embryo causing the corpus luteum to degenerate in turn. The reduction in progesterone release stimulating shedding of the endometrial uterine lining, and initiating menstrual bleeding in humans (Sadler, 2004).

1.1.4. Embryonic Development

Pronuclei first replicate their DNA before chromosomes align on a mitotic spindle, allowing somatic cell division to begin. (see Fig.1.1.4.1.) Cleavage of cells roughly every 24 hours as mitosis continues leads to an increase in the number of cells, each called blastomeres, while the entire embryo remains the same size. Division of the cytoplasmic contents appears to have no bias, uneven cell division indicating lower developmental potential (Hardarson *et al.* 2001). Cells at the 2Cell and 4Cell stage are loosely arranged with no interaction between cells. After the third division, around the 8Cell stage, the cells undergo a process known as compaction. Cells increase their contact with each other, held together by tight junctions, and communicate more freely with each other via gap junctions (Sadler, 2004). The next divisions yield a compact ball of ~16-32 cells, known as a morula. It is at this stage where cells begin to become distinguishable from one another- the inner cells are in close contact with communicating gap junctions, whereas the outer cell layers are somewhat segregated (Sadler, 2004; Niakan *et al.* 2012).

The morula enters the uterine cavity, and cell differentiation occurs with the subsequent cell divisions, creating the blastocyst embryo. The inner cells known as the inner cell mass (ICM) are a group of pluripotent stem cells, which will go on to become the developing foetus (Sadler, 2004; Niakan *et al.* 2012). The outer cell layers flatten and become known as the trophoblast, which develops to form the placenta in order to provide an exchange of blood and vital nutrients between the mother and foetus. In human, human chorionic gonadotrophin (hCG) is secreted from differentiating blastocyst trophectoderm cells, maintaining the corpus luteum so that it continues to secrete progesterone in order to maintain the uterine wall, until the placenta forms and takes over progesterone secretions. The blastocyst embryo is characterised by the appearance of a blastocele- a fluid-filled cavity. The ZP detaches from the blastocyst in a process known as ‘blastocyst hatching’, allowing

implantation of the embryo into the uterine wall (Sadler, 2004). Foetal development follows.

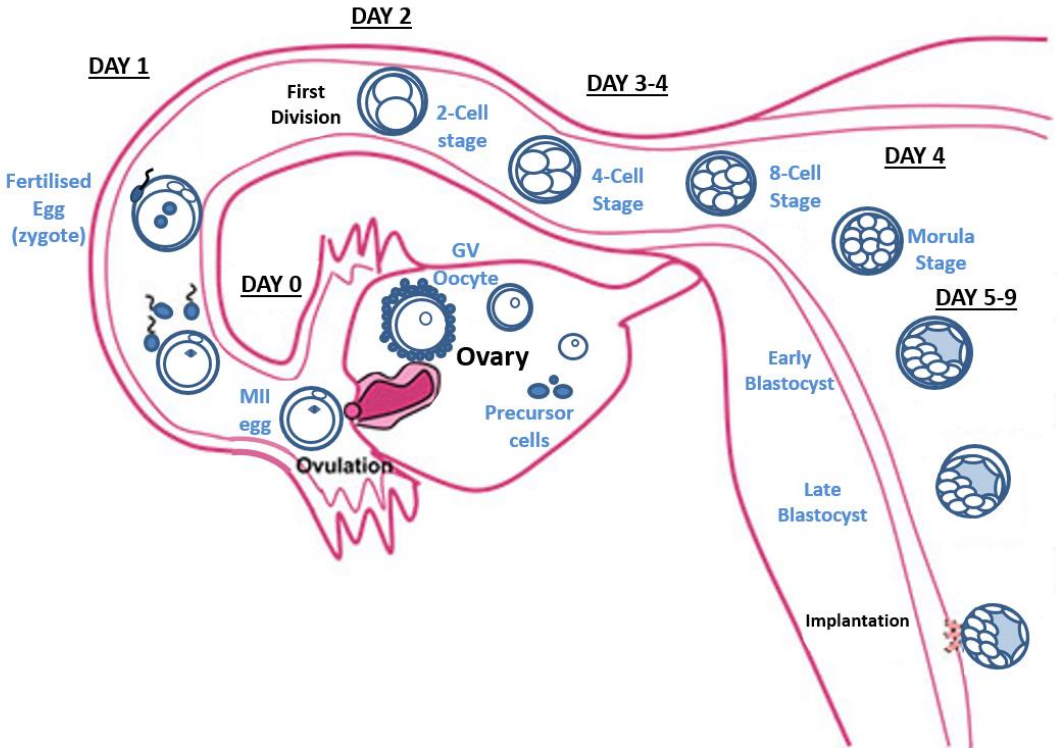

Fig.1.1.4.1. Embryonic Development Following Egg Fertilisation

Fertilisation of the MII egg by sperm in the fallopian tube completes meiosis, pronuclei form and fuse, and the zygote enters the mitotic cell cycle. Symmetric division occurs every ~24hrs. At the 8Cell-morula stages ~day 4, gap junctions start to form between cells. From ~day 5, cell differentiation begins, forming an inner cell mass (ICM) of pluripotent stem cells, which will go on to form the foetus, and an outer layer of trophoblast cells, which will continue to develop the placenta. At this stage, the embryo is at blastocyst stage. The blastocyst embryo hatches from its protective 'shell', the zona pellucida (ZP), and implants into the mother's uterus.

1.2. Infertility and developmental quality

Infertility is a prevalent issue worldwide. In the UK, 1 in 7 couples has trouble conceiving, whether it be due to problems with the female or male gametes, issues with the reproductive anatomy itself, or more general problems with the health of the individual (official Human Fertilisation and Embryology Association- HFEA statistics).

A globally growing industry is that of assisted reproduction, with over 60,000 treatments being performed each year in the UK alone (HFEA). Techniques such as intra-uterine insemination (IUI), *in vitro* fertilisation (IVF) and intra-cytoplasmic sperm injection (ICSI) are becoming widely available both on the NHS and in private fertility clinics, with donor eggs and sperm regularly used to overcome certain problems or limitations couples or individuals may face.

While safe and effective, IVF and other assisted reproductive techniques carry the risk of multiple pregnancy, therefore it is often preferred to transfer a single embryo to the mother in these methods. However, where age and other factors reduce the likelihood of pregnancy with only single embryo transfer, two or three embryos may be transferred in one cycle. The danger of multiple pregnancies is a resulting low birth weight or premature birth. There is also multiple times higher a risk of death before birth if carrying twins (4 times greater) or triplets (7 times greater) (Land and Evers, 2003; HFEA). Efforts are made by the UK's embryology regulatory body (the HFEA) to limit the number of assisted fertility-associated multiple pregnancies in Britain. Single embryo transfer is currently seen to reduce the number of multiple births by 30% (HFEA).

Other potential risks of fertility treatments include an adverse reaction to the fertility drugs and hormones administered. Although these are usually mild, ovarian hyper-stimulation syndrome is a rare but painful condition that arises in 5% of patients. High concentrations of FSH used in superovulation may cause irreparable damage to the meiotic spindle, lowering the oocyte's developmental potential (Li et al. 2013). The chances of an ectopic pregnancy are also higher in IVF situations, especially when problems reside with the fallopian tubes. It is also argued that birth defects or

long-term health issues are more common in assisted fertility (Land and Evers, 2003). Results of these are inconclusive, as the technique is still relatively new.

In vitro growth or maturation (IVM) of oocytes collected from the female at the immature GV stage also poses the problem that eggs matured in culture have a lower developmental potential than those matured *in vivo*. It is likely that IVM is not optimal for subsequent development, and possibly delays the time to MII arrest (Rizos *et al.* 2002, Gilchrist and Thompson, 2007; Hunter, 2000).

A number of assessments of gamete 'quality' are recognised but these are often invasive, and impractical in assisted reproduction techniques. Thus, less invasive, more informative and highly accurate assessment methods are sought.

1.2.1. Causes of Infertility

Infertility or subfertility, can occur as a result of many different factors concerning both the male and female gametes or reproductive organs, or often a combination of these issues.

Often causes are unidentifiable, but possible reasons for infertility in the female may include issues with ovulation itself, whether it be due to insufficient hormone production, impaired follicle development or conditions such as polycystic ovary syndrome. The maturation environment of oocytes within the ovaries is crucial for their successful development. Cumulus-oocyte interactions help maintain oocyte quality, while the composition of the follicular fluid such as oxygen (O_2) and growth factor levels have a significant effect upon the success of development (Gilchrist et al. 2008; Van Blerkom et al. 1997; Preis et al. 2007; Sudiman et al. 2014; Richani et al. 2014; Preis et al. 2007; Revelli et al. 2009).

Delayed puberty or the absence of a menstrual cycle may also be a cause. A female's reproductive potential rapidly declines after the age of 35. The primary oocytes within the ovary have been dormant at the GV stage up until this point, and though eggs may be ovulated and fertilised, they may not reach blastocyst stage. Embryos from females of advanced reproductive age frequently present with chromosomal and mitochondrial abnormalities, hence the improvement seen with mitochondrial transfer (Eichenlaub-Ritter *et al.* 2003, 2011; Wilding *et al.* 2001; Nagai *et al.* 2004).

After this stage, menopause may be reached, when ovulation ceases and natural conception can no longer occur.

Damage to or blockages of the fallopian tubes would affect collection of ovulated eggs by fimbriae, or it may reduce or prevent the movement of eggs or zygotes along the tubes. This would also cause issues with sperm reaching the egg, along with potentially hostile cervical mucus through which the sperm cannot penetrate, or damages the sperm on entry. Women may even be immune to their partner's sperm, making fertilisation difficult as natural defences attack sperm and kill it before it reaches the egg.

Many issues can occur with fertilisation, resulting in an unsuccessful embryo. Polyspermy must be prevented, and successful Ca^{2+} signalling achieved to activate the egg. The zygote must then carry out complete nuclear maturation, zygotic genome activation (ZGA) and cell division; chromosomal or genetic defects may affect transcription and further development. Thus, there are many hurdles at which the embryo can fall (Hansen, 2002). Conditions affecting the uterus such as endometriosis may prevent implantation of fertilised eggs. A past history of gynaecological issues such as ectopic pregnancy or miscarriages, may also make becoming pregnant more difficult. Other factors may include medical conditions such as diabetes or thyroid problems, and of course lifestyle factors such as stress, being overweight or underweight, and smoking influence a patient's general health and ability to conceive.

One third of infertility cases occurs due to issues with the male patient (HFEA). Most common are issues with the sperm itself, having a low sperm count or low sperm quality, where the morphology is abnormal. This often has repercussions on sperm motility, affecting the ability of sperm to reach the ovulated egg. Sperm may even not be fully mature by the time they are deposited in the female tract, making sperm-egg fusion difficult. Anti-sperm immunity has also been reported in males, where an autoimmune response attacks and kills sperm cells, causing infertility.

Issues with the male reproductive organs may include erectile dysfunction, or difficulty ejaculating. Blockage of the vas deferens- the tubes transporting the sperm

from the testes to the penis- would also affect sperm deposition. Inflammation or infection in the testes, or any of the associated glands, such as the prostate, has implications on the quality of the sperm and the environment in which it matures and survives. Torsion, or trauma to the testes may not allow sperm transport, or any resulting nerve damage could provide issues. Prior infections or diseases, surgery, drug treatment, radiotherapy or current medical conditions such as diabetes may all influence fertility potential.

Insufficient hormone production in either the hypothalamus or pituitary may also be a factor. If fertilisation is successful, male genetic or chromosomal defects could cause the zygote to arrest in development. Furthermore, absence or presence of a defective version of the male sperm factor (PLCζ) may be responsible for a lack of egg activation.

As in females, lifestyle factors such as smoking, weight or contact with chemicals or radiation also affect sperm quality. Paternal obesity has been linked to decreased development to blastocyst (Fullston et al. 2012; Hassan et al. 2010). It is thought that male fertility also decreases with age, however, this decline is not as sharp as seen in females and the extent is not clear.

1.2.2. Assisted Reproductive Techniques

Intra-uterine insemination (IUI) involves the introduction of sperm directly into the uterus in order to maximise the number of sperm accessing the fallopian tubes. This method overcomes minor male fertility problems such as insufficient ejaculation, a low sperm motility, and bypasses any issues usually encountered within the female tract e.g. impenetrable cervical mucus. It is also used in cases where vaginal intercourse is difficult, or where sperm can undergo 'washing' to reduce the likelihood of transmission of certain infections e.g. HIV. IUI may also be used where donor sperm is required for insemination.

IUI can only be performed if the female has no problems with her fallopian tubes, as the sperm must be able to freely reach the ampullary region.

The risks involved in this method are few, but there is always a small risk of adverse reactions to the superovulatory hormones often used, and the risk of multiple

pregnancy is high. The success of IUI is dependent on the absence of any other problems which may cause subfertility, the highest live birth outcome currently standing at ~16% in women under 35 (official HFEA statistics).

The most common fertility treatment available is *in vitro* fertilisation (IVF). Described by Edwards *et al.* (1980), IVF involves introducing sperm to the egg in a small drop of media *outside* of the body in a culture dish, overcoming the obstacles sperm usually require to reach the egg in the fallopian tubes and maximising the chance of sperm-egg fusion and thus fertilisation. Fertilised eggs are then cultured and monitored throughout embryonic development until a stage where they can be transferred to the uterus for implantation and foetal development. IVF is used if there are male issues with sperm count or motility, but these are not severe enough to hinder sperm fusion with the egg (Cohen *et al.* 1985). Female problems such as blockage of the fallopian tubes, or obstacles within the female tract are also overcome. IVF is also used in cases of use of donor sperm, or using frozen sperm or eggs which have been harvested at an earlier stage. Another advantage of IVF is to avoid transmission of genetic diseases, by genetic screening of blastomeres before embryo transfer.

Intra-cytoplasmic sperm injection (ICSI) is also a common technique used in assisted reproduction, comprising 53% treatments (Yoshida and Perry, 2007; HFEA). It is the introduction of the sperm head directly to the cytoplasm of the unfertilised egg, in order to overcome issues with sperm morphology, motility or sperm-egg fusion. It is also used if sperm must be surgically removed from the testis epididymis. ICSI carries some risks, more so than IVF, as it involves handling and injection of the egg, which may cause damage (Dumoulin *et al.* 2001).

The success rates (treatments resulting in live birth) of IVF and ICSI are currently around 32% in women under 35, dropping to below 13% in women over 40, and only 2% in women over 45 (official HFEA statistics).

A newly-established technique sometimes known as mitochondrial replacement therapy (MRT) is soon to be available in the UK, and involves mitochondrial donation to overcome inherited mitochondrial diseases (Craven *et al.* 2010). In this technique, the mother's egg and the donor's egg are fertilised with the sperm of the desired father, then the pronuclei are transferred from the mother's zygote to the cytoplasm of the donor zygote which has had its pronuclei removed. The donated egg with its undamaged mitochondria will improve the chances of a successful pregnancy.

1.2.3. Assessment of oocyte, egg and embryo quality

Assessing the quality of an oocyte, egg or embryo can be difficult, as no one way is proven or seen to be the best measure of developmental potential. In clinical and laboratory situations, eggs and embryos are generally assessed by their morphology, as the appearance of the cells and their characteristics can be an indication of their developmental health.

Immature oocytes can often be assessed by their morphology, as a large perivitelline space and irregular shape can be indicative that the oocyte isn't quite 'healthy'. A centrally positioned GV is thought to confer indications of developmental potential (Brunet and Maro, 2007; Bellone *et al.* 2009). Meanwhile, another widely investigated phenomenon is nuclear chromatin localisation around the nucleus. Oocytes whose chromatin neatly surrounds the nucleolus (SN) in a ring, are found to be more likely to mature, fertilise and develop to blastocyst, possibly due to the fact that maternal transcription is higher in SN oocytes until after meiotic division. Conversely, oocytes with chromatin in a 'messy', more diffuse arrangement, not surrounding the nucleolus (NSN) are thought to be of lower quality and have a lesser developmental potential (Christians *et al.* 1999). That being said, live and healthy offspring are yielded from such oocytes.

It is thought that granulosa cells have an effect on chromatin conformation, repressing transcription in order to maintain a SN configuration (Zuccotti *et al.* 2002; Christians *et al.* 1999; De La Fuente and Eppig, 2001). Thus, the presence of cumulus cells is likely to increase oocyte cell quality.

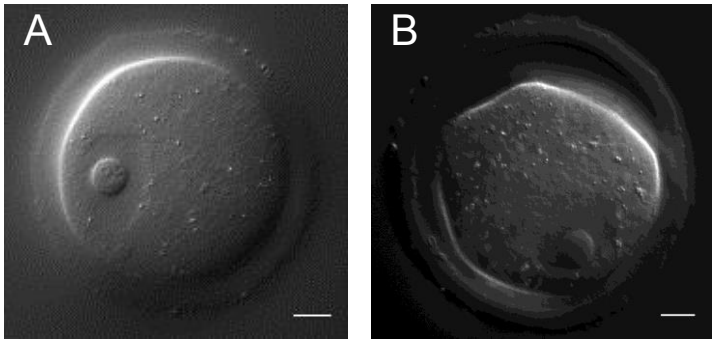

Fig.1.2.3.1. Examples of 'Good' versus 'Bad' Morphology Oocytes
(A) An example of what is considered to be a 'good' morphology oocyte: spherical in shape, with no perivitelline space; (B) an example of a 'bad' morphology oocyte: not spherical, with large gaps in the perivitelline space. Scale bars represent 10µm.

The morphology of mature eggs is also an indicative feature. Again, the presence of a large perivitelline space is suggestive of a lower quality egg. The presence of the MII spindle is essential for further development, and the appearance of the cytoplasm itself is thought to be informative. It is thought that a darker, more granular cytoplasm is apparent in eggs of lower quality in multiple species (Xia, 1997; Bilodeau-Goeseels and Panich, 2002; Ebner *et al.* 2001). Assessing the presence and morphology of the PB is a controversial method of quality assessment. It is thought that an intact PB is better for development, and a PB that has begun to degenerate or fragment indicates a lower quality (Rose and Laky, 2013). However, this is countered by alternative studies which argue that the PB has no effect on subsequent development (Ciotti *et al.* 2004, Verlinsky *et al.* 2003).

Embryos tend to be assessed in assisted reproduction techniques (ART) also by their general morphology, and the lack of fragmentation. It is assumed that those embryos with symmetric, healthy-looking blastomeres are of better quality and more likely to develop to blastocyst or further. Those that have reached blastocyst are assessed by confirming the presence of the blastocele, the ICM and the outer trophoblast layer (Gardner *et al.* 2000). The timing of embryonic cell divisions is also closely

monitored, as it is thought that inappropriate and asynchronous cleavage timing also gives warning signs about an embryo's health (Ajduk and Zernicka-Goetz, 2012). Pre-implantation genetic screening (PGS) or diagnosis (PGD) is a technique where blastomeres can be extracted from developing embryos without causing any detriment to development, in order to genetically screen embryos for chromosomal abnormalities or inheritable disorders (Ajduk and Zernicka-Goetz, 2012). While PGD is intended to decrease the likelihood of passing on specific genetic mutations to future offspring, PGS is designed to improve ART outcomes in aged mothers, whose embryos are more likely to suffer from chromosomal abnormalities or aneuploidy.

Biochemical markers of egg and embryo health are also often investigated. Although the egg or embryo itself cannot be stained for markers in a clinical situation, the follicular fluid from the egg collection, or the media used for cell culture can be tested for certain factors that will aid or impair development. Techniques for metabolic profiling include gas chromatography, mass spectrometry, and nuclear magnetic resonance spectroscopy. Metabolic profiling of follicular fluid composition can give indications as to the exposure of the developing oocyte to metabolites critical or detrimental to their growth within the ovary (O'Gorman *et al.* 2013). Culture fluid can be measured before and after culture, for the use or production of metabolites such as O_2 and nutrient uptake, to allow assessment of the developmental state of the egg or embryo, as metabolism can be significant as a marker of developmental potential (Collado-Fernandez *et al.* 2012; Ajduk and Zernicka-Goetz, 2012).

1.3. Metabolism in eggs and embryos

Until glycolysis commencement at the blastocyst embryo stage, the metabolism of mammalian oocytes and pre-implantation embryos is critically dependent upon oxidative phosphorylation in the ~100,000 mitochondria (Acton *et al*. 2004). Metabolic substrates in the oocyte or embryo's developmental environment provide a source for the oxidative metabolism in the mitochondria. Pyruvate is commonly thought to be the primary source of energy production in species such as mouse and human. However, fatty acids (FAs) have recently been suggested as an important alternative substrate for oxidative phosphorylation in many species. Metabolism of FAs is a significant energy source for mitochondria in oocytes of domesticated animals, such as pigs, sheep, cats, dogs and cows, that contain very large lipid droplets (LDs) (McEvoy *et al.* 2000). FA metabolism appears to be essential for preimplantation development in all mammalian embryos including those with less lipid content (Downs *et al.* 2009; Dunning *et al.* 2010).

1.3.1. Mitochondria

Mitochondria are the most abundant organelles in the mammalian oocyte and embryo, responsible for energy production in the form of adenosine triphosphate (ATP) within the cells (Van Blerkom, 2004). Typically, mitochondria are oval or rod-shaped structures, separated from the cytoplasm by a smooth outer membrane (outer mitochondrial membrane- OMM) and an inner membrane (IMM) dense with protein, with invaginations called cristae. The innermost part of the mitochondria is the mitochondrial matrix (see Fig.1.3.1.1.). In the mammalian egg however, the mitochondria are characteristically more spherical to oval, with very few, irregular cristae (Sananthan and Trouson, 2000). Within the egg, >100,000 mitochondria exist, approximately 0.3-0.5μm in diameter, and their morphology remains constant throughout fertilisation and preimplantation development (Sananthan and Trouson, 2000). Taking up ~30% of the cytoplasm, the distribution of these organelles, however, changes throughout development. They move within the cell, thought to be governed by remodelling of microfilaments (Yu *et al.* 2010), and they can fuse to

form networks. In a number of mammalian species, redistribution of mitochondria is described throughout development (Sun *et al.* 2001; Bavister and Squirrell, 2000; Yu *et al.* 2010). At immature stages, mitochondria are accumulated around the GV, and as maturation ensues, they disperse to a more homogenous distribution throughout the cytoplasm. Effective achievement of this process is thought to yield more successful development to MII, and beyond to blastocyst stage (Stojkovic *et al.* 2001).

Mitochondria also contain their own DNA and ribosomes for protein synthesis, contained within the mitochondrial matrix. Thought to be of bacterial origin due to the circular nature, the mitochondrial DNA (MtDNA) possesses 37 genes, encoding 24 RNAs and 13 proteins essential for mitochondrial function (Anderson *et al.* 1981). All other mitochondrial proteins are encoded by the nucleus; thus mitochondria would not survive outside of the host cell.

After ovulation, eggs no longer receive ATP or substrate provision from cumulus cells, thus the cells rely solely on their mitochondria to supply the energy demands of development until implantation of the blastocyst stage embryo.

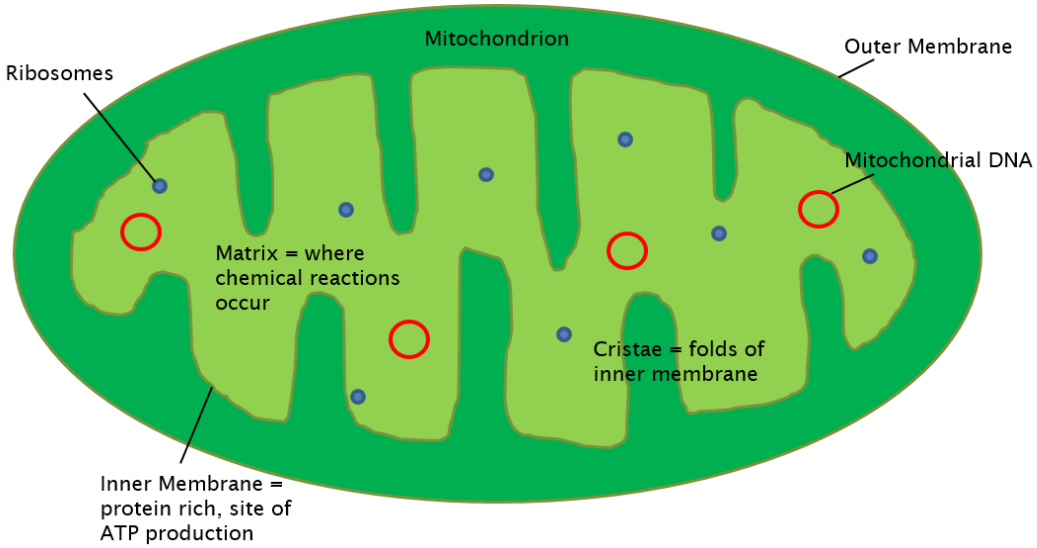

Fig.1.3.1.1. Structure of Mitochondria within the Mammalian Egg

Mitochondria are organelles with a double membrane, responsible for energy production in the form of ATP. Mammalian egg and embryo mitochondria are unusual in that they have very few invaginations of the protein-rich inner membrane (cristae). The dense mitochondrial matrix is where vital chemical reactions take place. Mitochondrial DNA and associated ribosomes present in the matrix are responsible for manufacture of proteins within the inner mitochondrial membrane (IMM).

1.3.2. Metabolic Substrates

Successful development of mammalian oocytes and early embryos depends on the generation of sufficient ATP by their abundant mitochondria. Glycolysis is inactive in the mouse oocyte and subsequent developmental stages, until the blastocyst embryo stage (Krisher & Bavister, 1998; Downs 1995; Harris *et al.* 2009; Barbehenn *et al.* 1974). Within its ovarian follicle, the immature GV oocyte is surrounded by nutritive cumulus cells performing metabolism of various substrates such as glucose, which supply substrates and ATP to the oocyte via gap junctions (Downs, 1995; Sutton-McDowall *et al.* 2010; Collado-Fernandez *et al.* 2012). The oocyte can also take up nutrients directly from the follicular fluid, receiving metabolic molecules from the blood plasma. MII eggs and developing early embryos must use their internal supply of metabolic substrates once ovulated, but this is not sufficient to allow for full-term development, so they may also take up certain substrates from fluid within the uterine tubes (Collado-Fernandez *et al.* 2012).

The two main substrates thought to be metabolised by mitochondria in mammalian eggs and embryos are pyruvate and fatty acids. Pyruvate ($C_3H_4O_3$) is a carbon-rich derivative of glucose, readily metabolised by mitochondria to yield ~30 ATP molecules. It is thought that pyruvate is used as a primary energy source for developing mouse and human eggs or embryos (Dunning *et al*. 2011; Dumollard *et al*. 2008; Collado-Fernandez *et al*. 2012; Leese, 2002). In cell culture, pyruvate is included in cell culture media at ~0.2mM and is vital for *in vitro* egg and embryo development. Pyruvate is transported into the mitochondrial matrix via monocarboxylate transporters (MCTs) (Garcia *et al.* 1994), and undergoes decarboxylation by the pyruvate dehydrogenase complex (PDH) in order to yield 2-carbon acetyl co-enzyme A (CoA) and carbon dioxide (CO_2), along with mitochondrial co-factor, reduced nicotinamide adenine dinucleotide (NADH). Pyruvate in the mitochondria may also undergo carboxylation by pyruvate carboxylase to produce 4-carbon oxaloacetate (see Fig.1.3.2.2.) (Downs and Mastropolo, 1994; Dumollard *et al.* 2004; Schell and Rutter, 2013; Sugden and Holness, 2011).

FAs are also carbon-dense molecules which are highly energy-rich, generating a large amount of ATP per molecule (~106 ATP molecules). Thus, they are a valuable substrate for the developing egg or embryo. FAs are made up of a carboxylic acid with a long saturated or unsaturated aliphatic chain (see Fig. 1.3.2.1.). The majority of fatty acids are esterified to a glycerol molecule and stored within the cell cytoplasm as neutral triglycerides, or triacylglycerols (TAGs) within hydrophobic vesicles known as LDs (Ambruosi *et al.* 2009; Dunning *et al*. 2011). FAs not contained within LDs are known as non-esterified FAs (NEFAs) or free FAs (FFAs) which are located freely in the cytoplasm. Fatty acids are often referred to by the number *n* of carbon atoms making up their chain and the number *m* of carbon-carbon double bonds present, using the notation (*n*:*m*). Saturated fatty acids contain no double bonds, while unsaturated fatty acids contain double bonds, and can be mono-unsaturated (with one double bond), or poly-unsaturated (with multiple double bonds). The fatty acids most commonly found in mammalian eggs and embryos are saturated palmitic (16:0) and stearic (18:0) acids, and mono-unsaturated oleic (18:1) acid (McEvoy *et al.* 2000).

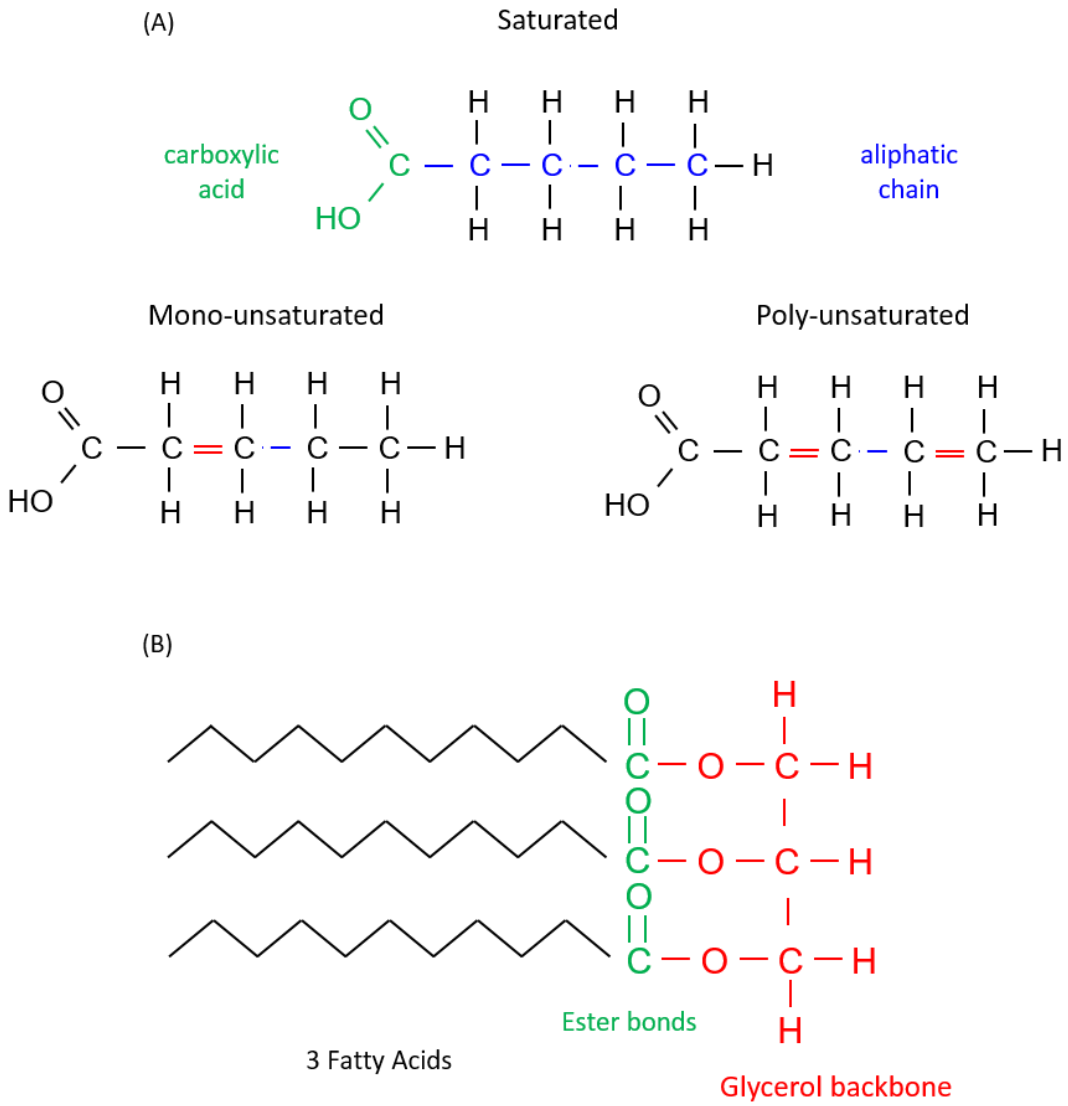

Fig.1.3.2.1. Structure of Fatty Acids and Triacylglyerols

(A) Fatty acids comprise of a carboxylic acid (COOH) with a long aliphatic chain (CH_2^n) with an equal number (n= 4-28) of carbon atoms, and a methyl group (CH_3). Saturated fatty acids contain no carbon-carbon double bonds (C=C), whereas monounsaturated fatty acids contain one double bond, and poly-unsaturated fatty acids contain multiple double bonds. (B) Triacylglycerols (TAGs) are neutral lipids composed of three fatty acid chains esterified (COO^-) to a glycerol backbone.

Fatty acids are liberated from LDs by lipolysis via lipase enzymes, breaking TAGs down into glycerol and three fatty acyl-CoA chains. These chains are transported to the mitochondria to undergo the process of fatty acid metabolism, known as β-oxidation (see Fig.1.3.2.2.). The process of β-oxidation begins with uptake of fatty acids into the mitochondria themselves, via L-carnitine transport. L-carnitine exists in the cytoplasm, outside the mitochondria, in order to transport fatty acids into the mitochondrial matrix. L-carnitine replaces CoA in liberated fatty acyl-coAs and binds to proteins called Carnitine palmitoyl transferases (CPTs) on the inner and outer mitochondrial membranes (Dunning *et al.* 2010; Sturmey *et al.* 2009). CPTs shuttle the fatty acyl-carnitine molecules into the matrix. Once inside the mitochondria, the role of L-carnitine is to release the fatty acyl chains, and bind excess acetyl CoA to transport it back into the cytoplasm. Fatty acyl chains are once again bound to CoA, and undergo oxidation by acyl-CoA dehydrogenase, producing mitochondrial co-factor, reduced flavin adenine dinucleotide ($FADH_2$). The molecule is then hydrated by H_2O addition, and undergoes further oxidation via β-hydroxyacyl-CoA dehydrogenase. Finally, thiolytic cleavage produces a 2-carbon molecule of acetyl CoA and a shorter fatty acyl-CoA which will undergo the above oxidation steps again (see Fig.1.3.2.2.). This cycle continues until the fatty acyl chain is completely oxidised, one fatty acid yielding half the number of acetyl CoA molecules as carbons in its acyl chain.

Alongside fatty acids and pyruvate, it is understood that amino acid glutamine also contributes to the promotion of egg and embryo metabolism, as it contributes to the production of 5-carbon α-ketoglutarate (Rieger, 1992). However, it has been shown that glutamine cannot support the production of ATP in the zygote (Dumollard *et al.* 2008).

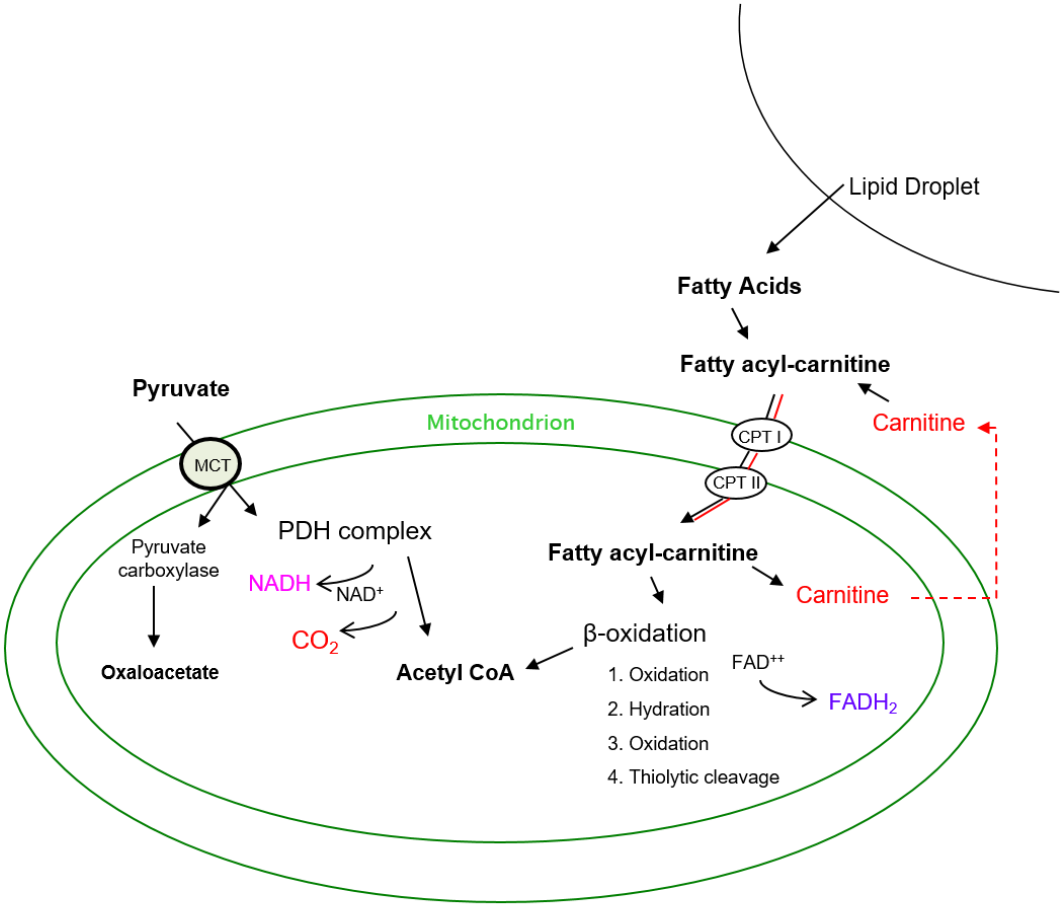

Fig.1.3.2.2. Oxidation Pathways of Common Metabolic Substrates

Pyruvate is taken up into the oocyte mitochondria via membrane-bound mono-carboxylate transporters (MCTs), before undergoing decarboxylation by the pyruvate dehydrogenase (PDH) complex to yield Acetyl co-A and mitochondrial co-factor NADH, or carboxylation by pyruvate carboxylase to produce oxaloacetate. L-carnitine replaces CoA in cytoplasmic fatty acyl-coAs, binds to mitochondrial membrane carnitine palmitoyl transferases (CPTs) in order to shuttle the fatty acyl-carnitine molecules into the matrix. L-carnitine releases the fatty acyl chains and bind excess acetyl CoA to transport it back into the cytoplasm. Fatty acyl chains are once again bound to CoA, and undergo oxidation by Acyl-CoA dehydrogenase, producing mitochondrial co-factor $FADH_2$. The molecule is then hydrated by H_2O addition, and undergoes further oxidation via β-hydroxyacyl-CoA dehydrogenase. Finally, thiolytic cleavage produces a 2-carbon molecule of acetyl CoA and a shorter fatty acyl-CoA which will undergo the above oxidation steps again.

1.3.3. The TCA Cycle and Oxidative Phosphorylation

Acetyl CoA derived from oxidation of pyruvate and FAs is a molecule composed of a carboxyl group (CH_3) attached to a carbonyl (C=O) (acetyl) and β-mercaptoethylamine linked to pantothenic acid (CoA). It is metabolised in what is known as The Citric Acid cycle (TCA cycle). Also known as the Kreb's cycle or the tri-carboxylic acid cycle, TCA cycle is a series of chemical reactions occurring in the matrix of the mitochondria, producing vital components of the working cell (see Fig.1.3.3.1.).

Acetyl CoA enters the TCA cycle by combining with the 4-carbon TCA cycle product, oxaloacetate, in order to produce a 6-carbon citrate molecule. The following chemical reactions are carried out by various enzymes, and are a number of oxidation (dehydrogenation) steps in order to liberate hydrogen atoms for the subsequent steps of ATP production. Mitochondrial co-factors, nicotinamide adenine dinucleotide (NAD^+) and flavin adenine dinucleotide (FAD^{++}) accept liberated hydrogen, becoming reduced to NADH and $FADH_2$, respectively. Citrate undergoes enzymatic action of isocitrate dehydrogenase. This produces one molecule of NADH and one proton (H^+), and citrate loses a carbon as CO_2 is given off as a waste product, becoming α-ketoglutarate (a 5-carbon molecule). α-ketoglutarate dehydrogenase also creates one molecule of NADH and a H^+, and CO_2 in order to produce succinate (4-carbon). IMM-bound Succinate dehydrogenase transfers two hydrogen atoms (H_2) to FAD^{++}, in order to produce $FADH_2$ and fumarate (4-carbon). Fumarate is then hydrated with water (H_2O) to become malate (4-carbon), which is then oxidised by malate dehydrogenase to produce further NADH, and oxaloacetate (4-carbon), allowing the cycle to begin again (Downs and Mastropolo, 1994; Dumollard *et al.* 2004).

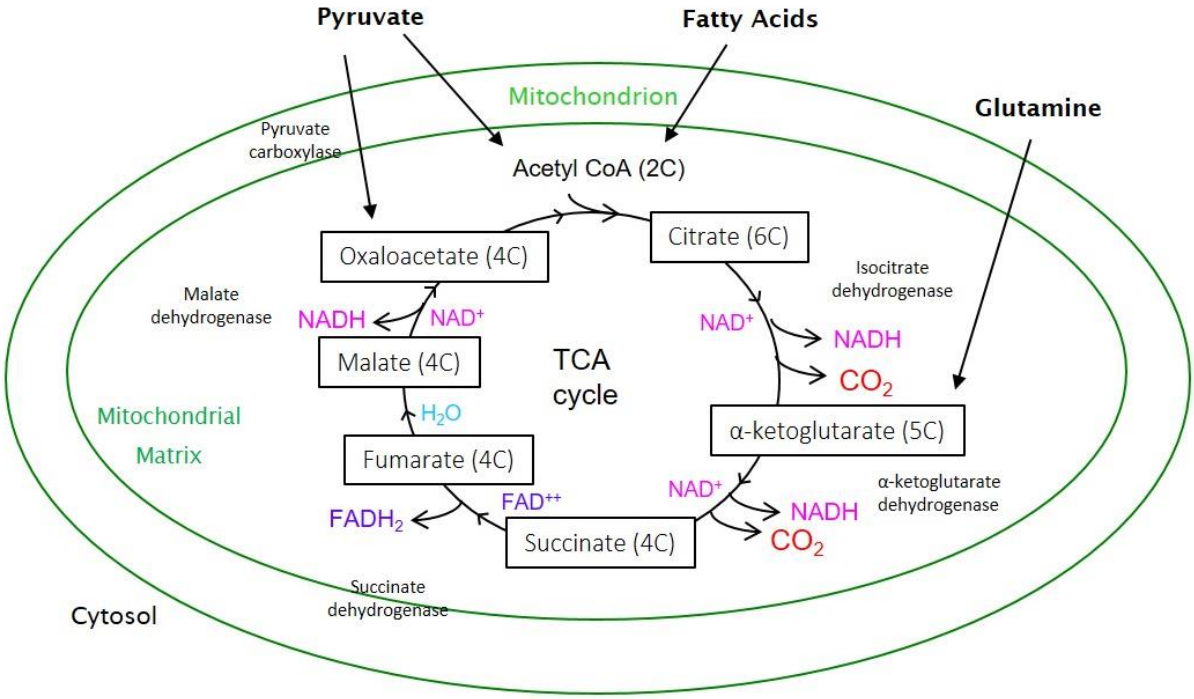

Fig.1.3.3.1. The Citric Acid Cycle

The Citric Acid Cycle is a cyclical series of oxidative reactions within the mitochondrial matrix, combining 2-carbon (2C) acetyl coA from substrate metabolism with 4-carbon (4C) oxaloacetate in order to produce citrate (6C). Oxidation of citrate by isocitrate dehydrogenase produces α-ketoglutarate (5C), CO_2 as a biproduct, and reduces mitochondrial co-factor NAD^+ to NADH enabling it to act as an electron carrier. α-ketoglutarate is oxidised to succinate (4C), producing CO_2 and also reducing NAD^+. Succinate dehydrogenase in the inner mitochondrial membrane removes H_2 from succinate to create fumarate (4C), reducing co-factor FAD^{++} to $FADH_2$. Hydration of fumarate produces malate (4C), which undergoes oxidation to produce further NADH and oxaloacetate, allowing the cycle to continue. Pyruvate may also undergo decarboxylation to produce oxaloacetate.

Reduced NADH and FADH produced from reactions of the TCA cycle are able to undergo oxidation in order to liberate hydrogen. H atoms released from $FADH_2$ and NADH and are split into protons (H^+) and electrons (e^-). Free protons within the mitochondrial matrix are then transported across the IMM into the inter-membrane space in order to fuel the Electron Transport Chain (ETC). The ETC consists of a number of membrane-bound complexes on the IMM, which transfer e^- between them and to the final acceptor, O_2 with the ultimate goal of producing ATP (see Fig.1.3.3.2.).

Electrons from NADH enter the ETC at Complex I (CI), known as NADH reductase. CI pumps $4H^+$ from the mitochondrial matrix into the intermembrane space, while transferring $2e^-$ to mitochondrial co-factor, ubiquinone. Electrons from $FADH_2$ enter the ETC at Complex II (CII), which is seen in the TCA cycle as succinate dehydrogenase. CII does not pump H^+ across the IMM, instead transferring $2e^-$ to ubiquinone, which carries $4e^-$ to Complex III (CIII). CIII, the Cytochrome b-c complex, transports $4H^+$ into the intermembrane space while transferring $2e^-$ to mitochondrial membrane protein, cytochrome c. Cytochrome c delivers these e^- to Complex IV (CIV), cytochrome oxidase, which transports $2H^+$ from the matrix, and combines $2e^-$ with an oxygen atom. H^+ pumped across the IMM generates a chemical gradient, which forms the mitochondrial membrane potential (MMP), an electrical gradient across the mitochondrial IMM due to the difference in charge of the intermembrane space and the mitochondrial matrix. Under normal cellular conditions, the MMP is -150mV negative to the cytosol. The MMP in turn, along with the existing pH (chemical) gradient creates an electrochemical proton-motive force, and H^+ flow back into the more negative mitochondrial matrix through Complex V (ATP synthase) (Perry *et al.* 2011). This generates ATP by the reduction of O_2 to H_2O and the phosphorylation of adenosine diphosphate (ADP) in a process known as oxidative phosphorylation (see Figs.1.3.3.2. and 1.3.3.3.).

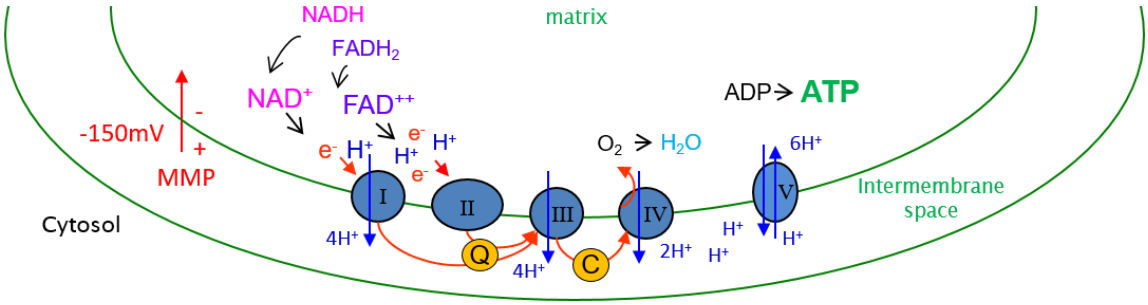

Fig.1.3.3.2. The Electron Transport Chain

Electron carriers NADH and $FADH_2$ release their hydrogens which dissociate into their comprising electrons (e^-) and protons (H^+). The electron transport chain is comprised of a number of protein complexes embedded in the inner mitochondrial membrane (IMM). Complex I accepts e^- from NADH, and passes them to co-factor ubiquinone (Q), meanwhile, it pumps $4H^+$ from the matrix into the intermembrane space. Complex II accepts e^- from $FADH_2$, also passing these to Q. Q passes these $4e^-$ to Complex III which transports $4H^+$ across the IMM and passes $2e^-$ via membrane protein cytochrome c (C) to Complex IV, which shuttles $2H^+$ across the IMM. Transfer of e^- from Complex IV to an oxygen atom causes a proton-motive force, inducing Complex V to pump $6H^+$ from the intermembrane space back into the matrix, fuelling reduction of O_2 to H_2O, and phosphorylation of ADP to create much-needed energy in the form of ATP.

The rate of NADH and $FADH_2$ generation by the TCA must equal the rate of e^- transfer along the ETC in order to maintain the driving force, the redox potential, for oxidative phosphorylation and ATP production. The redox potential can be described by the ratios of reduced NADH or $FADH_2$ to their oxidised forms, NAD^+ and FAD^{++}, respectively, and it is possible that this can be used as a measure of egg or embryo developmental potential, by its indication of the level of metabolic activity. The rate of pyruvate and fatty acid uptake and metabolism in developing mammalian embryos *in vitro* has been extensively investigated, along with redox potential, amino acid metabolism and O_2 consumption (Harris *et al.* 2009; Brison *et al.* 2004; Dumollard *et al.* 2007). Leese (2002, 2007) describes the 'quiet embryo hypothesis', suggesting that a 'quieter' metabolism expends less energy repairing cellular damage, and that an active metabolic level leads to the production of reactive oxygen species (ROS) with subsequent harmful effects. A high supply of substrates and an

increase in respiration may hyperpolarise the MMP, causing H^+ to be pumped back into the mitochondrial matrix. This results in a saturated level of reduced NADH and $FADH_2$ meaning free e^- and oxygen can form ROS, highly reactive molecules able to cause damage to numerous cellular components. It is thought that sub-optimal metabolic activity causes depolarisation of the MMP, increasing the amount of H^+ in the intermembrane space, and yields insufficient ATP for adequate development.

Mitochondrial activity can be assessed by measurement of such factors as the MMP, ATP production and redox potential. Fluorescent MMP dyes are usually cationic compounds that are sequestered into mitochondria, dependent on the level of membrane polarisation, and subsequently quenched, allowing assessment of the effect of various conditions on the proficiency of the mitochondria to produce ATP (Perry *et al.* 2011). Luminescence imaging can be used as an assay of ATP production. The action of luciferase upon luciferin produces luminescence in the presence of ATP, and has been previously used to measure mitochondrial activity in eggs (Saunders *et al.* 2002; Campbell and Swann, 2006; Dumollard *et al.* 2008). Alternatively, NADH and FAD^{++} emit autofluorescence, in the blue (460nm) and green (535nm), respectively. This can be exploited as performed by Dumollard *et al.* (2007), to allow the assessment of redox state and potentially developmental assessment, through fluorescence imaging.

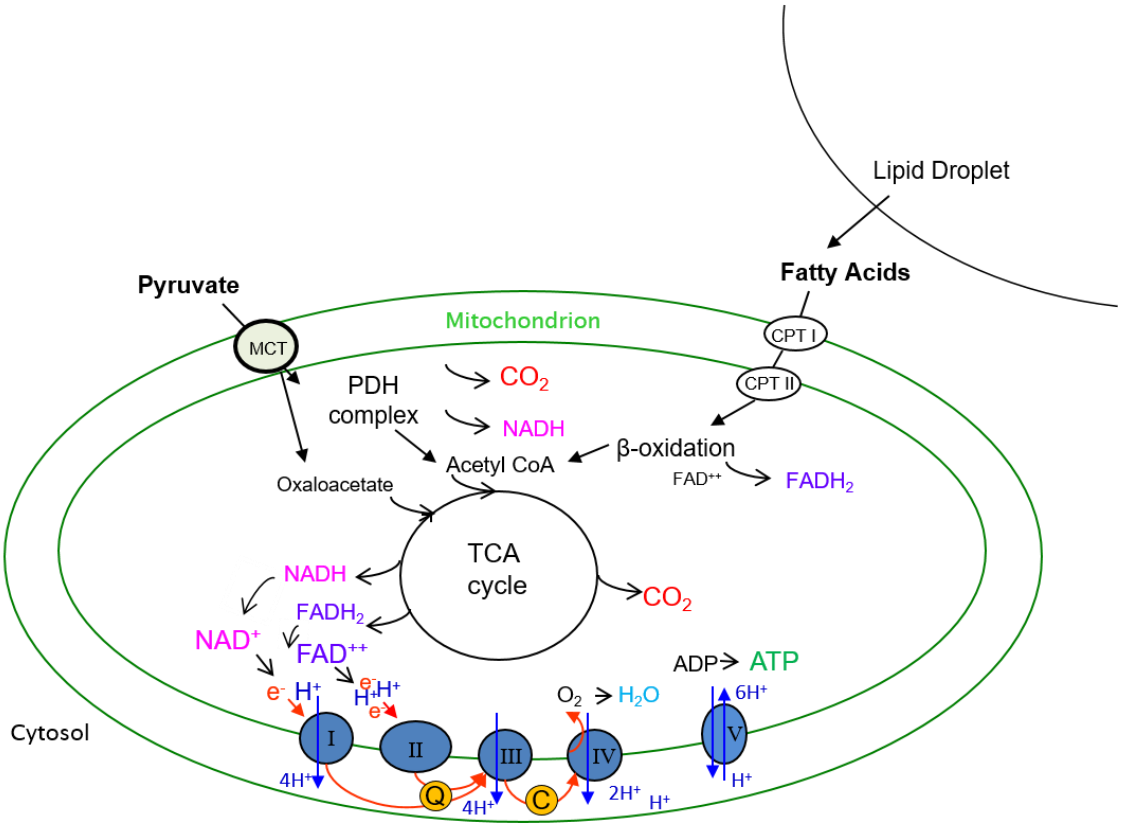

Fig.1.3.3.3. The Oxidation of Common Substrates in Order to Produce ATP

Oxidation of fatty acids and pyruvate fuels the TCA cycle, which transfers electrons to the ETC in order to produce ATP.

1.4. Lipid Droplet Biology

LDs are dynamic intracellular organelles present in most cell types, with a wide range of roles including lipid storage for later ATP synthesis, and membrane maintenance. They are cytoplasmic vesicles generally composed of a neutral TAG core, surrounded by a single phospholipid layer, with multiple protein interactions. Many hydrophobic TAGs aggregate within these droplets, shielded from the cytoplasm by the phospholipid monolayer. The number and size of LDs depends on the cell type and species, some being as small as a few hundred nanometres in diameter, some growing to a size of ~100μm in adipocyte cells (Walther and Farese, 2012). The composition of these dynamic organelles differs greatly between cell types, the lipid content and protein inclusions reflecting its role and the present cellular functions (Thiele and Spandl, 2008; Walther and Farese, 2012; Wilfling *et al.* 2014).

The process of LD formation is still mostly unclear, but a number of models have been suggested, from *de novo* synthesis at the ER to fission of existing droplets. The most widely accepted method of LD growth is fusion of existing droplets, or expansion via synthesis of new TAGs either at the LD surface, or transferred from synthesis at the ER. Fusion events are rare but may occur under specific conditions within the cell (Thiele and Spandl, 2008; Walther and Farese, 2012; Wilfling *et al.* 2014). Conversely, LD degradation occurs in the form of lipolysis. TAG metabolism by lipase enzymes liberates fatty acids for metabolism (Thiele and Spandl, 2008; Walther and Farese, 2012).

1.4.1. Lipid Droplet Formation

Theories of LD formation are few, but it is not yet completely clear which is the primary method of storing lipids in these intracellular vesicles. The most probable and widely accepted method, is the notion of *de novo* synthesis. Neutral lipids are synthesised by the action of enzymes localised at the ER, joining free fatty acyl chains (fatty acids) to glycerol to make TAGs. It is thought that these newly synthesised TAGs then accumulate within the bilayer membrane of the ER, forming

a bulge in the membrane that becomes unstable and buds off as a new LD (see Fig. 1.4.1.1 (A) i.) (Wilfling et al. 2014; Thiel and Spandl, 2008; Kohlwein *et al.* 2013). This method explains the presence of a monolayer membrane surrounding the LD. Other theories suggest that LDs form at the surface of the ER, as an out-budding of both layers of the ER membrane, before the membrane encloses them to form the LD (see Fig. 1.4.1.1 (A) ii. and iii.) (Thiel and Spandl, 2008; Walther and Farese, 2012; Kohlwein *et al.* 2013). This method would explain the presence of ER membrane proteins within LD monolayers (Fujimoto and Parton, 2011). Fission of existing LDs is also suggested as a method of LD formation, however this is only likely during LD breakdown (lipolysis), due to increased monolayer fluidity, and has only been observed in yeast (Thiam *et al.* 2013; Wilfling *et al.* 2014). Thiele and Spandl (2008) do not believe LD formation through fission is probable.

There is also a chance that LDs could form via pinocytosis, where lipid is transported into the cell, and vesicles are formed at the cell membrane. It is highly difficult to determine which of these theories is correct. Imaging the process of LD formation at this scale is very difficult, as it is likely that these newly-formed LDs are below optical resolution (i.e. < 200nm). LD growth is responsible for their usual size within the cytoplasm, so theories are mostly speculative (Wilfling et al. 2014; Walther and Farese, 2012).

1.4.2. Lipid Droplet Growth and Fusion

Growth of LDs after they are newly formed or during cellular processes, is thought to occur through coalescence of existing droplets, and recruitment of free fatty acids for lipid synthesis at the LD surface. It is generally understood that LD growth is an active mechanism and does not occur spontaneously, likely to be a method of storing surplus lipid, or a protective mechanism to prevent lipotoxicity (Fujimoto and Parton, 2011; Walther and Farese, 2012). It is certainly found that proteins involved in TAG synthesis are expressed at the LD surface, especially during lipid loading (Walther and Farese, 2012; Wilfling *et al.* 2013). For example, feeding cells with oleic acid leads to LD formation, possibly in an attempt to minimise the number of free fatty acids in the cytoplasm (Walther and Farese, 2012). LDs are thought to

closely associate with the ER for availability of enzymes for lipid synthesis and accumulation of newly-synthesised TAGs and phospholipids (see Fig. 1.4.1.1 (B) i.) (Wilfling et al. 2014; Yang *et al.* 2012). Conversely, newly-synthesised lipids may be transported to LDs, but evidence of this is lacking (see Fig. 1.4.1.1 (B) ii.) (Walther and Farese, 2012). It is currently unclear whether with increased lipid synthesis, LDs get larger, or more LDs form (Wilfling *et al.* 2014; Yang *et al.* 2012)

Although fusion events are rare, mechanisms are in place in many cell types allowing the coalescence of LDs, possibly to reduce lipotoxicity and increase lipid storage (Yang *et al.* 2012; Thiele and Spandl, 2008; Walther and Farese, 2012; Wilfling *et al.* 2014). Murphy *et al.* (2010) describe the fusion of homotypic LDs, suggesting that monolayer membranes fuse very quickly, followed by a slower transfer of lipid contents. The phospholipids making up the LD membranes are thought to be involved in stabilisation of LDs under normal conditions, and destabilisation of LDs for fusion to occur (Thiam *et al.* 2013; Yang *et al.* 2012; Walther and Farese, 2012). A higher concentration of phospholipid phosphatidyl choline is present in more stable LDs, whereas, fusogenic phosphatidic acid is present at a higher concentration in LDs able to fuse (Yang *et al.* 2012; Walther and Farese, 2012). Fat-specific protein (Fsp27) is seen to be abundant at LD-LD contact sites (Gong *et al.* 2011), while SNARE (soluble N-ethylmaleimide-sensitive factor attachment receptor) proteins binding ATPases are also thought to promote LD fusion (see Fig. 1.4.1.1 (B) iii.) (Yang *et al.* 2012; Bostrom *et al.* 2007).

It is thought that clustering of LDs may precede fusion, with the involvement of LD-associated proteins such as perilipin1 and seipin (Yang *et al.* 2012; Walther and Farese, 2012; Martin and Parton, 2006). The movement and remodelling of LDs is thought to be microtubule-dependent, combined with action of actomyosin complexes (Walther and Farese, 2012; Dutta and Sinha, 2015), and fusion events are seen to be inhibited with microtubule inhibition (Bostrom *et al.* 2005).

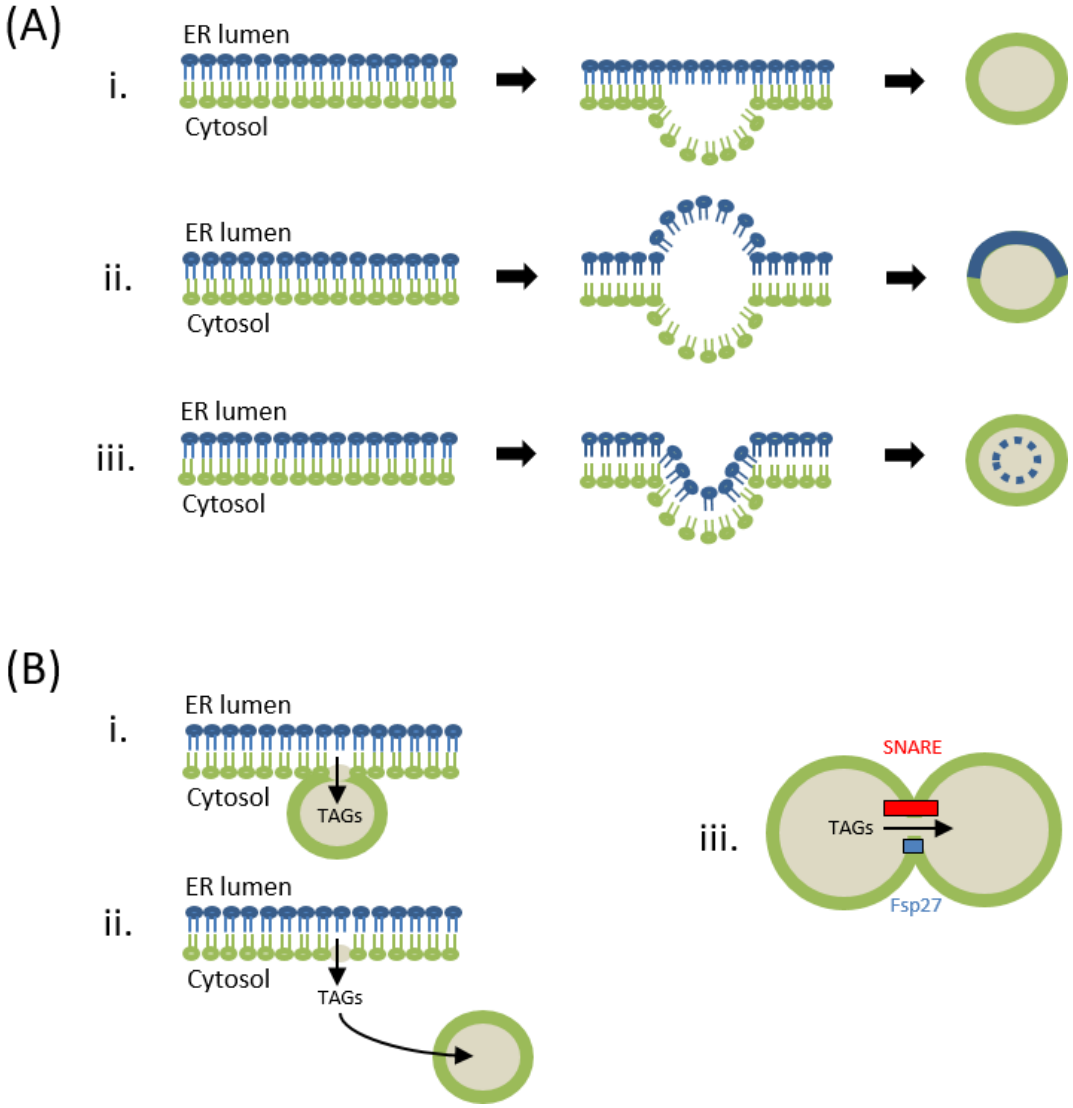

Fig.1.4.1.1. Theories of Lipid Droplet Formation and Growth

(A) Theories of lipid droplet formation: i. TAGs accumulating between phospholipid 'leaflets' of the ER membrane create a bulge which buds off as an LD, the LD monolayer comprised from one layer of the ER bilayer; ii. TAGs accumulating between leaflets of the ER membrane cause bulging of both ER bilayers, the LD buds off and its membrane has contributions from both ER membrane layers; iii. A budding off of the ER bilayer to create an LD causes a small inclusion of the inner leaflet of the ER membrane, requiring rearrangement. (B) Theories of lipid droplet growth: i. LDs associate with the ER and accumulate newly-synthesised TAGs; ii. Newly-synthesised TAGs from the ER are transported to LDs within the cytoplasm; iii. LD fusion occurs, facilitated by LD-membrane proteins such as SNARE proteins and Fsp27, allowing transfer of TAGs.

1.4.3. Lipid Droplet Degradation

LD degradation involves a process known as lipolysis, an enzymatic break down of TAGs comprising LDs into FFAs and glycerol, in order to liberate FAs for multiple roles including mitochondrial metabolism or plasma membrane synthesis.

It has been shown that in some cell types, lipolysis begins with LDs dispersing, and larger droplets splitting, in order to expose a larger surface area for FA liberation (Marcinkiewicz *et al.* 2006; Thiele and Spandl, 2008). Although logical, there is limited evidence for this.

TAG breakdown is governed by a number of LD-specific resident lipolytic enzymes called lipases, which sequentially hydrolyse LD lipids into their FA components (Thiam *et al.* 2013; Kohlwein *et al.* 2013; Fujimoto and Parton, 2011). LD monolayer phospholipids are likely also enzymatically removed by phospholipases, while associated proteins will be degraded, leading to LD shrinkage (Walther and Farese, 2012; Thiam *et al.* 2013). How lipolysis is regulated is unknown (Kohlwein *et al.* 2013). However, the family of LD-surface proteins perilipins are found to interact with lipases at the LD surface, or in the cytosol thought to regulate TAG breakdown (Yang *et al.* 2012; Martin and Parton, 2006; Ducharme and Bickel, 2008). Perilipin1 is also thought to sterically protect LDs from lipase action, further supporting this hypothesis (Walther and Farese, 2012).

1.5. Characterisation of Lipid droplets in mammalian eggs

Many studies have been carried out in an attempt to characterise LDs and the lipid content of mammalian oocytes. Most notably, the lipid content of oocytes varies considerably between species. Domestic species such as pig and dog oocytes contain large amounts of lipid, their cytoplasm dense with large LDs. Bovine and ovine oocytes appear less densely packed with lipid, but droplets are still large (>1µm diameter) and abundant. Mouse and human oocytes are the most studied and are biologically relevant species. Due to the similarities seen between cell types, mice can be used as a model system, enhancing the medical implications of this research. The lipid content of mouse and human oocytes and embryos is relatively low, and LDs are small (typically <1µm diameter). It is often hypothesised that the lipid content of cells reflects the extent to which they perform and rely upon metabolism of fatty acids as a source of energy.

Efforts to image LDs and lipid content of human or mouse eggs prove difficult, as lower lipid contents are less easy to quantify, and smaller LD sizes require sub-micron-resolution imaging techniques to be resolved (Watanabe *et al.* 2010). The lipid content of mammalian oocytes and embryos has traditionally been assayed by destructive chemical analysis (Ferreira et al. 2010; McEvoy *et al.* 2000; Loewenstein and Cohen, 1964), or by fluorescence imaging of lipophilic dyes (Genicot *et al.* 2005; Yang *et al.* 2010). However, these methods have multiple limitations and are not compatible with continued oocyte or embryo development. Perilipins such as Perilipin2 have been found to exist on the surface of LDs in oocytes, indicating that mechanisms of fatty acid metabolism are similar to those described above (section 1.4.3.) (Yang *et al.* 2010; Dunning *et al.* 2014b).

1.5.1. Conventional Methods of Investigating LDs and Lipid Content

Imaging of LDs in mammalian eggs and embryos has taken many forms. Prates *et al.* (2012) describe imaging of LDs in porcine oocytes, assessing their positioning and area using differential interference contrast (DIC). This technique is minimally invasive, despite using visible light wavelengths, whereas most imaging techniques

used to examine LDs are destructive. Electron microscopy has been performed in order to assess the position and size of LDs within fixed ovine and bovine oocytes and embryos (Bettencourt *et al.* 2015; Ordonez-Leon *et al.* 2014). The most popular technique of LD visualisation is fluorescence, using lipophilic staining techniques. Multiple studies have used fluorescent lipid dyes such as Nile red and BODIPY 493/503 to examine the LD distribution in different mammalian species, and their localisation in relation to mitochondria (Niu *et al.* 2014; Yang *et al.* 2010; Sturmey *et al.* 2006). Multiple drawbacks of using fluorescent dyes include the invasive nature of using a stain, photo-bleaching and associated toxicity, and the often unspecific staining patterns.

Evidence from these studies show that there is no overly-consistent LD distribution in oocytes or embryos across different species. Co-localisation of LDs with mitochondria in the egg cytoplasm is likely. Most domestic animals show LDs and mitochondria to reside within ~10nm of each other (Sturmey *et al.* 2006), however equine oocytes appear to present polar aggregations of LDs (Ambruosi *et al.* 2009; Cui *et al.* 2009). A degree of LD movement is seen at certain developmental stages, thought to be aided by microtubule transport, potentially facilitating lipid metabolism (Yu *et al.* 2010; Walther and Farese, 2012; Welte, 2009).

Typically, lipid content of mammalian oocytes, eggs or embryos has been assessed through destructive means such as chemical extraction (Loewenstein and Cohen, 1964). Gas chromatography has been performed to assess the lipid content of multiple species, involving vaporisation of components (Haggarty *et al.* 2006; Matorras *et al.* 1998; Kim *et al.* 2001; McEvoy *et al.* 2000; Khandoker *et al.* 1997; Homa *et al.* 1986; Wang *et al.* 1998). Mass spectrometry uses ionisation of molecules to create a chemical map of the cells, in order to examine their lipid content (Apparicio *et al.* 2012; Ferreira *et al.* 2010).

Alternatively, lipid content in mammalian oocytes has been imaged by staining with dyes such as Nile red (Genicot *et al.* 2005; Romek *et al.* 2009; Niu *et al.* 2014; Jeong *et al.* 2009; Barcelo-Fimbres and Seidel, 2011; Ordonez-Leon *et al.* 2014). However, along with the above mentioned disadvantages to using fluorescent stains, they fail to provide quantitative information about lipid content, and often are unable to

resolve individual droplets within the cytoplasm. Providing only a semi-quantitative assay of lipid content, lipid dyes have a limited specificity, with uncontrolled variability in different cell types, and, as mentioned, are limited by issues such as photo-toxicity and photo-bleaching.

No methods currently exist to dynamically measure the uptake or loss of fatty acids from LDs in living cells. It is also currently difficult to image or monitor LD formation at the ER, or their movement, possibly to co-localise with mitochondria in order for fatty acid liberation and metabolism to occur. Novel, preferably non-invasive methods to study LDs in living mammalian oocytes and embryos with high spatial and temporal resolution are required.

1.5.2. LD content of Different Mammalian Species

These methods have been used to analyse the lipid contents of eggs and embryos of various mammalian species. It is found that the actual natural lipid content and LD characteristics of eggs and embryos differs greatly between species. However, the types of lipid present remain constant, oocytes of all species found to contain both saturated and unsaturated fatty acids, most prominently palmitic, stearic and oleic acids (Ferreira et al. 2010; McEvoy *et al.* 2000; Loewenstein and Cohen, 1964).

Mammalian oocytes are of considerably different sizes, successful sheep oocytes having a diameter of between 110-150µm (Shirazi and Sadeghi, 2007), while bovine oocytes of ~110-120µm have the best chance of a successful development (Fair *et al.* 1995). Human oocytes are also ~120µm, while pig oocytes measure 105µm, and mouse, 72µm (Griffin *et al.* 2006). The LD content of different species also varies hugely. Oocytes of domestic species such as dog and pig are famously almost opaque to light transmission, due to their abundant and large LDs, taking up much of the cytoplasmic space (Prates *et al.* 2012; McEvoy *et al.* 2000; Romek *et al.* 2009; Genicot *et al.* 2005; Apparicio *et al.* 2012). LDs of bovine and ovine eggs are smaller and of fewer number (Genicot *et al.* 2005; McEvoy *et al.* 2000), while human and mouse oocytes, eggs and embryos contain very few LDs not identified by

conventional brightfield microscopy, their cytoplasm transparent as a result (Genicot *et al.* 2005; Prates *et al.* 2012).

Although not completely accurate in their quantification methods, these described techniques are able to give a reliable estimation as to the amount of lipid in oocytes of each species. Pig oocytes, with their abundant LDs were found to contain 156ng lipid per cell (McEvoy *et al.* 2000; Crosier *et al.* 2000), while ovine oocytes claimed to contain 89ng (McEvoy *et al.* 2000; Coull *et al.* 1998). A bovine oocyte lipid content of 58ng is described (Kim *et al.* 2001; Ferguson and Leese, 1999), while only 4ng lipid has been measured in mouse oocytes (Loewenstein and Cohen, 1964). These values can be used to calculate the amount of lipid (ng/μm^3) of each species (see Table 1.).

Genicot *et al.* (2005) use fluorescence imaging in an attempt to measure the lipid content of LDs (in TAG form) of mammalian oocytes relative to each other. They demonstrate that pig oocytes contain 2.4 fold more TAG than bovine oocytes, and 1.8 times more than sheep. The pig:mouse lipid ratio is 6.8, while the sheep:mouse is 3.8, and cow oocytes contain 2.8 times more lipid in their LDs than mouse (Genicot *et al.* 2005). However, it is not clear how reliable these results are, due to the lack of specificity and staining discrepancies possibly unnoticed. Other findings are not entirely consistent, for example McEvoy *et al.* (2000) find that pig oocytes contain 74ng TAG, sheep oocytes 25ng and cows 23ng, while Ferguson and Leese (1999) find that bovine embryos between the 2Cell and blastocyst stage contain 33ng TAG. Sturmey and Leese, (2003) describe a decrease in pig oocyte cellular lipid content between GV and MII stages (135-122ng TAG), and no change in the 118ng measured between zygote and blastocyst embryo stages. Romek *et al.* (2009) however, see a decrease in lipid from 179ng to 131ng as embryo development continues. This measurement is of total lipid, so is likely to include free fatty acids, and may be an accurate representation.

Species	Oocyte Diameter (µm)	Oocyte Volume (μm^3)	Fatty Acid Content (ng)	Normalised Fatty Acid Content ($ng/\mu m^3$)
Human	120	9.05×10^{5}	?	?
Mouse	72	1.95×10^{5}	4	2.05×10^{-5}
Cow	125*	1.02×10^{6}	58	5.69×10^{-5}
Sheep	130‡	1.15×10^{6}	89	7.74×10^{-5}
Pig	105	6.06×10^{5}	156	25.7×10^{-5}

*Average between 110-140µm (Fair *et al.* 1995; McEvoy *et al.* 2000)
‡ Average between 110-150µm (Shirazi and Sadeghi, 2007)

Table 1. Fatty Acid Lipid Content of Oocytes of Different Mammalian Species, Normalised to Volume
Approximate lipid content ($ng/\mu m^3$) of oocytes of the most-studied mammalian species. Data collated from: McEvoy *et al.* 2000; Crosier *et al.* 2000; Loewenstein and Cohen, 1964; Ferguson and Leese, 1999; Kim *et al.* 2001; Coull *et al.* 1998; Fair *et al.* 1995; Shirazi and Sadeghi, 2007; and Griffin *et al.* 2006.

The extent and importance of fatty acid metabolism also depends on species, and appears to reflect the amount of lipid, and number and size of LDs present. Pig oocytes have a high level of lipid metabolism, fatty acids thought to be primarily used as a source of ATP (McEvoy *et al.* 2000; Ambruosi *et al.* 2009; Sturmey *et al.* 2006; Prates *et al.* 2014). Oocytes of sheep and cow species appear to metabolise a moderate level of fatty acids, as well as pyruvate in order to produce energy (Gardner *et al.* 1993; Ferguson and Leese, 2006; Sutton-McDowall *et al.* 2010), while mouse and human egg resting lipid metabolism has been measured to be low, favouring pyruvate as a major energy source (Harris *et al.* 2009; Haggarty *et al.* 2006; Downs *et al.* 2009; Biggers *et al.* 1967; Dumollard *et al.* 2007; Conaghan *et al.* 1993). It is currently not understood why lipid metabolism and content of oocytes and embryos of mammalian species differs so greatly. Suggested mechanisms

responsible have included the prolonged time to implantation in pigs: while rates of development to blastocyst are relatively similar, porcine embryos attach to the uterine lining ~day 11 post-fertilisation, compared to ~day 6 in the human (Prates *et al.* 2014; Schatten and Constantinescu, 2008). Other differences are also apparent once implantation has occurred, for example porcine embryos maintain their ICM for ~6-7 days post-attachment, compared to ~1-3 days in mouse and human embryos (Oestrup *et al.* 2009).

1.6. Multiphoton Microscopy

Prior methods of imaging and quantifying lipids in mammalian eggs or embryos, while providing vital information, have obvious limitations. Mammalian oocytes and embryos are particularly sensitive to light, hence light exposure has to be minimized in order to maintain viability (Takenaka *et al.* 2007). For use in assisted reproductive technologies, no staining methods or fixation can be used, as these also compromise the viability of the egg or embryo.

Label-free optical methods such as DIC microscopy have been used extensively to image multiple biological tissues, however these are unable to provide any chemical information, vital to be able to further understand cell systems and functions. In order to non-invasively measure and assess the lipid content of mammalian eggs or embryos in clinical situations, chemically-specific, label-free imaging techniques are sought. Various multiphoton imaging techniques are emerging, with many applications in biology. Using near-infrared laser sources and localised non-linear light-matter interaction, multiphoton techniques allow optical sectioning hundreds of microns deep into biological tissues. With less than $1\mu m^3$ focal volume where high photon densities are reached, intrinsic three-dimensional (3D) spatial resolution is enabled without the need of a confocal detection pin-hole, and scattering and photo-damage are reduced, allowing for compatibility with live cell imaging (Zipfel *et al.* 2003).

Raman Spectroscopy involves the interaction of light with vibrational resonances of endogenous chemical bonds within biological samples. While it has been successfully used in the label-free imaging of LDs in mouse eggs (Davidson *et al.* 2012), the signal gained from Raman scattering is very weak, and the long image acquisition times needed to generate sufficient contrast have effectively limited its use to fixed material (Wood *et al.* 2008). Consequently, there are no methods reported to date for quantitatively assessing lipid content in mammalian oocytes and early embryos in a non-destructive manner.

Coherent anti-Stokes Raman Scattering (CARS) microscopy has emerged in recent years as a powerful multi-photon microscopy technique which overcomes some of the limitations met with spontaneous Raman scattering. CARS also involves the interaction of optical fields with vibrational resonances of chemical bonds, but vibrations are driven coherently, enhancing the signal obtained. Consequently, CARS enables label-free chemical and quantitative analysis of lipids in living cells, with high acquisition speeds (Zumbusch *et al.* 2013). CARS has previously been successfully used to image LDs in various living cells in culture and in whole organism invertebrate embryos (Hellerer *et al.* 2007; Zumbusch *et al.* 2013).

1.6.1. Raman Spectro-Microscopy

Raman spectro-microscopy involves the interaction of a light field, typically monochromatic at a given optical frequency, with vibrating chemical bonds of a molecule within the sample (see Fig.1.6.1.1. (A)). Raman scattering can be understood as originating from the molecule acquiring an induced dipole (in the presence of the incident light) which oscillates at a shifted frequency compared to the incident light, due to the change of the molecular polarisability from the vibrating atoms. This inelastic scattering is usually detected as a so-called Stokes shift to a lower frequency (Downes and Elfick, 2010; Davidson *et al.*, 2013). A schematic way to understand Raman scattering uses an energy-level representation from quantum mechanics, where the molecule is ‘excited’ from its ground state to a virtual energy state by the incident photon, and ‘emits’ a lower frequency photon by returning to an excited vibrational level (inverted commas acknowledge that this is qualitative

terminology; the correct quantum mechanical description of this process is beyond the scope of this thesis). The emitted photon is stokes-shifted to a lower energy by an amount exactly equal to the energy difference between these vibrational levels (see Fig.1.6.1.1. (A)) (Potma and Xie, 2004). Due to the different chemical bonds comprising different molecules, Raman spectra (which show the intensity of scattered light versus frequency shift from the incident light field) are unique to each molecule, allowing identification of sample molecular composition. Raman is also an example of a linear optical effect, as the intensity of the Raman scattered light is linearly proportional to the incident intensity. It is also proportional to the number of chemical bonds in the examined sample, meaning molecules can also be quantitatively analysed. However, with this method, bonds vibrate incoherently and the signal generated is usually very weak- with typically only one photon emitted per molecule per 10^{10} incident photons (Potma and Xie, 2004). Raman micro-spectroscopy does therefore require high powers, long acquisition times and a high number of molecules in order to generate sufficient signal, compromising the use of Raman with living cells.

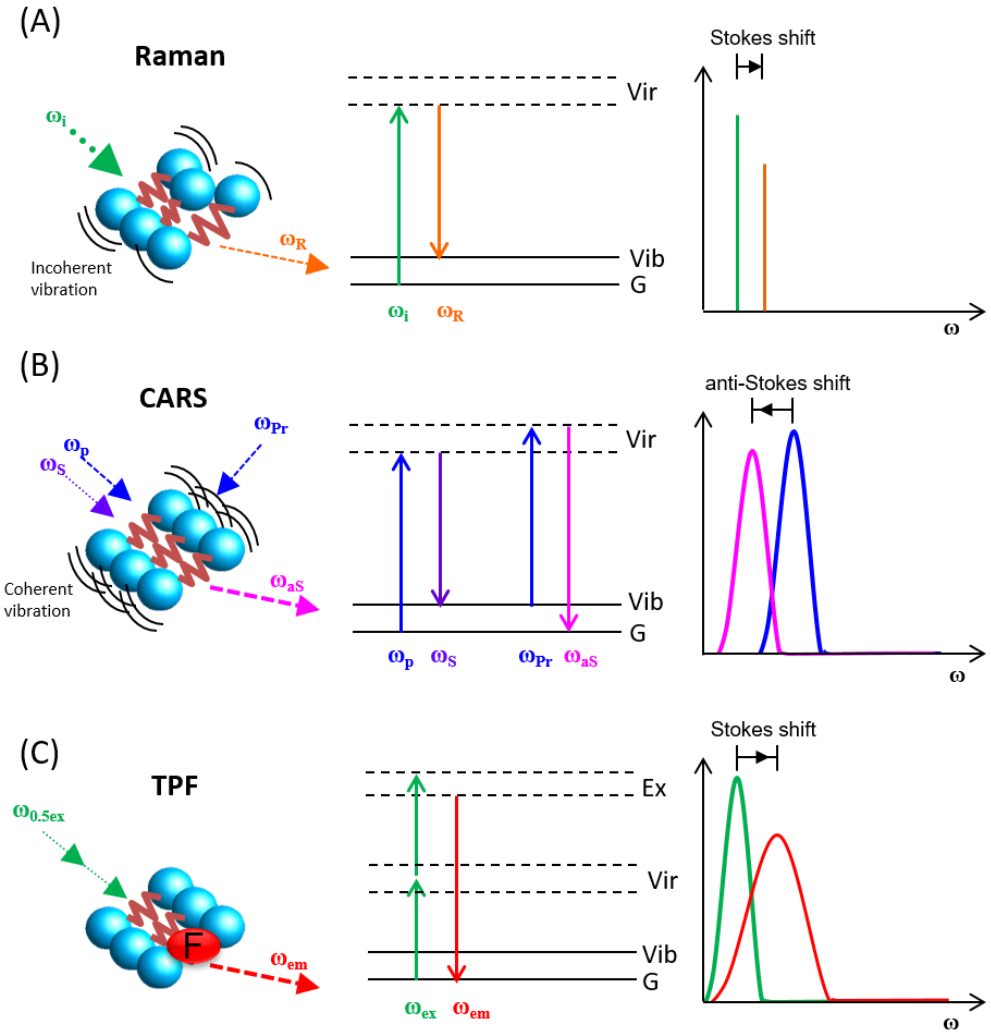

Fig.1.6.1.1. Principles of Raman Spectroscopy, Coherent Anti-Stokes Raman Scattering (CARS) Microscopy and Two-Photon Fluorescence Microscopy

Schematics representing the various processes, using energy levels and excitation/emission spectra. (A) Raman scattering involves the interaction of a light field, typically monochromatic at a given optical frequency ω_i, with incoherently vibrating chemical bonds of a molecule within the sample. This inelastic scattering is usually detected as a Stokes shift to a lower frequency (ω_R). (B) Coherent anti-Stokes Raman Scattering (CARS) microscopy involves coherent vibration of chemical bonds by two incident beams, the pump beam of frequency ω_p, and the Stokes beam of frequency ω_S. Scattering of a third beam, the probe beam of frequency ω_{pr} by this coherent vibration causes emission of a higher-energy photon of frequency ω_{aS}, the anti-Stokes shift enabling detection. (C) Two-Photon Fluorescence (TPF) involves the excitation of a fluorophore (F) into a real electronic excited states by two photons of half the frequency required for one-photon absorption ($\omega_{0.5ex}$). Excitation of the fluorophore generates fluorescent emission at a lower energy than the incident beam, following vibrational relaxation (ω_{em}), this Stokes shift enabling detection.

1.6.2. Coherent anti-Stokes Raman Scattering (CARS) Microscopy

CARS arises as a result of a third-order nonlinear process (four-wave mixing) in which two near-infrared pulsed laser fields, the pump (of frequency ω_p) and Stokes (ω_S) beams, coherently excite a molecular vibration resonant at the frequency ω_{vib}. When $\omega_p - \omega_S$ is equal to ω_{vib}, all the examples of this chemical bond within the focal volume can be driven to simultaneously oscillate. Thus, in CARS microscopy, the incident pump and Stokes beam frequencies can be tuned to vibrate desired chemical bonds of known vibrational resonance. The resulting coherent vibration modulates a third beam known as the probe beam ω_{pr}, causing emission of an anti-Stokes photon (ω_{as}). In a typical two-pulse experiment, the probe beam coincides with the Pump beam, i.e. $\omega_{pr} = \omega_p$ and the anti-Stokes frequency is $\omega_{as} = 2\omega_P - \omega_S = \omega_p + \omega_{vib}$. This CARS frequency is higher and blue-shifted to the incident beam frequencies and is thus free from (one-photon) auto-fluorescence background (Follick *et al.* 2011) (see Fig.1.6.1.1. (B)).

CARS can also be understood in terms of an energy level diagram (see Fig.1.6.1.1. (B)). As the incident pump field interacts with the electron cloud and molecular bonds of molecules within the sample, the molecules are excited from the ground state to a virtual energy state. Interaction with the Stokes field 'relaxes' these molecules to a vibrational energy state, or more precisely the interference between pump and Stokes fields drives their coherent vibration. The probe beam then excites these molecules to an even higher virtual energy state, relaxation from which back to ground state causes emission of a photon at a higher frequency than the pump beam, which can be detected as the CARS signal (Potma and Xie, 2004; Follick *et al.* 2011; Evans *et al.* 2008).

Like Raman, the CARS signal is proportional to the number of chemical bonds within the sample. However, rather than a linear relationship, it is quadratically dependent, and generates signal intensities several orders of magnitude higher than spontaneous spectroscopy. This is due to the constructive interference of the Raman signal generated by vibration of all chemical bonds of a given type within the focal volume. CARS is particularly efficient when imaging lipids since they contain a large number of identical CH bonds within their aliphatic chain. Within cells, the hydrophobic nature of lipids often governs that numerous molecules aggregate in

LDs, increasing the signal obtained even further (Zumbusch *et al.* 2013). Due to the fact that the multiphoton CARS process only takes place within the focal volume, and near infrared (NIR) wavelengths are used, scattering effects and photo-damage are reduced. This, along with short acquisition times, makes CARS compatible with live cell imaging, unlike Raman micro-spectroscopy.

A limitation of CARS microscopy is the presence of a non-resonant background. This is a background signal that remains even when the two incident beams are not in tune with a particular vibrational resonance. Due to this background, spectra gained from CARS microscopy cannot be directly compared with true Raman spectra of molecules. In order to quantitatively analyse CARS signals and investigate chemical composition of the sample, the non-resonant background must be taken into account and removed.

1.6.3. Two-photon Fluorescence (TPF) Microscopy

Two-photon fluorescence (TPF) microscopy is a multiphoton technique used to excite fluorophores or autofluorescence with higher penetration depth than conventional fluorescence microscopy techniques. TPF uses the principle that two photons of half the energy required to excite a fluorophore into a real electronic excited state, simultaneously directed at the fluorophore, cause absorption and, in turn, fluorescence emission (see Fig.1.6.1.1. (C)). The fluorescent molecule is excited from its ground state to a real excited energy state, where its undergoes vibrational relaxation before emitting a photon of lower energy than the one-photon absorption transition. This difference in energy means that the emitted photon can be detected via specific frequency selection (see Fig.1.6.1.1. (C)).

The smaller energy of the incident photons means they have a longer wavelength, and are consequently able to better penetrate the sample. The NIR light (>800nm) is less scattered than visible wavelengths, and less absorbed by endogenous chromophores. Although debated in the literature, this might also result in less photo-damage to the sample. As excitation only occurs in the focal volume, TPF benefits from intrinsic 3D resolution (Zipfel *et al.* 2003; Zumbusch *et al.* 2013). TPF is dependent on two photons being simultaneously absorbed (within ~10^{-16} sec), so a

pulsed laser is used to increase probability of this happening, while maintaining moderate average power (Zipfel *et al.* 2003; Zumbusch *et al.* 2013). The use of femtosecond pulses also allows for multimodal imaging e.g. simultaneous CARS and TPF.

The use of fluorophores is invasive, often altering the biological properties of the sample. Fluorophores are too big to image metabolites, and often overexpression of probes is needed in order to see anything of value. Thus, TPF cannot be regarded as a non-invasive technique, unless imaging of autofluorescence is performed.

1.6.4. Raman and CARS Microscopy of Lipids in Biological Tissues

Raman spectroscopy and CARS imaging have been extensively used to image lipids in biological tissues, due to the high signal gained and the chemical quantification methods possible. Due to large number of identical bonds present in lipids, signals from lipids are extremely high, making CARS and Raman microscopy methods ideal for lipid research. The known dependence of Raman and CARS intensities on the number of CH_2 bonds gives a good measure of the amount of lipid present in the sample, and the ability to extract Raman spectra from both imaging techniques allows for detailed investigation of chemical composition. The NIR wavelengths of light allow for less endogenous absorption, meaning decreased photo-damage to cellular material. Raman and CARS also benefit from being chemically-specific techniques, negating the requirement for unspecific or unreliable fluorophores, or destructive techniques such as chemical extraction.

As previously described, Raman generates a weak signal, requiring high powers and long acquisition times, making it impractical for live cell imaging. However, CARS microscopy allows examination of multiple lipid behaviours occurring in living cells. As described, lipids in cellular systems are dynamic and of particular interest when it comes to investigating metabolism.

The majority of biologically relevant vibrational frequencies lie within the range of $1200cm^{-1}$-$3800cm^{-1}$ (Pope *et al.* 2013; DiNapoli *et al.* 2014b). These vibrational resonances include chemical bonds such as the C-C bond ($1150cm^{-1}$), CH_2 stretch ($2850cm^{-1}$), and double-bonded =CH stretch ($3010cm^{-1}$), C=C ($1660cm^{-1}$) and C=O

(1740cm^{-1}) vibrations (Di Napoli *et al.* 2014). Conventional lipid spectra are likely to have a large peak at 2850cm^{-1} due to the large number of CH_2 bonds making up the acyl chain, whereas peaks at 1660cm^{-1} or 3010cm^{-1} will only be present in spectra of lipids comprised of unsaturated fatty acids. Therefore, Raman spectra provide a lot of information as to the chemistry of lipids within the sample. Specific techniques of gaining these spectra from biological samples differ (see Zumbusch *et al.* 2013 for an overview). However, hyperspectral imaging, over a number of sequential vibrational resonances, can provide a CARS spectrum at each spatial position within a sample, enabling identification of specific lipids within the sample, and the chemical composition of LDs present in biological specimens (Pope *et al.* 2013; Rinia *et al.* 2008; Di Napoli *et al.* 2014b Parekh *et al.* 2010).

Previous efforts have been made to use CARS to investigate cell and organelle membranes (Potma and Xie, 2005), however, lipid bilayers such as these are essentially two-dimensional hence have very few molecules in the focal volume, so CARS signals are low and require long acquisition times (Zumbusch *et al.* 2013).

Various living cells and biological tissues have thus far been imaged for lipids using CARS microscopy, including fibroblasts, HeLa cells and high fat-containing adipocytes (Nan *et al.* 2003; Rinia *et al.* 2008; Paar *et al.* 2012). Breast cancer has been investigated *in situ* and *in vitro* (Yang *et al.* 2011), while tissues such as skin and neurons have also been assessed for their lipid content (Evans *et al.* 2005; Wang *et al.* 2005). Hellerer *et al.* (2007) used CARS to examine whole Caenorhabditis elegans **(***C. elegans*) organisms. Other studies have taken advantage of the ability to simultaneously use CARS and TPF to gain further knowledge of medical issues such as atherosclerosis and liver fibrosis (Le *et al.* 2007; Lin *et al.* 2011). CARS clearly has many biologically and medically relevant applications, allowing further advances in research to be made.

1.6.5. Raman and CARS Microscopy of oocytes eggs and embryos

Mammalian oocytes and embryos are delicate cells, highly sensitive to the light levels used in conventional microscopy methods, and susceptible to damage from

preparatory techniques often required in these methods. Raman spectro-microscopy has been used to successfully assess lipid content of fixed mammalian oocytes and embryos, giving a promising indication of similar future success using CARS microscopy on live oocytes and embryos. Wood *et al.* (2008) were the first to examine the lipid characteristics of mouse oocytes, describing a higher lipid content of MII eggs, and a higher fraction of unsaturated fatty acids. Davidson *et al.* (2012, 2013) found differences in lipid and protein contents of GV oocytes, MII eggs and embryo stages, claiming that Raman profiles can be used to identify developmental stage. They also describe the finding that the ratio between the peaks associated with protein and lipid concentrations allows measurement of oocyte quality- those with a higher protein:lipid ratio correlating with the current morphological grading system of oocyte quality. Bogliolo *et al.* (2012) used Raman spectro-microscopy to assess ovine oocytes, demonstrating that freezing of eggs induces biochemical changes to the ZP. In 2013, they also identified that aged oocytes had reduced lipid and protein profiles, similar to that seen with oxidative stress (Bogliolo *et al.* 2013).

In clinical or laboratory situations, where an embryo must be transferred into the mother after fertilisation, invasive methods of quality assessment are simply not viable. Non-invasive methods of egg and embryo assessment are desirable in order to minimise the time spent in culture, and the imaging time of the embryo, whilst maximising the chances of a successful pregnancy. There is also a possibility that CARS would be beneficial in improving cryopreservation of oocytes or embryos, where fast freezing of the cells allows for their use in ART at a later date. It has been found that eggs or embryos of a higher lipid content have a lower cryotolerance than those with less lipid (Wirtu *et al.* 2013; Takahashi *et al.* 2013)- a characteristic that could be assessed in a clinical laboratory by CARS microscopy.

1.7. Summary and Aims

It is clear that complex metabolism mechanisms are occurring throughout mammalian egg and embryo development, and the cells are relying solely on their mitochondria for production of ATP for cell growth, cell cycle processes, cell division and ultimately cell survival. It is thus far known that lipid metabolism is performed at these early developmental stages, along with pyruvate oxidation, but that too little or too much oxidation of either substrate is detrimental to the health of the egg or embryo. These cells can only survive and go on to produce a viable embryo if an optimum level of metabolism is occurring at the mitochondrial level.

Lipids in cells are packaged by the ER as TAGs into cytoplasmic vesicles known as lipid droplets, with an outer lipid monolayer, associated with functional proteins. Here, fatty acids are recruited or liberated in concurrence with the metabolic demands of the cell. Until now, imaging of LDs in eggs or embryos has been achieved through destructive means such as lipophilic fluorescence staining, requiring cell fixation and harmful levels of light. Alternatively, non-invasive methods have proved to be incapable of resolving LDs as small as those found in mouse or human eggs (Watanabe *et al*. 2010).

CARS microscopy has been recently developed as a tool proficient in imaging lipids in biological tissues, due to their high-density aggregation within LDs, resulting in a large CARS signal. Here, use of CARS microscopy is intended to image LDs in live mouse eggs and embryos at the 2850cm^{-1} CH vibrational resonance, and to perform hyperspectral imaging on individual LDs within eggs and embryos, in order to qualitatively and quantitatively investigate the number of LDs, their size and their chemical composition throughout development from the GV stage oocyte to the blastocyst stage embryo. The aim is also to be able to prove that this method of imaging such sensitive cells is coincident with cell viability, while potential conclusions about developmental potential can be drawn from LD distribution patterns. It is hypothesised that use of this imaging method will point out the short-comings of fluorescent staining compared to CARS microscopy, and will recognise the additional information capable of being obtained in a short space of time using CARS. Finally, it is possible to investigate fatty acid metabolism within the egg and

early embryo using fluorescence and luminescence microscopy. It is expected that the extent of fatty acid metabolism contribution to egg or embryonic cellular redox potential can be measured. Meanwhile, the effects of altered metabolism on mitochondrial and ER processes can also be investigated. CARS microscopy alongside alteration of metabolic activity will demonstrate the effect this has on LD distribution, enabling conclusions to be drawn as to the patterns that are seen.

Chapter 2. Materials and Methods

2.1. Animals

Female MF1 mice, and male F1-hybrid mice, were obtained from Harlan Laboratories.

All animals were handled according to UK Home Office regulations, and procedures carried out under a UK Home Office Project License.

2.2. Gamete collection and manipulation

2.2.1. Female gamete collection

4-6 week old female MF1 mice were intraperitoneally injected with 5 international units (IU) pregnant mare's serum gonadotrophin (PMSG) to mimic the action of FSH and induce ovarian follicle growth. 48hrs later, 10IU human chorionic gonadotrophin (hCG) was injected to mimic LH secretion, to cause superovulation.

Oviducts containing mature MII eggs were collected from culled mice 15hrs later, into warmed M2 (embryo-tested, Sigma) at 37°C. Oviducts were punctured with a syringe needle and liberated eggs were collected via mouth pipette. Cumulus cells were removed by brief exposure to 300µg/ml hyaluronidase. Ovaries containing immature GV oocytes were collected from un-injected culled mice, into warmed M2 medium at 37°C, containing 100µM isobutyl-1-methylxanthine (IBMX, Sigma) to maintain MI arrest. Ovarian follicles were punctured multiple times and liberated oocytes were collected via mouth pipette. Cumulus cells were removed by gentle, repeated pipetting, and release from GV arrest was obtained by washing oocytes in multiple drops of M2 medium. During experiments and incubation, oocytes/eggs were kept at 37°C in drops of M2 medium (with or without IBMX) covered in mineral oil (embryo-tested, Sigma) to prevent evaporation.

In vivo fertilisation was carried out by mating female MF1 mice with male F1-hybrid mice overnight after hCG injection (48hrs after PMSG), and oviductal zygotes were

collected as above 15hrs later. Eggs/embryos were manipulated in all conditions by mouth pipetting, using a fine-bored glass pipette, pulled over a Bunsen flame and connected to plastic tubing with a plastic mouth piece.

Bovine ovaries were collected from various culled cattle, and COCs liberated into HEPES-buffered M199 media (see Appendix 1). Maturation was allowed in supplemented M199 media (10% serum, see Appendix 1) at 39°C, with 5% CO_2 overnight, before treating with 300μg/ml hyaluronidase and removing cumulus cells by gentle pipetting with a fine-bore pipette. Bovine eggs were held and imaged in standard M2 medium at 37°C.

2.2.2. Male gamete collection

Spermatozoa were collected from culled 10-24 week old male F1-hybrid mouse cauda epididymis. Epididymi were collected into warmed M2 media at 37°C. Spermatozoa were liberated by puncturing the tissue multiple times with a syringe needle, then pipetted into equilibrated Tyrodes 6 (T6) medium (see Appendix 2) containing 15mg/ml bovine serum albumin (BSA), at 37°C and 5% CO_2. 2-3 hours were allowed for capacitation before *in vitro* fertilisation carried out.

2.3. Culture conditions

2.3.1. In vitro *Maturation*

In vitro maturation (IVM) of mouse oocytes was allowed by washing and culturing oocytes in standard M2 medium at 37°C or Minimum Essential Medium (MEM) (Sigma, see Appendix 3) containing 3mg/ml BSA (Sigma). Drops of media were covered with mineral oil (embryo-tested, Sigma) to prevent evaporation. IVM was allowed overnight for ~18hrs.

2.3.2. In vitro *Fertilisation*

MII eggs were added a drop of T6 media (see Appendix 2) containing capacitated sperm for 2 hours before washing out and culturing in KSOM as below.

2.3.3. Embryonic maturation media

Embryos from the zygote stage were washed in multiple drops of, and then subsequently cultured in, KSOM medium (EmbryoMAX, Merck Millipore) at 37°C, 5% CO_2 under oil for up to 5 days, when blastocyst stage is reached.

2.3.4. Experimental holding media

Pyruvate starvation was carried out by incubating MII eggs in Hepes-buffered KSOM medium (HKSOM, see Appendix 4) containing 3mg/ml BSA (both Sigma), lacking pyruvate and lactate, for ~6 hours before imaging.

Experimental variations of MEM media (Appendix 3) were supplemented with 4mg/ml fetal calf serum (FCS) (Sigma), 3mg/ml fatty-acid-free BSA (Sigma) instead of standard BSA, or BSA conjugated to oleic or palmitic acids (see below) in experimental concentrations of 100µM, 200µM, 250µM, 400µM or 700µM. 5mM oleic acid (OA)- or palmitic acid (PA)-BSA stocks were achieved by dissolving 14.1mg OA or 12.8mg PA into 500µl sodium hydroxide (NaOH) using a boiling water bath to make 0.1M fatty acid-sodium salt; this salt was then dissolved into warmed (37°C) phosphate buffered saline (PBS) with 100mg/ml BSA in a water bath at 55°C for 15mins. Care was taken not to allow the palmitic salts to precipitate, by keeping all equipment used warm (including pipette tips).

2.3.5. Fixation and staining

Where stated, egg/embryos were fixed in 1% paraformaldehyde (PFA) in PBS with 1% polyvinyl alcohol (PVA) to prevent adhesion, for 10mins before holding in PBS. Fixed cells were stained for lipid droplets using 1 µg/ml BODIPY 493/503 or HCS LipidTOX green neutral lipid stain at a 1:5000 stock dilution (both Life Technologies) for 1hr for subsequent TPF imaging. Nile red stain was used at 10µg/ml for 2hrs for subsequent confocal imaging. Fixed cells were imaged in PBS to avoid any chemical interactions from other media e.g. M2 giving non-biological effects.

Live oocytes were treated with 100nM tetramethylrhodamine ethyl ester (TMRE) before measuring effects of etomoxir on mitochondrial membrane potential.

2.4. Microinjection

GV and MII eggs were injected with the desired reagent within a shallow drop of M2 under mineral oil to prevent evaporation, upon an unheated microscope stage (Nikon TE2000). For mitochondrial observation, MitoTurboGFP RNA was injected. For luminescence measurements, click-beetle luciferase RNA mixed with potassium chloride (KCl) Hepes buffer (~1μg/ml final concentration), or firefly luciferase protein (10μg/ml final concentration) was injected. For measurement of changing Ca^{2+} levels, a 1:1 mix of OGBD (Oregon green BAPTA-dextran):Alexa596 was injected. ~1μl of a reagent sample is pipetted into a microinjection needle using a sterile microloader pipette tip (Eppendorf). Needles are pulled on a vertical puller (P-30, Sutter Instruments) and, once loaded, are connected to an intracellular amplifier (Cyto721, WPI). A holding pipette holds eggs in place via suction, and the injection needle can be manipulated to penetrate the egg. A small amount of reagent is introduced into the egg (~3-5% its volume) via a short pressure pulse of ~20psi from a Picopump (WPI Ltd) operated by a foot pump.

2.5. Intra-cytoplasmic Sperm Injection (ICSI)

ICSI was performed as described by Yoshida and Perry (2007). Briefly, ICSI microinjection needles were pulled from borosilicate glass capillaries using a pipette puller. Needles were forged to appropriate standard with a microforge, to give a flush edge of ~0.5mm diameter and 30º angle for injection. The backs of the injection needles were blunted on a flame before back-loading with ~1μl Fluorinert (Sigma), making sure no air bubbles were present in the column up to the very back end of the needle. Needles were then mounted firmly to the stage, ensuring that no air bubbles were present in the needle column. A gentle increase in positive pressure was applied in the injector to advance the oil and Fluorinert to the tip of the needle. It was then brought down into the prepared drop of injection media, so that it was in focus under the desired magnification. The end of the needle was flushed with Fluorinert by increasing positive pressure, before decreasing pressure to bring a small amount of injection media into the very tip of the needle, maintaining Fluorinert in the field of view.

A fresh sperm sample was prepared in T6 media (as described in section 2.2.2, recipe can be observed in Appendix 2), or a frozen sperm sample previously prepared was thawed, and sperm were decapitated by brief sonication before cooling on ice. A small amount was then pipetted into the injection drop, and sperm heads were picked up by a gentle decrease in pressure in the injection needle, either individually or a few at a time.

A holding pipette was used to keep eggs to be injected in place, in a suitable orientation so that injection needle has enough space between the ZP and the cytoplasmic membrane, and so that the meiotic spindle would not be affected by injection. The injection needle was then brought into contact with the ZP, large piezo pulses (intensity= 3, frequency= 6) were used to bore through the ZP to gain access to the inside of the cell. Applying a small amount of positive pressure gently removed the ZP 'plug' from the injection needle, and brought the sperm head to the very end of the injection needle.

The needle was then pushed against the cytoplasmic membrane, traversing the majority of the cell until it was in close proximity to the holding pipette, causing a large invagination of the cell membrane, in order to place the sperm head at the opposite pole. A small peizo pulse (intensity= 1, frequency= 1) accompanied by a small amount of positive pressure introduced the sperm head to the cytoplasm, and the injection needle was swiftly but gently withdrawn from the cell.

Injected eggs were kept in M2 media overnight at 37ºC, and zygotes with pronuclei were then washed in and incubated in KSOM media at 37ºC and monitored daily for embryonic development.

2.6. Chemical Treatments

Cyano-hydroxycinnamate (CIN) (Sigma) was added to media with a final concentration of 0.5mM, to prevent pyruvate transport into mitochondria by specific inhibition of monocarboxylic transport. Eggs were either incubated in media containing CIN, or it was added during measurements. Etomoxir (Sigma) was added to media at 100μM, to inhibit lipid metabolism by CPT1 inhibition. Eggs were either incubated in media containing etomoxir, or it was added whilst measurements were taking place. Rotenone was added to eggs during measurements at 10μM, to inhibit electron transfer from Complex I to ubiquinone in the ETC. 2mM sodium cyanide

(CN^-, Sigma) was used to induce a fully reduced redox state, while ETC uncoupler, FCCP (Carbonyl cyanide-*4*-(trifluoromethoxy)phenylhydrazone) (Sigma) was added to media with a final concentration of 200nM for a fully oxidised redox state. Perfusion of media in the microscope dish with fresh medium throughout measurements allowed the subsequent addition of these drugs within the same experiment, enabling observation of multiple responses. Sarco/endoplasmic reticulum Ca^{2+} ATPase (SERCA) pump inhibitor thapsigargin was added to media at 10µM in order to inhibit Ca^{2+} uptake into the ER, and to raise cytosolic Ca^{2+}. Ca^{2+} ionophore, ionomycin was used to deplete the ER Ca^{2+} store, in order to raise cytosolic Ca^{2+}.

2.7. Epifluorescence, Confocal Fluorescence and Luminescence Imaging

2.7.1. Epifluorescence Imaging

Epifluorescence measurements were performed using a Nikon Ti-U microscope. Excitation light was provided by a halogen lamp and a Photometrics CoolSnap HQ2 CCD camera was used to collect fluorescence data. Filters used were as described in Table 2. Switching experiments took two measurements every 10 seconds.

	Excitation Filters	**Emission Filters**
FAD autofluorescence	460nm (10nm bandpass)	510-550nm
NADH autofluorescence	350nm	450-490nm
Simultaneous FAD and NADH auofluorescence	480nm (30nm bandpass)	510-550nm
OGBD	490nm	510-550nm
Alexa596	580nm	600nm
Rhod Dextran	550nm	600nm
TMRE	550nm	580nm

Table 2. List of Excitation and Emission filters used in Epifluorescence Measurements

Oocytes/eggs and embryos were briefly exposed to acid Tyrode's solution (Sigma) prior to placing in the microscope dish, in order to remove the zona pellucida so that they stick to the glass cover slip, allowing addition of experimental chemical treatments to the surrounding media without disturbance of the eggs/embryos. InVivo software was used to collect data, ImageJ was used to collect data per egg using the MultiMeasure Plug-in, selecting regions of interest (ROIs). SigmaPlot and Origin were used for normalisation and plotting of data. The intensity of fluorescence emission is presented in arbitrary units.

In experiments where FAD or MMP was measured, graphs were normalised by: $\frac{x_0 - x_{min}}{x_{max} - x_{min}}$ where x_0 is the resting fluorescence level before drug addition, and x_{min} and x_{max} are the minimum and maximum fluorescence levels reached, respectively. In the case of FAD experiments, the area under the curve was found for comparison between conditions or developmental stage.

In experiments where fluorescence of OGBD and Alexa were measured, the OGBD (sensitive to Ca^{2+}) data were divided by the Alexa (insensitive to Ca^{2+}) data in order to provide a ratio. The intensity level was divided by the intensity just before thapsigargin addition (F/F_0), and the area under the curve was found, for comparison between conditions.

A perfusion apparatus was set up in order to replace imaging media with fresh media throughout experiments requiring addition of multiple drugs with opposing mechanisms e.g. washing out of CN^- before FCCP addition.

2.7.2. Confocal Imaging

Eggs stained with Nile Red were imaged with a Leica SP2 A0BS confocal laser scanning microscope, with a 63x oil immersion objective and 2x optical zoom. Laser power was set to 39% and excitation and emission wavelengths set to 488nm and 500-580nm respectively. Images were acquired with a 0.6µm step size over ~60µm, scanned at 400Hz (512x512 pixel resolution).

2.7.3. Luminescence Imaging

Eggs injected with either luciferase RNA (~1µg/ml) or protein (10µg/ml) were pipetted into HKSOM media (Appendix 4) containing 100µM luciferin, under mineral oil, on the heated stage of a Zeiss Axiovert S100 microscope within a purpose-built dark box. Photek software was used to collect data per ROI; Origin was used for normalisation and plotting of data. Graphs were normalised by: $\frac{x_0 - x_{min}}{x_{max} - x_{min}}$ where x_0 is the resting luminescence level before drug addition, and x_{min} and x_{max} are the minimum and maximum luminescence levels reached, respectively. The luminescence values in experiments represent the absolute number of measured photon counts per 10 seconds.

For *in vitro* maturation luminescence experiments, Sigmaplot 'Regression Wizard' was used to find the residuals of the data before using Origin to plot the final data.

2.8. CARS, TPF and DIC Microscopy

2.8.1. CARS and TPF Microscopy

SecureSeal imaging spacers (Sigma) of ~120µm thickness and 13mm diameter where attached onto standard microscope slides. Petroleum jelly was thinly spread around the well of the spacer for an airtight seal. Eggs were pipetted into a small drop ~10-20µl of M2 media, embryos into PBS with PVA, and a coverslip used to create a sealed chamber.

For imaging requiring exchange/addition of media over time, CO_2 exposure, or future imaging, living cells/embryos were pipetted into a drop of M2 media covered in oil, on a 25mm round glass coverslip placed in an in-house-built imaging dish with a removable glass lid (see Fig.2.8.1.1.). For live cell compatibility, the microscope stage was heated to maintain media at 37ºC, and contained in an environmental chamber enabling 5% CO_2 provision.

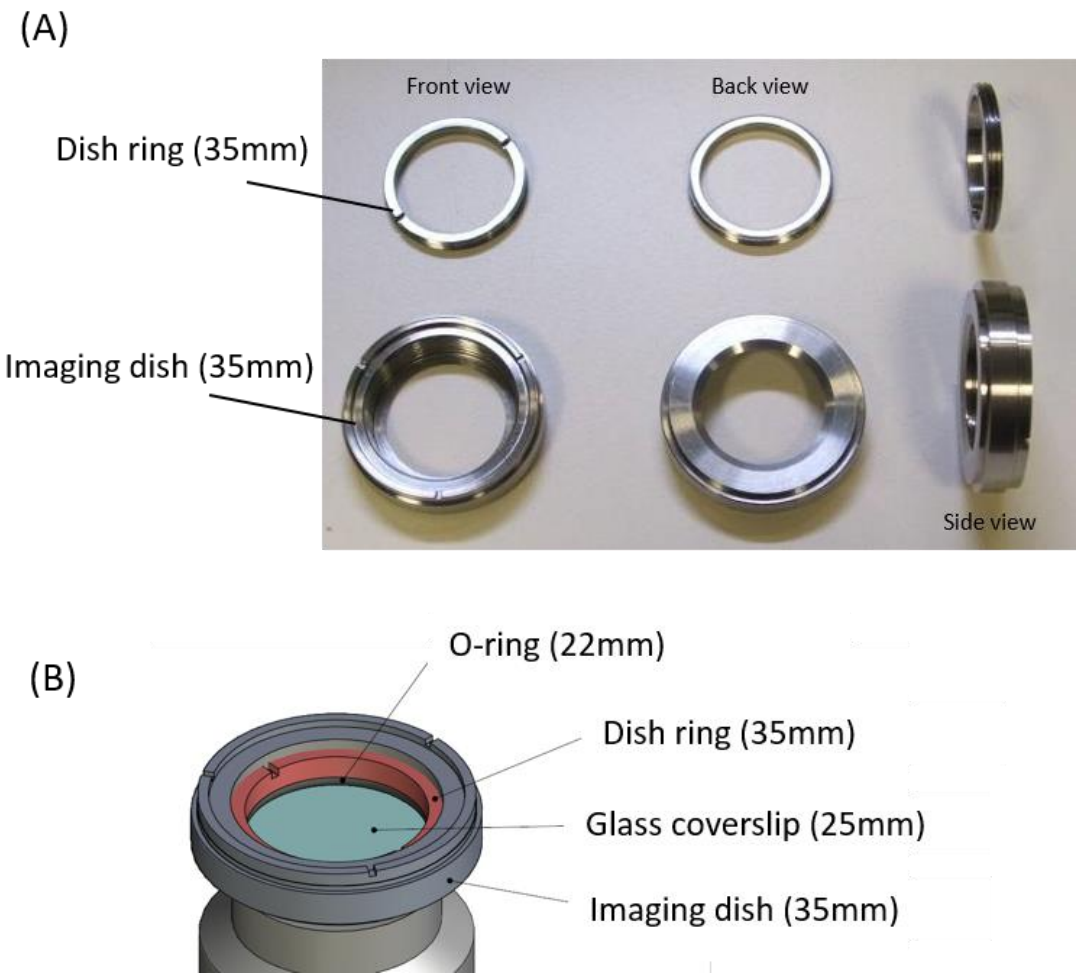

Fig.2.8.1.1. CARS Imaging Chambers

(A) In-house-built imaging dish composed of a 35mm dish and a 35mm ring which screws into the centre of the dish. (B) Assembly of the imaging dish: A 25mm round glass coverslip is placed in the imaging dish. A 22mm rubber O-ring is placed on top of the glass coverslip, and sealed by a 35mm dish ring, which screws into place inside the imaging dish. Live oocytes and embryos were held in a drop of M2 media pipetted onto the coverslip, and covered in oil. A removable glass lid allows removal and subsequent culture of eggs or embryos after CARS imaging.

The CARS microscope was set up as described by Pope *et al.* 2013, with TPF, SHG and DIC imaging capabilities (see below). Figure 2.8.1.2. shows the experimental set-up. A single Ti:sapphire laser source (Venteon, Pulse:One PE) is used to generate broadband 5fs pulses (spectral width of 660nm-970nm) enabling provision of simultaneous CARS and TPF excitation. A short-pass mirror (Eskma Optics; DM1a in Fig. 2.8.1.2.) reflects wavelengths >900nm, and a long-pass filter removes the part of the spectrum that coincides with the CARS signal detection range. Pump and Stokes components for the CARS excitation are obtained by spectrally separating this laser output with an appropriate dichroic beam splitter (CVI Melles Griot; DM2 in Fig. 2.8.1.2.), resulting in a pump beam with centre wavelength at 682 nm, 65nm bandwidth, and a Stokes field of 806 nm, with a 200nm bandwidth.

Although fs pulses allow probing of a broad spectral range, vibrational resonances in liquids are optimally coherent in the picosecond (ps) time scale, corresponding to Raman linewidths of ~10 cm^{-1}. A high spectral resolution of 10 cm^{-1} is achieved in our CARS set-up through spectral focusing as described by Pope *et al.* 2013. In short, pump and Stokes pulses are linearly chirped using glass blocks of known dispersion (refractive index versus wavelength). The linear chirp stretches the pulses in time to ~ps duration and is adjusted to maintain a constant instantaneous frequency difference (IFD) in the CARS vibrational driving process over the stretched pulse duration. In practice, this is achieved using glass blocks of SF57 material with variable lengths (0mm-60mm in 5mm steps) in the Stokes beam path, to adjust the length through which the Stokes beam travels (see Fig. 2.8.1.2.), while the chirp in the pump beam is the one accrued from propagation through the scan lens, the tube lens and the microscope objective. The resulting pulse durations are ~1ps for the pump pulses and 4ps for the Stokes pulses. Notably, the IFD can be tuned to particular vibrational resonances wishing to be investigated by simply changing the delay time between pump and Stokes pulses.

The excitation pulses are recombined using a third dichroic beamsplitter with the same characteristics as DM1a (DM1b, Fig. 2.8.1.2.) and directed via a home-built beam-scanning head into a Nikon Ti-U inverted microscope. For high resolution imaging and high collection efficiency, a 1.27 NA x60 water immersion objective (Nikon λS series) and a 1.4NA oil condenser equipped with a DIC module (see

section 2.8.2.) are used (0.3μm lateral and 0.6μm axial as CARS intensity point-spread function).

In terms of detector layout (available both in forward and epi directions), a dichroic beamsplitter (Semrock; DM4 in Fig. 2.8.1.2.) allows CARS transmission while reflecting the shorter TPF and SHG wavelengths. CARS at the anti-Stokes frequency in the CH stretch vibrational range is selected by an appropriate band-pass filter (Semrock, 542-582 nm; F1 in Fig. 2.8.1.2.), which rejects the pump and Stokes beams. The CARS signal is detected in the forward direction by a Hamamatsu H7422-40 photomultiplier tube (PMT1 in Fig. 2.8.1.2.).

3D CARS images were taken as *z*-stacks over 50 μm depth in 0.5 μm steps. This volume and step-size was a result of a compromise made in order to enable imaging of as much of the oocyte as possible in a restricted time frame, whilst having a reasonable *z* resolution, and to adhere to strict file size limits at the beginning of the project. Later in the project, with faster acquisition times and better equipment for larger file sizes, settings were maintained for consistency of measurements and data analysis. CARS images in *xy* were taken with 0.1μm pixel size, typically in a 100 μm x100 μm frame, with 0.01 ms pixel dwell time, and time-average total power of ~20 mW at the sample. Movement of the sample stage and *z*-objective is provided by automated stepper motors (Prior ProScan III). All images were measured at the CH_2 symmetric stretch vibration at ~2850 cm^{-1}, abundant in the acyl chain of FAs, and an ideal target for single-frequency CARS microscopy of LDs present in the egg or embryo. The in-house developed MultiCARS software was used to collect and regularise images from the CARS microscope. ImageJ was used to assemble image stacks into maximum intensity projections, depth colour-coded projections, merged-channel stacks and videos.

Hyperspectral imaging is performed by changing the relative delay time between the equally linearly-chirped pump and Stokes pulses. A delay stage on the pump beam path (PI, M-404.42S; see Fig. 2.8.1.2.) controls the delay time between the pump and Stokes beams, in order to shift the IFD. This results in a tuning of the IFD across the entire 1200-3800 cm^{-1} vibrational range, owing to the large bandwidth of the Stokes pulse (Pope *et al.* 2013), enabling probing of many biologically-relevant resonances.

In practice, scans were taken between 2600-3800 cm^{-1} in 5 cm^{-1} steps over a 10 μm x 80-100 μm area, with 0.1 μm pixel size and a pixel dwell time of 0.001 ms, ten times less than the single frequency CARS images, to reduce photo-damage and motion artefacts. In-house developed MultiCARS software was used to collect and regularise images.

TPF imaging of lipid and mitochondrial stains absorbing at ~480nm and emitting at 510nm ± 40nm, simultaneously with CARS, was possible using the third near-infrared beam centred around 930 nm (70nm bandwidth) described above. TPF and SHG wavelengths (>900nm) are independently optimised in time domain using reflecting prisms (Fortune Optronics; see RP in Fig. 2.8.1.2.) to provide Fourier-limited pulses of approximately 30fs duration at the sample for maximum TPF excitation (see Pope *et al.* 2013).

TPF in the wavelength range 498-540nm was detected simultaneously with CARS, the signal isolated via appropriate dichroic beamsplitters and band pass filters (Semrock; DM4, F3 in Fig. 2.8.1.2.) before forward detection by a Hamamatsu, H10770A-40 PMT (PMT3, Fig. 2.8.1.2.). The SHG detector was used for imaging of autofluorescence, simultaneously with TPF and CARS. Detected in the wavelength range 451-487nm using appropriate dichroic beam splitters and band pass filters (Semrock; DM4, F2 in Fig. 2.8.1.2.), SHG was collected in the forward direction by a third PMT (Hamamatsu, H10721-210; PMT2, Fig. 2.8.1.2.).

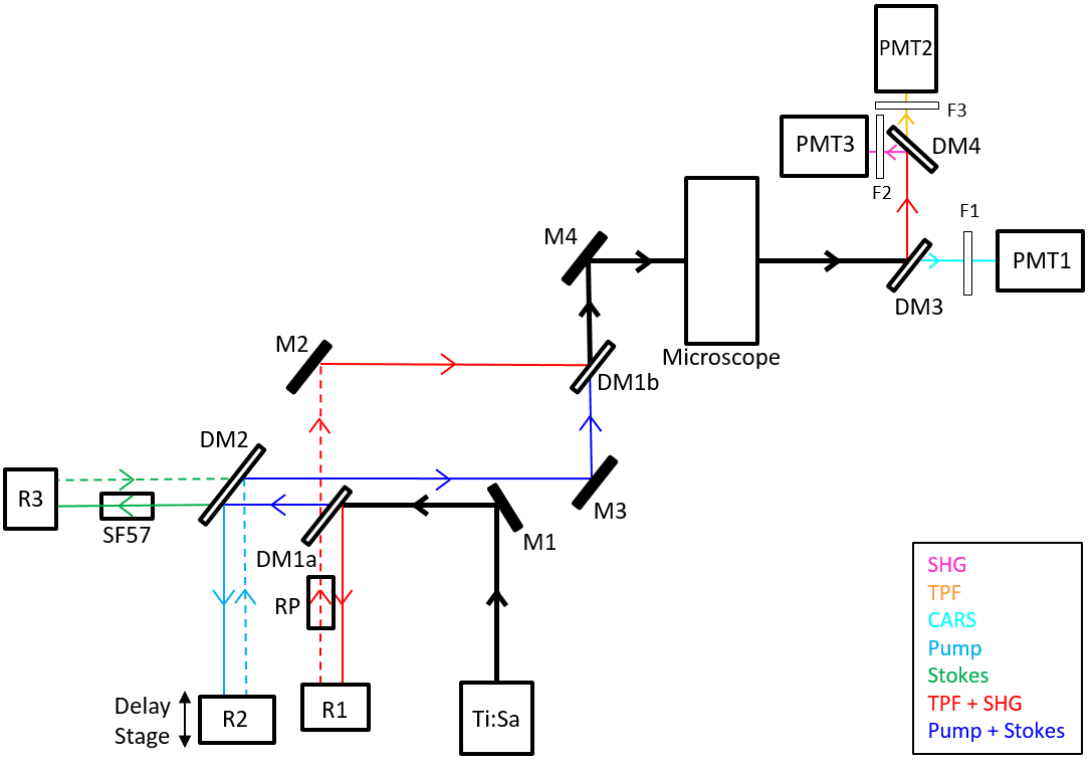

Fig.2.8.1.2. CARS Microscope Set Up

Ti:Sa: Titanium Sapphire laser; M: mirror; DM: dichroic mirror; SF57: 0-60mm glass block; R: reflecting mirrors; RP: Reflecting prisms; F: filters. M1= directs laser ouput (black line) to DMs; DM1a= reflects >900nm (TPF and SHG wavelengths- red line); DM2= splits pump (light blue line) and Stokes (green line) beams, and recombines them on their return; SF57= glass block of differing lengths, to linearly chirp Stokes to match the pump; R1-3= displacing prism reflectors; RP= reflecting prism pair for chirp recompression; M2= changes TPF and SHG direction, M3= changes pump and Stokes direction; DM1b= recombines TPF, SHG, pump and Stokes beams; M4= scan mirrors direct beams into microscope; Output from sample, DM3= reflects SHG and TPF, allows anti-Stokes (very light blue line) emission; F1= 542–582nm; PMT1= H7422-40 for CARS detection; D45= splits SHG (pink line) and TPF (orange line); F2= 468–487nm; PMT2= H107210-210 for SHG detection; F3= 468–552nm; PMT3= H10721-20 for TPF detection.

2.8.2. DIC and Epi-fluorescence Microscopy

A 1.27 NA x60 water immersion objective (Nikon λS series) and a 1.4NA oil condenser were used for high resolution DIC. A motorized sample stage enabled lateral *xy* sample movement and a motorized objective focussing enabled axial *z* movement (Prior ProScan III), and images are acquired by a monochrome CCD camera (Hamamatsu Orca-285).

3D DIC images were taken with 20 ms frame exposure time and as *z*-stacks over the full cell depth (~70μm) in 0.5μm steps, using the software MicroManager. A 12.5º polarisation angle in the de-Senarmont DIC illuminator was used, yielding a 25º phase offset, as this is found to be sufficiently small to enable good image contrast and sufficiently high to enable quantitative analysis of small phase objects such as lipid membranes (McPhee *et al.* 2013).

In order to follow LD distribution throughout IVM, DIC images were taken at (10min) time points over (24hrs), beginning at GV immediately after release from IBMX-induced prophase I arrest. IVM was then imaged overnight (one *z* plane), and ImageJ used for qualitative analysis.

The microscope is also equipped with epi-fluorescence illumination provided by a metal-halide light source (Prior Lumen 200). Epi-fluorescence images are acquired by a monochrome CCD camera (Hamamatsu Orca-285).

2.9. Data Analysis

2.9.1. Aggregation Analysis

The in-house developed CCDPlot software was used to find the 3D coordinates and amplitude maxima of LDs from the single-frequency CARS images. The background signal was subtracted, and the square root of the data was calculated to give amplitudes proportional to the number of CH_2 bonds in the sample. Peaks were fitted with a Gaussian function in three dimensions, and their amplitude, *xyz* width, and *xyz* centre was used to describe the LD. Origin was used to plot these parameters and analyse them statistically.

An Origin script (see Appendix 5) was used to assign an index to LDs separated from their nearest neighbour by less than a user-defined value *L*, the index being identical for all LDs belonging to the same cluster. The occurrence of this index was then used to calculate the number of LDs in each aggregate (called aggregate size) and the number of aggregates. We found that the optimum parameters to account for the observed clustering in the CARS images were obtained by calculating the distance between two LDs in resolution units, i.e.

$d_{ij} = \sqrt{\left(\left(\frac{x_i - x_j}{RL}\right)^2 + \left(\frac{y_i - y_j}{RL}\right)^2 + \left(\frac{z_i - z_j}{RA}\right)^2\right)}$ with x_i, y_i, z_i coordinates of the i-th LD, $RL = 0.3$µm and $RA = 0.6$µm being the lateral and axial CARS resolution respectively, and using

$0 < d_{ij} < L = 1.5\sqrt{3}$ i.e. L equal to 1.5 times the distance in resolution units. This value was deduced from trial and error, using varying distances between neighbouring LDs in the analysis, until the distance $L = 1.5\sqrt{3}$ was found to give the correct number of aggregates and their comprising LDs.

A script was also written to generate a random case of 2000, 4000 or 6000 'droplets' within a 50x50x50µm cube, in order to investigate aggregation occurrence in a random situation (see Appendix 6).

A simple t-test was performed to initially compare the amount of LD aggregation seen in populations of eggs or embryos at differing developmental stages, or under different conditions. The total number of isolated LDs (those not in a cluster) within an egg or embryo was provided by the algorithm above. Using the total number of LDs within the egg or embryo provided by CCDPlot analysis, the percentage of un-aggregated droplets could be found and compared between populations. Comparison was made using Excel. The t-test used was type 2, as the numbers within each population of cells varied, and it was two-tailed in order to account for a statistical relationship in either direction. The difference between two populations of cells is considered significant if the output *P value* is ≤0.05 (within 95% confidence limits).

In order to more quantitatively compare mean aggregate sizes across different developmental stages, the probability P_k of each size $k = 1, 2, 3\ldots$ (including size 1. i.e. isolated LDs) was calculated from the histogram of the aggregate size, as $P_k = O_k/O$, where $O = \sum_k O_k$ and O_k is the occurrence of size k. The mean square aggregate size was then calculated as $\langle s^2 \rangle = \sum_{k=1}^{+\infty} (k-1)^2 P_k$ for each egg or embryo (where we subtracted 1 to obtain the number of partner LDs in an aggregate). Origin was used to plot the square root of $\langle s^2 \rangle$ $(\sqrt{\langle s^2 \rangle})$ of all eggs or embryos of a given developmental stage, against the total number of LDs at that stage.

2.9.2. Total Lipid Analysis

In order to analyse the total amount of lipid at each developmental stage or in each cell population, the total lipid amount of each cell was found using a number of the parameters given by the in-house developed CCDPlot software (see section 2.9.1). The volume of each LD was found by calculating $V_i = W_{ix}W_{iy}W_{iz}$ where W_i is the diameter of the i-th LD in each *xyz* dimension given by 3D fitting of the CARS amplitude. In order to account for sub-resolution droplets, the amplitude of each droplet was normalised to the amplitude of the brightest droplet: A_i/A_b where A_i is the CARS amplitude of the LD (the square root of the CARS intensity), and A_b represents the amplitude of the brightest droplet in the entire egg/embryo. This normalisation works because the CARS amplitude is proportional to the number of bonds within the focal volume (in the regime where the resonant contribution dominates). Hence the lipid volume of each droplet (including those which are sub-resolution) is calculated as the normalised quantity $V_i(A_i/A_b)$. The total lipid amount per egg/embryo is calculated as the sum of the lipid volumes of all LDs: $\langle TL \rangle = \sum(V_i(A_i/A_b))$, and the average lipid volume per LD is calculated as: $\langle TL \rangle / Total\ number\ of\ LDs$ $\left(\langle \frac{TL}{LD} \rangle\right)$. The $\langle \frac{TL}{LD} \rangle$ was found per population, and was plotted against total LD number using Origin, in order to compare developmental stages and effects of experimental conditions.

2.9.3. Lipid Droplet Size Analysis

In order to compare mean LD sizes across different developmental stages, the volume of each LD was calculated as discussed above in section 2.9.2, i.e. using $V_{in} = V_i(A_i/A_b)$. A LD effective diameter was then calculated as $d_i = (V_{in})^{1/3}$. The probability P_{di} of each diameter d_i was calculated from a histogram of the diameters of LDs (bins of $1\text{x}10^{-3}$µm) present within that particular egg or embryo, as $P_{di} = O_{di}/N$, where N is the total number of LDs and O_{di} is the occurrence of diameter d_i. The mean diameter was then calculated as $\langle d \rangle = \sum_i d_i\, P_{di}$ for each egg or embryo. Origin was used to plot the mean $\langle d \rangle$ of all eggs or embryos of a given developmental stage, against the total number of LDs at that stage.

2.9.4. Hyperspectral Image Analysis

Raman-like spectra were retrieved from CARS spectra using in-house developed hyperspectral image analysis (HIA) software (Masia *et al.* 2015). Hyperspectral images were background-corrected by subtracting an image measured under identical excitation/detection conditions but with pump and Stokes pulses out of time overlap, then were noise-filtered using a singular value decomposition (SVD) algorithm on the square root of the CARS intensity to retain only components above noise (Masia *et al.* 2013). CARS intensity ratios were calculated by dividing the background-corrected CARS intensity by the corresponding non-resonant CARS intensity measured in glass under the same excitation and detection conditions. As there is a Kramers-Kronig relationship connecting the real and imaginary parts of the CARS signal, a phase-corrected Kramers-Kronig (PCKK) method was developed to retrieve the complex CARS third-order susceptibility ($\chi^{(3)}$) from the CARS intensity ratio, normalised to the non-resonant background in glass, and proportional to the concentration of chemical components (Masia *et al.* 2013, Di Napoli *et al.* 2014a). Shown spectra are the retrieved imaginary part of the susceptibility ($\mathrm{Im}(\chi)$) normalised to the total area, and the software Origin was used to plot these against eggs or embryos of the same developmental stage/conditions.

The spectra were analysed quantitatively by finding the ratio between certain peaks seen in spectra from different LDs. For example, the ratio between peaks at ~2930 cm^{-1} (CH_3 and asymmetric CH_2) and ~2850 cm^{-1} (CH_2), can be used as a measure of chain disorder and is expected to be higher in polyunsaturated fatty acids. The ratio between peaks at ~3010 cm^{-1} (=CH) and ~2850 cm^{-1} (CH_2) can be used as a measure of unsaturation, thus is expected to be near zero in saturated fatty acids.

2.9.5. Colocalisation Analysis

Correlation studies were carried out using an Image J 'Correlation Threshold' plug-in. The Pearson's correlation coefficient is calculated by coordinate correlation of pixels above a certain intensity threshold. Individual thresholds are calculated with ImageJ itself as intensities which give a Pearson's coefficient of 0. The resulting Pearson's coefficient for all pixels above threshold (RColoc) is a number between 0

and 1, to show the degree of significant correlation between CARS and TPF images. A correlation is accepted with a Pearson's coefficient of >0.5, but a significant correlation is considered with a coefficient of >0.95 (95% statistical confidence limit). The output correlation scatter plots show the linear relationship between pixels in corresponding CARS (x axis) and TPF (y axis) images.

Chapter 3. CARS Imaging of Lipid Droplets throughout Mouse Egg/Embryo Development

3.1. Introduction

One of the main aims of this project is to image lipid droplets in living mouse eggs and embryos in a label-free, yet chemically-specific manner. The presence of LDs in eggs and embryos of certain species has been well characterised using various microscopy techniques such as transmission electron microscopy (TEM) and fluorescence imaging, especially in pigs, cows and sheep where LDs are large (>1μm) and abundant. Interestingly, lipid metabolism in oocytes of these species is significant (McEvoy *et al.* 2000). LDs of mouse and human eggs and embryos, however, have been less well investigated.

Mouse oocytes and embryos are widely used as a model for human egg and embryo development, due to their similarities in cell size, cell-cycle timing and processes, and fertilisation, to name a few. Oocytes of both species have a clear cytoplasm with cytoplasmic inclusions unresolvable through conventional microscopy methods, in comparison to the eggs of species such as dogs and pigs, where the cytoplasm is opaque with very large lipid droplets (>5μm) (Homa *et al.* 1986; Apparicio *et al.* 2012). It is known that lipid metabolism is in fact occurring in both human and mouse eggs and embryos, and that the presence of lipids in their TAG and FFA forms are vital for successful development (Dumollard *et al.* 2007; Dunning *et al.* 2011). However, a quantitative investigation of the LDs themselves, their size, content and spatial distribution throughout development in living eggs and embryos is still lacking.

Traditionally, the lipid content of mammalian oocytes and embryos has been destructively analysed by means such as mass spectrometry and chemical extraction (Apparicio *et al.* 2012; Ferreira et al. 2010; McEvoy *et al.* 2000; Loewenstein and Cohen, 1964), fluorescence investigation of TAG hydrolysis (Sturmey and Leese, 2003; Ferguson and Leese, 1999), and invasive techniques of imaging of the LDs

such as TEM, and fluorescent lipid stains (Romek *et al.* 2009; Genicot *et al.* 2005; Crocco *et al.* 2013; Ordonez-Leon *et al.* 2014). While these previous efforts to image LDs in mammalian eggs and embryos have provided evidence of LDs in these cell types, they are inadequate to give sufficient quantitative information about the presence of lipids in eggs. TEM methods, and levels of fluorescence emission are unable to give a precise or absolute measure of the amount of lipid present in a sample. Fluorescent dyes are also often unspecific in their staining pattern. Furthermore, all previous efforts are unable to be reproduced in living cells, and less invasive techniques of analysis are required.

Harmonic Generation Microscopy (HGM) is an emerging multiphoton technique which can image cells label-free, through measurement of second and third harmonic generation of light (SHG and THG, respectively) (Thayil *et al.* 2011). However, these are not chemically specific, and rely on specific geometries (lack of inversion symmetry) of the structures to be imaged (SHG) or on the presence of interfaces (THG). THG has been applied to image LDs in mouse eggs by Watanabe *et al.* (2010), however they did not resolve individual droplets, causing multiple droplets to appear as one large, yet not spherical, droplet.

One important motivation behind our aim to visualise individual LDs in living mouse and human eggs or embryos in a chemically specific way is the idea that the LD spatial distribution, and chemical content, could give an indication of the metabolic state of the egg or embryo, allowing for a method of quality assessment. In clinical practise, eggs and embryos are assessed primarily by their morphology. However, it is difficult to draw conclusions as to the quality of oocytes, eggs or embryos simply from their morphology. This is a shortcoming of typical methods of egg or embryo assessment used in assisted reproduction. As previously described in Chapter 1 (section 1.2.3.), an egg or oocyte may be considered to be of 'abnormal' morphology, or 'bad quality' if they have an abnormal (i.e. non-spherical) shape, a large-perivitelline space, or a particularly granular cytoplasm. Embryos that become fragmented or arrested in their mitotic cycle may give an example of 'bad quality' specimens. These can be compared with normal-looking 'healthy' eggs and embryos, but it is unclear how correct and reliable this method may be.

Demonstration of a central GV versus a non-central GV is considered to be a valid measure of oocyte quality, a central GV conferring a higher developmental potential

(Bellone *et al.* 2009; Brunet and Marot, 2007). While the neat arrangement of chromosomes forming a ring around the nucleolus in a GV oocyte, revealed by Hoechst staining, has also been found to be an indicator of developmental potential, the use of fluorescent stains such as Hoechst defeats the idea of a non-invasive quality detection method, and cannot be used in clinical practise. (Bellone *et al.* 2009; Bouniol-Baly *et al.* 1999). The analysis of GV oocytes in reproductive treatments would mean they would subsequently require *in vitro* maturation (IVM) before fertilisation. It is commonly thought that IVM yields MII eggs of a poorer quality than those matured naturally within the mother. While culture media are designed to provide the nourishment maturing oocytes need, it can be argued that the handling and light exposure they are subjected to, and the unnatural media environment, is inferior compared to a natural maturation (Rizos *et al.* 2002, Gilchrist and Thompson, 2007). Despite the fact miscarriage rates are higher after IVM, it has been found that healthy offspring can result from IVM (Eppig *et al.* 2009). Overall, there is a clear need for better methods of assessing egg and embryo quality reliably and quantitatively.

Raman spectro-microscopy is a label-free imaging technique that has been implemented to investigate lipid content of oocytes and embryos (Davidson *et al.* 2012), however, this method requires sample fixation. CARS microscopy is a label-free, multiphoton imaging technique, compatible with live cell imaging, that has the advantage of being chemically-specific. CARS has previously been used to image lipids in other cell types, and multiple species (Hellerer *et al.* 2007; Wang *et al.* 2009). Thus, we proposed that CARS could be used to non-invasively and qualitatively investigate the distribution of LDs within living mouse oocytes, eggs and embryos, and methods could be devised of quantitatively assessing LD number, size and distribution, as well as lipid content.

As shown in the following results sections, CARS imaging of oocytes from the GV stage throughout development to the embryonic blastocyst stage allowed vast amounts of qualitative and quantitative information to be accumulated, giving unprecedented insight into the lipid content of a previously unsuccessfully investigated species, and enabling a broad scope of further investigation. Comparison of CARS images of ‘healthy’ oocytes, eggs and embryos with abnormal

eggs or arrested embryos gave information as to the links between LD distribution and quality assessment, and imaging of alternative species also allowed a comparison between LDs of cells with metabolic states known to differ.

3.2. Germinal Vesicle- and MII-Arrested Stages

Qualitative CARS Analysis

In order to examine the lipid content of mouse eggs and embryos of different stages, DIC and CARS z-stacks were taken throughout the majority of the egg/embryo volume. High magnification DIC microscopy enables identification of distinct characteristics and assessment of the general morphology of an egg embryo, enabling assessment of the egg's developmental stage, and general well-being prior to further imaging. Taking CARS z-stacks throughout cells at different developmental stages allowed chemically-specific visualisation and characterisation of the size and distribution of LDs present in the cytoplasm throughout development. Owing to the high NA of the objective used (1.27), we were able to image LDs with high spatial resolution (0.3μm lateral, 0.6μm axial). A 50μm volume was chosen for practicality of timing and consistency, and included the majority of the LDs present to be imaged with CARS. High magnification *z*-stacks are taken throughout an egg at a vibrational resonance of 2850cm^{-1} in order to visualise the cellular lipid content. An image taken when there is no time overlap of pump and Stokes pulses (see Appendix 7) shows a small background (that is eventually subtracted from the CARS image- see Chapter 2, section 2.9.) and confirms that the signal collected at 2850cm^{-1} is CARS of highly aggregated CH_2 bonds. CARS images were compiled into a depth colour-coded z-stack projection of a CARS stack through an entire cell, clearly showing the droplets and their spatial distribution.

DIC images taken of an immature oocyte demonstrate its clearly visible GV containing the nucleus, its zona pellucida surrounding the entire cell, and multiple unidentifiable cytoplasmic inclusions. Fig.3.2.1. (A) shows a single z-plane image through the approximately equatorial plane of GV oocyte, displaying these features. Inclusions within the cytoplasm are consistently seen in all cells imaged, but not

chemically identifiable by DIC alone. Examination of CARS images throughout a GV oocyte, shows that the lipids within these cells are assembled into roughly uniformly-sized lipid droplets (~0.5µm diameter, for a quantitative LD size analysis see section 3.4 and Fig.3.4.4) scattered apparently homogenously throughout the cytoplasm, but not within the GV itself (Fig.3.2.1. (B)).

In comparison, DIC images of mature MII eggs enables visualisation of common features such as the polar body, and often the metaphase spindle. Again, the cytoplasm is seen to include many unidentifiable vesicles (indicated in the inset, Fig.3.2.1. (C)). CARS imaging of MII eggs reveals ~0.5µm diameter LDs assembled into clusters, with a spatial distribution appearing very different to the distribution seen in GV oocytes (Fig.3.2.1. (D)). These aggregations are formed by several resolvable individual droplets (indicated in the inset, Fig.3.2.1. (D)). Single LDs and LD clusters are distributed throughout the entire volume of the egg, with seemingly no bias towards any side, the centre or the periphery.

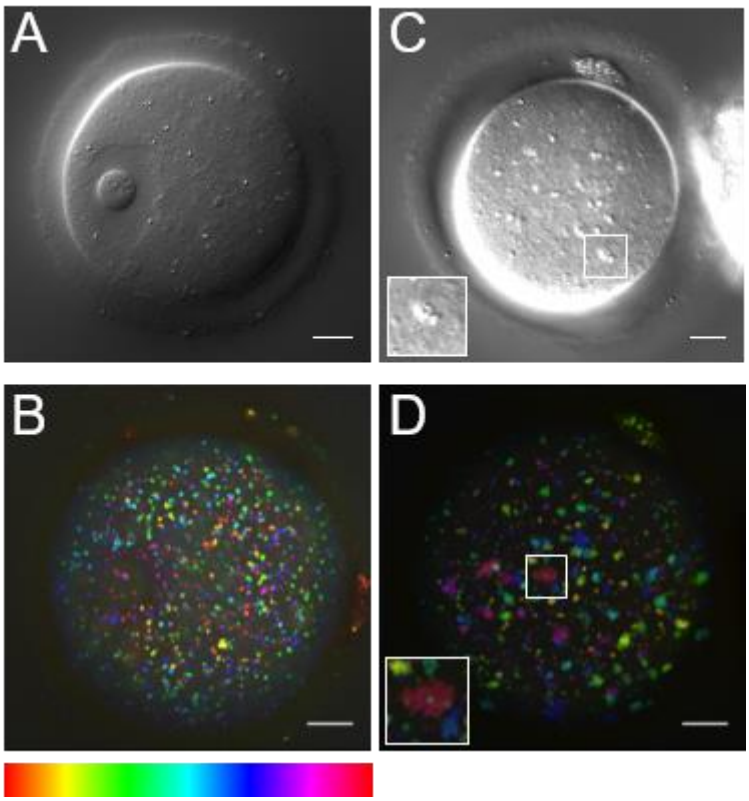

Fig.3.2.1. DIC and CARS Imaging of GV and MII Stage Mouse Eggs

(A) and (C) Single-plane (approximately equatorial) DIC images of representative of (A) immature GV stage oocytes (n=~90) and (C) mature MII eggs (n=~70) using a 1.27 NA water objective and a 1.4 NA oil condenser. Inset in (C) shows an unidentified cytoplasmic vesicle cluster. (B) and (D) Depth colour-coded images of CARS z-stacks at wavenumber 2850cm^{-1} through the same eggs, showing LDs at these developmental stages. Inset in (D) shows a typical LD cluster seen at this stage. 0.1x0.1µm *xy* pixel size; 0.5µm *z*-step; 0.01ms pixel dwell time; ~14mW (~9mW) Pump (Stokes) power at the sample. Scale bars represent 10µm; colour bar shows depth colour-coding from -25µm-25µm of 101 *z*-stacks (0µm being the approximately equatorial plane of the egg), the brightness of each colour is the maximum intensity at each corresponding *z*-plane. Data from ≥2 trials, using 1-3 mice each.

Imaging of GV oocytes before and after *in vitro* maturation (IVM) to MII eggs provides further evidence of this clustering phenomenon (Fig.3.2.2.). GV oocytes were washed out of GV-arresting IBMX media, and imaged immediately with both DIC and CARS (Fig.3.2.2. (A-B)). Oocytes were then allowed to mature overnight (~16hrs) in a heated chamber before imaging again the next morning, once MII stage had been reached (Fig.3.2.2. (C-D)). As described before, CARS images showed that GV oocytes prior to maturation appeared to contain fewer aggregations of LDs

(Fig.3.2.2. (B)), whereas, after maturation, the LDs of these same eggs appear to have changed conformation and become a lot more clustered (Fig.3.2.2. (D)).

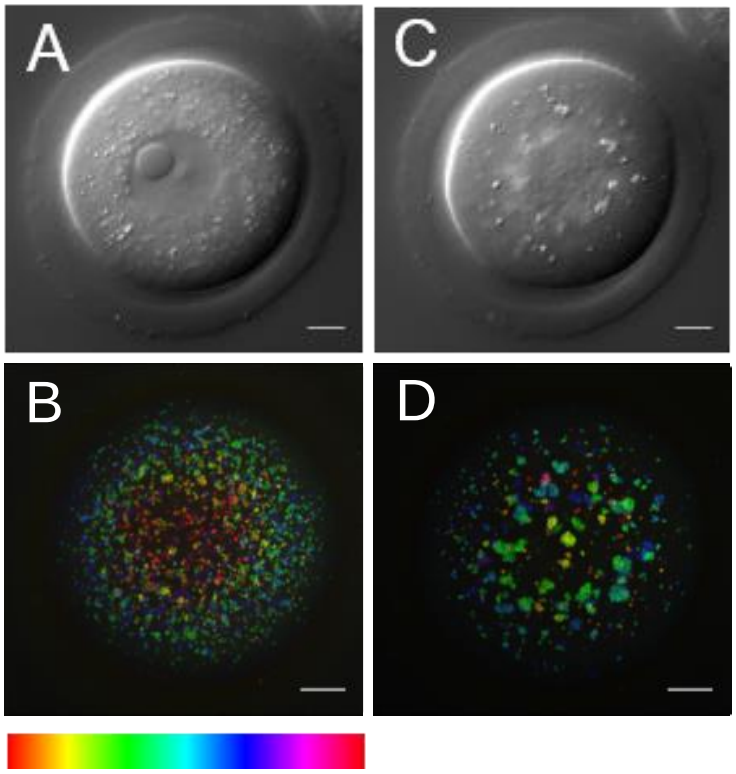

Fig.3.2.2. DIC and CARS Imaging of the same Mouse Egg at GV and MII Stage, before and after* in vitro *Maturation

(A) and (C) Single *z*-plane DIC using a 1.27 NA water objective and a 1.4 NA oil condenser; and (B) and (D) depth colour-coded images of CARS stacks at wavenumber 2850cm^{-1}, of an egg before (A and B) and after (C and D) *in vitro* maturation, showing that development can still occur after live imaging with CARS (n=40). 0.1x0.1µm *xy* pixel size; 0.5µm *z*-step; 0.01ms pixel dwell time; ~13mW (~9mW) Pump (Stokes) power at the sample. Scale bars represent 10µm; colour bar shows depth colour-coding from -25µm-25µm (0µm being the equatorial plane). Data from >5 trials, using 1-3 mice each.

Following identification of lipid vesicles allowed by the CARS measurements observed above, it was possible to observe changes in LD distribution using DIC alone. Time-lapse DIC images were taken during the ~16hrs allowed for IVM, after washing GV oocytes out of IBMX, and images were compiled into a film clip (Fig.3.2.3.). LDs were very motile during cell maturation events, and vesicles went in and out of the plane of focus, however, it is possible to follow a number of LDs

between frames, and it is possible to visualise clusters of droplets forming in the later stages.

Fig.3.2.3. DIC Following Aggregation of Lipid Droplets during* in vitro *Maturation from GV to MII stage

2D video of a GV oocyte maturing to an MII egg over 22 hours. Images were taken every 10 minutes. Video is shown at 7 frames per second. Please scan the QR code above using your smart phone camera (you may need to install a QR Code Reader. Alternatively, video can be accessed at: https://www.youtube.com/watch?v=lgy1XVZSlp4

Quantitative CARS Analysis

The in-house developed software, CCDPlot was used to fit the CARS signal peaks given by individual LDs in the imaged 3D volume, providing output parameters such as the 3D co-ordinates of the centre of each droplet and the LD diameter. These output parameters can be further quantitatively analysed using Origin software (see Chapter 2, section 2.9.1.). It was revealed using this method that the number of LDs in each cell differed greatly, usually ranging from ~1000 - ~6000 droplets.

In order to quantitatively analyse the LD clusters seen within the qualitative CARS images, an algorithm (see Appendix 5) was developed to utilise the output parameters from CCDPlot analysis, in order to count the number of clusters and the total number of droplets within each of these aggregates. A droplet was considered as being part of a cluster when its distance to its nearest neighbouring LD was less than 1.5 times the 3D spatial resolution, consistent with the experimental observation

of distance distribution in aggregates containing many droplets (see Chapter 2, section 2.9.1.). Results of this analysis are shown in Fig.3.2.4., where the numbers of LDs comprising a cluster were plotted as a histogram against the number of occurrences of that particular size of cluster, allowing direct comparison between eggs and embryos of the same developmental stage or between each other. GV oocytes prove to have aggregates containing mostly between 2 and 10 LDs, with ~60-70% of LDs being separate and singular (Fig.3.2.4. (A)). Comparing this to MII eggs, we typically see several clusters of more than 10 LDs, with between only ~30-50% of droplets isolated (Fig.3.2.4. (B)). Notably, we observe the same phenomenon even within the same egg when comparing before and after *in vitro* maturation (Fig.3.2.4. (C-D)). These results were compared to a simulated case of random 3D spatial distribution of 2000, 4000 or 6000 droplets in a 50µm x 50µm cube, as these were the typical ranges observed experimentally (see Figure 3.2.5. and see Appendix 6 for algorithm). These simulations resulted in 94%, 88% and 83% isolated droplets, respectively. Comparison of our experimental results with these simulations indicated that the distribution and aggregations of LDs seen in oocytes/eggs are not random.

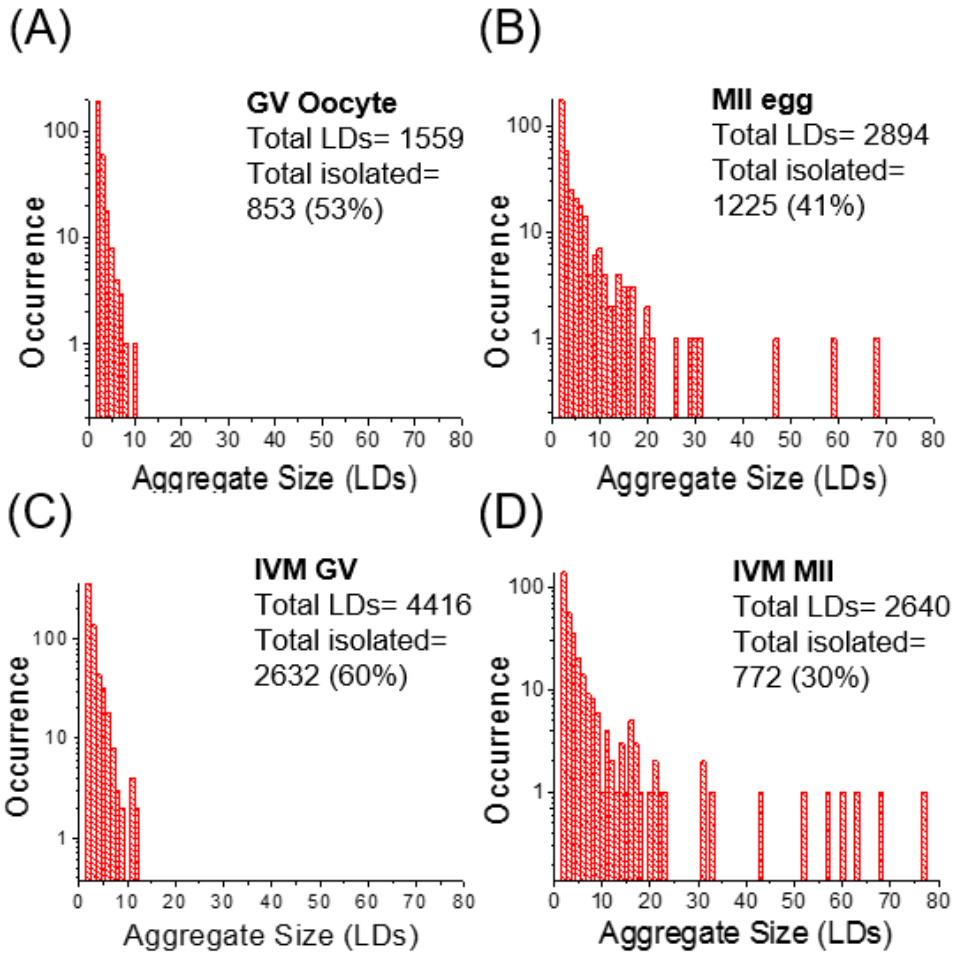

Fig.3.2.4. Histograms of Lipid Droplet Aggregation in GV and MII Stage Mouse Eggs, before and after* in vivo *Maturation, and before and after* in vitro *Maturation

Histograms of the number of LDs making up clusters in (A) a GV oocyte (n=33), (B) an MII egg matured *in vivo* (n=20), (C) a GV oocyte before *in vitro* maturation, and (D) an MII egg after *in vitro* maturation (n=10), demonstrating the change in LD distribution over time. Total number of LDs and total number of un-clustered LDs are also indicated.

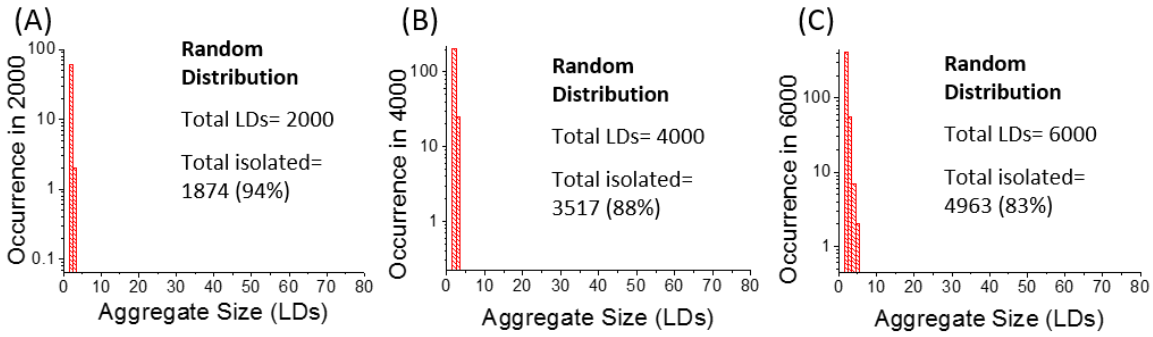

Fig.3.2.5. Histograms of 'Lipid Droplet Aggregation' in a case of 2000, 4000, and 6000 'Droplets' Randomly Distributed in a 50µm x 50µm cube

Histograms of algorithm-generated random distributions of typical numbers of 'droplets': (A) 2000 droplets, (B) 4000 droplets, and (C) 6000 droplets.

Simple t-test statistical analysis of the percentage of isolated droplets within all GV oocytes imaged and all MII eggs imaged shows a significant difference (*P value* of 0.025) between these two stages of development. Further quantitative analysis of the clustering of LDs was performed, allowing us to reliably compare the extent of aggregation between cells and populations of cells. The square root of the mean squared aggregate size ($\sqrt{\langle s^2 \rangle}$) (defined as detailed in Chapter 2, section 2.9.1.) was calculated for each individual egg and, in turn, for each population of GV oocytes, and MII eggs. Figure 3.2.6. shows a two-dimensional plot of $\sqrt{\langle s^2 \rangle}$ against the total number of LDs, where the distribution of these two variables for each population representing a particular developmental stage is plotted as an average (symbol) and standard deviation (bar). Although there is a substantial variability within each group, the MII group (red circle) is distinguished through larger values of $\sqrt{\langle s^2 \rangle}$ than those seen at GV stage (black square). Comparing these with the simulated random distributions (cyan, magenta and orange points), the average $\sqrt{\langle s^2 \rangle}$ in random distributions is below that observed experimentally in each group. Therefore, even though less aggregations are seen in the GV stage, they still show more LD clustering than expected from a random distribution, suggesting a physiological reason or cause for LD aggregation.

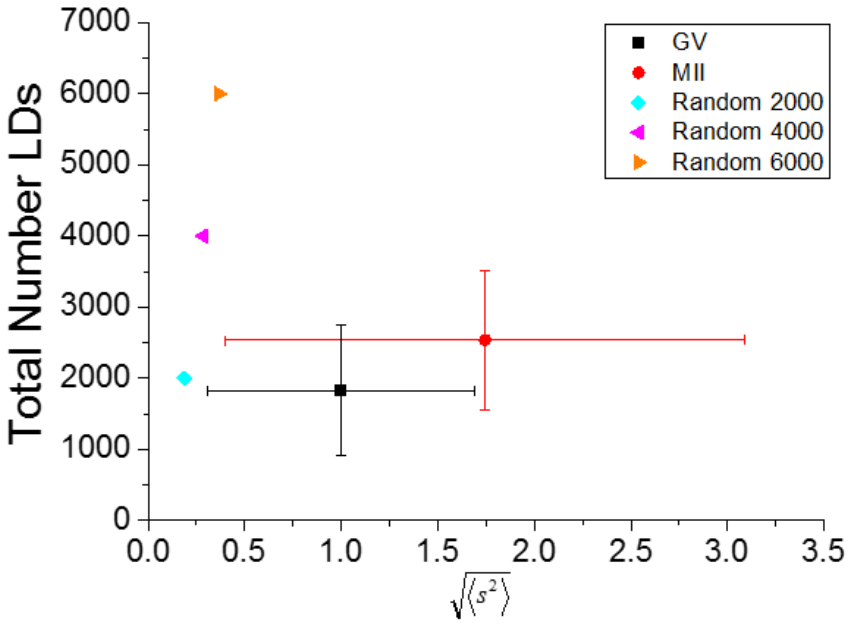

Fig.3.2.6. Scatter plot of Extent of Lipid Droplet Aggregation ($\sqrt{\langle s^2 \rangle}$) in GV and MII stage Mouse Eggs

Scatter plot of the square root of the mean squared aggregate size ($\sqrt{\langle s^2 \rangle}$) against the total number of LDs, in ensembles of GV oocytes (n=33) and MII eggs (n=30), against random distributions of 2000, 4000 and 6000 droplets. The distribution of each variable in the corresponding ensemble is shown as an average (symbol) and standard deviation (bar).

It was also possible to assess the volume of LDs using the LD width in *xyz* given by CCDPlot. To account for sub-resolution droplets, the amplitude of the CARS signal (square root of the CARS intensity- see Chapter 2, section 2.9.2.) obtained from each droplet within the measured sample was normalised to the amplitude of the brightest droplet. From the volume of each lipid droplet, the total lipid amount (sum of LD volumes) per egg can be calculated ($\langle TL \rangle$), as well as the average lipid amount per droplet ($\langle \frac{TL}{LD} \rangle$) (see definitions in Chapter 2, section 2.9.2.). The mean and standard deviation of the $\langle \frac{TL}{LD} \rangle$ was calculated per population, allowing this to be plotted against the total LD number. Fig.3.2.7. shows a scatter plot of the $\langle \frac{TL}{LD} \rangle$ against the total number of LDs at each developmental stage. Within the shown standard deviation, there is little difference in $\langle \frac{TL}{LD} \rangle$ between the GV (black square) and MII (red circle) stages. It could be noted that on average there is less total lipid in the GV

stage due to a lower mean total LD number, although the difference is within the standard deviation of the distributions for the total LD number.

Fig.3.2.7. also shows that when comparing $\langle\frac{TL}{LD}\rangle$ in the same cell developing from GV (orange triangle) to MII (violet hexagon) stages, there is almost no difference between the amount of lipid in the two developmental stages. In this case, the total number of LDs appears to decrease as development continues in the same egg from its GV stage to its MII stage. This occurs even though the total number of LDs at MII is on average slightly higher than in the GV stage, as mentioned above. It is also notable that MII eggs after maturation in culture have a slightly higher total number of LDs than MII eggs matured *in vivo* (see section 3.3. below).

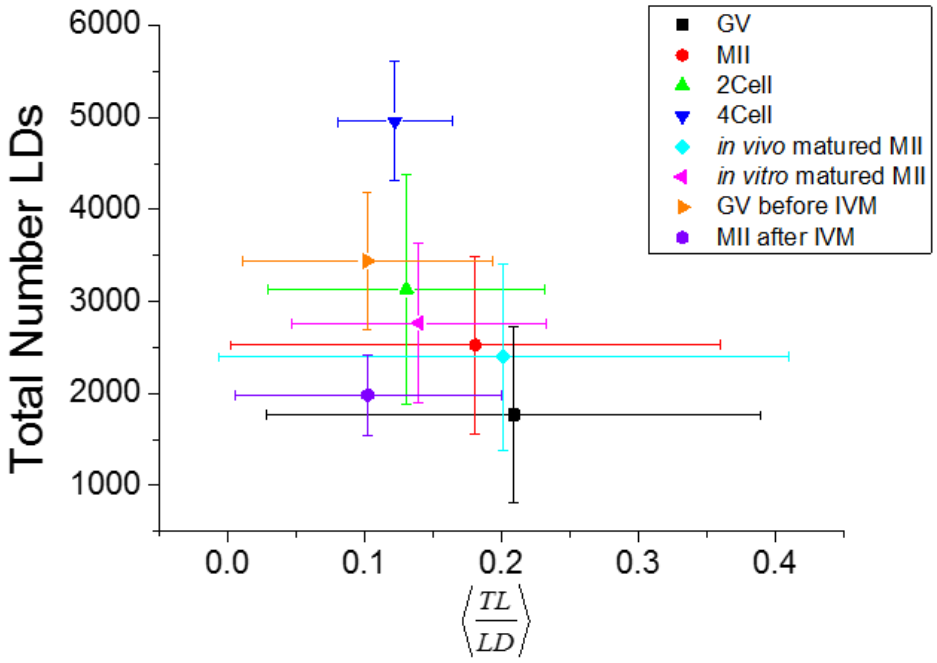

Fig.3.2.7. Scatter plot of the Total Lipid Amount per LD ($\langle\frac{TL}{LD}\rangle$) of Populations of Mouse Eggs and Early Embryos

Scatter plot of the total amount of lipid per droplet ($\langle\frac{TL}{LD}\rangle$) in populations of GV oocytes (n=33), MII eggs (=30), 2Cell stage embryos (n=10), 4Cell stage embryos (n=8). The MII population is split into sub-ensembles of *in vivo* matured MII eggs (n=20) and *in vitro* matured MII eggs (n=10). Also shown are the same oocytes before (GV) and after (MII) IVM (n=4). The distribution of each variable in the corresponding ensemble is shown as a mean (symbol) and standard deviation (bar).

3.3. In vivo vs. in vitro *Maturation*

This project allowed the difference in LD distribution between MII eggs matured *in vivo* and those matured *in vitro* to be investigated. GV oocytes collected and matured in MEM overnight were imaged with DIC and CARS microscopy the following day, once the MII stage (confirmed by the presence of a PB, n= 40/47) was reached. Some GV oocytes were imaged before maturation, and others were not, in order to compare the two groups.

Depth colour-coded images of CARS z-stacks show that IVM yields MII eggs with a similar distribution of aggregated LDs to those matured *in vivo*, whether they were imaged before maturation or not (Fig.3.3.1.). Quantitative and statistical analysis of LD distribution gives a clear idea of how maturation *in vitro* affects LD characteristics, as there is seen to be very little or insignificant differences in droplet distribution between MII eggs matured *in vitro* versus those matured *in vivo* (Fig.3.3.2.). A simple t-test comparing the aggregation of the two populations of MII eggs provided a *P value* of 0.599, thus it is assumed that IVM has negligible effect on the metabolic state of the egg where LD patterns are concerned.

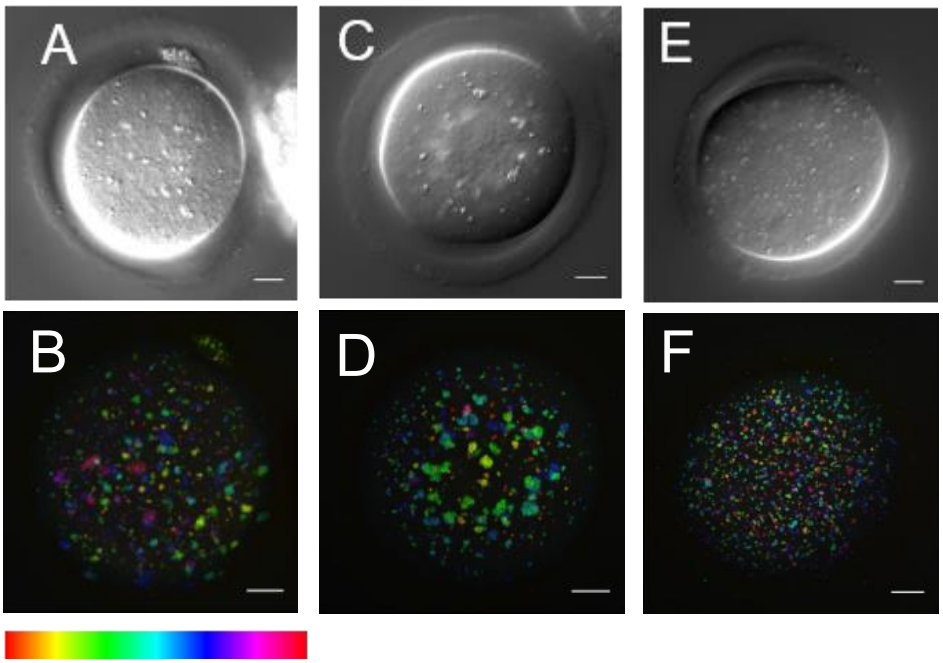

Fig.3.3.1. DIC and CARS Imaging of MII Stage Mouse Eggs, After* in vitro *and in vivo Maturation

(A), (C) and (E) Single-plane (approximately equatorial) DIC images of representative of (A) MII eggs matured *in vivo* (n=20), (C) MII eggs imaged with CARS before and after maturation *in vitro* (n=4), and (E) MII eggs that were not imaged with CARS prior to maturation *in vitro* (n=6) using a 1.27 NA water objective and a 1.4 NA oil condenser. (B), (D) and (F) Depth colour-coded images of CARS *z*-stacks at wavenumber 2850cm^{-1} through the same eggs, showing LDs. 0.1x0.1µm *xy* pixel size; 0.5µm *z*-step; 0.01ms pixel dwell time; ~14mW (~9mW) Pump (Stokes) power at the sample. Scale bars represent 10µm; colour bar shows depth colour-coding from -25µm-25µm of 101 *z*-stacks (0µm being the approximately equatorial plane of the egg), the brightness of each colour is the maximum intensity at each corresponding *z*-plane. Data from ≥2 trials, using 1-3 mice each.

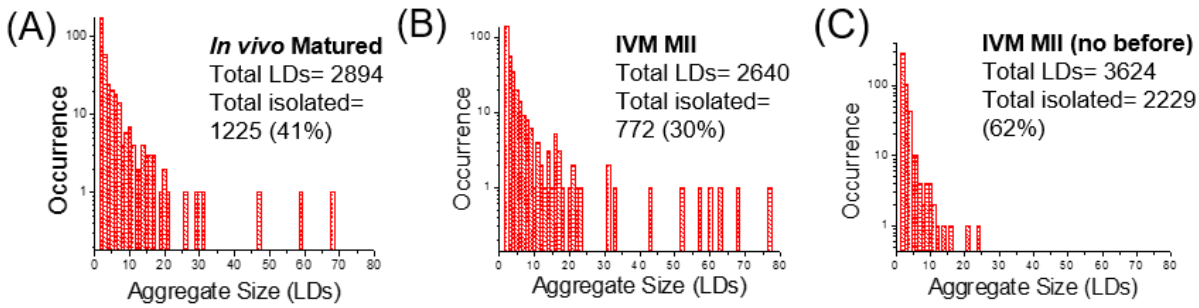

Fig.3.3.2. Histograms of Lipid Droplet Aggregation in GV and MII Stage Mouse Eggs, After* in vitro *and in vivo Maturation

Histograms of the number of LDs making up clusters in (A) an MII egg matured *in vivo* (n=20), (B) an MII egg imaged with CARS before and after maturation *in vitro* (n=4), and (C) an MII egg that was not imaged with CARS prior to maturation *in vitro* (n=6). Total number of LDs and total number of un-clustered LDs are also indicated.

A comparison of $\sqrt{\langle s^2 \rangle}$ for each *in vivo* and *in vitro* population of eggs also gave no indication of a significant difference in the distribution of LDs between the two, as shown in Fig.3.3.3. There is a difference seen in the $\sqrt{\langle s^2 \rangle}$ of eggs imaged before and after maturation compared to those only imaged afterwards, however this is not significant, as the values are within SDs. It is possible that the slightly higher number of LDs observed in the *in vitro* matured population may be significant, due to the difference in conditions between maturation in the follicular fluid versus maturation in fatty acid- containing culture medium. However, there was a noted difference between the total LD number within the same cells imaged before and after IVM. It appears that during this maturation, despite the presence of fatty acids in the culture media, (conjugated to the BSA added) the number of LDs decreases by approximately 40% (the mean LD loss was calculated as 42%).

Comparison of the lipid amount per LD ($\langle \frac{TL}{LD} \rangle$) in both *in vivo* and *in vitro* matured eggs shows that there is very little difference between the two conditions (Fig.3.2.7.). It may be noted that there is a slightly higher $\langle \frac{TL}{LD} \rangle$ in eggs matured *in vivo* (cyan diamond), while the group of eggs matured *in vitro* (magenta triangle) have less lipid per LD, but an overall higher total number of LDs. MII eggs matured *in vitro* after

being imaged with CARS in their GV stage (violet hexagon) have a lower $\langle \frac{TL}{LD} \rangle$, and fewer droplets, but results are still within the SDs.

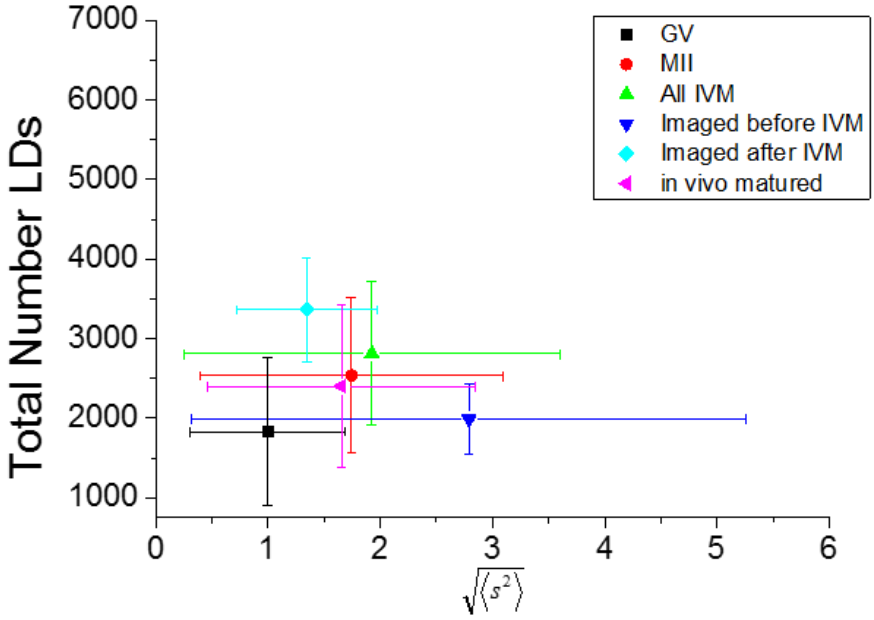

Fig.3.3.3. Scatter plot of the Extent of Lipid Droplet Aggregation in GV and MII Stage Mouse Eggs ($\sqrt{\langle s^2 \rangle}$), Compared with MII Stage Eggs Imaged Before and After* in vitro *Maturation

Scatter plot of the square root of the mean squared aggregate size ($\sqrt{\langle s^2 \rangle}$) against the total number of LDs, in ensembles of GV oocytes (n=33), MII eggs (n=30), MII eggs matured *in vitro* (IVM) (n=10), MII eggs imaged with CARS before being matured *in vitro* (n=4), MII eggs that were not imaged prior to being matured *in vitro* (n=6), and MII eggs matured *in vivo* (n=20). The distribution of each variable in the corresponding ensemble is shown as an average (symbol) and standard deviation (bar).

3.4. 2Cell and 4Cell Early-Embryo Stages

In vivo fertilisation was carried out by mating male and female mice overnight after female superovulation. Culture of collected embryos (see Chapter 2, section 2.3.3.) for 24hrs yielded 2Cell stage embryos, and culture for 48hrs allows development of 4Cell stage embryos, available for imaging. DIC imaging of 2Cell stage embryos allowed visualisation of both cells, their cytoplasm and nuclei, surrounded by the zona pellucida (Fig.3.4.1. (A)). Subsequent CARS imaging revealed that LDs in 2Cell-stage embryos appear to have a similar distribution as those in MII eggs, with widely-distributed clusters, which can be seen in both DIC images, and CARS projections (Fig.3.4.1. (B)). Droplets still appear to be of a similar size confirmed later by lipid droplet size analysis, and they occupy the entire cytoplasmic space, excluding the nucleus. Quantitative analysis of 2Cell embryo CARS stacks show aggregation patterns similar to both GV oocytes and MII eggs, with multiple large aggregations (made up of >10 LDs), but with a percentage of isolated LDs at around 60% (Fig.3.4.2. (A)). A simple t-test on the percentage of isolated droplets reveals that there is a significant difference between LD distribution in 2Cell embryos and MII eggs (P= 0.027). Comparing 2Cell embryos and GV oocytes shows an insignificant difference (P= 0.645) indicating a more GV-like LD distribution at this early embryonic stage. Comparing the $\sqrt{\langle s^2 \rangle}$ of 2Cell embryos and MII eggs also shows a slight difference between the aggregations of LDs in the two developmental stages, revealing that the extent of aggregation in 2Cell embryos is more similar to that of GV oocytes (see Fig.3.4.3.).

The 4Cell stage embryos are identifiable by brightfield microscopy, and further detail is revealed by DIC imaging (Fig.3.4.1. (C)). CARS projections show the distribution of LDs throughout these embryos, obviously dispersed throughout each of the cells, but again with seemingly fewer clusters than seen in the previous developmental stages (Fig.3.4.1. (D)). Quantitative aggregate analysis confirms that some clusters still remain, and a percentage of isolated droplets similar to MII eggs is seen (Fig.3.4.2. (B)). A simple t-test on the percentage of isolated LDs shows that there is a significant difference between this developmental stage and the previous 2Cell stage (P = 0.029), and the distribution is more like that of MII eggs (P =

0.635). Plotting $\sqrt{\langle s^2 \rangle}$ for this developmental stage allows for comparison of these populations with earlier stage oocytes/eggs, demonstrating that, like 2Cell embryos, the LDs within 4Cell embryos are less clustered than those in eggs at the MII stage (Fig.3.4.3.).

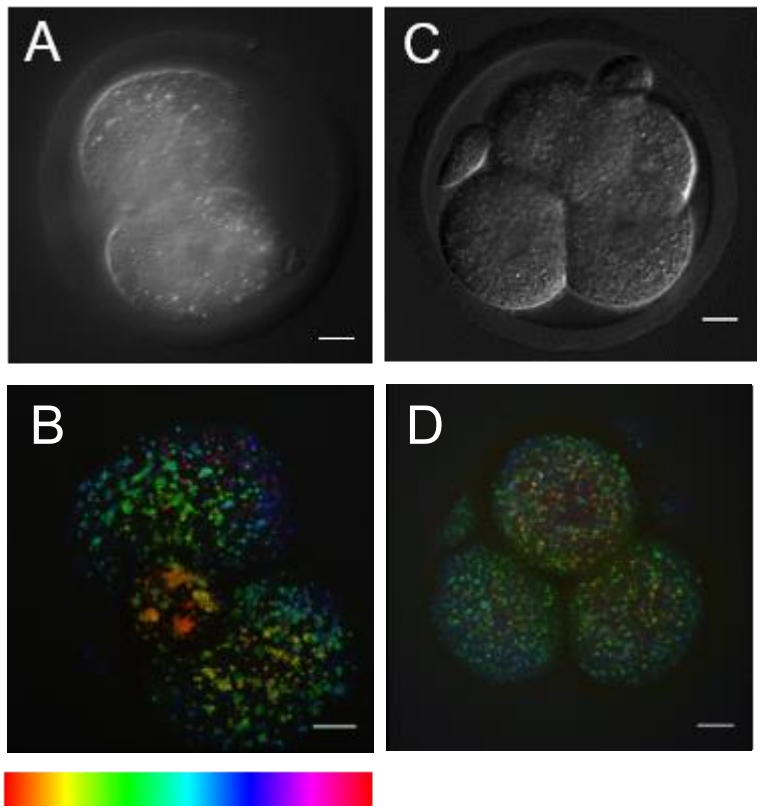

Fig.3.4.1. DIC and CARS Imaging of 2Cell and 4Cell Mouse Embryos

(A) and (C) Single-plane (approximately equatorial) DIC images of representative (A) 2Cell stage embryos (n=~65) and (C) 4Cell stage embryos (n=~60) using a 1.27 NA water objective and a 1.4 NA oil condenser. (B) and (D) Depth colour-coded images of CARS *z*-stacks at wavenumber 2850cm^{-1} through the same embryos, showing LDs at these developmental stages. 0.1x0.1µm *xy* pixel size; 0.5µm *z*-step; 0.01ms pixel dwell time; ~14mW (~9mW) Pump (Stokes) power at the sample. Scale bars represent 10µm; colour bar shows depth colour-coding from -25µm-25µm of 101 *z*-stacks (0µm being the approximately equatorial plane of the egg), the brightness of each colour is the maximum intensity at each corresponding *z*-plane. Data from ≥2 trials, using 1-3 mice each.

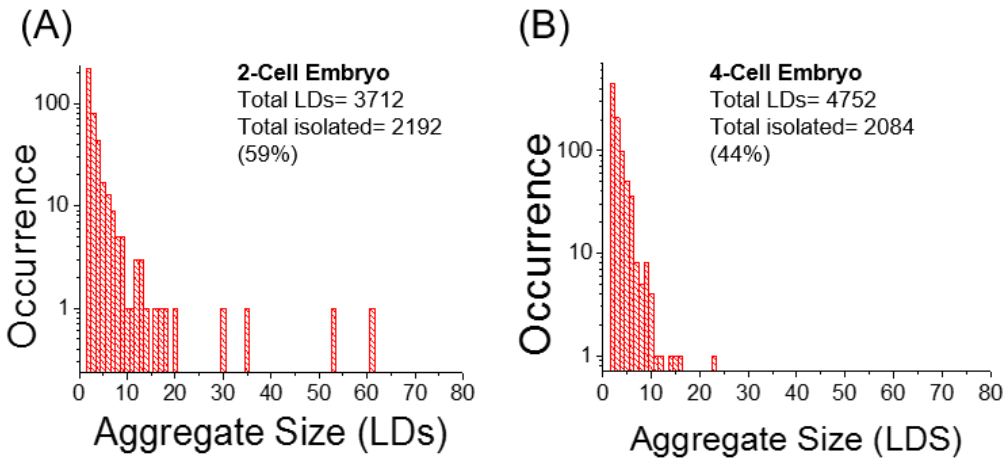

Fig.3.4.2. Histograms of Lipid Droplet Aggregation in 2Cell and 4Cell Mouse Embryos

Histograms of the number of LDs making up clusters in (A) a 2Cell stage embryo (n=10), and (B) a 4Cell stage embryo (n=8). Total number of LDs and total number of un-clustered LDs are also indicated.

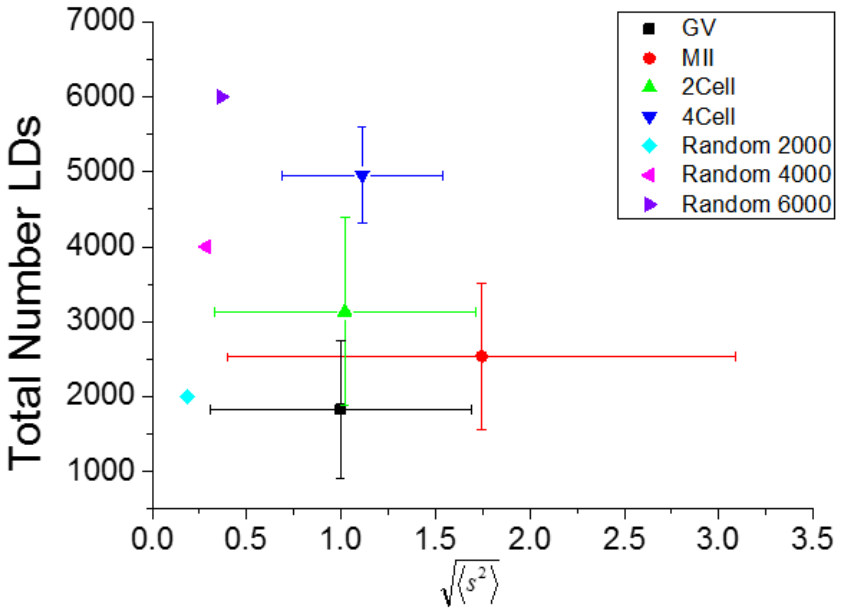

Fig.3.4.3. Scatter plot of the Extent of Lipid Droplet Aggregation throughout Mouse Egg and Early Embryo Development ($\sqrt{\langle s^2 \rangle}$)

Scatter plot of the square root of the mean squared aggregate size ($\sqrt{\langle s^2 \rangle}$) against the total number of LDs, in ensembles of GV oocytes (n=33), MII eggs (n=30), 2 Cell stage embryos (n=10) and 4 Cell stage embryos (n=8). The distribution of each variable in the corresponding ensemble is shown as a mean (symbol) and standard deviation (bar). The case of a random LD distribution simulated for a range of total number of LDs is also shown for comparison.

As already mentioned, the fit analysis with CCDPlot also provides the size of individual LDs, allowing comparison of LD diameters across developmental stages. Figure 3.4.4. shows a scatter plot of the mean LD diameter in populations of oocytes, eggs and embryos. This is calculated from the LD volume (using the LD width parameters in *x*, *y* and *z* obtained from CCDPlot) normalised to the CARS signal amplitude to account for sub-resolution droplets (see Chapter 2, section 2.9.3.). Histograms were made of all LD diameters within an egg (an example is given in Fig.3.4.4. (A)), which enabled the mean LD diameter per egg and per population to be found. LDs seen in all populations of early developmental stages show a relatively narrow LD size distribution around a mean value of 0.5μm (Fig.3.4.4. (B)). Also observed is that there appears to be a net increase in the mean total LD number as development continues. The mean total LD number in GV oocytes is around 2000, which increases to ~2500 in MII eggs, ~3000 are seen in 2Cell embryos, and this increases to ~5000 by the 4 Cell stage. The $\langle \frac{TL}{LD} \rangle$ of 2Cell (green triangle) and 4Cell (dark blue triangle) embryos are shown in Fig. 3.2.7. Again, very little difference is seen, however, it appears 4Cell embryos contain more lipid than at the 2Cell stage due to the higher number of total LDs.

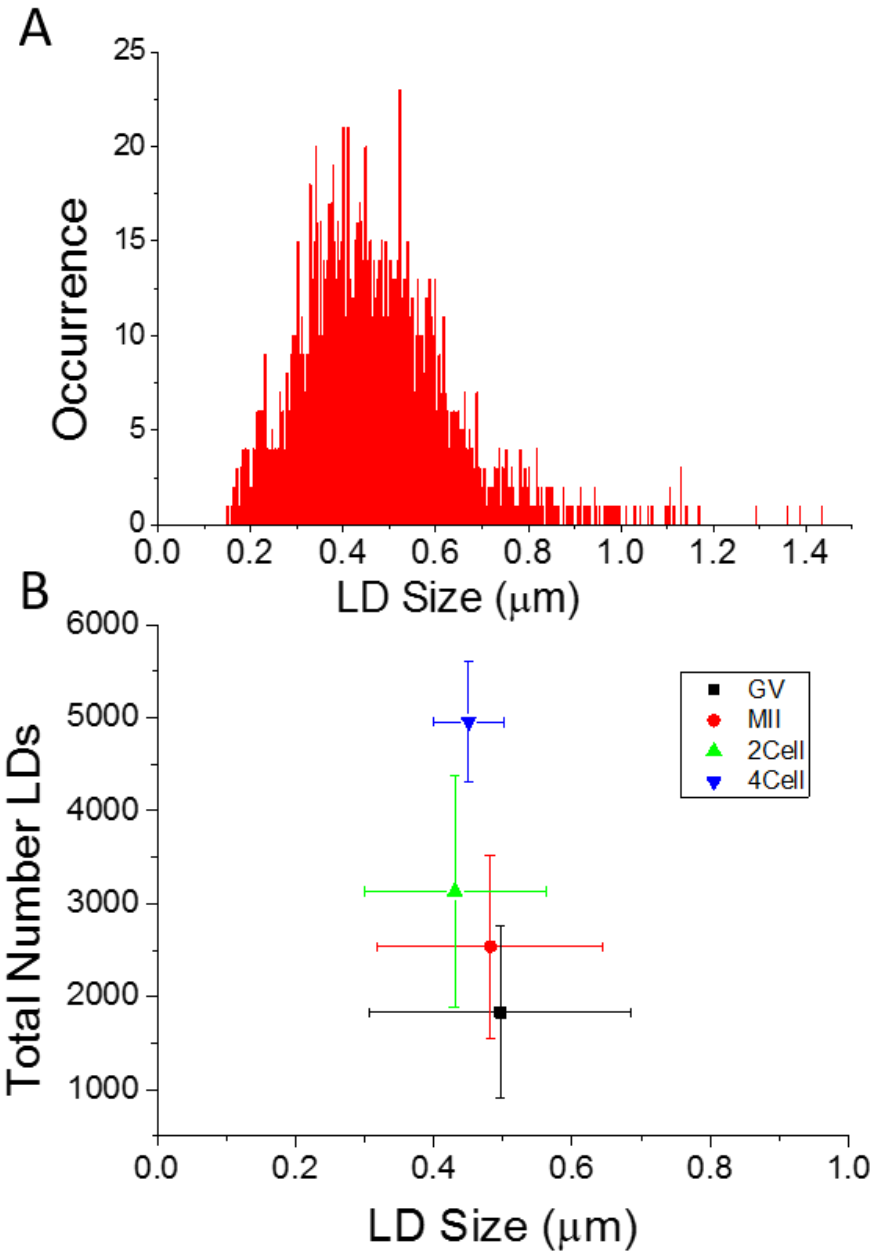

Fig.3.4.4. Scatter plot of the Mean Lipid Droplet Size in Populations of Mouse Eggs and Early Embryos

(A) Histogram of LD sizes within a representative MII egg from which diameters were calculated. Bin size = $1x10^{-3}$. (B) Scatter plot of the diameter of LDs in μm ($\langle d \rangle$) against the total number of LDs, in ensembles of GV oocytes (n=33), MII eggs (n=30), 2Cell stage embryos (n=10) and 4 Cell stage embryos (n=8) to show the consistency of LD size across early developmental stages. The distribution of each variable in the corresponding ensemble is shown as a mean (symbol) and standard deviation (bar). Data is from multiple trials, using 1-3 mice for each.

3.5. 8Cell, Morula and Blastocyst Early-Embryo Stages

Culture of *in vivo* fertilised embryos for 3 days yields embryos developed to the 8Cell stage. Fig.3.5.1. (A) shows a maximum projection of the DIC stack through an 8Cell embryo, in order to visualise more of the cells present. CARS projections of 8Cell embryos show the LDs in a number of these cells (Fig.3.5.1. (B)). It is clear that the LDs are distributed throughout the cells as before, but there is also a notable presence of larger LDs than previously seen (indicated by arrows in Fig.3.5.1. (B)). Further to this observation, it was found that 16-32Cell morula stage embryos that are achieved after 4 days in culture contain LDs that are much larger and varying in size. Interestingly, these were visible in DIC images of embryos at this stage (Fig.3.5.1. (C)) as well as being chemically revealed using CARS (Fig.3.5.1 (D)). DIC and CARS imaging of blastocyst stage embryos- after 5 days in culture- also show this same phenomenon (Fig.3.5.1. (E-F)). It is apparent that there are much fewer overall droplets throughout these later early-embryo stages, and although small droplets are still present and some show aggregation e.g. as seen in the cells of the trophectoderm of the blastocyst embryo (Fig.3.5.1. (F)), the dominating LDs are very large and singular. This suggests that, as development continues, coalescence of small LDs occurs. A comparison of DIC and CARS images across all pre-implantation developmental stages can be seen in Fig.3.5.2.

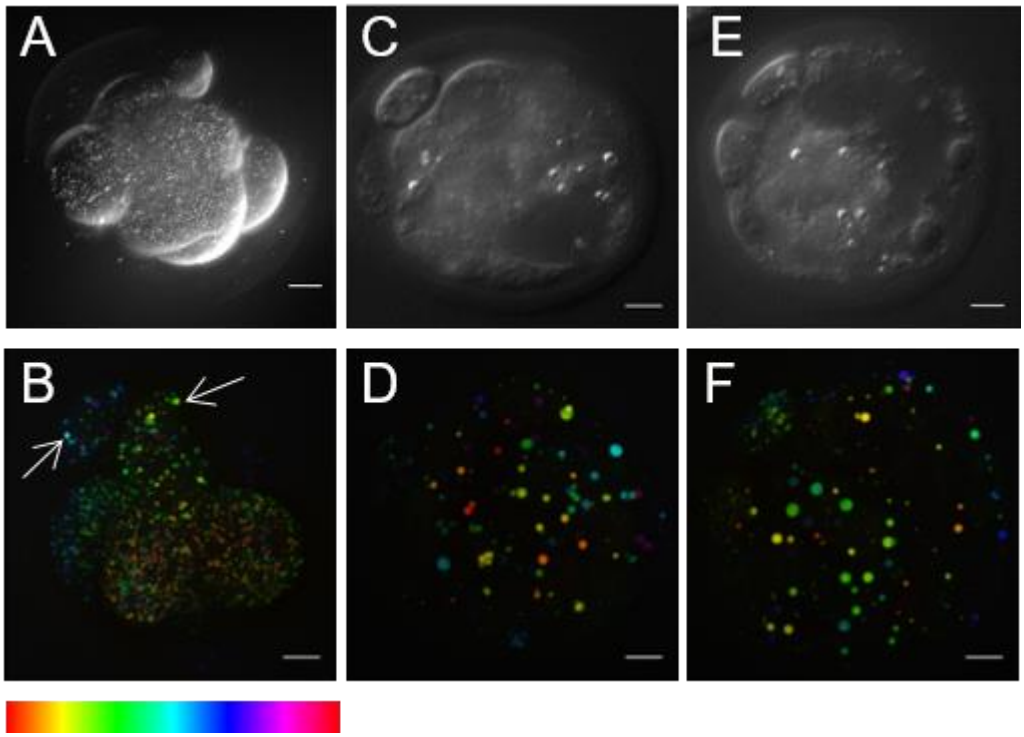

Fig.3.5.1. DIC and CARS Imaging of 8Cell, Morula and Blastocyst Stage Mouse Embryos

(A), (C) and (E) Single-plane (approximately equatorial) DIC images of representative of (A) 8Cell stage embryos (n=~10), (C) Morula stage embryos (n=~35), and (E) Blastocyst stage embryos (n=~20) using a 1.27 NA water objective and a 1.4 NA oil condenser. (B), (D) and (F) Depth colour-coded images of CARS *z*-stacks at wavenumber 2850cm^{-1} through the same embryos, showing LDs at these developmental stages. In (B) examples of larger droplets in the 8Cell embryo are indicated. 0.1x0.1µm *xy* pixel size; 0.5µm *z*-step; 0.01ms pixel dwell time; ~14mW (~9mW) Pump (Stokes) power at the sample. Scale bars represent 10µm; colour bar shows depth colour-coding from -25µm-25µm of 101 *z*-stacks (0µm being the approximately equatorial plane of the egg), the brightness of each colour is the maximum intensity at each corresponding *z*-plane. Data from ≥2 trials, using 1-3 mice each.

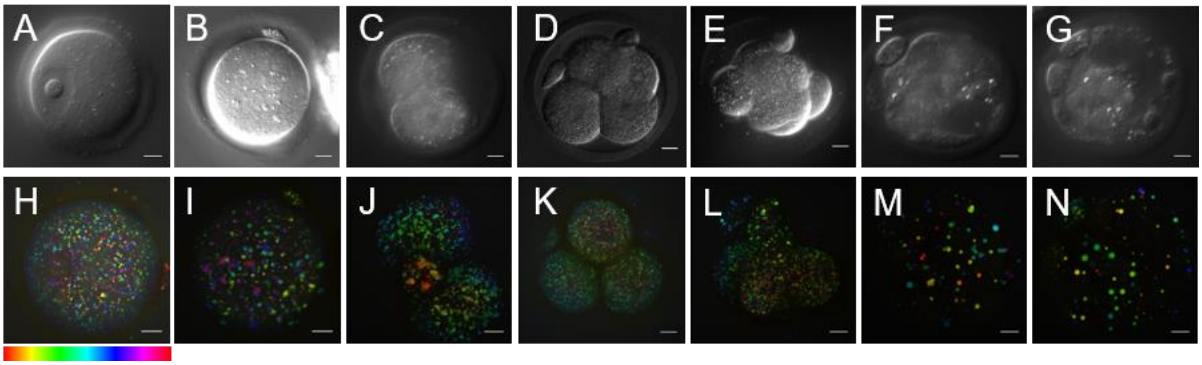

Fig.3.5.2. DIC and CARS Images Throughout Mouse Egg and Early Embryo Development

(A-G) DIC images (Single *z*-plane, except E which is a maximum intensity projection) representative of populations of mouse eggs and embryos, from (A) immature GV stage (n=~90), (B) MII eggs (n=~70), (C) 2Cell (n=~65), (D) 4Cell (n=~60), (E) 8Cell (n=~10), (F) morula (n=~35) and (G) blastocyst stage (n=~20) embryos using a 1.27 NA water objective and a 1.4 NA oil condenser. (H-N) Depth colour-coded images of CARS *z*-stacks at wavenumber 2850cm^{-1} through the same eggs and embryos, showing LDs throughout these developmental stages. 0.1x0.1µm *xy* pixel size; 0.5µm *z*-step; 0.01ms pixel dwell time; ~14mW (~9mW) Pump (Stokes) power at the sample. Scale bars represent 10µm; colour bar shows depth colour-coding from -25µm-25µm of 101 *z*-stacks (0µm being the approximately equatorial plane of the egg/embryo), the brightness of each colour is the maximum intensity at each corresponding *z*-plane. Data from ≥2 trials, using 1-3 mice each

Quantitative analysis of these later early-embryo stages using CCDPlot was thus far not possible, due to the fact that the larger droplets resulted in a plateaued intensity profile, rather than a Gaussian profile, not included in the CCDPlot fitting algorithm in the present form. Similar observations were made in all morulae and blastocysts imaged with both CARS (morula n=~35; blastocyst n=~20) and DIC (morula n=~35; blastocyst n=~36), and are likely to be statistically significant.

3.6. Abnormal Oocytes, Eggs and Arrested Embryo Stages

Central GV vs. Non-Central GV Oocytes

GV position was compared with LD distribution and aggregation, in order to observe whether the previously-conceived measures of GV oocyte developmental potential correlate with particular LD distribution patterns. Results gave no indications of a link between the two. Both GV oocytes with a 'central' GV (Fig.3.6.1. (A)) and those with a 'non-central' GV (Fig.3.6.1. (B) showed very little difference in LD distribution (Fig.3.6.1. (C) and (E), and (D) and (F), respectively). A simple t-test performed on the percentages of individual LDs in populations of GV oocytes with central (n=14) versus non-central (n=19) GVs reveals that there is no significant difference between the two groups (*P value*= 0.453). Comparison of $\sqrt{\langle s^2 \rangle}$ of the two populations of cells (Fig.3.6.4.) reveals very little difference between the two, those with a central GV (green point) having a slightly higher total number of droplets than the non-central GV group (dark blue point), but the difference is well within standard deviations. As well as showing no difference in LD aggregation, the lipid amount per LD ($\langle \frac{TL}{LD} \rangle$) of central GV versus non-central GV oocytes appears to be very similar. Figure 3.6.5. shows that non-central GV oocytes (yellow star) have a slightly higher $\langle \frac{TL}{LD} \rangle$ than central GV oocytes (violet hexagon), but slightly lower total number of LDs per egg, all within SDs.

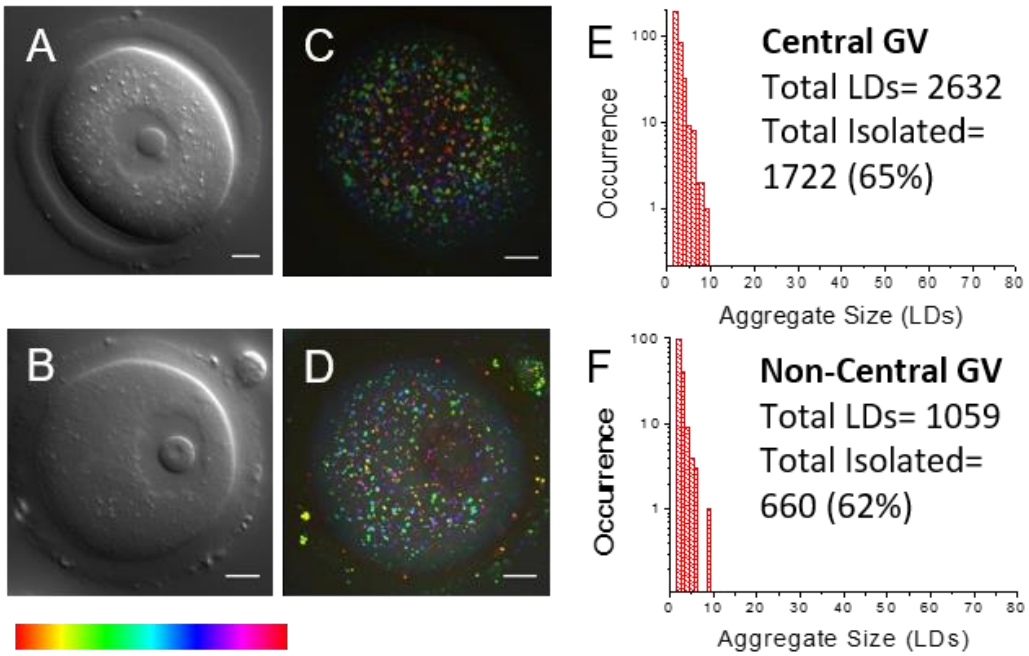

Fig.3.6.1. DIC and CARS images, and Histograms of Lipid Droplet Aggregation in GV Oocytes with a Central or Non-Central GV

(A) and (B) DIC Single-plane (approximately equatorial) DIC images of representative of (A) GV oocytes with a 'central' GV (n=14), and (B) GV oocytes with a 'non-central' GV (n=19) using a 1.27 NA water objective and a 1.4 NA oil condenser. (C) and (D) Depth colour-coded images of CARS *z*-stacks at wavenumber 2850cm^{-1} through the same cells, showing LDs. 0.1x0.1µm *xy* pixel size; 0.5µm *z*-step; 0.01ms pixel dwell time; ~14mW (~9mW) Pump (Stokes) power at the sample. (E) and (F) Histograms of the number of LDs making up clusters in these same oocytes. Total number of LDs and total number of un-clustered LDs are also indicated. Scale bars represent 10µm; colour bar shows depth colour-coding from -25µm-25µm of 101 *z*-stacks (0µm being the approximately equatorial plane of the egg), the brightness of each colour is the maximum intensity at each corresponding *z*-plane. Data from ≥2 trials, using 1-3 mice each.

Good vs. Bad GV Oocytes

Only a small population of GV oocytes with irregular morphology was imaged during this project, in favour of getting measurements from 'good', representative oocytes. DIC and CARS images of a representative 'bad' oocyte, with irregular morphology, are shown in Fig.3.6.2. (A-B). It was found that some imaged oocytes deemed to have a 'bad' morphology appear to have a larger amount of clusters, more like the LD distribution seen in MII eggs (confirmed by aggregate analysis Fig.3.6.3. (A)), whereas others have a normal amount of clustering for a GV oocyte. Quantitatively comparing the overall populations of 'good' and 'bad'-looking GVs with a t-test performed on the percentages of individual LDs reveals no significant difference (*P value*= 0.110), although only a small population of 'bad' oocytes were imaged (n=3). $\sqrt{\langle s^2 \rangle}$ comparison reveals a much larger difference in the extent of aggregation between the two populations (black and red points, Fig.3.6.4.). However, the values are still within SDs and due to the small number of 'bad' oocytes imaged, there is no conclusive evidence for this result. The $\langle \frac{TL}{LD} \rangle$ of 'good' oocytes (magenta triangle) and 'bad' oocytes (orange triangle) appears almost identical (Fig.3.6.5.).

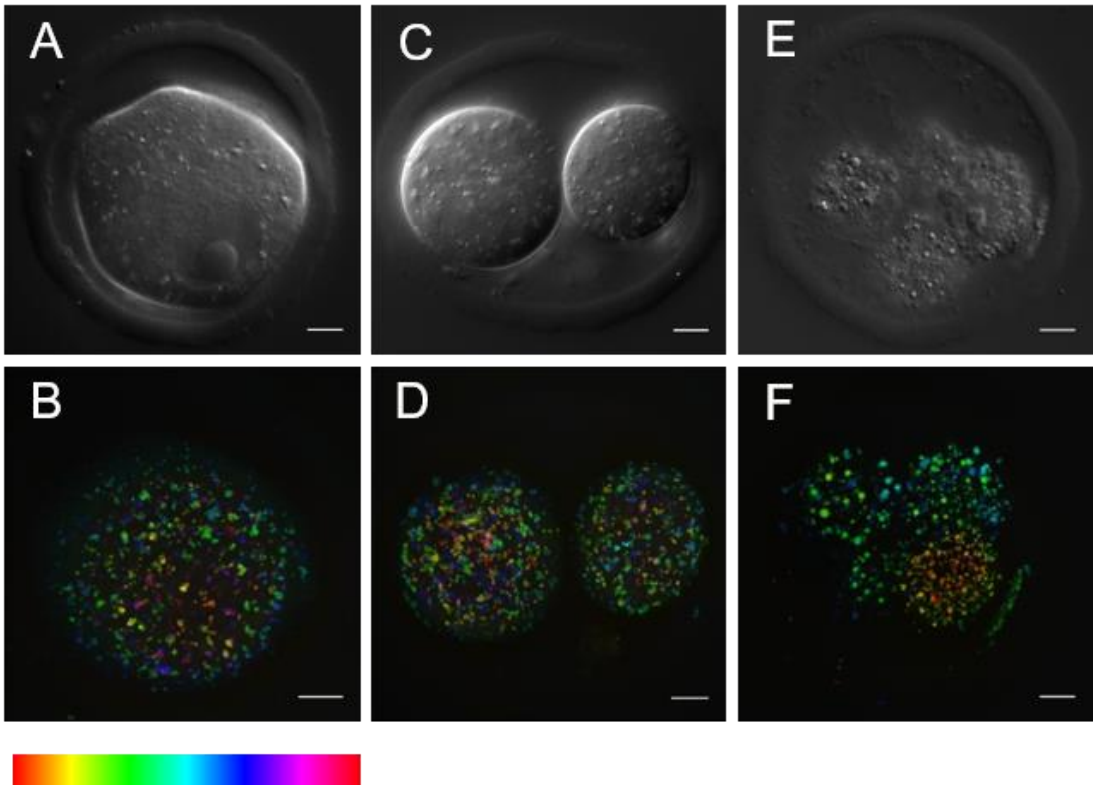

Fig.3.6.2. DIC and CARS Imaging of Abnormal GV stage Mouse Eggs and Arrested Early Embryos

(A), (C), and (E) Single-plane (approximately equatorial) DIC images of representative of (A) Abnormal GV oocytes (n=3), (C) Arrested 2Cell stage embryos (n=3), and (E) Arrested 4Cell stage embryos (n=2) using a 1.27 NA water objective and a 1.4 NA oil condenser. (B), (D), and (F) Depth colour-coded images of CARS *z*-stacks at wavenumber 2850cm^{-1} through the same cells, showing LDs. 0.1x0.1µm *xy* pixel size; 0.5µm *z*-step; 0.01ms pixel dwell time; ~14mW (~9mW) Pump (Stokes) power at the sample. Scale bars represent 10µm; colour bar shows depth colour-coding from -25µm-25µm of 101 *z*-stacks (0µm being the approximately equatorial plane of the egg), the brightness of each colour is the maximum intensity at each corresponding *z*-plane. Data from ≥2 trials, using 1-3 mice each.

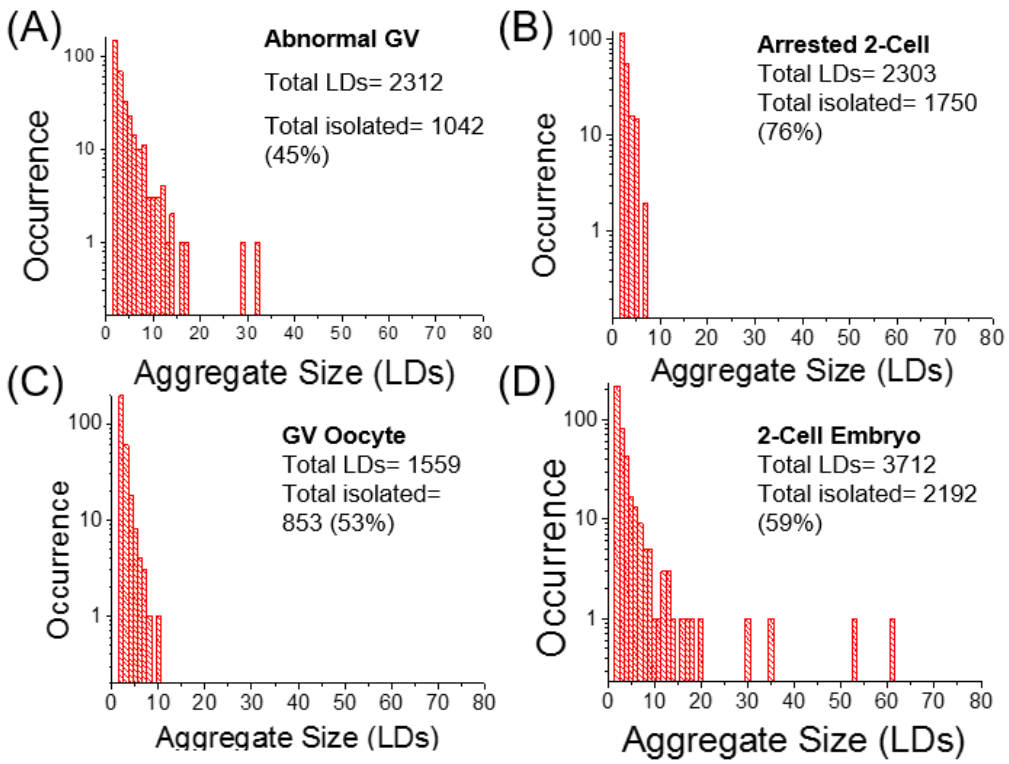

Fig.3.6.3. Histograms of Lipid Droplet Aggregation in Abnormal and Arrested Mouse Eggs and Early Embryos

Histograms of the number of LDs making up clusters in (A) an abnormal GV oocyte (n=3), and (B) an arrested 2Cell stage embryo (n=3), compared to (C) a normal GV oocyte (n=33) and (D) a normal 2Cell embryo (n=10). Total number of LDs and total number of un-clustered LDs are also indicated.

Good vs. Bad MII Oocytes

Comparing 'good' versus 'bad' MII eggs was less clear. Most of the MII eggs considered as 'bad' eggs had simply not properly matured, so were likely to be at the MI or early meiosis II stage. They would therefore would be expected to have a more 'GV-like' distribution, reminiscent of an earlier developmental stage. Results of a t-test give a *P value* of 0.361, suggesting that 'bad' and 'good' MII eggs had fairly similar percentages of isolated LDs. However, comparison of the aggregate size parameter $\sqrt{\langle s^2 \rangle}$ shows a more 'GV-like' LD distribution for 'bad' MII eggs, with cells also containing fewer total LDs (magenta triangle, Fig.3.6.4.). This indeed suggests a distribution of LDs as for an earlier cell-cycle stage egg. 'Bad' MIIs have a fairly noticeable larger $\langle \frac{TL}{LD} \rangle$ than 'good' MII eggs, along with a lower total number of lipids (navy blue pentagon and red circle, respectively, Fig.3.6.5.)

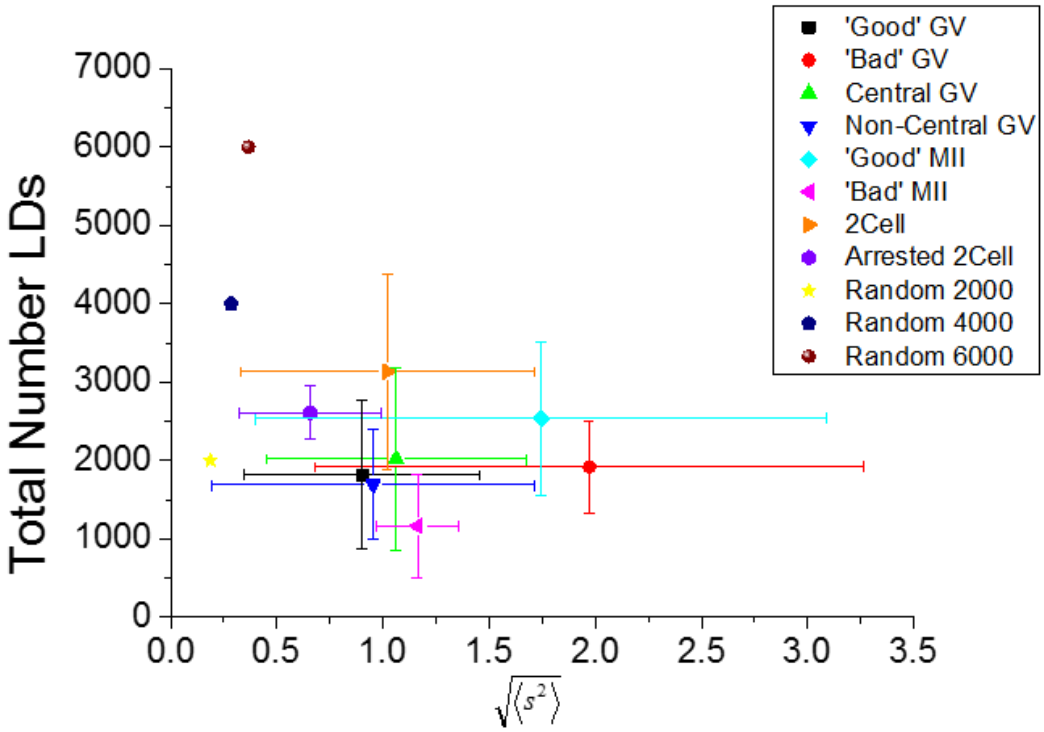

Fig.3.6.4. Scatter plot of the Extent of Lipid Droplet Aggregation ($\sqrt{\langle s^2 \rangle}$) in Abnormal Mouse Eggs and Arrested Early Stage Embryos

Scatter plot of the square root of the mean squared aggregate size ($\sqrt{\langle s^2 \rangle}$) against the total number of LDs, in ensembles of 'Good' GV oocytes (n=30) and 'Bad' GV oocytes (n=3), GV oocytes with a central GV (n=14), GV oocytes with a non-central GV (n=19), 'Good' MII eggs (n=30), 'Bad' MII eggs (n=3), 2Cell stage embryos (n=10) and arrested 2Cell stage embryos (n=3). The distribution of each variable in the corresponding ensemble is shown as a mean (symbol) and standard deviation (bar). The case of a random LD distribution simulated for a range of total number of LDs is also shown for comparison.

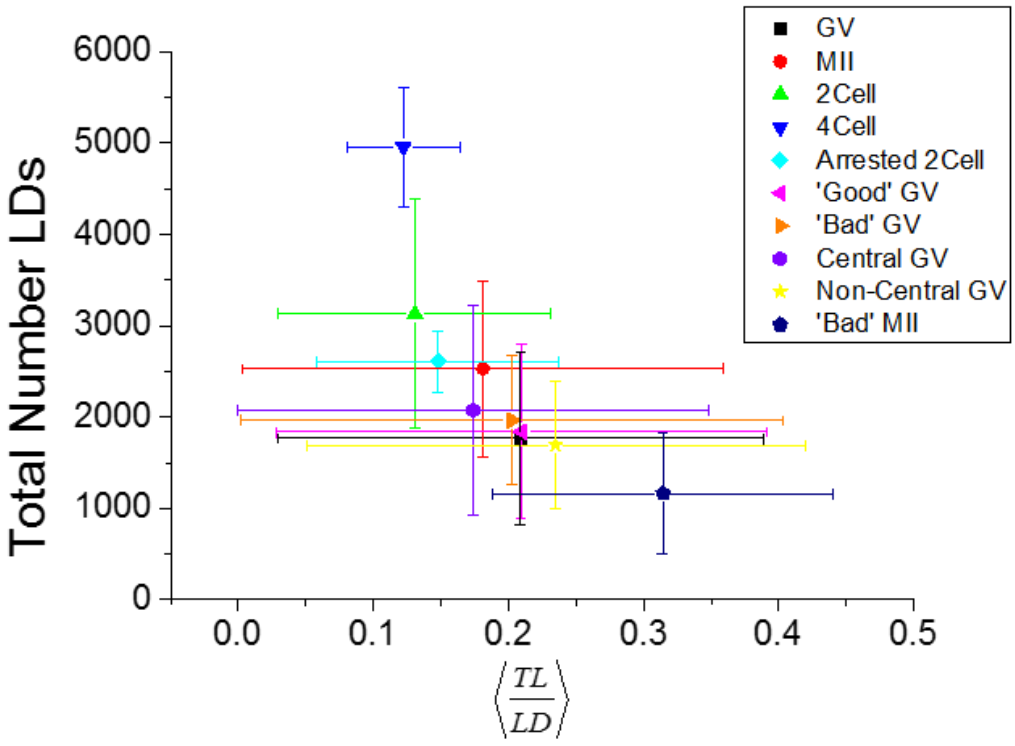

Fig.3.6.5. Scatter plot of the Total Lipid Content per LD ($\langle\frac{TL}{LD}\rangle$) of Abnormal Populations of Mouse Eggs, Early Embryos, and Arrested Early Embryos

Scatter plot of the total amount of lipid per droplet ($\langle\frac{TL}{LD}\rangle$) in populations of GV oocytes (n=33), MII eggs (=30), 2Cell stage embryos (n=10), 4Cell stage embryos (n=8) and arrested 2Cell stage embryos not included in the 2Cell population (n=3). The GV population is split into 'Good' GV oocytes (n=30) and 'Bad' GV oocytes (n=3), and also into GV oocytes with a central GV (n=14) and GV oocytes with a non-central GV (n=19). 'Bad' MII eggs not included in the MII population (n=3). The distribution of each variable in the corresponding ensemble is shown as a mean (symbol) and standard deviation (bar).

Arrested Embryos

Embryos that become arrested at different stages during development are a good example of 'bad' embryos, as this arrest is clearly an indication of inadequacy and a consequence of underlying damaging processes occurring within the cells. However, as was the case with imaging of 'bad' morphology GV and MII eggs, within the time-frame of the current project, healthy embryos were favoured for CARS imaging. The majority of embryo arrest occurs at the 2Cell stage, likely to be due to the vulnerability of embryos at the stage of embryonic genome transcription.

Examining both DIC and CARS images of live arrested 2Cell embryos reveals a number of large droplets that aren't usually seen at this stage of development (Fig.3.6.2. (C-D)). Embryos arrested at the 4Cell stage also reveal these larger LDs, similar to those usually seen at the 8Cell stage or later (Fig.3.6.2. (E-F)). Embryos arrested at both stages tend to have a higher percentage of isolated droplets, but the n numbers are too low (2Cell n=3; 4Cell n=2) for statistically significant conclusions to be drawn. Furthermore, a t-test shows no significant difference between healthy 2Cell embryos and arrested 2Cell embryos (*P value*= 0.540). Comparison of $\sqrt{\langle s^2 \rangle}$ for 2Cell embryos and arrested 2Cell embryos reveals a slightly more dispersed, and less aggregated arrangement of LDs in arrested embryos compared to healthy embryos, however, this difference is not significant as the results are still within SDs (orange triangle and violet hexagon, Fig.3.6.4.). Analysis of total lipid amount also shows the arrested 2Cell embryos as having slightly fewer total LDs, and higher $\langle \frac{TL}{LD} \rangle$, but again these variations are within SDs and were provided by such a small number of analysed examples that they cannot be considered statistically significant (cyan diamond, Fig.3.6.5.).

3.7. Oocytes and Eggs from Bovine Species

As a comparison to mouse egg LD distribution and content, DIC and CARS imaging were performed on *in vitro* matured bovine eggs. As seen in DIC images, bovine eggs look similar to those of mice, but are slightly larger (>100µm diameter as opposed to the 70µm mouse oocyte) and have a more granular-looking cytoplasm (Fig.3.7.1. (A), (C), and (E)). CARS images reveal that LDs in mature bovine eggs prove to be larger (>1µm) than those in mouse (Fig.3.7.1. (B), (D), and (F)), and non-uniform in size, although not as those seen in murine morula and blastocyst stages. Bovine eggs were not always collected from the same species of cow, and differences were seen between experiments. For example, some eggs were larger than others (~120-150µm diameter), some contained larger LDs (~5µm), and some LDs gave a CARS intensity orders of magnitude larger than others. It was not possible to quantitatively investigate LDs of bovine eggs, due to the differences in sizes of the droplets, making CCDPlot analysis difficult. Large droplets have a plateaued intensity profile, currently not included in the CCDPlot fitting algorithm.

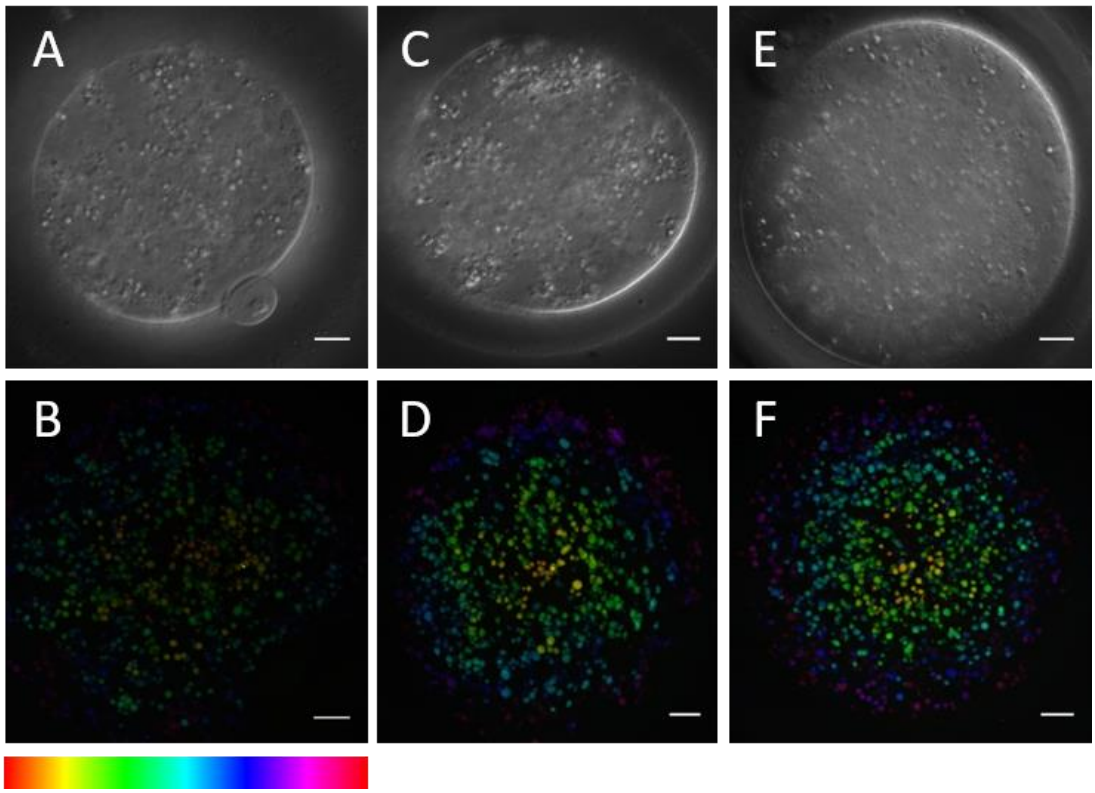

Fig.3.7.1. DIC and CARS Imaging of Bovine Eggs

(A), (C) and (E) Single-plane (approximately equatorial) DIC images of representative of MII stage bovine eggs (n=13) using a 1.27 NA water objective and a 1.4 NA oil condenser. (B), (D) and (F) Depth colour-coded images of CARS *z*-stacks at wavenumber 2850cm^{-1} through the same cells, showing LDs. 0.1x0.1µm *xy* pixel size; 0.5µm *z*-step; 0.01ms pixel dwell time; ~14mW (~9mW) Pump (Stokes) power at the sample. Scale bars represent 10µm; colour bar shows depth colour-coding from -25µm-25µm of 101 *z*-stacks (0µm being the approximately equatorial plane of the egg), the brightness of each colour is the maximum intensity at each corresponding *z*-plane. Data from ≥2 trials, using 1-3 cows each.

3.8 Discussion

From previous research, it is thus far known that mammalian oocytes, eggs and early stage embryos rely almost exclusively upon the metabolism of pyruvate and FAs by their mitochondria for generating energy in the form of ATP (Acton *et al*. 2004; Dumollard *et al.* 2008). From this current study, it was possible to visualise the lipid stores from which these precious cells get their nutrition, as they make their journey from the ovary to the uterus.

CARS has proven to be a useful tool in the chemically-specific and label-free identification of intracellular organelles. CARS imaging at the symmetric stretch vibration of CH_2 bonds abundant in the acyl chain of lipids allowed us to resolve the spatial distribution of lipid droplets in living mammalian oocytes, eggs and early stage embryos (this chemical attribution was further supported by hyperspectral CARS imaging shown in Chapter 5).

Individual lipid droplets were resolvable by the CARS microscope used to acquire the images. THG was used by Watanabe *et al.* (2010) to image LDs in living oocytes and embryos without being detrimental to development, but the methods used in their study could only be used for limited periods of time, and they were not able to properly resolve individual LDs. As THG is not able to distinguish chemical composition of LDs, it is not a method that allows extensive quantitative measurements as to the cellular lipid content.

The 3D spatial resolution, and hence pixel sampling size number, used in our study proved sufficient to consistently image a large proportion of the egg or embryo whilst maintaining a reasonable acquisition time (and file-size limits). Owing to the resolution of individual droplets, it was possible to quantitatively investigate CARS images in order to give the total number of LDs, their size and their distribution in 3D. By finding the co-ordinates of each droplet and mapping their distribution in relation to each other, the patterns in LD distribution were able to be analysed. Comparing the percentage of isolated droplets per egg or embryo population, along with the extent of aggregation ($\sqrt{\langle s^2 \rangle}$ parameter) allowed the quantitative assessment of the clustering phenomenon seen between developmental stages.

The spatial distribution of the LDs at immature GV stage was more dispersed, albeit not random. It was notable, also through time-course imaging of the same egg over maturation, that LDs became more clustered in mature MII eggs in comparison to GV stage oocytes, an observation which was statistically relevant. In terms of comparing this observation with the literature, LD movement has been recorded in a number of cell types and species. Fluorescence observation of LDs in pig and mouse eggs, for example, has shown that they relocate during maturation (Sturmey *et al.* 2006; Yang *et al.* 2010). However, fluorescence techniques are usually limited to fixed cells, and lipid staining is often unspecific. LD movement is thought to be orchestrated by microfilaments and microtubules (Dutta and Sinha, 2015), and is suggested to be associated with mitochondrial localisation, thus possibly having a metabolic explanation.

The dispersed distribution of LDs in GV oocytes suggests an availability of FAs for metabolism at this stage, the separation allowing for a larger accessible surface area for FA liberation, and increased contact with mitochondria. Meanwhile, the clustering seen with maturation to the MII stage, may indicate a decreased requirement for β-oxidation. However, it is not clear exactly how this difference between LD spatial distribution in GV and MII eggs is related to metabolic changes, because oxidative phosphorylation predominates at both stages (Dumollard *et al.* 2008). It is not expected that at this subsequent stage of development, the metabolism would change dramatically.

Clustering of LDs as mouse oocyte and early embryo development continued has been previously described by Watanabe *et al.* (2010) using THG, and Davidson *et al.* (2012) noted lipid aggregations and higher concentrations of lipid at the MII stage compared with the GV stage via Raman spectroscopy. However, while these techniques are label-free, again, they utilise methods that are unable to resolve individual droplets. A study in 1985 (Hishinuma *et al.*) also described clustering of LDs, but these were observed in ‘abnormal’, aged mouse eggs and embryos with delayed development, or that had fragmented. Mitochondrial clustering is noted with obesity and insulin resistance (Igosheva *et al.* 2010; Wu *et al.* 2010), which may result in a clustering of LDs, but this does not explain the LD aggregations seen after maturation of apparently normal eggs to the MII stage.

The total number of LDs varies greatly from cell to cell, however there appears to be a net increase in LD number as development continues from single-cell to early embryo stages. This may be due to the continuous *in vitro* culture of embryos, and an increase in lipid synthesis due to the presence of fatty acid-containing BSA in the culture medium (shown to be best for development- Downs *et al.* 1989, 2009). It has previously been observed that there is a small increase in neutral lipid in bovine and mouse eggs during IVM, due to diffusion or active transport, if the eggs are matured in serum-containing medium (Aardema *et al.* 2011; Yang *et al.* 2010), supporting our observation of a slightly higher total number of LDs in IVM eggs as opposed to those matured *in vivo*.

There is very little difference in the average lipid amount (volume) per LD (described as $\langle\frac{TL}{LD}\rangle$) between GV oocytes and MII eggs matured *in vivo*, but the total number of LDs is higher in MII eggs, as suggested by Davidson *et al.* (2012). However, in IVM experiments following the same egg from its GV stage to its MII stage, the total number of LDs appears to significantly decrease as development continues, while the average $\langle\frac{TL}{LD}\rangle$ remains constant. This is in contrast with the observation that the total number of LDs at MII is generally higher, and previous observations from the literature that maturation in culture media containing BSA leads to an even higher lipid amount (Romek *et al.* 2009). Our observation is consistent with findings from Sturmey and Leese (2003) where they see an overall decrease in TAG content during bovine IVM. Aardema *et al.* (2011) describe the differing effects on intracellular lipid storage seen with differing culture media FA compositions. They note that saturated palmitic and stearic acids hinder lipid-storage in a dose-dependent manner, while unsaturated oleic acid promotes lipid storage. Differences in culture media compositions may thus explain the inconsistencies observed between studies.

IVM has been found to result in reduced development to blastocyst and decreased pregnancy rates compared to those matured *in vivo* (Rizos *et al.* 2002, Gilchrist and Thompson 2007; Eppig *et al.* 2009) possibly due to the premature removal of the oocyte from the follicle, where there is sufficient substrate provision. Our comparison between the amount of lipid in MII eggs matured *in vivo* to those matured *in vitro*, indicates that there is a lower $\langle\frac{TL}{LD}\rangle$ after IVM. *In vivo* matured eggs

also had a higher extent of LD aggregation ($\sqrt{\langle s^2 \rangle}$) than in those matured in culture, however both of these comparisons are not statistically significant and are unlikely to be responsible for the previously-recorded short-comings of IVM.

The LD distribution at the 2Cell stage appeared to be more dispersed, as that seen at GV, but with a higher total number of droplets than at MII stage. There also appeared to be a lower $\langle \frac{TL}{LD} \rangle$ with development from the MII to the 2Cell stage, consistent with findings from Davidson *et al.* (2012). It is suggested that a decrease in lipid at this stage is due to the use of lipids for increased cell membrane synthesis; Pratt and George (1989) describe a 74% increase in cell membrane from the 2Cell to the 4Cell stage. With subsequent development to the 4Cell stage, however, we observed no difference in $\langle \frac{TL}{LD} \rangle$, only an increase in LD number was observed (consistent with prolonged cell culture). The aggregation pattern of 4Cell embryos was also more reflective of MII stage eggs. It is possible that at the 2Cell stage, LDs become dispersed in order for lipid mobilisation for future embryonic cell membrane synthesis, and that this lipid liberation does not occur after the 4Cell stage, thus promoting LD clustering. While it is arguable that the $\langle \frac{TL}{LD} \rangle$ at the 4Cell stage would be lower if this were the case, perhaps this loss of TAGs for FA liberation is compensated for by increased storage of lipids from the culture media.

Interestingly, the appearance of larger LDs at the morula and blastocyst stage was observed. This was preceded by the occasional occurrence of larger droplets in some blastomeres of the 8Cell stage. Notably, around the later stages of pre-implantation development there is a switch in metabolism to the greater use of glycolysis which is previously not active. It also follows a period of LD clustering, seen from the 4Cell stage. Therefore, the observed larger LDs may be indicative of the beginnings of a phase of LD fusion, for FA storage and reduced reliance on β-oxidation. Although rare under normal cellular circumstances, and not previously recorded in mammalian oocytes or embryos, LD fusion has been previously described in many cell types, aided by LD-associated proteins (Wilfling *et al.* 2013, 2014; Thiele and Spandl, 2008; Paar *et al.* 2012). It is also possible that these large LDs seen at morula and blastocyst stages are positioned near the rapidly-increasing cell membrane, or at the

prospective furrow created during cell division, in order for use in cell membrane manufacture. While this is not consistent with the proposal of LD dispersion at the 2Cell stage for FA liberation in order for cell membrane production, the mechanisms of cell membrane growth in the developing mammalian embryo are not clear.

Unfortunately, no quantitative analysis of later embryo stages was possible due to the size of these larger droplets and the corresponding CARS amplitude distribution, with plateaued profiles not included in the fitting algorithm. CCDPlot software development may be needed to incorporate a fit function for a plateau amplitude profile such as those presented by large LDs, in order to analyse pre-implantation embryos in the same way as the earlier cleavage stages. Alternatively, counting the LDs by eye or by commercially-available particle tracking software might be possible. This may have particular potential in counting LDs of the ICM, however it may prove difficult in the trophoblast where many, smaller droplets are seen.

It could be that the appearance of these larger droplets is time-dependent, rather than due to metabolic requirement. Johnson and Day (2000) suggest that egg cells are on 'timers', where they are programmed to complete certain processes at specific times. For example, even when the cell cycle is blocked, glycolysis still kicks in around the same time it usually would with blastocyst development (Martin and Leese, 1999). It was noted that no difference was seen in LD distribution between 2Cell embryos and those which became arrested at the 2Cell stage, but large LDs are often seen in those that are prematurely arrested, imaged 5 days after fertilisation.

It is hard to identify objective criteria that can classify an egg cell as 'abnormal', although characteristics such as a large perivitelline space, or non-spherical morphology are commonly used to predetermine unsuccessful development. Brunet and Maro (2007) describe the best morphological assessment of immature oocytes to be the positioning of their GV. It was found that more competent cells present a central GV, whereas less competent cells have a peripheral GV- less than half with a peripheral GV extruding a polar body. However, we saw no difference in the LD distributions of 'central GV' versus 'non-central GV' oocytes, meaning a correlation between the two cannot be used as a predictor of developmental success. A difference was seen in the extent of LD aggregation between 'good' and 'bad' GV oocytes- the 'bad quality' oocytes displaying more clustering than seen at normal

MII stages, however the $\langle \frac{TL}{LD} \rangle$ remained constant. It is possible that the observation of extensive LD aggregation at the GV stage is indicative of a change in metabolism or cell processes dictating cell quality.

'Bad quality' MII and arrested-development 2Cell embryos appeared to have fewer LD aggregations and fewer total LDs compared to their 'healthy' counterparts, and 'bad' MII cells proved to have a higher amount of lipid per LD. However, most results are within SDs, and small n numbers may mean more investigation is required to be statistically significant. Also, a large variability in LD clustering is seen within each population of GV and MII eggs, potentially affected by the developmental potential of the oocytes (even when not obviously appearing abnormal), so this also requires further dedicated study.

It is possible that the $\langle \frac{TL}{LD} \rangle$ is indicative of developmental competence; Jeong *et al.* (2009) found that bovine oocytes of a darker colour in brightfield transmission (i.e. with a higher amount of lipid) were more successful at reaching blastocyst, and rate to blastocyst was improved compared to paler oocytes containing less lipid. However, it is unclear whether a higher or lower $\langle \frac{TL}{LD} \rangle$ would be more beneficial to developing mouse eggs and embryos.

Qualitative and quantitative measurements were not taken for dead cells due to time constraints and a higher level of interest in live cells. However, imaging LDs of dead cells would also be interesting, to give an idea of how LD distribution reflects egg quality or developmental potential, as these could also be counted as 'bad quality', and are clearly susceptible to cell death. Equally, these dead cells may not be a good measure of difference in quality, as there may be underlying processes which aren't obvious determining cell death.

It may prove useful to investigate polar body degeneration and LD distribution, as often polar bodies degenerate quickly and some remain. However, there is very little, and inconsistent research on this. It may also be interesting to consider the age of eggs, assessing the lipid droplet distribution and content in MII eggs the day after harvest. Eggs collected from aged mothers are also considered to be of lower quality, but mitochondrial damage may play a large role here.

Further CARS assessment of GV oocytes may be possible, as oocytes with a chromatin conformation surrounding the nucleus (SN) are recognised to be of better developmental competence than those whose chromatin is not surrounding the nucleus (NSN). It was found that transfer of SN nuclei into NSN oocytes improved their maturation rates, however their development to blastocyst was unaffected (Inoue *et al.* 2008).

Previous efforts to quantify lipid content in oocytes have mostly been performed in domestic species such as pig, sheep and cow (McEvoy *et al.* 2000), but some investigations have been carried out to assess the content of mouse cells. Fluorescent staining techniques with Nile red, and destructive means such as chemical extraction have been used to quantify lipid content of in various species, allowing comparison with mouse eggs (Romek et al. 2011; Genicot *et al.* 2005; Loewenstein and Cohen, 1964), finding that lipid comprises approximately 12.5% the dry mass of a mouse oocyte, and porcine oocytes contain 6.8 times more lipid than mouse eggs, ovine oocytes 3.8 times more, and bovine oocytes 2.8 times more lipid. However, none of these techniques are compatible with live cell imaging and cell viability, and they produce inconsistent results. It also does not seem that any previous studies have attempted to quantify the amount of lipid in developing mouse embryos. It has been shown that TAG synthesis is active during mouse pre-implantation development (Dunning *et al.* 2010). Quantification of mouse embryo lipid content is something that is possible with CARS microscopy- with the correct fitting procedure of CARS signal from large LDs, the content of these later pre-implantation stage embryos could be assessed.

It is well established that cells of different species metabolise lipids differently, and eggs of species such as dog, pig, cow and sheep contain a larger proportion of LDs and metabolise more lipid (McEvoy *et al.* 2000). It appears that the amount of lipid in an egg accurately reflects the amount of lipid metabolism occurring in cells of that species, and that a higher amount of lipid in species which metabolise a large amount of lipid is beneficial to development.

Comparison of the LD distribution of mouse eggs with those of alternative species such as bovine gives an interesting insight into the different processes occurring in

these cells. It is known that there is differing levels of lipid metabolism present in egg cells of different species, so a comparison of LD distributions may give further information as to the link between LDs and lipid metabolism. For example, LDs in bovine eggs appear to be larger (>1μm) with less aggregation, possibly indicating that lipid metabolism is active. Also, imaging eggs of different bovine species shows differing LD distributions. It would be useful and informative to continue this investigation, comparing images seen in this study with further species, such as pigs and humans.

Not only has CARS microscopy proved to be a useful imaging tool, it has also shown us that DIC microscopy alone can be useful to identify certain cell characteristics. Following chemical identification of LDs using CARS, it was possible to compare CARS and DIC images of the same eggs and embryos, and identify the same structures in both sets of images. LDs can clearly be seen with DIC imaging, but were previously unidentifiable cytoplasmic vesicles.

In this chapter, we have shown that CARS microscopy can be used to chemically-specifically image LDs in mammalian oocytes, eggs and embryos. Observations were made of a change in LD distribution from a dispersed arrangement in GV oocytes, to a statistically significantly different ‘clustered’ distribution at MII stage. As embryonic development continued, fewer, larger LDs were identified, suggesting an altered physiology. The vast information gained from CARS measurements allows LD size, number, and lipid amount to be investigated, and may be utilised for assessment of egg or embryo metabolism. In order for this information to be useful for ART progression, however, the technique must be established as compatible with successful embryo culture and development.

Chapter 4. Viability of eggs and embryos after live-cell CARS imaging

4.1. Introduction

In Chapter 3, we were able to use CARS to visualise LDs in all stages of egg and early embryo development. However, in order for CARS to be used as an effective research or diagnostic tool, cells must survive imaging conditions so that embryonic development can continue. Being a non-invasive imaging technique, CARS requires no labelling or fixation of cells, unlike conventional methods used to study lipid droplets. It uses a near-infrared wavelength of light in the so-called "transparent window" around 800nm which reduces one-photon absorption and scattering, and thus damage within the cells. Laser powers used are comparable to other live cell imaging multiphoton techniques (two-photon fluorescence, third harmonic generation). However, considering the lack of previous studies of CARS applied to living mammalian oocytes, optimal conditions for continued egg/embryonic development need to be established.

Egg cells tend to be adequately robust cells, able to survive techniques such as fluorescent staining and microinjection, however, they are also highly sensitive to conditions such as the environment temperature, and the level of light to which they are exposed. Increases in temperature, even by 1ºC, are detrimental to most cells; decreases in temperature can slow cellular processes down considerably, although viability is usually still maintained (Boone *et al.* 2010). Exposure of eggs and embryos to visible light (400-700nm) is unnatural and harmful to cells (Ottosen *et al* 2007). Long (>5mins) exposure to lots of light (>0.5W/m^2), and shorter wavelengths of light have been proven to be detrimental to development (Takahashi *et al.* 1999; Takenaka *et al.* 2007; Ottosen *et al* 2007). UV light (250-400nm) proves to be harmful to developing eggs, one-photon absorption processes causing production of ROS, damage to DNA and apoptosis (Takenaka *et al.* 2007; Pomeroy and Reed, 2013; Ottensen *et al.* 2007).

Various imaging techniques used to date to investigate LDs include steps that cannot maintain cell viability. Fluorescence dyes often require fixation, but even when they are used on live cells, stains can interfere with normal cell processes. Moreover, photo-bleaching of stains occurring upon light excitation limits quantitative analysis and is often associated with photo-toxicity. When using one-photon excitation with visible wavelengths, direct cellular absorption might also occur and cause photo-damage. TPF techniques can overcome this limitation, as shown by Squirrell *et al.* (1999): in comparison to confocal imaging at visible wavelength, which arrested embryo development, TPF uses two photons of near-infrared wavelength to excite a fluorophore, resulting in negligible one-photon absorption by cellular components, less scattering and reduced photo-damage as a result, allowing continued embryonic development and even live birth.

Techniques such as HGM are supposedly non-invasive, being label-free and using long wavelengths of light, and theoretically should maintain egg and embryo viability. However, Watanabe *et al.* (2010) found that prolonged imaging (>10mins at an intensity of ~650mW/μm^2) using THG induced photo-toxicity, allowed embryo development to blastocyst stage, but no birth of live offspring.

Although compatible with live cell imaging (Hellerer *et al.* 2007; Folick *et al.* 2011), there is currently no proof of egg or embryo viability after CARS imaging. There is a possibility that cells are susceptible to three photon absorption (ThPA) when using ~800nm wavelength in short pulses, by cellular components with ~260nm one-photon absorption such as the DNA. Multiphoton imaging techniques such as HGM and CARS may lead to such ThPA, which induces damage to DNA by causing production of cylobutane pyrimidine dimers, which alter the structure of DNA and inhibit further replication (Meldrum *et al.* 2 003). Wavelengths of incident light >900nm might therefore be better for live cell imaging to avoid ThPA by the DNA.

Human 4Cell, and mouse 2Cell embryos are known to be highly vulnerable stages of embryonic development in each species; it is often at these stages that embryonic arrest is seen and development to later stages does not continue. It is suggested that embryonic arrest may occur due to a delay in zygotic gene activation, as this coincides with switching from maternal to zygotic transcription, and occurs at the

2Cell stage in mouse embryos and the 4Cell stage in human (Qui *et al.* 2003; Niakan *et al.* 2012; Wong *et al.* 2010).

Mouse eggs are a good model for human egg and embryo development, as their morphology, size and cellular processes are very similar, their differences only becoming more apparent in later preimplantation stages (Niakan *et al.* 2012). The particular mouse strain used in this study was chosen for the parallels with human eggs in embryonic development (Kamjoo *et al.* 2002); normal success rates for development of both to blastocyst stage are 50%, and allow the investigation of the effects of live cell imaging on the viability of these embryos.

In this chapter, the excitation conditions in our CARS experiments which allowed for live-cell imaging, and continued egg/embryonic development to blastocyst stage were investigated in detail, and CARS microscopy revealed itself to be a truly non-invasive and valid technique. IVM of GV oocytes to MII eggs was used to assess the viability of eggs after imaging with CARS at immature stages. IVM is a valid technique producing viable eggs and later embryos, however, it is widely understood that IVM yields lower quality eggs/embryos than natural *in vivo* maturation (Rizos *et al.* 2002, Gilchrist and Thompson, 2007), despite IVM producing viable offspring (Eppig *et al.* 2009).

ICSI is used to investigate the viability of embryos after CARS imaging at the one-cell zygote stage. ICSI is a widely-used technique in assisted reproductive technologies, involving sperm injection directly into the egg cytoplasm, in order to overcome any issues with sperm motility or fusion. This technique is more effective in oocytes where the cumulus cells have been removed, as must be performed before CARS imaging. However, the action of ICSI itself, piercing the egg, makes the egg susceptible to damage, especially if care is not taken to avoid disruption of the meiotic spindle, and often success rates aren't as high as standard IVF (Yoshida and Perry, 2007; Dumoulin *et al.* 2001).

4.2. In vitro *Maturation after CARS Imaging*

It was found that immature GV oocytes were able to mature up to MII stage *in vitro* after CARS imaging of the whole cell under the same excitation conditions as previously used in Chapter 3 (see also, Chapter 2, section 2.8.1.). Typically, an *xyz* volume of 100x100x50 $(\mu m)^3$ size was scanned with 0.1µmx0.1µm *xy* pixel size in 0.5µm *z*-steps, with 0.01ms pixel dwell time, at the 2850cm^{-1} resonance, with a power of no more than 25mW at the sample, before allowing maturation overnight.

Fig.4.2.1 shows DIC and CARS projections of a fully-scanned GV oocyte prior to IVM, and the same cell after 18 hours in culture, once it had reached a mature MII stage. Notably, before maturation, (Fig.4.2.1 (A-B)) the GV oocyte had a widely dispersed LD spatial distribution, and after IVM (Fig.4.2.1. (C-D)) the same cell is seen as an MII egg with characteristically aggregated LDs, as seen in Chapter 3. This difference was confirmed by quantitative analysis (Fig.4.2.2). It is found that the imaging of the whole egg did not hinder its subsequent meiotic development, as 40/47 oocytes matured to MII in these experiments.

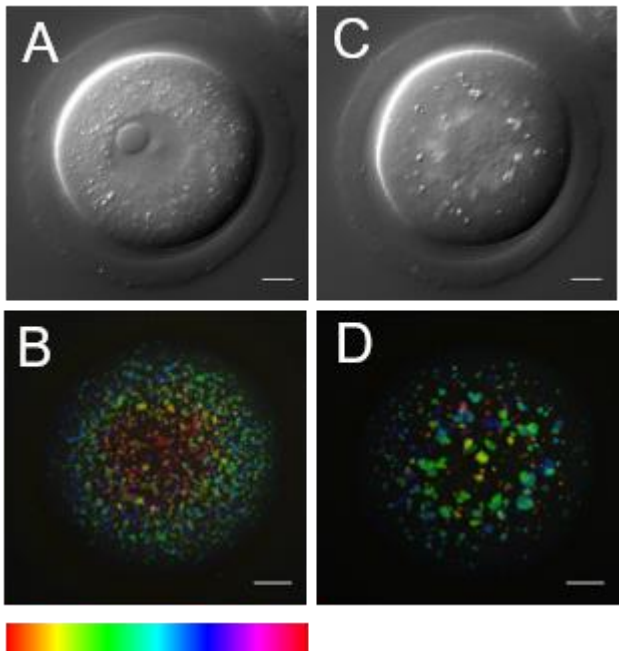

Fig.4.2.1. DIC and CARS Imaging of GV and MII Stage Mouse Eggs, Before and After in vitro *Maturation*

(A) and (C) Single z-plane DIC using a 1.27 NA water objective and a 1.4 NA oil condenser; and (B) and (D) depth colour-coded images of CARS stacks at wavenumber 2850cm^{-1}, of the same egg before (A and B) and after (C and D) *in vitro* maturation, showing that development can still occur after live imaging with CARS (n=40). 0.1x0.1µm xy pixel size; 0.5µm z-step; 0.01ms pixel dwell time; ~13mW (~9mW) Pump (Stokes) power at the sample. Scale bars represent 10µm; colour bar shows depth colour-coding from -25µm-25µm (0µm being the equatorial plane). Data from >5 trials, using 1-3 mice each.

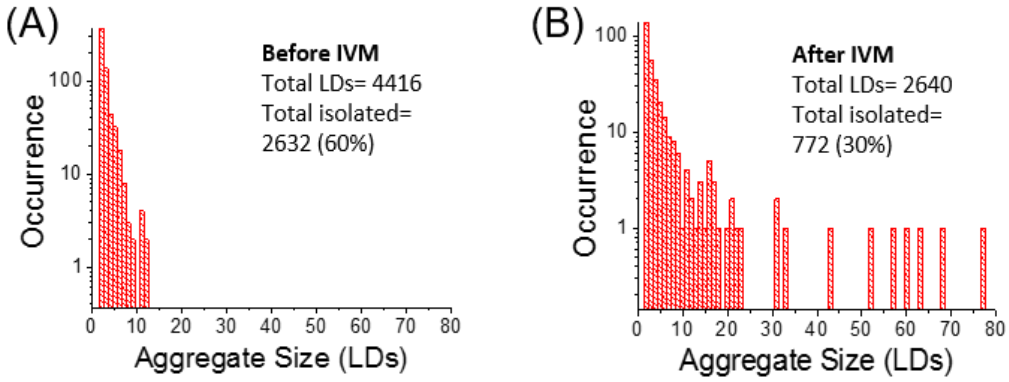

Fig.4.2.2. Histograms of Lipid Droplet Aggregation in GV and MII Stage Mouse Eggs, Before and After in vitro *Maturation*

Histograms of the number of LDs making up clusters in (A) a GV oocyte before maturation, and (B) the same egg after it was matured *in vitro* to MII stage. Total number of LDs and total number of un-clustered LDs are also indicated.

Comparing the $\sqrt{\langle s^2 \rangle}$ of the egg population imaged both before and after IVM, versus the population of eggs that were only imaged after IVM, there appears to be a larger extent of LD aggregation in those eggs that were imaged with CARS before maturation (Fig.4.2.3.). However, there is a large variability, and the results remain within SDs, so are not likely to be significant.

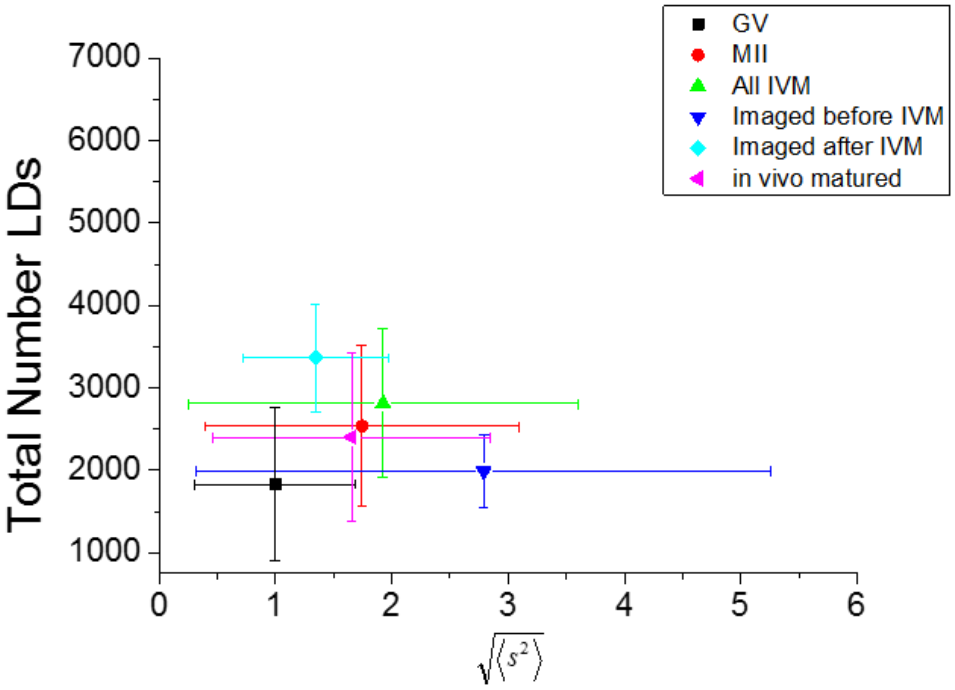

Fig.4.2.3. Scatter plot of the Extent of Lipid Droplet Aggregation ($\sqrt{\langle s^2 \rangle}$) in MII Mouse Eggs Matured* in vitro *after CARS imaging, vs. MII Mouse Eggs Matured* in vitro *without CARS imaging

Scatter plot of the square root of the mean squared aggregate size ($\sqrt{\langle s^2 \rangle}$) against the total number of LDs, in ensembles of GV oocytes (n=33), MII eggs (n=30), MII eggs matured *in vitro* (n=10), MII eggs imaged with CARS prior to being matured *in vitro* (n=4), MII eggs that were not imaged prior to being matured *in vitro* (n=6), and MII eggs matured *in vivo* (n=20). The distribution of each variable in the corresponding ensemble is shown as an average (symbol) and standard deviation (bar).

4.3. In vitro *Embryonic Development after CARS Imaging*

It was found that imaging zygotes with CARS immediately after ICSI, and then individually culturing them in KSOM allowed development of embryos to the blastocyst stage.

The CARS settings were the same as previously used (see Chapter 2, section 2.8.1.), but a singular, approximately equatorial, *xy* image was taken of each zygote before culturing for 5 days. The rate of blastocyst success was assessed and compared with un-imaged controls (developed in joint culture). In both imaged and un-imaged population, the rate to blastocyst development was not as high as the normal (expected rate of 50%) indicating that ICSI itself had been inducing damage.

Fertilised zygotes imaged with CARS lead to 13/34 to develop to blastocyst. Notably, a higher number of blastocysts were achieved in the CARS imaged populations, than in the control (un-imaged) populations, which yielded 5/30 blastocysts, suggesting that CARS imaging from the 1Cell stage does not affect development to blastocyst. Fig.4.3.1. shows DIC and CARS images of a freshly-fertilised zygote (A-B), and the same embryo after development to the blastocyst stage (C). Fig.4.3.1. (D) shows a blastocyst developed from the un-imaged control group.

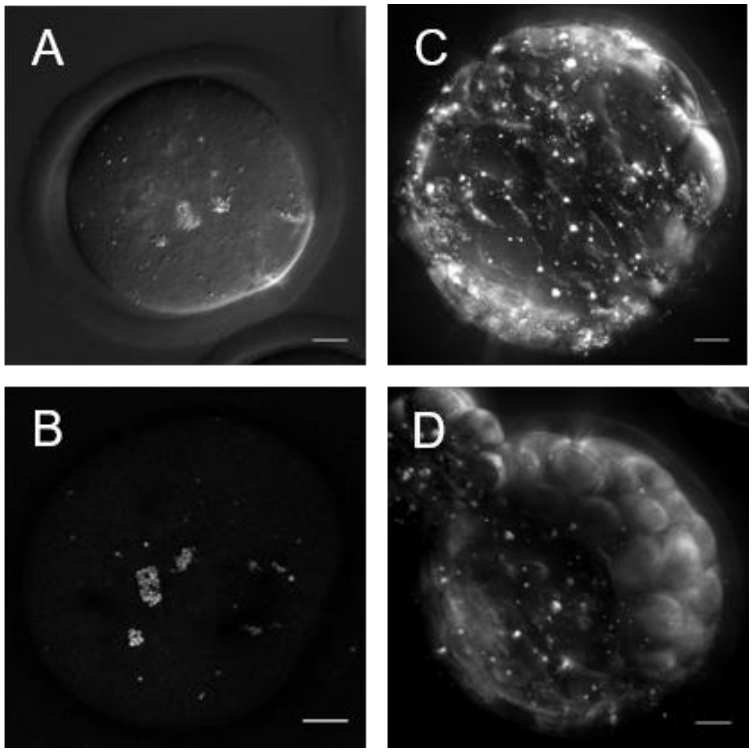

Fig.4.3.1. DIC and CARS Imaging of 1Cell Mouse Zygotes after ICSI, and Subsequent Successful Blastocyst Development

(A) Single z-plane DIC image (using a 1.27 NA water objective and a 1.4 NA oil condenser) and (B) single *z*-plane CARS image (at wavenumber 2850cm^{-1}) of the same zygote shortly after ICSI (n=34); (C) maximum intensity projection DIC images of a blastocyst, 5 days after imaging with CARS (n=13); (D) maximum intensity projection DIC images of a control blastocyst, beginning to hatch, 5 days after no imaging with CARS (n=5). 0.1x0.1µm xy pixel size; 0.01ms pixel dwell time; ~13mW (~9mW) Pump (Stokes) power at the sample. All scale bars represent 10µm. Data is from 5 separate trials, using 2-3 mice for each.

DIC and CARS imaging at the 2Cell stage was then assessed with the same parameters, and a number of different imaging conditions. All imaging conditions: taking images at 1 *z*-plane, 11 images over a 50µm thickness, 21 images over a 10µm thickness or 41 images over 20µm, appeared to hinder development to later embryonic stages, even when very few z-planes were imaged. Fig.4.3.2. (A-B) shows DIC and CARS images of a 2Cell embryo, and (C) shows the same embryo arrested at its 2Cell stage, after 5 days in culture. 100% arrest at 2Cell stage was observed (n=49) in comparison to 15/24 which continued development to blastocyst in the un-imaged control group.

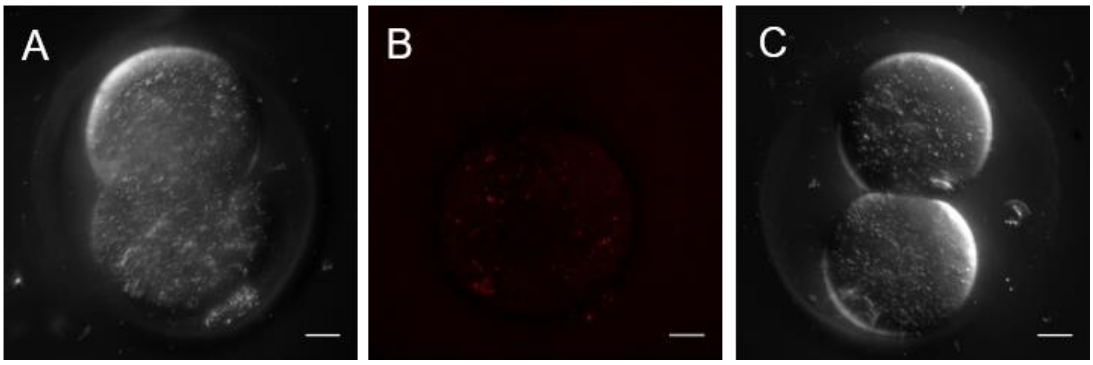

Fig.4.3.2. DIC and CARS Imaging of 2Cell Mouse Embryos after* in vivo *Fertilisation, and Failed Subsequent Development

(A) Single z-plane (approximately equatorial) DIC image using a 1.27 NA water objective and a 1.4 NA oil condenser and (B) single-plane CARS image at wavenumber 2850cm^{-1}, of a 2Cell embryo after *in vivo* fertilisation, and (C) DIC image of the same embryo 5 days later, demonstrating embryonic arrest (n=49). 0.1x0.1µm pixel size; 0.01ms pixel dwell time; ~14mW (~9mW) Pump (Stokes) power at the sample. Scale bars represent 10µm; colour bar shows depth colour-coding from -25µm-25µm (0µm being the equatorial plane). Data from >5 trials, using 1-3 mice each.

Imaging from the 4Cell stage onwards - a much less vulnerable stage of development than 2Cell in mouse embryos (Qui *et al.* 2003) - allowed development to blastocyst stage at the normal rate of 50% expected from the strain of mouse used, and normal human success rates (Kamjoo *et al.* 2002) (Fig.4.3.3.). A number of experimental *z*-step-size settings were investigated; all images were taken with imaging parameters previously described (see Chapter 2, section 2.8.1.). Experimental embryos were cultured individually, while control embryos were included in group culture. Embryos that were imaged with CARS every 0.5µm in *z* over a total of 20µm thickness (Fig.4.3.3. (F) and (J)) continued to develop further, 5/10 reaching a recognisable blastocyst stage (Fig.4.3.3. (N)). 4Cell embryos imaged with the same parameters over 10µm thickness (Fig.4.3.3. (E) and (I)) also continued to develop further, 4/9 developing to blastocyst (Fig.4.3.3. (M)). Of those imaged more sparsely, every 5µm in *z* over a 50µm *z*-range (Fig.4.3.3. (D) and (H)) all developed and 4/10 were classed as blastocysts (Fig.4.3.3. (L)). Similarly, taking a singular CARS image at the centre of the 4Cell embryo (Fig.4.3.3. (C) and (G)), or solely imaging with DIC (Fig.4.3.3. (A)) gave rise to a blastocyst yield at the normal rate: 5/9 (Fig.4.3.3. (K)) and 5/10 (B), respectively, giving the same rate of development as a control group that was not imaged (5/10).

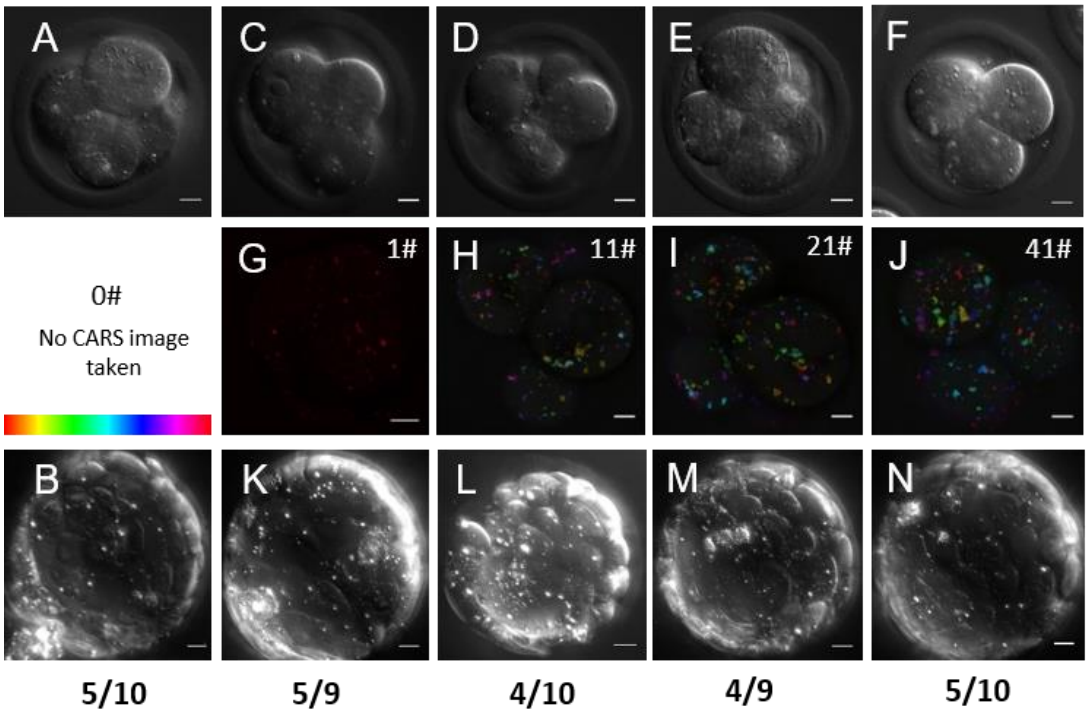

Fig.4.3.3. DIC and CARS Imaging of 4Cell Mouse Embryos after* in vivo *Fertilisation, and Subsequent Successful Blastocyst Development

(A) Single z-plane (approximately equatorial) and (B) maximum intensity projection DIC images taken with a 1.27 NA water objective and a 1.4 NA oil condenser of the same embryo at (A) 4Cell stage and (B) blastocyst stage, after development was allowed without CARS imaging (n=10). (C-F) Single z-plane DIC and (G-J) depth colour-coded CARS stacks of 4Cell embryos before their development to blastocyst stage after different extents of CARS imaging at 2850cm^{-1}. Number of CARS images taken is indicated in the top right corner; (G) 1 CARS xy image (n=9), (H) 11 CARS xy images with 5µm z-steps (n=10), (I) 21 CARS xy images with 0.5µm z-steps (n=9), (J) 41 CARS xy images taken with 0.5µm z-steps (n=10). (K-N) Maximum intensity projection DIC images of blastocyst stages of the same embryos seen at the 4Cell stage in panels C-J; blastocyst developmental rate is indicated beneath panels. 0.1x0.1µm pixel size; 0.01ms pixel dwell time; ~14mW (~9mW) Pump (Stokes) power at the sample. Scale bars represent 10µm; colour bar shows depth colour-coding from -25µm-25µm (0µm being the equatorial plane). Data from >5 trials, using 1-3 mice each.

4.4. Discussion

In mammalian embryology, there is limited availability, and extensive variability and vulnerability of samples. This means there is a particular requirement for techniques that are time-efficient and non-invasive, which provide sufficient quantitative information on egg or embryo viability, so that a prognosis can be made regarding their developmental success (Ebner *et al.* 2003). DIC and CARS imaging of live oocytes and embryos does not harm embryo development to later embryonic stages at the normal rate, as shown in this chapter, whilst providing quantitative information as to biochemical parameters which may have the potential to be correlated with subsequent development, as described in Chapter 3.

Under DIC, the cells are not imaged for more than 5 minutes each, using low light levels, a 530nm bypass filter, and an infrared filter, thus imaging with DIC does not harm the specimen. CARS imaging settings were the same as the previous measurements shown in Chapter 3, but a varying number of *xy* images along the axial direction were taken for developing embryos, in order to probe what extent of imaging they could undergo, whilst maintaining viability. It was possible to show that imaging GV oocytes with CARS in 3D over their entire volume with high spatial resolution prior to their maturation to MII did not affect their development. Therefore, it would be possible to compare quantitative information gained from 3D CARS imaging through a GV oocyte with previously suggested techniques of oocyte quality assessment. Although invasive methods of oocyte selection, such as the assessment of chromatin organisation in the GV nucleolus, simply cannot be used in ART procedures (Bellone *et al.* 2009), they are regarded as valid predictors of developmental competence. Therefore, these methods could be compared with information provided by CARS imaging, in order to give more insight into the LD distribution and content as a measure of oocyte quality. However, it is not clear that immature oocyte selection is the best measure of quality due to the subsequent need for IVM and its potential to produce lesser-quality eggs and embryos (Rizos *et al.* 2002, Gilchrist and Thompson, 2007). It is also not clear how effective both invasive and non-invasive methods of oocyte quality assessment, such as the cytoplasmic positioning of the GV, really are, due to inconclusive evidence. It may be that

multiple tests need to be performed in order to effectively predict the potential of an oocyte (Bellone *et al.* 2009).

Although not performed here due to time constraints, it is highly likely that MII eggs, being more robust than GV oocytes, would be able to survive CARS imaging and go on to produce viable embryos. Comparison of CARS images with methods currently used to assess MII stage eggs, such as the appearance of their cytoplasm, or presence of a polar body (Sananthan and Gunasheela, 2007), may provide information as to how the LD distribution in MII eggs could also predict embryonic success.

In clinical practice, the assessment of embryo competence is more likely to be performed after fertilisation, once embryonic development has commenced. Imaging at the 2Cell stage in mouse embryos appeared to halt their development. The 2Cell stage has proved to be a particularly vulnerable stage in mouse embryonic development, as this coincides with the timing of ZGA, and the embryo is even more susceptible to DNA damage (Qui *et al.* 2003). In human embryonic development, ZGA is initiated at the 4Cell stage, therefore imaging at the 2Cell stage may not cause any harm, and assessment of developmental competence may be possible at an earlier stage (Niakan *et al.* 2012; Wong *et al.* 2010).

Imaging a smaller portion of the mouse embryo volume at the 1Cell stage after fertilisation, or at the 4Cell stage was compatible with continued embryonic development. Single CARS images were taken of fertilised zygotes before pronuclear formation commenced, and this allowed for blastocyst formation at even higher rates as un-imaged controls, while imaging multiple *z*-planes at the 4Cell stage also did not appear to hinder blastocyst development rates. Through knowledge gained from previous measurements throughout entire cells (see Chapter 3), for future analysis of LD distribution and content as a measure of embryonic developmental potential, it is thought that one equatorial image should give enough information as to the LD distribution within the zygote, in order for informed conclusions to be drawn regarding their developmental competence. It is possible that future studies of LD distribution and developmental potential could provide a potential diagnostic tool for selecting embryos in clinical IVF or animal reproductive technologies, and an earlier prognosis of developmental competence is favourable in

order to minimise embryo handling and manipulation, and to maximise reproductive success.

Interestingly, a higher number of CARS imaged embryos developed to blastocyst stages, than un-imaged embryos. These un-imaged controls were developed in group culture, and included those kept in culture in the incubator, and those that were transferred to an imaging dish and placed on the microscope slide for an appropriate length of time without imaging. This control was in order to rule out any negative effects of the microscope stage or imaging gasket themselves (i.e. controls were not simply performed for the laser power). It is therefore unclear why this result was achieved in numerous experiment repetitions (5 trials). It is clear, however, that the CARS imaging technique does not harm subsequent development. Dumoulin *et al.* (2001) showed that ICSI, although a useful and reliable technique of fertilisation, may have a lower success rate than traditional IVF. The lower than expected blastocyst scores may be due to the damaging effects of ICSI, but there was still a fairly high rate of success in blastocyst formation (~38%). ICSI was used rather than IVF due to avoid CARS imaging of cumulus cells. During initial CARS imaging sessions, it was found that the COCs were very dense and lipid-rich causing light beam deflection (from refractive index in homogeneities) and shadowing artefacts when imaging the egg or embryo cytoplasm.

Different extents of CARS imaging were performed at the 4Cell stage, ranging from one single *xy* image to 41 images covering a 20µm axial depth. Blastocyst success rates were almost consistently normal, ranging from 40%-55%, under all conditions, showing CARS is not detrimental to embryonic development if performed at this stage. Scoring of embryos was carried out in the usual way- blastocysts having a clear blastocoel, ICM and trophoblast, and fragmented embryos were discarded. However, fragmented blastocysts still may be developmentally viable; it has been suggested that temporal and spatial patterns of fragmentation may define whether this response is apoptotic, or a survival mechanism of healthy blastomeres (Van Blerkom *et al.* 2001). Thus far it is impossible to comment, but future investigation into certain fragmented embryos may be able to pinpoint characteristics of viable fragmented blastocysts.

Current non-invasive methods of embryo selection have questionable predictive value. Parameters such as pronuclear formation rates and positioning, and cell

cleavage rates, are thought to be early indicators of embryonic competence (Ebner *et al.* 2003). Uneven cleavage presents a risk of higher chromosomal abnormalities (Hardarson *et al.* 2001), and as late as the blastocyst stage, ICM cell number and trophectoderm development can assess quality (Gardner *et al.* 2000). These factors could experimentally be used alongside CARS microscopy, in order to draw parallels between predictors of quality, and quantitative information gained from CARS images.

Further studies into the viability of the blastocysts yielded after CARS imaging would be necessary. Implantation and birth of live offspring should be monitored to determine if these imaged embryos can develop past the blastocyst stage after transfer into surrogate mothers.

It was found that live offspring could be born after prolonged TPF imaging of 2Cell hamster embryos (Squirrell *et al.* 1999). Long-term HGM, however, was not compatible with live births, unless imaging times were severely shortened (Watanabe *et al.* 2010; Hsieh *et al.* 2008). It is likely that these cell deaths were due to multi-photon damage as a result of the pulsed light excitation, thus the CARS imaging conditions (excitation intensity, wavelength, pulse duration, repetition rate) used in the current study must also be tested for long-term cell viability.

ThPA in DNA is a multi-photon phenomenon that may occur during imaging with short laser pulses of ~800nm wavelength. Damage to DNA could be a factor in 2Cell arrest with CARS imaging when embryonic genome transcription is occurring. It may be possible to test whether there is DNA damage, alongside CARS. Notably, CARS microscopy using excitation at longer wavelengths than used in the present study (>900nm) is technically possible (and currently being implemented in our laboratory), and should allow for lower photo-toxicity, due to the suppression of ThPA by DNA, along with increased penetration depth. This implementation can be combined with THG imaging, which can be used for non-chemically specific LD imaging, and stimulated Raman scattering (SRS) imaging. SRS is a technique that exploits the same light-matter interaction mechanism of CARS, but measures the loss (gain) of energy at the pump (Stokes) beam as it interacts with the sample, instead of the anti-Stokes scattering. SRS benefits from the absence of non-resonant

CARS background, and allows for improved image contrast when probing only a single vibrational frequency.

In this chapter, we were able to demonstrate that CARS microscopy is a non-invasive imaging technique, compatible with continued egg and embryo development. IVM of GV oocytes to MII stage, and normal rates of embryo development to blastocyst stage were observed after CARS imaging, when measurements were taken before or after the vulnerable 2Cell embryo stage. Establishment of CARS as a viable technique allows continued use of this method for investigation into the metabolism of mammalian eggs and embryos, with a confidence that findings are physiological, and not a consequence of experimental techniques.

Chapter 5. Hyperspectral CARS Imaging of eggs and embryos

5.1. Introduction

CARS imaging of LDs in eggs and embryos allows us to gain a great deal more information than merely visualising and counting LDs within the cytoplasm. CARS enables the examination of specific LDs and their chemical content, allowing investigation into the chemical composition of LDs in oocytes, eggs and embryos at different developmental stages, in both their 'normal' state, and in situations where the types of fatty acids stored in these LDs may be detrimental to the overall health of the egg or embryo.

Methods of chemical extraction, as described in Chapter 3, have previously been used to assess the lipid content of mammalian oocytes, but with CARS it is possible to specifically observe the chemical content of individual LDs, whilst maintaining cell viability.

Chemical information can be provided by hyperspectral CARS microscopy which can be performed due to the broadband laser source used in this work with 310nm bandwidth, allowing excitation over a large vibrational range of 1200-3800cm^{-1}. This range includes biologically-relevant resonances such as that of the CH_2 symmetric stretch bond (2850cm^{-1}) and the =CH bond (3010cm^{-1}), allowing excitation and imaging of various lipids (Pope *et al.* 2012). Compared with single-frequency CARS, hyperspectral imaging involves changing the IFD of the pump and Stokes beams to image over a number of sequential vibrational resonances, and acquiring a spectrum of CARS frequencies for each spatial point, in order to provide specific information regarding the chemical composition of LDs present in eggs and embryos, including their degree of saturation (Parekh *et al.* 2010; Masia *et al.* 2013; Di Napoli *et al.* 2014b).

Every molecule has its own Raman spectrum, made up of all the vibrational resonances comprising it. In order to extract any quantitative information from the CARS IFD measurements, Raman spectra must be retrieved from the hyperspectral CARS signal gained from each spatial point, allowing for chemically-specific assessment of the content of the imaged specimen. Existing knowledge of the Raman signatures of different chemical compounds is essential for identifying the chemical composition of the sample.

CARS holds many advantages over simple Raman spectro-microscopy, namely that the signal strength is much higher, and in turn acquisition times are greatly decreased, allowing imaging of live cells. However, the signal gained from CARS imaging is complex, and does not reflect the precise Raman profiles of the molecules it detects.

The CARS intensity generated by coherence of vibrating bonds is proportional to the square of the third-order susceptibility/non-linearity ($\chi^{(3)}$), i.e. the CARS intensity scales as $\left|\chi^{(3)}\right|^{(2)}$ (Pope *et al.* 2012; Di Napoli *et al.* 2014a). $\chi^{(3)}$ arises from the sum of the resonant (real and imaginary parts) and non-resonant (just the real part) components (Evans *et al.* 2004; Di Napoli *et al.* 2014a; Vartiainen *et al.* 2006) and is linearly dependent on the number of bonds vibrating in the sample (Pope *et al.* 2012). As the non-resonant background contributes to the real part of the susceptibility, this can be subtracted from the CARS complex susceptibility, allowing for analysis of the resonant signal, comparison with known Raman spectra, and identification of specimen components (Evans *et al.* 2004; Di Napoli *et al.* 2014a; Vartiainen *et al.* 2006; Chimento *et al.* 2009). Masia *et al* 2013 introduced a specific procedure to retrieve the CARS susceptibility from hyperspectral CARS intensities acquired from IFD scans (see Chapter 2, section 2.9.4.), allowing the imaginary part to be isolated, and directly compared with known Raman spectra (Masia *et al.* 2013, Chimento *et al.* 2009).

Raman profiles of conventional FAs show distinct peaks, characteristic of the chemical bonds that might compose them. For example, a peak at ~2850cm^{-1} corresponds to the CH_2 symmetric stretch vibration, and is prominent in most FA spectra; a peak around 2930 cm^{-1} occurs due to the CH_3 and asymmetric CH_2 stretch, and is enhanced by the broadening

and shift of the CH deformations in the liquid phase. Poly-unsaturated fatty acids (PUFAs) with high acyl chain disorder (double bonds introduce kinks to the chain conformation) are liquid at room temperature and exhibit a significant band around 2930 cm^{-1}. A peak at ~3010 cm^{-1} corresponds to the =CH stretch, its intensity is proportional to the number of C=C bonds in the main lipid chain, and again is seen in spectra of unsaturated fatty acids (Di Napoli *et al.* 2013; Di Napoli *et al.* 2014b).

The lipid profile of an egg or embryo can be an indicator of their developmental competence. The molecular composition of the follicular or uterine environment is hugely influential over the chemical content of the developing oocyte or embryo, having implications on their later embryonic development (Aardema *et al.* 2011; Ferguson and Leese, 1999; Adamiak *et al*. 2006; Sata *et al.* 1999; Kim *et al.* 2001). When a mother has a high fat diet or is obese, the elevated concentrations of FFAs in the blood, and systemic changes that can occur such as high blood insulin, or inflammation can have direct effects on the ovarian environment, leading to fertility complications (van Hoeck *et al.* 2011; Robker *et al.* 2009; Jungheim *et al.* 2011b). High concentrations of FFAs during oocyte growth and maturation leads to apoptotic follicles, fewer matured oocytes, poor COC morphology, cellular defects and reduced rates of blastocyst formation, while exposure of embryos to elevated FFAs increases the incidence of birth defects and smaller foetuses with low birth weights, and offspring have long-term problems (van Hoeck *et al.* 2011; Jungheim *et al.* 2011b, 2011a, 2010). It has been shown that blastocysts transferred from mice on a high fat diet to surrogate normal mice have serious developmental defects (Luzzo *et al.* 2012), whereas, IVF of obese patients has increased success if eggs from a donor of normal weight are used (Luke *et al.* 2011; Jungheim *et al.* 2013). Weight loss is also seen to improve both natural and assisted fertility in obese patients (Clark *et al.* 1998).

The types of fatty acid present in the developing environment is also thought to influence cellular and embryonic potential. A developing egg or embryo normally has abundant oleic, palmitic and stearic acid within its lipid profile (Jungheim *et al.* 2011b). However, higher levels of saturated fatty acids such as palmitic acid (PA) are found to coincide with reduced fertilisation rates, lesser developmental success, or birth defects (Jungheim *et al.* 2011a; Shaaker *et al.* 2012; Nonogaki *et al.* 1994), while higher concentrations of unsaturated fatty acids in embryos is indicative of more promising developmental success (Haggarty *et al.* 2006). Interestingly, the

negative effects of saturated PA can be counteracted by monounsaturated oleic acid (OA), which has a protective role in cells (Das *et al.* 2010; Aardema et al. 2011; Shaaker *et al.* 2012).

Overall, based on the overview above, it is clear that the chemical identification of lipids comprising LDs in living mouse eggs and embryos by hyperspectral CARS microscopy can provide very valuable information, which I have addressed in this study as described in the following results sections. The hyperspectral CARS measurements described in this study have shown that feeding cells with certain fatty acids can change their lipid profile, unveiling a whole new level of understanding of lipid metabolism in the mammalian egg or embryo.

5.2. Hyperspectral imaging of oocytes and MII eggs

Hyperspectral CARS images of LDs in GV oocytes and MII eggs were taken with the settings described in Chapter 2, section 2.8.1. They were analysed with in-house developed software HIA to retrieve Raman-like spectra by determining the imaginary part of the complex CARS susceptibility at each spatial point (Masia *et al.* 2013, 2015).

The shape of the retrieved vibrational spectra at LD positions in both developmental stages is characteristic of poly-unsaturated FAs (Fig.5.2.1 (A) and (C)). A prominent band is seen at ~2930 cm^{-1} (labelled on spectra as ϕ) from the CH_3 stretch and asymmetric CH_2 stretch vibrations enhanced by the broadening and shift of the CH deformations in the liquid disordered phase, a less prominent peak at ~2850 cm^{-1} (labelled on spectra as *) corresponds to the symmetric CH_2 stretch, and a third peak at ~3010 cm^{-1} (labelled on spectra as ψ) corresponds to the =CH stretch (Di Napoli *et al.* 2014a, 2014b). Spectra were consistently of similar shape both across multiple LDs within the same cell, as shown in Fig.5.2.1. (B) and (D), and across different cells of both developmental stages (Fig.5.2.1. (A) and (C)), and line-shape was not affected by LD position or brightness.

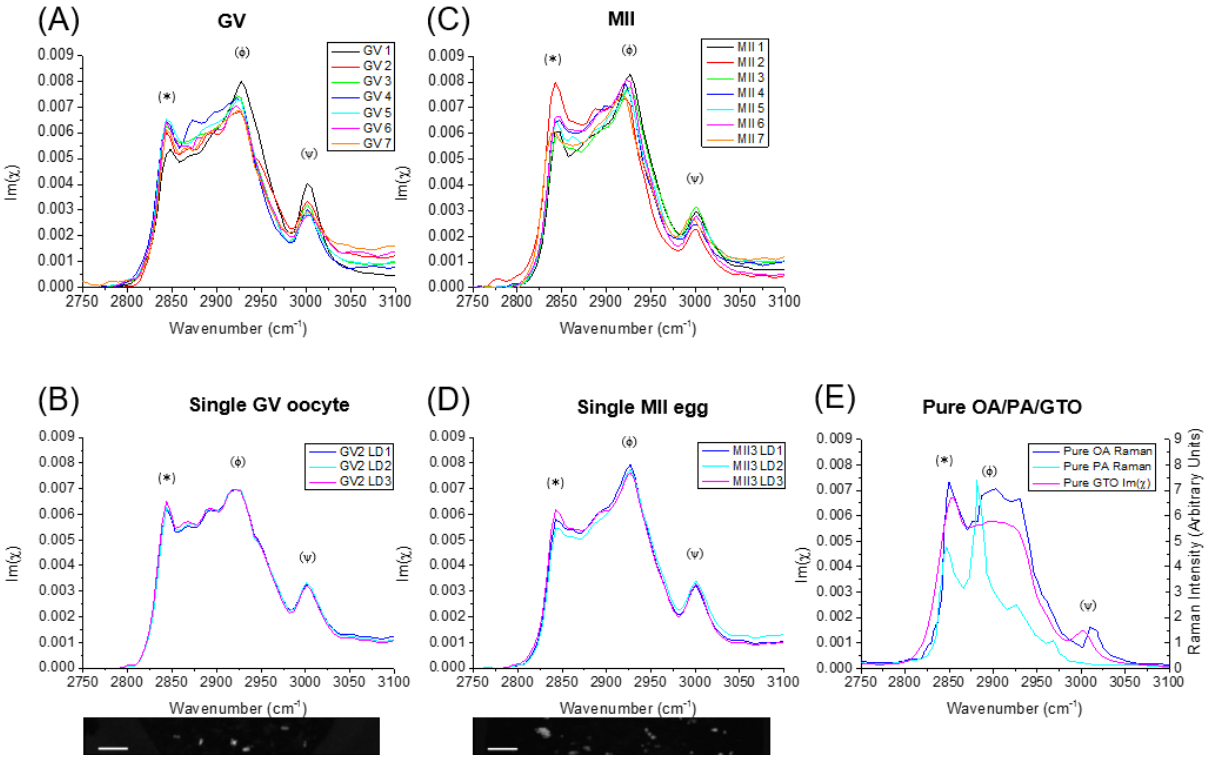

Fig.5.2.1. Hyperspectral Analysis of Lipid Droplets in GV and MII Stage Mouse Eggs

Vibrational Raman-like spectra Im(χ) obtained from CARS hyperspectral images of (A) example LDs in all GV oocytes (n=7) and (B) 3 LDs in the same GV oocyte, shown in the accompanying image; (C) example LDs in all MII eggs (n=7) and (D) 3 LDs in the same MII egg, shown in the accompanying image. (E) Raman spectra of pure oleic acid (OA) and palmitic acid (PA) in the solid (ordered) phase (digitised from spectra given by Sigma), against the retrieved PCKK spectrum of glycerol trioleate (GTO- oleic acid in its triglyceride form. Spectra are normalised to the total area. Peaks: (*) ~2850 cm^{-1} correspond to the symmetric CH_2 stretch; ($^{\delta}$) ~2880 cm^{-1} to the asymmetric CH_2 stretch, especially enhanced in ordered/solid-phase; ($^{\phi}$) ~2930 cm^{-1} to CH_3 and asymmetric CH_2 stretch vibrations, enhanced in disordered/liquid-phase acyl chains; ($^{\Psi}$) ~3010 cm^{-1} correspond to the =CH stretch. Note, the intensity ratio between bands at 2880 cm^{-1} and 2850 cm^{-1} can be used as a measure of acyl chain order; the ratio between peaks at 2930 cm^{-1} and 2850 cm^{-1} can be used to ascertain chain disorder. Accompanying images show the 10µm x 80-100µm area over which hyperspectral scans were obtained. Scale bars represent 10µm. Data from ≥2 trials, using 1-3 mice each.

Quantitative analysis of these peaks enables further confirmation of the LD composition in these populations of eggs, and are shown in Table 3. The ratio between peaks at ~2930 cm^{-1} (CH_3 and asymmetric CH_2) and ~2850 cm^{-1} (CH_2), can be used as a measure of chain disorder and is expected to be higher in polyunsaturated fatty acids. The ratio between peaks at ~3010 cm^{-1} (=CH) and ~2850 cm^{-1} (CH_2) can be used as a measure of unsaturation, thus is expected to be near zero in saturated fatty acids. It is clear that spectra of LDs in both GV and MII eggs show characteristics of poly-unsaturated fatty acids: the $2930cm^{-1}/2850cm^{-1}$ ratio values, showing chain disorder (1.19 and 1.21, respectively), are higher than both those of pure mono-unsaturated OA (0.91) and pure saturated PA (0.53). Furthermore, the $3010cm^{-1}/2850cm^{-1}$ ratio values, demonstrating the extent of =CH stretch ratio values (0.53 and 0.43, respectively) are also higher than those of pure OA (0.22) and pure PA (0.03).

Hyperspectral analysis of MII stage bovine eggs revealed that the content of bovine egg LDs is similar to that of mouse: the main fatty acid component being of a poly-unsaturated nature, as described, the most prominent band seen at $2930cm^{-1}$ (Fig.5.2.2. (A)). The spectra remain consistent across LDs within the same egg (Fig.5.2.2. (B)), and across different eggs of different bovine species (Fig.5.2.2. (A)). Quantitative analysis shows that the level of disorder is high in bovine MII LDs, with a $2930cm^{-1}/2850cm^{-1}$ peak ratio value of 1.33 (compared with 0.91 in pure mono-unsaturated OA), and the $3010cm^{-1}/2850cm^{-1}$ ratio value of 0.43 (compared to 0.22 of OA) demonstrates a larger extent of unsaturation (Table 3.).

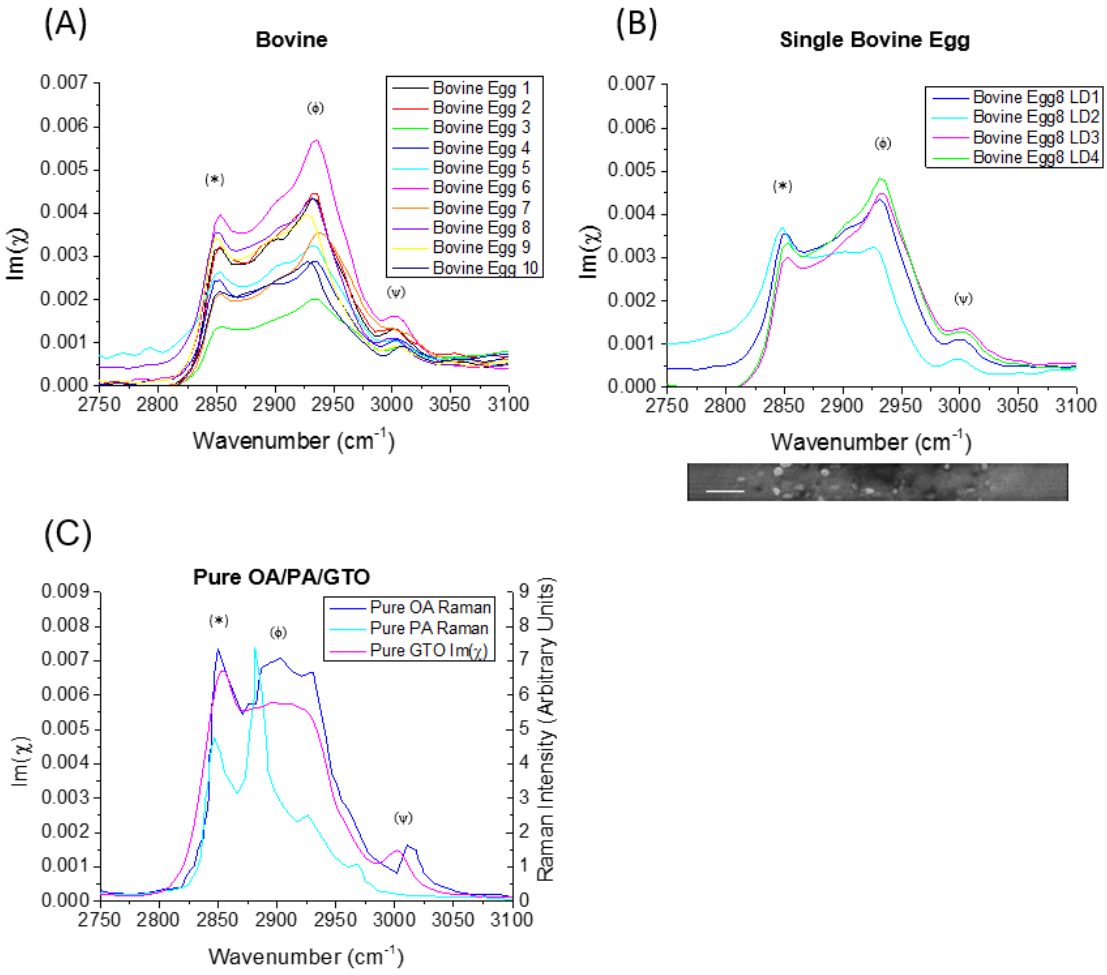

Fig.5.2.2. Hyperspectral Analysis of Lipid Droplets in MII Stage Bovine Eggs

Vibrational Raman-like spectra Im(χ) obtained from CARS hyperspectral images of (A) example LDs in all MII stage bovine eggs (n=10) and (B) 3 LDs in the same bovine egg, shown in the accompanying image; (C) Raman spectra of pure oleic acid (OA) and palmitic acid (PA) in the solid (ordered) phase (digitised from spectra given by Sigma), against the retrieved PCKK spectrum of glycerol trioleate (GTO- oleic acid in its triglyceride form. Spectra are normalised to the total area. Peaks: (*) ~2850 cm^{-1} correspond to the symmetric CH_2 stretch; ($^{\delta}$) ~2880 cm^{-1} to the asymmetric CH_2 stretch, especially enhanced in ordered/solid-phase; ($^{\phi}$) ~2930 cm^{-1} to CH_3 and asymmetric CH_2 stretch vibrations, enhanced in disordered/liquid-phase acyl chains; ($^{\Psi}$) ~3010 cm^{-1} correspond to the =CH stretch. Note, the intensity ratio between bands at 2880 cm^{-1} and 2850 cm^{-1} can be used as a measure of acyl chain order; the ratio between peaks at 2930 cm^{-1} and 2850 cm^{-1} can be used to ascertain chain disorder. Accompanying images show the 10µm x 80-100µm area over which hyperspectral scans were obtained. Scale bars represent 10µm. Data from 2 trials, using 1-3 cows each.

Vibrational Peak Ratio	Pure OA Raman Spectrum	Pure PA Raman Spectrum	GV Oocyte LDs (n=7)	MII Egg LDs (n=7)	Bovine MII Egg LDs (n=10)
2930cm^{-1}/2850cm^{-1} (ϕ/*)	**0.91**	**0.53**	**1.19**±0.14	**1.21**±0.14	**1.33**±0.14
3010cm^{-1}/2850cm^{-1} (ψ/*)	**0.22**	**0.03**	**0.53**±0.11	**0.43**±0.08	**0.43**±0.12

Table 3. Amplitude Ratios from the Vibrational Raman-like Spectra Im(χ) of Lipid Droplets in GV and MII Mouse Eggs, and MII Bovine Eggs, Against Pure Oleic and Palmitic Acid Raman Spectra

The ratio between peaks at ~2930 cm^{-1} (φ- corresponding to CH_3 and asymmetric CH_2 stretch vibrations) and ~2850 cm^{-1} (*- corresponding to the symmetric CH_2 stretch) can be used as a measure of chain disorder and is expected to be higher in polyunsaturated fatty acids. The ratio between peaks at ~3010 cm^{-1} (Ψ- corresponding to the =CH stretch) and ~2850 cm^{-1} can be used as a measure of unsaturation, thus is expected to be near zero in saturated fatty acids. Mouse GV and MII eggs, and bovine MII eggs show a value indicative of polyunsaturated fatty acids.

5.3. Lipid Droplet content after fatty acid-feeding

After incubation in different FAs, the chemical composition of LDs reflects that of the FA supplements. Hyperspectral imaging was performed with the same settings described above, on MII eggs that had been *in vitro* matured overnight in differing concentrations of mono-unsaturated oleic acid and saturated palmitic acid. After incubation overnight (~18hrs) with 100 µM OA (Fig.5.3.1. (A)), the retrieved vibrational spectrum from LDs in MII eggs was shifted from the spectrum of poly-unsaturated lipids originally observed in MII in Fig.5.2.1, towards the Raman spectrum of mono-unsaturated OA in its TAG form- glycerol trioleate (GTO) (Fig.5.3.1. (C)). After incubation with 100 or 250 µM PA (Fig.5.3.1. (B)), the Raman spectrum of MII LDs tends to shift even more towards a saturated FA-like line shape

(as seen in Fig.5.3.1. (C)), with a more pronounced peak at 2850 cm^{-1} and reduced =CH resonance at ~3010 cm^{-1}.

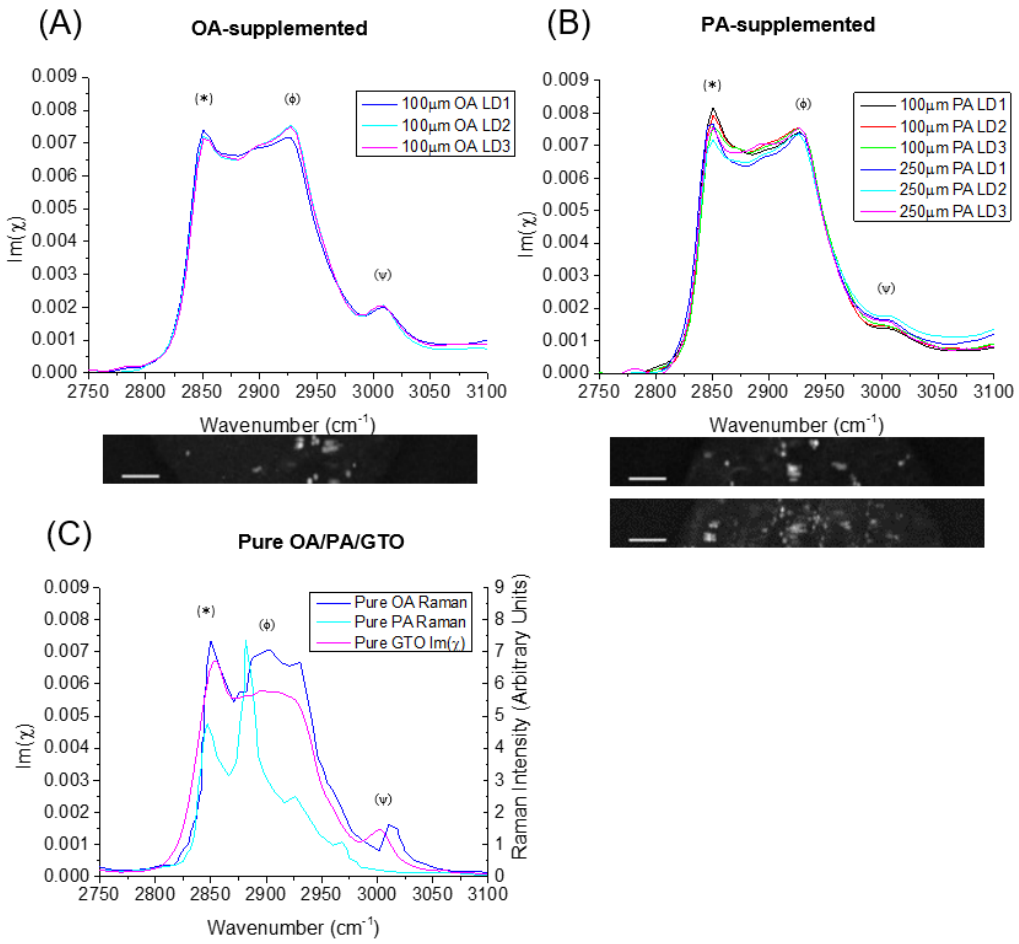

Fig.5.3.1. Hyperspectral Analysis of Lipid Droplets in GV and MII Stage Mouse Eggs after* in vitro *Fertilisation in Fatty Acid-Containing Media

Vibrational Raman-like spectra Im(χ) obtained from CARS hyperspectral images of (A) 3 LDs in an MII egg *in vitro* matured in 100µM oleic acid (n=16), and (B) 3 LDs in MII eggs *in vitro* matured in 100µM (n=31) or 250µM palmitic acid (n=33), LDs shown in the accompanying images. (C) Raman spectra of pure oleic acid (OA) and palmitic acid (PA) in the solid (ordered) phase (digitised from spectra given by Sigma), against the retrieved PCKK spectrum of glycerol trioleate (GTO- oleic acid in its triglyceride form. Spectra are normalised to the total area. Peaks: (*) ~2850 cm^{-1} correspond to the symmetric CH_2 stretch; ($^{\delta}$) ~2880 cm^{-1} to the asymmetric CH_2 stretch, especially enhanced in ordered/solid-phase; ($^{\phi}$) ~2930 cm^{-1} to CH_3 and asymmetric CH_2 stretch vibrations, enhanced in disordered/liquid-phase acyl chains; ($^{\Psi}$) ~3010 cm^{-1} correspond to the =CH stretch. Note, the intensity ratio between bands at 2880 cm^{-1} and 2850 cm^{-1} can be used as a measure of acyl chain order; the ratio between peaks at 2930 cm^{-1} and 2850 cm^{-1} can be used to ascertain chain disorder. Accompanying images show the 10µm x 80-100µm area over which hyperspectral scans were obtained. Scale bars represent 10µm. Data from 4 trials, using 1-3 mice each.

Quantitative analysis of these peaks shows that with fatty acid feeding, the chemical composition of LDs does in fact shift towards that of the exogenous fatty acid within the maturation media, reflected by the Raman spectra obtained and shown in Table 4. When supplemented with OA, the MII egg LDs shifted from their 2930cm^{-1}/2850cm^{-1} ratio value from 1.21 to 1.02 which is much closer to that of pure OA (0.91). The 3010cm^{-1}/2850cm^{-1} ratio value shifted from 0.43 to 0.38 which is, again, more reflective of the lower extent of unsaturation (0.22) seen in pure OA. When supplemented with PA, the eggs shifted their LD 2930cm^{-1}/2850cm^{-1} ratio value from 1.21 to 0.97, which is less than seen with OA, indicating a bigger shift towards the pure PA spectrum (2930cm^{-1}/2850cm^{-1} value of 0.53). The 3010cm^{-1}/2850cm^{-1} ratio value became 0.20, which was again lower than that of pure OA (Table 4.). Pure PA 3010cm^{-1}/2850cm^{-1} ratio value is as low as 0.03, but it is clear that there is still a mixed presence of fatty acids within the LDs, as feeding eggs with fatty acids will not completely replace the LD content.

Vibrational Peak Ratio	**Pure OA Raman Spectrum**	**Pure PA Raman Spectrum**	**MII Egg LDs (n=7)**	**OA-supplemented MII Egg LDs (n=3)**	**PA-supplemented MII Egg LDs (n-6)**
2930cm^{-1}/2850cm^{-1} (ϕ/*)	**0.91**	**0.53**	**1.21**±0.14	**1.02**±0.05	**0.97**±0.04
3010cm^{-1}/2850cm^{-1} (ψ/*)	**0.22**	**0.03**	**0.43**±0.08	**0.28**±0.01	**0.2**±0.03

Table 4. Amplitude Ratios from the Vibrational Raman-like Spectra Im(χ) of Lipid Droplets in Un-supplemented and Supplemented MII Mouse Eggs, Against Pure Oleic and Palmitic Acid Raman Spectra

The ratio between peaks at ~2930 cm^{-1} (φ- corresponding to CH_3 and asymmetric CH_2 stretch vibrations) and ~2850 cm^{-1} (*- corresponding to the symmetric CH_2 stretch) can be used as a measure of chain disorder and is expected to be higher in polyunsaturated fatty acids. Oleic- and palmitic acid-supplemented eggs appear to have a lower ratio of these peaks than un-supplemented MII eggs. The ratio between peaks at ~3010 cm^{-1} (Ψ- corresponding to the =CH stretch) and ~2850 cm^{-1} can be used as a measure of unsaturation, thus is expected to be near zero in saturated fatty acids. MII eggs show a value indicative of polyunsaturated fatty

acids, while oleic acid- and palmitic acid-supplemented eggs show increased saturation in the direction of pure oleic and palmitic acid spectra.

5.4. Hyperspectral imaging of embryos

Raman-like spectra derived from LDs of a 2Cell embryo are shown in Fig.5.4.1 (A). It is clear that these LDs are of a similar lipid composition as GV and MII stage eggs, and show poly-unsaturated FA spectral characteristics, with prominent peaks at 2930cm^{-1} and 3010cm^{-1}. This was also quantitatively shown by the 2930cm^{-1}/2850cm^{-1} ratio value of 1.16 and 3010cm^{-1}/2850cm^{-1} ratio value of 0.45, being higher than that of OA (Table 5.).

Retrieved spectra of the large LDs seen in a morula-stage embryo appeared to have a less prominent band at 2930cm^{-1} relative to the 2850cm^{-1} peak (Fig.5.4.1. (B)), and a less pronounced peak at 3010cm^{-1}, suggesting reduced unsaturation and increased chain order (more symmetry and fewer 'kinks' caused by the presence of double bonds). However, peak ratio analysis demonstrates that LDs in this embryo are in fact of poly-unsaturated nature, the ratio values of all peaks being higher than that of OA (Table 5.).

Hyperspectral imaging of the highly variable LDs observed in blastocyst-stage embryos, however, showed that within the same embryo, LDs had differing compositions of saturated and unsaturated FAs (Fig.5.4.1. (C)). Some LD profiles were seen to be similar to the previous developmental stages, but other droplets had a less prominent 2930 cm^{-1} band relative to the 2850 cm^{-1} peak characteristic of a lower extent of unsaturation and increased acyl chain order. There was no observed difference between bigger versus smaller LDs, nor comparing those of the ICM and trophoblast.

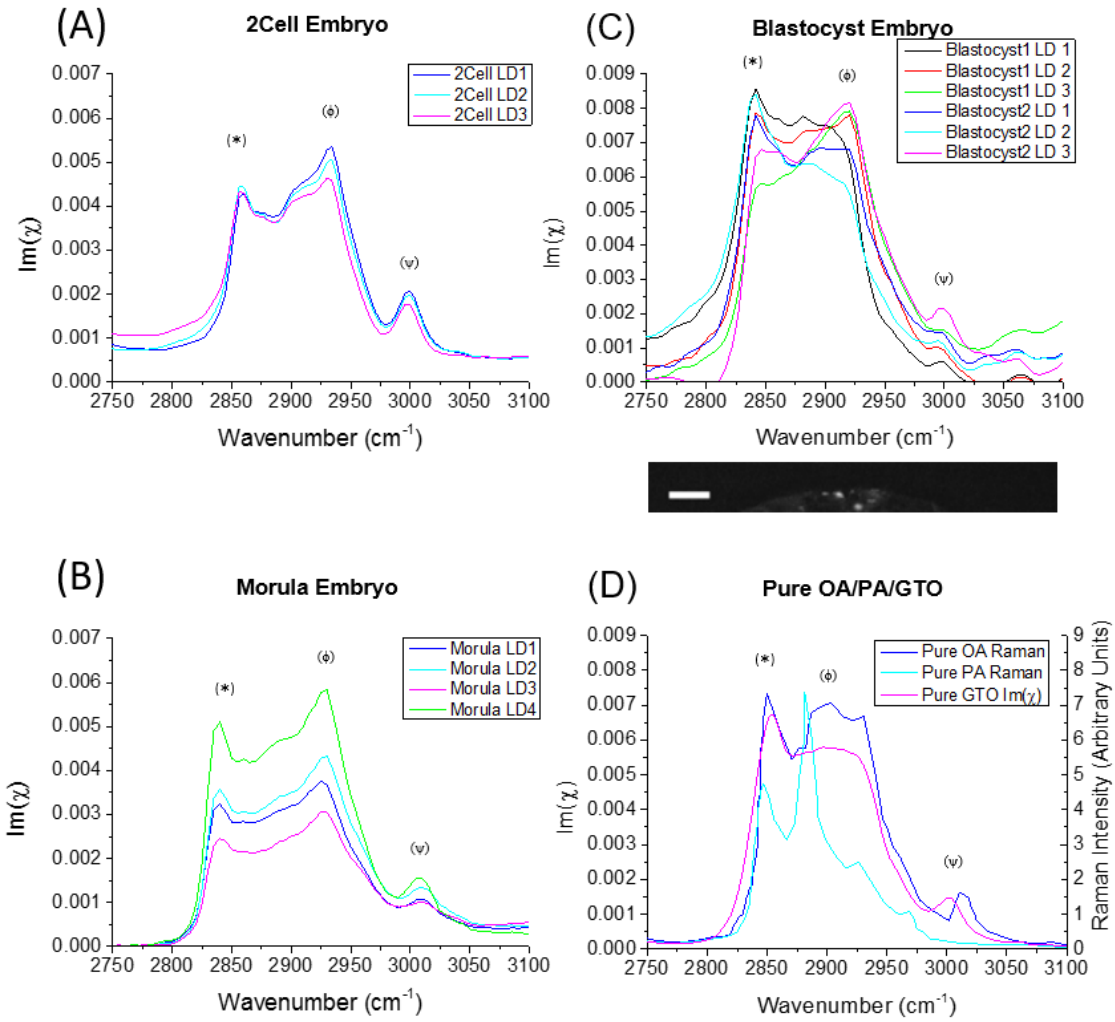

Fig.5.4.1. Hyperspectral Analysis of Lipid Droplets in 2Cell, Morula and Blastocyst Stage Early Mouse Embryos

Vibrational Raman-like spectra Im(χ) obtained from CARS hyperspectral images of (A) LDs in a 2Cell stage embryo (n=1); (B) LDs in a morula stage embryo (n=1); (C) 3 LDs in two different blastocyst stage embryos (n=14), 'Embryo 2' shown in the accompanying image; (D) Raman spectra of pure oleic acid (OA) and palmitic acid (PA) in the solid (ordered) phase (digitised from spectra given by Sigma), against the retrieved PCKK spectrum of glycerol trioleate (GTO- oleic acid in its triglyceride form. Spectra are normalised to the total area. Peaks: (*) ~2850 cm^{-1} correspond to the symmetric CH_2 stretch; ($^{\delta}$) ~2880 cm^{-1} to the asymmetric CH_2 stretch, especially enhanced in ordered/solid-phase; ($^{\phi}$) ~2930 cm^{-1} to CH_3 and asymmetric CH_2 stretch vibrations, enhanced in disordered/liquid-phase acyl chains; ($^{\Psi}$) ~3010 cm^{-1} correspond to the =CH stretch. Note, the intensity ratio between bands at 2880 cm^{-1} and 2850 cm^{-1} can be used as a measure of acyl chain order; the ratio between peaks at 2930 cm^{-1} and 2850 cm^{-1} can be used to ascertain chain disorder. Accompanying images show the 10µm x 80-100µm area over which hyperspectral scans were obtained. Scale bars represent 10µm. Data from 2 trials, using 1-3 mice each.

Quantitative information shows us that the 2930cm^{-1}/2850cm^{-1} and 3010cm^{-1}/2850cm^{-1} peak ratio values of LDs 1 and 2 within 'Blastocyst 2' was lower than that of OA, showing a more saturated FA composition, whereas, those of LD 3 were higher, and characteristic of the poly-unsaturated LDs previously seen, confirming this variability of LDs within the same embryo (Table 5.).

Vibrational Peak Ratio	**Pure OA Raman**	**Pure PA Raman**	**2Cell Embryo LDs (n=1)**	**Morula Embryo LDs (n=1)**	**Blastocyst Embryo 2 LDs 1 & 2 (n=2)**	**Blastocyst Embryo 2 LD 3 (n=2)**
2930cm^{-1}/2850cm^{-1} (ϕ/*)	**0.91**	**0.53**	**1.16** ±0.11	**1.18** ±0.05	**0.82** ±0.15	**1.32** ±0.11
3010cm^{-1}/2850cm^{-1} (ψ/*)	**0.22**	**0.03**	**0.45** ±0.04	**0.35** ±0.05	**0.12** ±0.05	**0.30** ±0.04

Table 5. Amplitude Ratios from the Vibrational Raman-like Spectra Im(χ) of Lipid Droplets in GV and MII Mouse Eggs, and 2Cell, Morula and Blastocyst Stage Mouse Embryos, Against Pure Oleic and Palmitic Acid Raman Spectra

The ratio between peaks at ~2930 cm^{-1} (φ- corresponding to CH_3 and asymmetric CH_2 stretch vibrations) and ~2850 cm^{-1} (*- corresponding to the symmetric CH_2 stretch) can be used as a measure of chain disorder and is expected to be higher in polyunsaturated fatty acids. The ratio between peaks at ~3010 cm^{-1} (Ψ- corresponding to the =CH stretch) and ~2850 cm^{-1} can be used as a measure of unsaturation, thus is expected to be near zero in saturated fatty acids. 2Cell and morula-stage embryos appear to show values reflecting poly-unsaturated fatty acids, whereas, the variable LDs in blastocyst embryos are shown to have differing characteristics, some of a poly-unsaturated nature, and some showing line-shapes that are saturated fatty acid-like.

5.5. Discussion

These data show that hyperspectral imaging using CARS microscopy can be used to provide information on and distinguish differences in the chemical composition of LDs within living oocytes and early embryos, specifically with regards to their degree of saturation. LDs in the normal mouse oocyte and egg stages, along with the early preimplantation embryo stages, were observed to be composed of a high proportion of poly-unsaturated FAs, and are quite homogeneous in composition across different LDs in the same cell. This was also shown to be true of bovine MII eggs, but is inconsistent with the previous reports that the most common fatty acids stored as TAGs in LDs of eggs of multiple species are saturated palmitic (16:0) and stearic (18:0) acids, and mono-unsaturated oleic acid (18:1) (McEvoy *et al.* 2000; Ferreira *et al.* 2010). Conversely, the variably large LDs found in blastocyst stage mouse embryos appear to be more heterogeneous, some displaying more saturated-like FA spectra. Quantitative interpretation of these results using ratios of the 2930cm^{-1} (CH_3 and asymmetric CH_2) peak relative to the 2850cm^{-1} band (CH_2) to show the level of chain disorder- as associated with unsaturated FAs- and the 3010cm^{-1} peak (=CH) relative to the 2850cm^{-1} peak as a measure of the extent of unsaturation, also demonstrates this observation.

Hyperspectral CARS has the potential to be an interesting analytical or diagnostic tool, as previous research has shown the lipid composition of eggs and embryos themselves, as well as their culture environment, have a profound effect on their developmental potential. With knowledge of the LD content of eggs and embryos under 'normal' conditions, the LD composition under abnormal or detrimental conditions can be investigated.

The environment in which a developing oocyte or embryo exists, has a significant influence over their lipid content, as well as their quality and competence. It has been previously shown that exposure of oocytes to excess FAs, both *in vivo* and *in vitro* affects subsequent embryo development after fertilization. van Hoeck *et al.* 2011 reported that elevated free fatty acids (FFAs) during maturation in culture lead to serious blastocyst defects and reduced their quality, and oocytes from women with higher concentrations of follicular fluid and serum FFAs are of poor morphology

(Jungheim *et al.* 2011b). These conditions are seen in women suffering from obesity, or who consume a high fat diet, and are associated with a reduction in successful fertility, despite efforts of the ovary to buffer against plasma fluctuations in FFAs (Fouladi-Nashta *et al.* 2009). Although the effects of obesity on oocyte, embryo and foetal development (outlined in section 5.1.) are likely to be multifactorial in affecting fertility, it has been shown that excess fatty acids undergo oxidation and produce cytotoxic ROS that are harmful to other organelles such as mitochondria (Wu *et al.* 2010, 2012). This may explain mitochondrial and spindle abnormalities also seen with obesity (Turner and Robker, 2014; Luzzo *et al.* 2012). However, it has been shown that not just excess fat is detrimental to blastocyst development, but underfeeding and lower body weight also presents reduced success rates and increased apoptosis (Grazul-Bilska *et al.* 2012; Kubandova et al 2014). It would be of interest to assess how the FA content of oocytes and embryos changes with exposure to different environmental factors such as obesity, a high fat diet, or underfeeding, in order to correlate LD composition with situations where known detrimental effects affect developmental potential. Hyperspectral CARS analysis would be a vital tool in improving knowledge and understanding of such cases.

Many biomarkers exist in follicular fluid that may be used as indicators of oocyte or embryo potential, however, the type of FA found in follicular fluid has also been shown to be predictive of IVF success rates (Aardema *et al.* 2011; Shaaker *et al.* 2012; O'Gorman *et al.* 2013). This suggests that in addition to the amount of lipid an oocyte is exposed to, the type of lipid LDs within an oocyte are composed of, or are exposed to will also influence its viability. Follicular fluid with higher concentrations of saturated FAs, likely to be taken up into the developing oocyte, is associated with poor embryonic development (O'Gorman *et al.* 2013). Whereas, unsaturated fatty acids are seen to improve fertility when included in the diet (Hammiche *et al.* 2011), and it was found that human embryos with higher concentrations of unsaturated FAs are more likely to develop beyond the 4Cell stage (Haggarty *et al.* 2006). This is potentially due to the fact that esterification of saturated fatty acids into TAGs is less efficient than that of mono-unsaturated fatty acids, meaning the FFAs become lipotoxic (Nolan and Larter 2009). Unlike previous studies, hyperspectral CARS imaging allows non-invasive assessment of the known predictors of cell quality, with regards to their LD content. Although no viability

tests were performed in conjunction with hyperspectral imaging, the scans were very fast (0.1µs per pixel, ~10seconds per image), over a small area (10µm x 100µm) of the egg and are highly unlikely to cause harm.

Positive or negative effects of lipids also tend to depend on the particular FAs present. Palmitic acid has been shown to have detrimental effects to the developing egg or embryo, leading to birth defects or embryonic arrest (Jungheim *et al.* 2011a; Nonogaki *et al.* 1994). This embryonic arrest cannot be rescued by the addition of antioxidants, suggesting lipid peroxidation is not the cause of PA-induced damage (Nonogaki *et al.* 1994). However, oleic acid has been found to have positive effects on eggs and embryos, promoting the formation of TAGs and their storage in LDs (Shaaker *et al.* 2012; Das *et al.* 2010; Aardema *et al.* 2011). OA has even been found to reverse the negative effects of palmitic acid and other saturated FAs (van Hoeck *et al.* 2011; Shaaker *et al.* 2012).

Here, the reports that the fatty acid composition of LDs in eggs reflects that of their culture environment are supported, and it is also shown that the lipid content of LDs can be changed if oocytes are exposed to saturated or unsaturated FAs. Eggs were matured in differing concentrations of OA and PA in order to see how the lipid profile of LDs changed in response to changing environmental fatty acid concentrations. The concentration range used were reflective of previously demonstrated effects upon embryo viability (Aardema *et al.* 2011; Jungheim et al 2011), and PA concentrations likely to be present in the follicular fluid of women over moderate bodyweight (Wu *et al.* 2012). When supplemented with a particular FA, the chemical composition of LDs resembled that of the FA supplements, providing information that promises to improve the understanding of the respective positive and negative effects of OA and PA. There is a lack of concordance between pure lipid spectra and those of fatty acid-supplemented LDs, due to the mixture of FAs still composing each droplet. It is highly unlikely that the FAs comprising the LDs will not become purely replaced by the supplement lipid. The spectra of pure PA shown is in its solid phase (melting point at 60º C) with the peak at 2880/cm in the Raman spectrum being a signature of such ordered state. The supplemented PA is likely to be in liquid phase (disordered), and the spectra from PA-supplemented eggs reflect this.

Due to the observations made, methods described here could be used in future studies of embryo quality. Previous knowledge of the content of embryos with successful embryonic development, and the characteristics of eggs or embryos likely to have low developmental competence, provides information as to allow the hyperspectral assessment of the most promising embryo in assisted reproductive technologies. These findings also present a promising notion that as well as the potential use of hyperspectral CARS for lipid analysis of eggs and embryos from women undergoing ART, the culture media used in such techniques can be manipulated on an individual basis in order to improve fertility outcomes. Polyunsaturated FAs (PUFAs) are thought to improve embryo development rates, especially those with a C=C bond in the n-6 (omega-6) position i.e. 6-carbons from the methyl end (Jungheim et al. 2013; Zachut *et al.* 2010; Hammiche *et al.* 2011). It may be possible that including n-6 PUFAs such as arachadonic acid (20:4, n-6) in IVF embryo culture media may improve the success rates of embryos previously exposed to high concentrations of saturated FAs e.g. from overweight or obese women. This would result in a shift in the average Raman peak ratios, allowing further indication for selection of the best quality embryos.

In this chapter, hyperspectral CARS imaging enabled investigation into the chemical composition of LDs in mammalian oocytes, eggs and embryos. Calculation of the ratios of saturated to unsaturated FAs showed that the majority of LDs appeared to be composed of poly-unsaturated FAs, while it was found that this LD content could be influenced by the composition of the surrounding media. These results provide further support for the use of CARS as an informative method of assessment of egg or embryo metabolic level.

Chapter 6. Comparison of CARS imaging and use of conventional lipid dyes

6.1. Introduction

Thus far, it has been established that CARS can be used to identify lipid droplets and assess their content in a non-invasive manner, compatible with continued early development. In order to compare CARS specificity to that of conventionally-used lipid dyes, a correlative study involving simultaneous CARS and TPF measurements was performed to identify if CARS is a superior technique and how it could be used instead of these stains. The broadband spectrum of the fs laser pulses used in the CARS set-up allows for TPF and SHG imaging simultaneously with CARS: the beam centred around 940nm can be used for two-photon absorption of fluorophores such as GFP or Alexa488 which create TPF emission at ~510nm. It can also be used for SHG emission at ~470nm. TPF and SHG are detectable separately to each other and CARS (see Chapter 2, section 2.8.).

Lipid biology is commonly studied using fluorescence microscopy. A large number of lipophilic dyes are available, which are able to stain lipids within droplets and lipid membranes, allowing visualisation of structures at high magnifications and high resolution e.g. confocal microscopy. Nile red is a red-emitting lipophilic dye that has been widely used to study LDs in oocytes and somatic cells across multiple species. Previous studies have used Nile red to quantify LD number and total lipid content of cells, and it has also been used in co-localisation studies with mitochondria (Genicot *et al.* 2005; Romek *et al.* 2011; Ghanem *et al.* 2014; Leroy *et al.* 2005; Sturmey *et al.* 2006). BODIPY 493/503 and LipidTOX are green-emitting neutral lipid stains commonly used to investigate lipid droplet biology. These are regarded as high-quality lipid dyes, with high photo-stability and absorption (ThermoFisher Scientific), and have, again, been used to demonstrate LD biology in multiple species. Uses such as LD quantification, measurement of LD size, distribution and

relative intensity have been described (Aardema *et al.* 2011; Sutton-McDowell *et al.* 2012; Wu *et al.* 2010; Yang *et al.* 2012; del Collado *et al.* 2015; Watanabe *et al.* 2010).

An obvious drawback of using lipid stains is the fact that the use of dyes is invasive. Multiple factors mean that fluorescent dyes are not useful for diagnostic assessments as required in the reproductive field. Introduction of molecules to cells is always a risk, due to the unknown disruption they may cause to cellular processes and development. The excitation light used for fluorescence often induces photo-toxicity, which is unacceptable in such sensitive cells as eggs or embryos, and dyes are often unspecific, staining more than is desired for imaging. Fluorescent dyes also often undergo photo-bleaching over time, making them less useful for repeated measurements over long periods of time. Furthermore, Nile red, BODIPY and LipidTOX dyes are best used on fixed cells, despite the fact that BODIPY 493/503 is marketed as able to stain live cells for imaging.

It is also found that Nile red and BODIPY are not specific in their staining of LDs, and their staining capacity differs from cell to cell (O'Rourke *et al.* 2009; Gocze and Freeman, 1994; Ohsaki *et al.* 2010). In comparison with CARS microscopy, it has been shown by several groups that these lipid dyes do not specifically stain LDs, for example in *C. elegans* (Hellerer *et al.* 2007; Klapper *et al.* 2011; Le *et al.* 2010; Wang *et al.* 2011b; Yen *et al.* 2010). CARS, on the contrary, is able to reliably identify lipids in biological tissues in a chemically-specific and label-free manner. The high signal obtained from lipids densely packed in 3D LDs allows for the specific investigation of these vesicles. Thus, CARS is an ideal method of microscopy for the desired measurements in reproductive specimens. Furthermore, fluorescent lipid dyes are notoriously difficult to quantify, due to differing intensity levels and staining patterns, making it difficult to come to valid conclusions about the amount of lipid or total number of droplets observed. CARS is potentially superior in that it is a quantifiable method that is chemically specific for lipids.

In order to examine how efficient BODIPY 493/503 and LipidTOX are in their staining of LDs in mouse eggs, TPF of fixed oocytes and eggs fluorescently-labelled with these dyes was used alongside simultaneous CARS measurements. BODIPY 493/503 and LipidTOX were chosen due to their green-emitting properties, which

are compatible with both the TPF incident light in the microscope set-up, and the ability to measure the fluorescence signal separately to the CARS signal being simultaneously obtained. The SHG detection channel was used to measure any autofluorescence from the sample, as this emission is blue-shifted compared to the green emission of the lipid dyes (and no endogenous SHG is expected in these samples). In addition, MII eggs stained with Nile red were imaged on a confocal microscope, in order to compare the staining pattern with LDs seen with CARS imaging. Simultaneous CARS measurements were not possible due to the red-emission of Nile red.

For those measurements that were taken simultaneously, correlation coefficients were calculated by assessing co-localisation of signals in the two channels (CARS and TPF) in order to quantitatively investigate the effectiveness of the lipid stains against the known-to-be specific CARS signal. Correlation assessments were enabled using the 'Correlation Threshold' Image J plug-in. Co-ordinate correlation of pixels above a certain intensity threshold is calculated to give a Pearson's correlation coefficient (see Chapter 2, section 2.9.5.)- a number between 0 and 1, which demonstrates the degree of significant correlation between CARS and TPF images. It is generally accepted that there is a correlation between channels if the Pearson's coefficient is >0.5, but this correlation is not significant unless the coefficient is >0.95 (95% statistical confidence limit). Through this method, scatter plots are generated to show the linear relationship between pixels in corresponding CARS (x axis) and TPF (y axis) images, giving a more visual idea of the high or low co-localisation of CARS (lipid droplets) and TPF (lipid dyes) signals.

It is hypothesised that CARS will present as a superior method of imaging lipids, as it is label-free and chemically-specific, and can be used on live cells. Fluorescent lipid stains are often unspecific, and are incompatible with continued cell culture and viability, while lacking the quantitative capabilities promised by CARS imaging.

6.2. Qualitative use of dyes vs. CARS

Both LipidTOX and BODIPY 493/503 dyes were used to stain GV and MII eggs. Fig.6.2.1. (A-D) shows maximum intensity DIC projections taken of eggs prior to CARS imaging.

Simultaneous CARS and TPF imaging revealed that when incubated as per manufacturer's instructions (see Chapter 2, section 2.3.5.), the dyes stained more structures than solely lipid droplets within the egg cytoplasm, at both developmental stages. This is seen when comparing TPF (Fig.6.2.1. (I-L)) images and CARS images (Fig.6.2.1. (E-H)), demonstrated clearly when overlaying TPF images with false-coloured CARS images (Fig.6.2.1. (M-P)). Many intracellular vesicles that are not lipid droplets were stained, shown in TPF images but not in CARS images. Whereas, in some cases LDs revealed by CARS were not stained at all and were missing from the TPF images, suggesting a low specificity and potentially low incorporation.

It appears that the BODIPY 493/503 stain is more specific to LDs than LipidTOX, however, it still stains other structures (see green staining in Fig. 6.2.1. (M-P)). BODIPY 493/503 also gives a stronger signal, seemingly the better of the two dyes (see ph.e^-/sec Fig.6.2.1.). Using the SHG channel, an emission is detectable in a spectral range blue-shifted from the green emission band of the lipid dyes, allowing simultaneous collection via a third PMT. Since these samples are unlikely to have endogenous SHG (known to originate from structures such as collagen fibres), SHG images effectively showed autofluorescence from multiple cellular organelles (Fig.6.2.2. (E)). Although producing a signal ~ 15 times lower than the fluorescent dye emission, this demonstrates that that these fluorescence imaging techniques are not free from background.

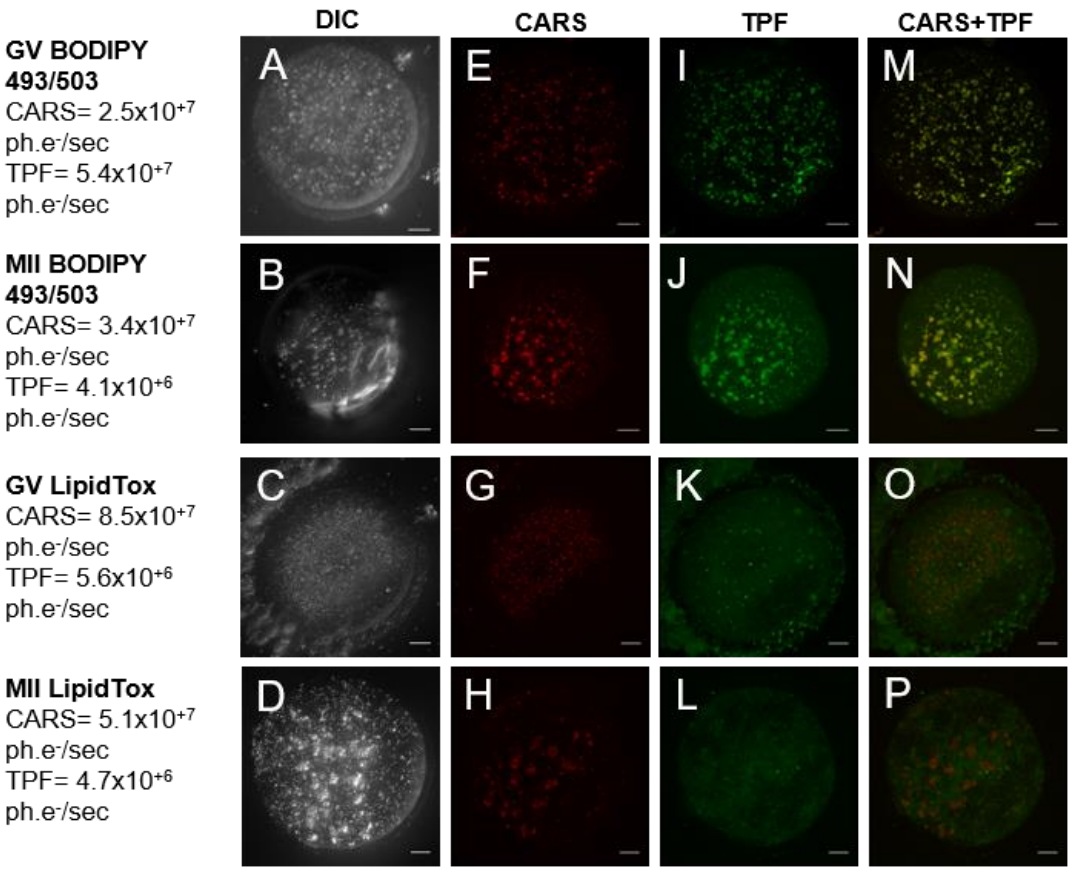

Fig.6.2.1. Two-Photon Fluorescence of BODIPY 493/503 and LipidTOX Staining of Lipid Droplets against CARS Imaging in GV and MII Stage Mouse Eggs

(A-D) Single plane (approximately equatorial DIC images using a 1.27 NA water objective and a 1.4 NA oil condenser, (E-H) false-coloured CARS images at wavenumber 2850cm^{-1} and (I-L) TPF xy images, accompanied by (M-P) false-coloured overlays, of fixed GV and MII eggs stained with BODIPY (n=23 and 30, respectively) or LipidTox green neutral lipid stain (n=7 and 20, respectively). All images are maximum intensity projections of stacks with 0.5µm z-steps. 0.1x0.1µm pixel size; 0.01ms pixel dwell time; ~12mW (~9mW) Pump (Stokes) power at the sample. CARS and TPF signal intensities are given in photoelectrons per second (ph.e$^-$/sec) and scale bars represent 10µm. Data from ≥4 trials, using 1-3 mice each.

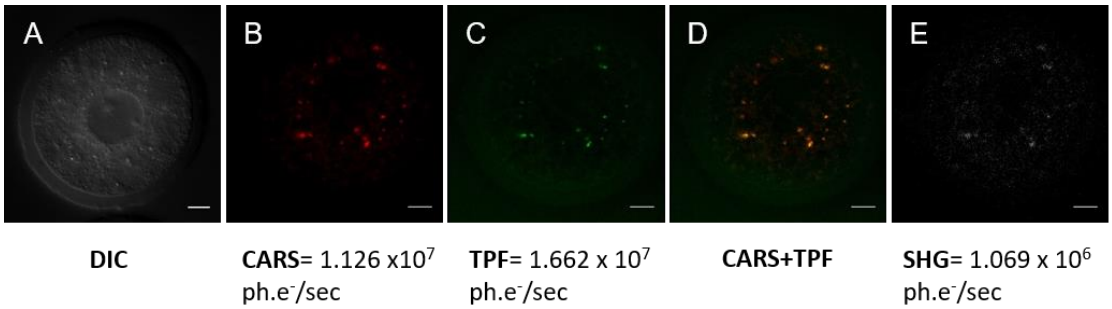

Fig.6.2.2. Two-Photon Fluorescence and Second Harmonic Generation Microscopy of BODIPY 493/503 Staining of Lipid Droplets against CARS Imaging in GV Stage Mouse Eggs

(A) Single z-plane DIC, (B) false-coloured CARS *xy* image at wavenumber 2850cm^{-1}; (C) TPF *xy* image; (D) false-coloured overlay of CARS and TPF images, and (E) SHG *xy* image of a fixed GV oocyte stained with BODIPY (n=10). 0.1x0.1µm pixel size; 0.01ms pixel dwell time; ~12mW (~9mW) Pump (Stokes) power at the sample. CARS, TPF and SHG signal intensities are given in photoelectrons per second (ph.e$^-$/sec) and scale bars represent 10µm. Data is from 1 trial, using 2 mice.

Nile red was also investigated, as it is an example of a commonly-used lipid stain. Due to its red emission, measurements were taken on a confocal microscope, and CARS images were not taken simultaneously (Fig.6.2.3.). It is apparent from confocal images that Nile red stains LDs, but it is not obvious if smaller droplets or those in aggregates are resolvable, and there is no way of quantifying the amount or type of lipids present. Due to the impossibility of comparing Nile red to CARS imaging in our set-up, there is also no way of determining how well Nile red is capable of labelling LDs, and how specific it is to these organelles only.

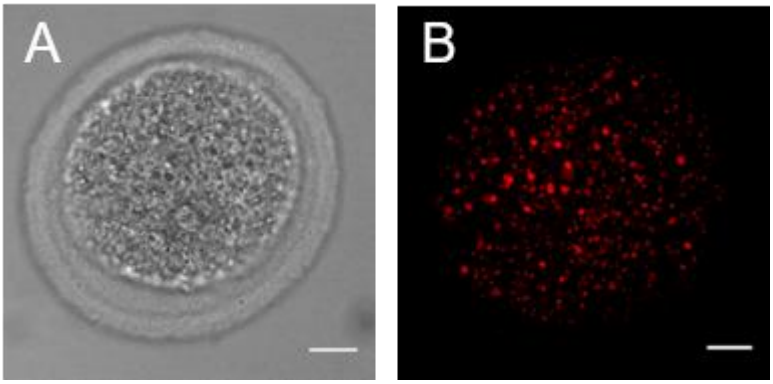

Fig.6.2.3. Confocal Fluorescence of Nile Red Staining of Lipid Droplets in MII Stage Mouse Eggs

(A) Single z-plane DIC and (B) false-coloured maximum intensity projection of confocal z-stack images of a fixed MII egg, LDs stained with Nile Red (n=9). 63x oil immersion objective with 2x optical zoom; 39% laser power, 488nm ex. 500-580nm em.; 0.6µm step size over ~60µm, scanned at 400Hz (512x512 pixel resolution). Scale bars represent 10µm. Data is from 2 trials, using 2-3 mice for each.

6.3. Quantitative use of dyes vs. CARS

In order to achieve a more quantitative analysis of the specificity of these stains, Image J was used to perform correlation studies of the signal received from CARS compared with the TPF emission from the dye-stained lipids. The extent of signal co-localisation was determined using Pearson's correlation coefficient analysis, where values of >0.5 indicate recognisable co-localisation, and coefficients of >0.95 demonstrate significant co-localisation.

An average Pearson's correlation coefficient of 0.132 was found with LipidTOX staining of GV oocytes, and 0.102 in MII eggs, indicating no real co-localisation between CARS and TPF images of this dye. Alternatively, using BODIPY 493/503 showed moderate co-localisation of CARS and TPF images with an average correlation coefficient of 0.792 for GV oocytes and 0.547 in MII eggs. Correlation scatter plots are provided as an output of this co-localisation analysis, in order to visually present the quantitative data. These show the extent of a linear relationship

between the pixels of CARS (x-axis) and TPF (y-axis) images (Fig.6.3.1.). LipidTOX demonstrates very little correlation in both GV and MII stages (Fig.6.3.1. (C) and (D)). BODIPY 493/503 shows more of a linear relationship between image pixels, clearly more so in the GV stage (Fig.6.3.1. (A) and (B)).

Due to the disparity between imaging systems and methods, it would not be possible to correlate CARS and Nile Red images.

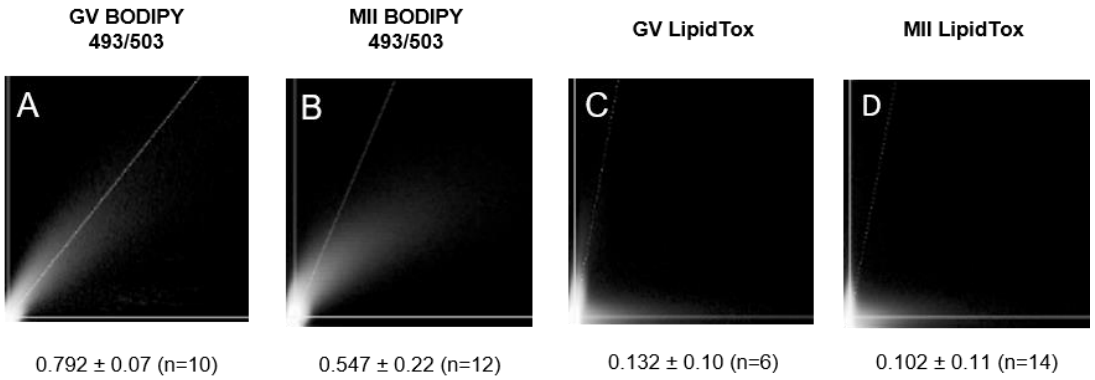

Fig.6.3.1. Scatter plots of Co-localisation of Two-Photon Fluorescence Measurements of Conventional Lipid Dyes with CARS Microscopy Measurements

(A-D) Scatter plots of pixel-coordinate correlation between CARS (x-axis) and TPF images (y-axis), and the mean Pearson's correlation coefficients of all investigated eggs, to show the degree of reliability of these dyes. A co-localisation is apparent with a Pearson's coefficient of >0.5, but is only considered significant if >0.95 as in accordance with normal 95% confidence limits. Data from ≥4 trials, using 1-3 mice each.

6.4. Discussion

Many fluorescent lipid dyes are available for investigation of lipid droplet biology in multiple cell types. Several have previously been used to examine LDs in mammalian eggs, in an attempt to understand LD distribution and to quantify the lipid content of such cells. These include neutral lipid dyes such as BODIPY 493/503, LipidTOX and Nile red (Yang *et al.* 2012; del Collado *et al.* 2015; Genicot *et al.* 2005). Other studies have made use of non-fluorescent lipid dyes such as methylene blue, Sudan III or Sudan black in order to measure the amount and size of LDs (Romek *et al.* 2009; Hishinuma *et al.* 1985; Abe *et al.* 2002).

These dyes are commonly used to assess the large LDs seen in porcine and bovine oocytes (Sturmey *et al.* 2006; Leroy *et al.* 2005, Romek *et al.* 2011; Aardema *et al.* 2011), but few efforts have been made to quantify mouse or human oocyte lipid content in this way.

Staining with these dyes is incompatible with oocyte maturation or embryo development, even those which do not require fixation. Addition of stains to eggs or embryos is invasive and likely to hinder development, due to the unpredictable effect fluorophores may have on the cellular environment. Fluorescent labels are often bigger than the molecules they target, introducing unknown complications to cellular process (Min *et al.* 2011), and staining is usually carried out on fixed samples, preventing the ability to follow subsequent development. Fluorescent dyes also come with the risks of photo-damage, which is detrimental to continued cell growth and incompatible with continued viability. In *in vivo* medical applications, it is better not to use fluorophores, and to seek a label-free method of investigation.

In addition to these shortcomings of the use of lipophilic dyes, and despite the sophistication of modern fluorescence applications, lipid staining raises critical concerns about specificity and thus their reliability. In the current study, the incubations were performed as described in manufacturer's instructions and in previous studies, with consistent concentrations and incubation times across all experiments. However, inconsistent staining patterns, and variability in the brightness of staining across the same and different cell populations is seen. Klapper *et al.* (2011) describe a method of staining LDs in *C. elegans* with BODIPY 493/503, using a shorter incubation time, and giving more efficient staining.

However, dyes often present these problems due to the unpredictability of the efficiency of their incorporation into cells and organelles (Wang *et al.* 2011b). For example, the extent of BODIPY staining has been shown to depend on the size of the LDs present (Harris *et al.* 2013), and it is unclear how well these dyes are able to penetrate the protective zona pellucida of egg cells.

BODIPY and Nile red have previously been shown to lack specificity. O'Rourke *et al.* (2009) describe how BODIPY and Nile red stain lysosome-like vesicles rather than LDs, and the staining is often inconsistent. Nile red has been found to display more variability than BODIPY (Gocze and Freeman, 1994). Furthermore, it has been reported that Nile red and BODIPY stains do not correlate with signals obtained from chemically-specific methods such as CARS and SRS in *C. elegans* (Wang *et al.* 2011b; Yen *et al.* 2010). It has also been shown that BODIPY 493/503 may produce red emission under certain conditions, so care must be taken that no erroneous results are recorded (Ohsaki *et al.* 2010).

Nile red has proven as useful tool for the investigation of LDs, previously used alongside MitoTracker green in order to demonstrate LD and mitochondrial co-localisation through the measurement of fluorescent resonance energy transfer (FRET) (Sturmey *et al.* 2006). However, the specificity of Nile red is uncertain, as it has been shown to stain other cellular structures such as the endoplasmic reticulum (ER) (Hellerer *et al.* 2007; Klapper *et al.* 2011; Wang *et al.* 2011b; Yen *et al.* 2010). Other methods of co-localisation investigation, such as using CARS may be beneficial.

Images from the SHG detection channel show an autofluorescence background signal, which is an additional pitfall of fluorescence staining techniques, further demonstrating that the dyes are not selective enough to be reliably used to quantify lipid content of mouse oocytes.

Co-localisation analysis was performed by calculating the Pearson's correlation coefficient for pixels of chemically-specific CARS images with TPF images of green lipid dye-emission. Considered to be a good measure of the overlap of signals obtained from each imaging method, this analysis clearly demonstrated that although BODIPY 493/503 stains a number of vesicles that appear to coincide with LDs identified by CARS imaging, there was only a moderate correlation. LipidTOX also

showed only a very weak correlation of CARS and TPF signals in both GV oocytes and MII eggs, despite being a widely popular LD probe. The scatter plots also output give more of an idea of the extent of a linear relationship between the two signals. It was interesting to find that no linearity existed between LipidTOX, and CARS signals, but more of a correlation was found in GV oocytes stained with BODIPY 493/503. Although Watanabe *et al.* (2010) describe a high degree of co-localisation between the THG signal and LipidTOX staining of LDs in mouse oocytes, THG is not a chemically-specific imaging method and overlay images obtained appear to be inconsistent with correlation values calculated.

It was not possible to simultaneously measure CARS and TPF with Nile red, as the excitation and emission spectrum of this red-emitting dye is not compatible with the current microscope set-up. Instead, confocal fluorescence images were taken in order to visually compare these with CARS images. Nile red appeared to effectively stain multiple cellular vesicles, however, it is impossible to correlate these with CARS and provide chemical identification of these labelled vesicles. Previous studies correlating Nile red staining with CARS in *C. elegans* demonstrate its lack of specificity, and its tendency to also stain the ER (Hellerer *et al.* 2007; Klapper *et al.* 2011; Wang *et al.* 2011b; Yen *et al.* 2010).

Unlike CARS, fluorescence microscopy is very limited in its ability to provide quantitative information on the lipid content of cells (Yen *et al,* 2010). Due to the demonstrated lack in specificity of fluorescent dyes, any quantitative measurements are unreliable. Many studies have used dyes such as BODIPY and LipidTOX to count the number of LDs in eggs of multiple species, and to measure their diameter (Aardema *et al.* 2011; del Collado *et al.* 2015). However, the current study suggests it is not clear that the stained vesicles included in the calculations are in fact LDs, and the absolute count obtained may not be accurate.

Dyes have also been extensively used in an attempt to quantify the lipid content of oocytes. However, fluorescence has a shortcoming in the fact that, unlike CARS microscopy, there is a lack of a linear relationship between the emitted signal and the actual quantity of lipid present (Wang *et al.* 2011b). Nile red has been used to quantify the lipid content in porcine and bovine oocytes (Romek et al 2011; Ghanem *et al.* 2014; Leroy *et al* .2005; Kim *et al.* 2012). Genicot *et al.* 2005 used Nile red to

quantify lipid content in multiple species relative to one another. While providing an interesting insight into the levels of lipid contained in different species with varying LD distribution, no absolute quantitative or specific chemical information is provided. It is also unclear how efficiently Nile red stains egg cells of different species, meaning results could be artefactual.

Furthermore, these studies all appear to measure the relative fluorescence intensity to compare populations of eggs, which may be affected by unpredictable staining efficiency, photo-bleaching or even increased fluorescence intensity over time. This is particularly crucial in experiments attempting to measure the amount of lipid under differing culture conditions. BODIPY 493/503 and LipidTOX have been previously used to demonstrate lipid accumulation with increased fluorescence intensity in oocytes supplemented with high fat concentrations (Sutton McDowell *et al.* 2012; Wu *et al.* 2010; Yang *et al.* 2012; del Collado *et al.* 2015). Whereas, Nile red has been used to demonstrate a decrease in fluorescence intensity with increased metabolism (Romek et al 2011; Ghanem *et al.* 2014). It is not clear whether the intensity of the staining performed by these dyes changes over time, with ongoing cell processes, or under microscope conditions.

Non-fluorescent lipid dyes such as methylene blue, Sudan III, and Sudan black have also been used to quantify LDs across multiple species (Romek *et al.* 2009; Hishinuma *et al.* 1985; Abe *et al.* 2002), but fixation methods associated with these may cause artificial fusion of LDs (Fukumoto and Fujimoto, 2002), and they often do not achieve results consistent with more reliable (albeit destructive) methods of lipid quantification previously employed (McEvoy *et al.* 2000).

Overall, these data exemplify the limitations of LD staining reliability and specificity, and the advantage of label-free CARS imaging as a highly sensitive, reliable and quantitative method for measuring LDs in live mammalian oocytes, eggs and early embryos.

Chapter 7. Dynamic Monitoring of Lipid Metabolism in the Mouse Egg

7.1. Introduction

In previous chapters, the characterisation of LDs in mouse eggs and embryos has been allowed by use of CARS microscopy. Another aim of this study is to examine how lipid metabolism changes throughout development, and how this may be influenced by other factors that may affect developmental potential.

The central metabolism of mammalian eggs and early preimplantation embryos relies solely on their extensive (>100,000) mitochondria, and the oxidation of various substrates for ATP production (Acton *et al.* 2004). The mitochondria of mammalian cells are recognised to be homogenously dispersed throughout the cytoplasm. However, it has been previously shown that at murine immature oocyte stages, mitochondria are clustered around the GV and it is at GVBD on initiation of maturation that they disperse and become more widely distributed (Yu *et al.* 2010; Sun *et al.* 2001; Nagai *et al.* 2006; Bavister and Squirrell, 2000). This redistribution of mitochondria is thought to be orchestrated by microfilaments, and is accompanied by 'bursts' of ATP (Yu *et al.* 2010). Sun *et al.* 2001 also find that mitochondria cluster around forming pronuclei after fertilisation, and at cleavage furrows as cell division continues. Divergence from this normal distribution of mitochondria is associated with lower developmental competence (Nagai *et al.* 2006; Wakai *et al.* 2014). It is an ambiguous phenomenon that lipid droplets and mitochondria colocalise within the egg cytoplasm. Sturmey *et al.* (2006) used FRET measurements to demonstrate that mitochondria do in fact associate with LDs in porcine oocytes. It is logical that LDs and mitochondria colocalise in order for easy FA transfer, however, as previously demonstrated in Chapter 6, lipid dyes aren't wholly reliable due to their lack of specificity and it is not known whether LDs co-localise with mitochondria in mouse oocytes, which are less dependent upon lipid oxidation.

Substrates metabolised by egg or embryo mitochondria vary depending on the species. For example, porcine and bovine oocytes contain large, prominent LDs and are thought to primarily metabolise fatty acids for energy. Whereas, pyruvate provided by surrounding follicular fluid, cumulus cells or culture media is understood to be the primary source of energy in mouse and human eggs, where LDs are smaller and less visible. Although lipid metabolism is shown to occur, and be essential for egg and embryo development, the contribution of β-oxidation to resting metabolism in the mouse egg is thus far unknown (Dunning *et al.* 2010). A number of techniques can be used to confirm the presence and importance of pyruvate and fatty acid oxidation as a source of energy. Measurement of pyruvate, amino acids or O_2 consumption from *in vitro* culture media have previously been used to measure the level of metabolism occurring in egg and preimplantation embryos (Harris *et al.* 2009; Houghton, 2006; Sturmey and Leese, 2003).

The metabolism of substrates occurring in the mitochondria establishes what is known as the redox state of the cell. The chemical reactions occurring as part of the TCA cycle and oxidative phosphorylation transfer electrons to TCA cycle cofactors FAD^{++} and NAD^{+} reducing them to $FADH_2$ and NADH, respectively. The redox potential is dependent on the amount of substrate available and extent of metabolism occurring, and can be determined by the ratios of $NADH/NAD^{+}$ or $FADH_2/FAD^{++}$ within the cell. Redox state can be used as a measure of the developmental competence of an egg or embryo, as it gives a measure of the amount of metabolism occurring. Reduced NADH and oxidised FAD^{++} display autofluorescence, with blue and green emission, respectively. Allowing fluorescence imaging of mitochondria in both oxidised and reduced states, it is possible to exploit this autofluorescence in order to measure the effects of metabolism of pyruvate and other substrates on the redox state of mouse oocyte mitochondria (Dumollard *et al.* 2007). NADH and $FADH_2$ transfer electrons from the TCA cycle to the ETC, a series of mitochondrial membrane-bound proteins which pump protons across the IMM to create an electrochemical gradient, responsible for the MMP and the generation of ATP (Wilding *et al.* 2009; Dumollard *et al.* 2009). TMRE is a positively-charged dye easily sequestered into mitochondria due to their negative MMP, and once sequestered its fluorescence is quenched. The level of TMRE fluorescence can be

measured to investigate changes in MMP under certain conditions (Perry *et* al. 2011). MMP can thus also be used to assess the redox state of cells, and their developmental competence (Van Blerkom *et al.* 2003).

ATP generation can also be used as a measure of the extent of mitochondrial activity within the egg. Due to the requirement for ATP to catalyse the action of luciferase upon luciferin, the level of ATP can be measured using luminescence imaging (Yu *et al.* 2010; Campbell and Swann, 2006). Simply insufficient ATP production can be detrimental to cellular and embryonic development if there is a limited availability of metabolic substrates. It is clear from previous research that mouse oocytes and embryos perform fatty acid oxidation throughout maturation and early development, and that this metabolism is crucial for development, quality and viability of eggs and embryos. For example, β-oxidation is stimulated by oocyte maturation in the mouse, and inhibition of fatty acid oxidation using drugs such as etomoxir, which specifically inhibits CPT-mediated transport of fatty acids into the mitochondria, prevents maturation of the oocyte and hinders development to blastocyst (Downs *et al.* 2009; Dunning *et al.* 2010). L-carnitine promotes fatty acid uptake into mitochondria via CPTs, and adding it to culture media has been found to improve the rate of oocyte maturation, and increase the rate of blastocyst development after fertilisation (Dunning and Robker, 2012; Dunning *et al*. 2010; 2011). Furthermore, mouse embryos in culture are found to benefit from the addition of BSA to culture media, providing further fatty acids available for metabolism (Downs *et al.* 2009).

Cinnamate is a specific inhibitor of monocarboxylate transport, including of pyruvate and lactate. Inhibiting pyruvate uptake into the mitochondria allows observation of the biochemical effects associated with this change in metabolic substrate availability. Rotenone inhibits electron transfer from Complex I to ubiquitin within the ETC, the effect of which would display any effects of inhibiting PDH activity. Starving mouse eggs of pyruvate affects the redox state, and ATP production, affecting developmental potential (Dumollard *et al.* 2007; 2008).

However, there are also negative effects of too much mitochondrial activity. Excess pyruvate and fatty acid metabolism lead to the production of ROS, which have detrimental effects to other organelles and cellular molecules. ATP production reaches a saturation point where no more ATP can be generated, leading to a back-up of TCA products and inefficient metabolism (Dumollard *et al.* 2009). Mice fed

with a high fat diet or bred to be genetically obese yield eggs that are of poor quality, have poor fertilisation rates, low rates of blastocyst development, developmental abnormalities and birth defects (Igosheva *et al.* 2010; (Jungheim *et al.* 2010). It is thought that many of these negative effects are repercussions of mitochondrial defects and altered mitochondrial activity (Turner and Robker 2014; Wu *et al*. 2010; Igosheva *et al.* 2010). It is clear from prior evidence that an intermediate level of mitochondrial activity is optimal for development. Thus, Leese (2002; 2007) proposes the 'quiet embryo' hypothesis: the quality of an egg or embryo is dependent on a low level of metabolic activity, reducing the risk of oxidative stress and apoptotic events.

As discussed in Chapter 5, the type of fatty acid taken up into the mitochondria is also found to have differing effects on the development of an egg or embryo. Mono-unsaturated OA and saturated PA are fatty acids commonly found in mammalian eggs and embryos (McEvoy *et al.* 2000). It appears that saturated fatty acids like PA have more of a detrimental effect on oocytes and embryos (Van Hoeck *et al.* 2011; 2013; Borradaille *et al.* 2006; Valckx *et al.* 2014). However, it has been shown that unsaturated fatty acids such as OA can have positive effects on development, promoting maturation, and can even reverse the negative effects caused by saturated examples (Aardema *et al.* 2011, 2013). This is thought to be due to the fact that oleic acid promotes the formation of TAGs and thus the recruitment of free fatty acids into LDs, or because mono-unsaturated fatty acids (MUFAs) are more efficiently esterified into TAGs than saturated FAs (Shaaker *et al.* 2012; Cnop *et al.* 2001; Nolan and Larter, 2009).

Also apparent under high PA concentrations is damage to the normal processes of the ER, known as ER stress (Das *et al.* 2010, 2008; Zhang *et al.* 2012; Gwiazda *et al.* 2009). The ER stress response, as induced by a high lipid environment is characterised by impaired ER function and loss of Ca^{2+} through IP_3 receptors on the ER membrane, disrupting the important Ca^{2+} homeostasis of the cell. This also leads to other pathways of impaired protein folding, and MMP disruption, leading to ROS production and ultimately apoptosis (Wu *et al.* 2015, 2012; Gwiazda *et al.* 2009; Rutkowski *et al.* 2006). How excess lipid causes ER stress is as yet unclear. At fertilisation, transient Ca^{2+} release from the ER into the cytoplasm means that Ca^{2+}

enters the mitochondrial matrix causing oscillatory increases in ATP (Campell and Swann, 2006). Sarco/endoplasmic Reticulum Ca^{2+} ATPase (SERCA) pumps in the ER membrane are responsible for pumping Ca^{2+} back into the ER Ca^{2+} store. It is likely that a large release of Ca^{2+} during the ER stress response results in too much Ca^{2+} entering the mitochondria, disrupting metabolic processes. Sutton-McDowall *et al.* (2016) found that FAD autofluorescence decreased with PA exposure, while Wu *et al.* (2012) describe a reduced MMP (less negative) in response to high concentrations of PA. Use of BAPTA to chelate Ca^{2+} in cells exposed to high concentrations of PA reduces cell death (Zhang *et al.* 2012), thus it is concluded that PA causes efflux of Ca^{2+} from the ER, likely due to activity at the SERCA pumps, preventing resorption of Ca^{2+} into the ER.

In this chapter, characterisation of the metabolism of lipids in mammalian eggs and embryos in comparison with pyruvate allows further understanding of the importance of fatty acid metabolism in these cells. It is hypothesised that a considerable amount of β-oxidation is occurring within the mouse egg, due to its importance in continued development. Meanwhile, mitochondrial and LD colocalisation is expected for β-oxidation to occur, and can be investigated using simultaneous CARS and TPF experiments. Assessment of redox state, MMP and ATP production alongside metabolic changes enables measurement of the contribution of this fatty acid metabolism to the mitochondrial output. It is expected that a reduction in substrate metabolism (i.e. inhibition of β-oxidation) will cause a reduction in mitochondrial productivity. Altered metabolism is also likely to contribute to ER stress, quantified by investigation into the effects of altering metabolism on Ca^{2+} from the ER.

Furthermore, CARS imaging allows visualisation of the effects of metabolism alteration on mammalian egg LDs, and gives further understanding of the natural changes that occur in LD distribution as seen in Chapter 3, suspected to reflect the amount of lipid metabolism occurring at each developmental stage.

7.2. Lipid Droplet and Mitochondrial Colocalisation

Simultaneous CARS and TPF imaging allows investigation into the spatial relationship between cytoplasmic LDs and mitochondria in the mouse egg. Mitochondria exhibit autofluorescence with excitation spectra that are suitable for the TPF beam in this CARS set-up. However, this autofluorescence is very weak, almost undetectable under the excitation and detection conditions of our experiments. Therefore, cRNA encoding for a mitochondrial-targeted GFP (MitoGFP) was injected into eggs, and TPF excitation allowed detection of the fluorescent marker, alongside CARS measurements of lipid content. Mitochondria targeted with MitoGFP demonstrated a distribution concurrent with previous explanations, in both GV and MII stages (Dumollard *et al.* 2006; Fig.7.2.1.). In TPF images, mitochondria of immature oocytes can be clearly seen surrounding the GV (C), but are more widespread in the mature egg (G). A small amount of bleed-through of the GFP fluorescence signal was found in the CARS detection channel, but the signal was approximately 1 order of magnitude lower than the CARS intensity given by LDs so did not prevent the ability to distinguish them (B and F). Image J was used to produce overlays of the TPF, and falsely coloured CARS channels, to give the best representation of how LDs and mitochondria are spatially located relative to each other (D and H). It does not appear in either developmental stage that the LDs are particularly arranged in the same distribution as the mitochondria, but this is not to say they are completely separate. Maximum intensity projections of the overlaid channels were made in an attempt to further investigate the colocalisation of organelles, but these gave no added insight due to the extensive amount of cytoplasmic space occupied by both LDs and mitochondria.

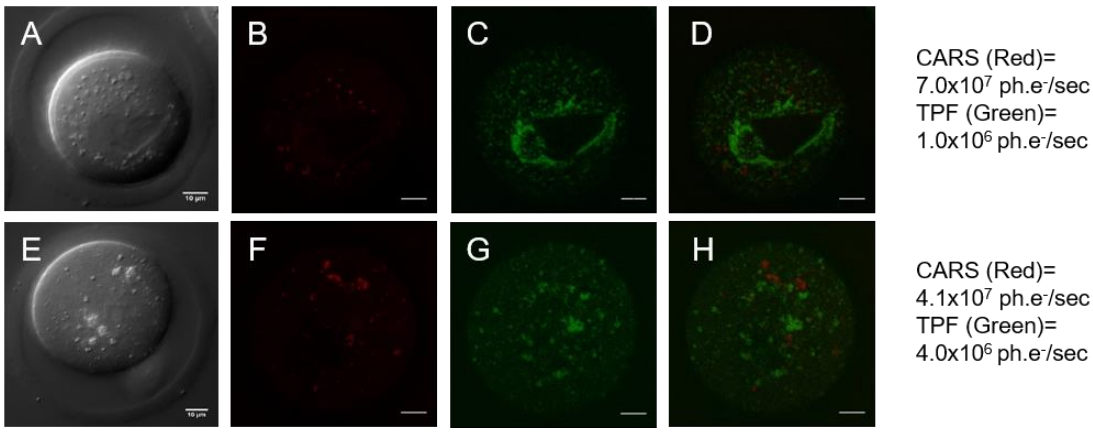

Fig.7.2.1. CARS of Lipid Droplets and Two-Photon Fluorescence of Mitochondria to Assess Colocalisation of Structures in GV and MII Stage Mouse Eggs

(A) and (E) Single plane (approximately equatorial DIC images using a 1.27 NA water objective and a 1.4 NA oil condenser, (B) and (F) false-coloured CARS images at wavenumber 2850cm^{-1}, (C) and (G) TPF xy images, accompanied by (D) and (H) false-coloured overlays, of GV and MII eggs injected with mitoGFP (n=6 and 9, respectively). All images are maximum intensity projections of stacks with 0.5µm z-steps. 0.1x0.1µm pixel size; 0.01ms pixel dwell time; ~12mW (~9mW) Pump (Stokes) power at the sample. CARS and TPF signal intensities are given in photoelectrons per second (ph.e$^-$/sec) and scale bars represent 10µm. Data from 2 trials, using 1-3 mice each.

A video of the merged TPF and CARS stacks gives the best representation of their distribution and apparent colocalisation, allowing visualisation of how the mitochondria appear to surround the LDs in 3D (Fig.7.2.2.). It seems the organelles are associated, but not to a large extent, as there are plenty of mitochondria and LDs residing without the other.

Again, there is the potential to correlate the signal given from CARS and TPF with DIC images of the eggs (Fig.7.2.1. (A) and (E)). Cytoplasmic ‘granules’ seen in DIC images may be discriminated as LDs or mitochondria once chemically confirmed by CARS and TPF techniques.

(A) (B)

Fig.7.2.2. Videos of Colocalisation of Lipid Droplets with Mitochondria in GV and MII Stage Mouse Eggs using CARS Microscopy and Two-Photon Fluorescence

Video through a 101-image *z*-stack (from bottom to top) of merged simultaneous CARS and TPF images of LDs and MitoGFP-tagged mitochondria, respectively, in (A) a GV oocyte, and (B) an MII egg. 0.1x0.1µm *xy* pixel size; 0.5µm *z*-step; 0.01ms pixel dwell time; ~14mW (~9mW) Pump (Stokes) power at the sample. Videos are shown at 7 frames per second.

Please scan either QR code above using your smart phone camera (you may need to install a QR Code Reader. Alternatively, videos can be accessed at:

(A) https://www.youtube.com/watch?v=VDm9-US_48U

(B) https://www.youtube.com/watch?v=gAlGIlzRsds

An attempt was also made at viewing mitochondria using CARS at the vibrational frequency of mitochondrial membrane protein cytochrome (1573cm^{-1}), as carried out by Walter *et al.* (2010). However, this effort proved to be unsuccessful due to the resonance of cytochrome being in the 'fingerprint region' of the lipid Raman spectrum (1200-2000cm^{-1}), where CH_2 and CH_3 deformations give off a signal. Consequently, mitochondrial structures in CARS images at 1573cm^{-1} could not be distinguished from the relatively large lipid signal obtained.

7.3. Effect of Alteration of Fatty Acid Metabolism on Mitochondrial Redox State and Membrane Potential

In order to investigate how the alteration of fatty acid metabolism affects mitochondrial redox state, conventional epifluorescence with a x20 objective was used, with 460nm excitation and 510-550nm emission filters to measure the green-emitted FAD autofluorescence over the entirety of each cell. The 'green' FAD autofluorescence in mouse eggs is almost exclusively derived from mitochondrial flavoproteins (Dumollard et al. 2007). Resting autofluorescence was recorded for a period of time before an inhibitor of lipid metabolism, etomoxir (100µM), was added to examine the subsequent effect on the resting redox state. Measurements were taken every 10 seconds and individual data sets were collected from each egg. It was found that there is a rapid and dramatic change in mitochondrial redox state when eggs are deprived of lipid metabolism at MII stage (Fig.7.3.1. (A)). Firstly, a decrease in FAD is seen (increase in reduced state $FADH_2$), thought to be due to a sharply increased uptake of pyruvate. The signal oscillates before recovering to a new resting level. It is clear from these results that ß-oxidation is contributing to redox state in the mammalian egg, as a disruption is seen with etomoxir addition, but after etomoxir a new steady state is achieved at a more reduced level. Further support of this observation comes from measurement of FAD and NADH autofluorescence simultaneously. A decrease in FAD is accompanied by an increase in NADH when etomoxir is added, and the signal settles to a new redox level (Fig.7.3.1. (B)).

Calibration of the FAD autofluorescence signal at MII stage was carried out by inducing maximum mitochondrial reduction and oxidation states. The ETC Complex IV inhibitor, CN^- is used to prevent the reduction of oxygen, causing maximal reduction of the mitochondrial FAD/FADH redox state. This is followed by a washing stage using a perfusion set-up, and then ETC uncoupler, FCCP is added to reverse the activity of ATP synthase, causing H^+ movement from the inter-membrane space into the mitochondrial matrix, causing it to become less negative, and causing maximum oxidation of FAD molecules (Fig.7.3.1. (C)). By doing this, it is shown that the resting redox state of an MII egg is ~50% of its maximum capacity. Adding etomoxir, it is clear that the resting state reached after etomoxir addition is

only a proportion of the normal resting rate of the egg redox state. ß-oxidation obviously provides a quantifiable contribution to the metabolic state of the unfertilised egg, shown here to be ~40% of the mitochondrial FAD/FADH redox state. It can also be shown that the majority of redox state contribution is in fact attributable to pyruvate oxidation by PDH. Pyruvate oxidation by PDH transfers protons to NAD, which in turn transfers protons to the ETC Complex I. Rotenone, is used as an inhibitor of Complex I, inhibiting transfer of any electrons formed from pyruvate metabolism. Rotenone, coupled with subsequent addition of CN^- can be used to investigate the extent of resting redox state for which pyruvate is responsible at the MII stage (Fig.7.3.1. (D)). Rotenone brings the FAD autofluorescence level down substantially, by ~60% of the resting metabolism and CN^- causes only a slight increase in this reduction.

The response of the FAD and NADH autofluorescence signals to L-carnitine was also measured. 1mM L-carnitine was added to MII eggs, but there was no immediate response in redox state (Fig.7.3.1. (E)). FAD does appear to drift downwards while NADH remains constant. It is likely that eggs need incubating in L-carnitine for some while to see a difference in redox state.

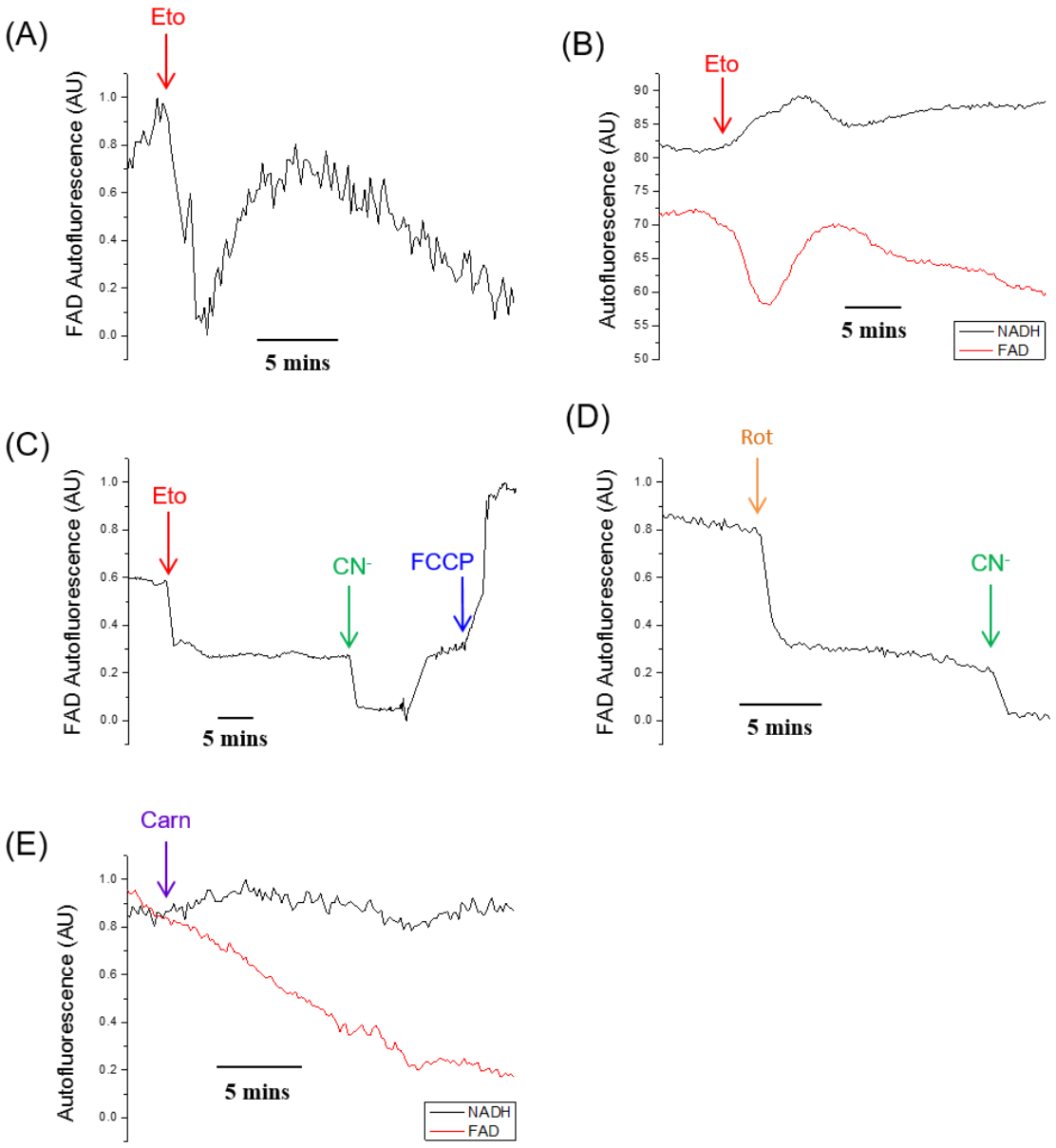

Fig.7.3.1. Effects of Alteration of Metabolism on Mitochondrial Autofluorescence in MII Stage Mouse Eggs

Traces of (A) Mitochondrial FAD autofluorescence signal in MII eggs treated with etomoxir (β-oxidation inhibition) (n=50), (B) FAD and NADH autofluorescence signal in MII eggs treated with etomoxir (n=3), (C) FAD autofluorescence signal in MII eggs treated with etomoxir, cyanide (maximum oxidation) and FCCP (maximum reduction) (n=19), (D) FAD autofluorescence signal in MII eggs treated with rotenone (Complex I inhibitor) and cyanide (n=4), and (E) FAD autofluorescence in MII eggs treated with L-carnitine (β-oxidation promotion) (n=4).

FAD autofluorescence was measured with etomoxir addition at all developmental stages (Fig.7.3.2.). GV stage oocytes show a similar FAD response to etomoxir to that of MII eggs (A-B). Inhibition of lipid metabolism at embryonic stages after fertilisation demonstrates that β-oxidation is occurring at all stages throughout development, but the decreased response as development continues may indicate a lowered capacity for fatty acid metabolism at these stages (C-F). Measurement of a response at arrested embryo stages demonstrated that while arrested in development, these embryos are still metabolising their lipid stores (G-H). Despite their arrest, they remain alive, and certain cell processes are obviously still on-going.

Normalisation of these graphs (see Chapter 2- section 2.7.1) allowed comparison of the area underneath the graphs, and thus a quantitative measure of the response to etomoxir at each stage (Fig.7.3.3.). It seems the change in redox state decreases as eggs and embryos develop from the GV stage through to the 4Cell stage, indicating a decrease in fatty acid contribution to the redox state as development continues. However, and increased response is seen at the 8Cell and blastocyst stages, suggesting β-oxidation becomes more prominent again. Results should be considered preliminary due to the fact that only one blastocyst was imaged. The embryos arrested at 2Cell stage have the same response as healthy 2Cell embryos, while the arrested 8Cell embryos appear to have a larger response. The large SEM seen here indicates that more samples are required, as results cannot be relied upon. They do, however, show that lipid metabolism is occurring and contributing to redox state at all stages, even when arrested in development, and that the oscillatory response is lost during development.

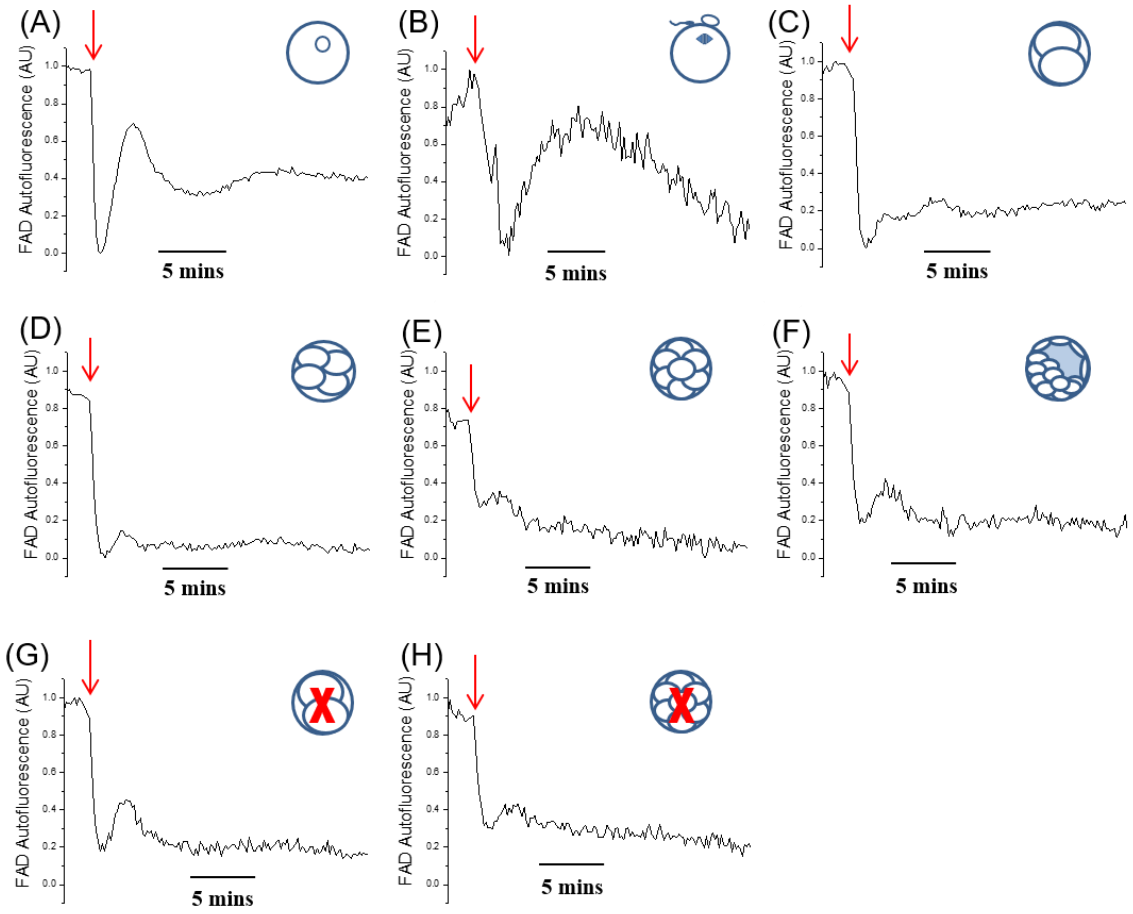

Fig.7.3.2. Effects of Alteration of Fatty Acid Metabolism on Mitochondrial Autofluorescence in Mouse Eggs and Early Embryos

Traces of FAD autofluorescence in response to etomoxir addition (β-oxidation inhibition) in (A) GV oocytes (n=17), (B) MII eggs (n=50), (C) 2Cell stage embryos (n=5), (D) 4Cell embryos (n=3), (E) 8Cell stage embryos (n=6), (F) blastocyst stage embryos (n=1), and arrested embryos at the (G) 2Cell (n=2) and (H) 8Cell stage (n=3).

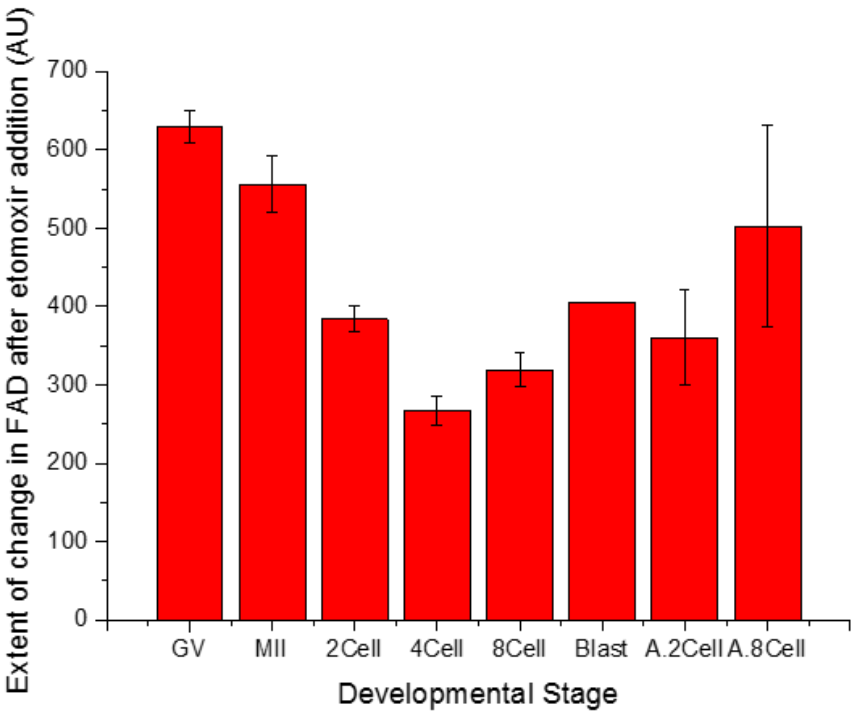

Fig.7.3.3. Effects of Alteration of Fatty Acid Metabolism on Mitochondrial Autofluorescence in Mouse Eggs and Early Embryos

Bar chart of FAD autofluorescence response to etomoxir addition (β-oxidation inhibition) in populations of GV oocytes (n=10), MII eggs (n=28), 2Cell stage embryos (n=5), 4Cell embryos (n=3), 8Cell stage embryos (n=6), blastocyst stage embryos (n=1), and arrested embryos at the 2Cell (n=2) and 8Cell stage (n=3). Mean values per population and SEMs shown.

The effect of inhibition of β-oxidation on MMP was also investigated using conventional epifluorescence microscopy. TMRE is a positively-charged fluorescent dye that is sequestered into the mitochondria with their negative MMP, and its fluorescence is subsequently quenched. With etomoxir addition to both GV and MII eggs, a temporary decrease in fluorescence is seen, which suggests and an increased (more negative) MMP (Fig.7.3.4.). This suggests that the loss of fatty acid metabolism causes a temporary increase in the proton gradient across the mitochondrial membrane. However, the resting MMP is regained soon after. Addition of the protonophore FCCP then caused a complete loss of MMP which lead to a de-quenching of TMRE fluorescence maximally and hence a large increase in TMRE overall fluorescence (Fig.7.3.4.).

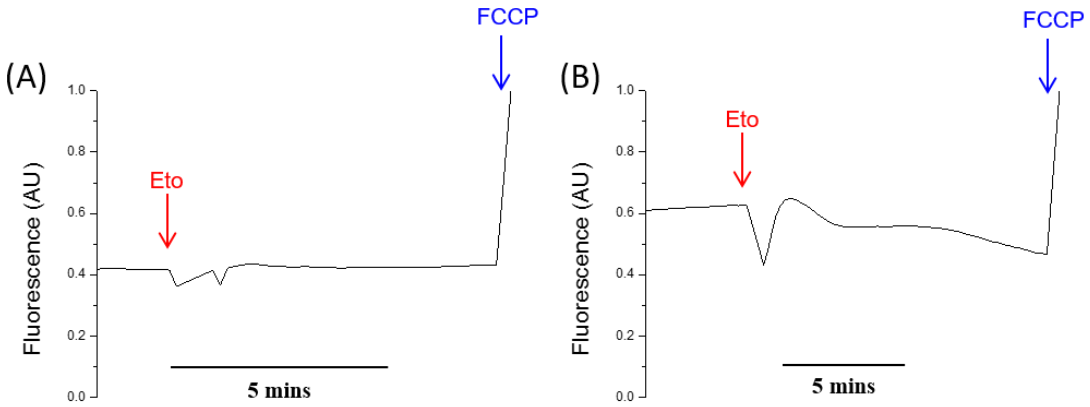

Fig.7.3.4. Effects of Alteration of Metabolism on Mitochondrial Membrane Potential in MII Stage Mouse Eggs

Fluorescence imaging of the effects of etomoxir (β-oxidation inhibition) on fluorescent mitochondrial membrane potential dye TMRE in (A) GV oocytes (n=7), and (B) MII eggs (n=11).

7.4. Effect of Alteration of Fatty Acid Metabolism on Mitochondrial ATP Production

To further investigate the contribution of ß-oxidation to ATP production, luciferase RNA (derived from the click-beetle) and protein (from the firefly) were microinjected into eggs prior to etomoxir addition alongside luminescence imaging. Luciferase requires luciferin, magnesium and ATP to produce a luminescent signal, so changes in luminescence signal indicate changes in ATP production, provided the pH remains stable.

MII eggs showed a decrease in ATP after etomoxir addition before a subsequent increase back to the previous resting level, and continuing to rise further (Fig.7.4.1. (A)). This is a similar response to that seen with FAD measurement, providing support for the idea of a partial recovery of metabolism by uptake of pyruvate. Addition of the pyruvate-uptake inhibitor, cinnmate (CIN), demonstrates a decrease in ATP when pyruvate is removed as a metabolic substrate. Subsequent addition of etomoxir sees a further decrease with maintained low level of ATP production when both pyruvate and fatty acid oxidation are inhibited (Fig.7.4.1. (B)). These results

provide further evidence that lipid metabolism is present in the mouse egg, and that inhibition of β-oxidation is compensated for by increased uptake of pyruvate, as resting ATP production is not regained after CIN addition.

L-carnitine was added to cells prior to etomoxir, to see the effect promotion of β-oxidation had on ATP production. It appeared that carnitine had no instantaneous effect on the level of ATP, possibly suggesting that incubation of eggs with carnitine is favourable for increased FA uptake (Fig.7.4.1. (C)).

Under normal conditions, bursts of ATP are detected during *in vitro* maturation from the GV stage to the MII stage but the mechanisms of this are as yet unclear (Yu *et al.* 2010). Etomoxir was added to maturing eggs in order to see the effect of inhibiting lipid metabolism on these mitochondrial episodes. The residuals of experimental signals (matured with etomoxir) against control eggs allowed to mature without etomoxir, and control oocytes held at GV stage in IBMX were plotted (Fig.7.4.1. (D)). Residual values are found with regression analysis, and show any deviations from the fitted curve, i.e. ATP bursts are shown as waves in (Fig.7.4.1. (D)- dark blue and magenta lines). It was found that inhibiting β-oxidation at this stage of development does not affect the ATP production, as bursts were seen in the experimental and control groups, compared to the population of oocytes not allowed to mature. However, most eggs did not fully mature to MII (36/40= 90% seemingly still at MI stage), suggesting that prevention of lipid metabolism prevented proper maturation as seen by Downs *et al.* (2009).

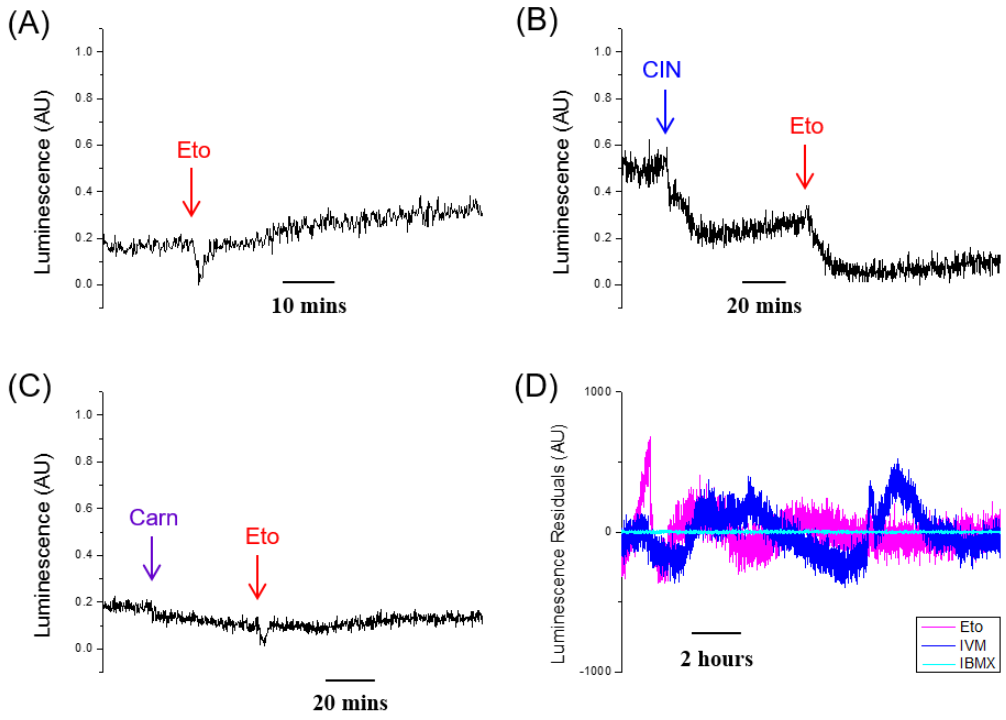

Fig.7.4.1. Effects of Alteration of Metabolism on Mitochondrial ATP production in MII Stage Mouse Eggs and during* in vitro *Maturation

Luminescence imaging of change in ATP production in response to (A) etomoxir (β-oxidation inhibition) (n=12), (B) cinnamate (pyruvate-uptake inhibition) and etomoxir (n=13), (C) carnitine (β-oxidation promotion) and etomoxir (n=8), (D) etomoxir during IVM (n=40), compared to controls in IBMX (n=23) and with no etomoxir addition (n=20).

7.5. Effect of Alteration of Fatty Acid Metabolism on Endoplasmic Reticulum

The theory that exposure of eggs to high concentrations of saturated fatty acids causes ER stress was further investigated. The extent of Ca^{2+} release after addition of SERCA pump inhibitor, Thapsigargin, was measured in eggs matured with differing concentrations of FAs. Eggs were supplemented with 100µM OA, or between 100 and 400µM PA overnight during IVM, as described by Wu *et al.* (2012) to be consistent with follicular fluid PA levels in normal and obese women. They were then injected with a 1:1 mix of Alexa 594 and OGBD. OGBD is a Ca^{2+}-sensitive fluorescent dye and Alexa is not, thus changes in signal can be normalised by calculating the Alexa/OGBD ratio. Fluorescence signal was measured for a short

period to establish a resting signal before Thapsigargin was added to give a final concentration of 10µM. The following change in Ca^{2+} signal was measured for the next ~20mins, and the OGBD/Alexa signal ratio was plotted per egg. The area under each curve was calculated, and the mean extent of Ca^{2+} release per population of eggs was plotted in a bar chart as seen in Fig.7.5.1. (A). It is clear that the amount of Ca^{2+} released from SERCA pumps in response to thapsigargin differed depending on the FA present, and its concentration. Control eggs show a 'normal' Ca^{2+} response to thapsigargin; eggs supplemented with 100µM OA interestingly show an increased Ca^{2+} release, whereas eggs supplemented with PA release less Ca^{2+} from their ER, this reduction being significantly more marked in those supplemented with higher concentrations.

The effect of high concentrations of PA on the immediate ER response was also investigated. 400µM PA has been shown to have negative effects on developmental potential (Jungheim *et al.* 2011a) and may be present in the follicular fluid of overweight women (Wu *et al.* 2012). GV oocytes were injected with OGBD and Alexa, and imaged on the epifluorescence microscope until a steady resting level of fluorescence was seen. A final concentration of 400µM PA was then added to the media, and the subsequent response was recorded. The ER stress response is characterised by a large increase in Ca^{2+} loss from the ER, as seen in response to Thapsigargin (Gwiazda *et al.* 2009). Fig. 7.5.1. (B) shows the instantaneous response of GV oocytes to PA addition: all eggs showed an initial decline in cytoplasmic Ca^{2+}, 6/12 showed a following increase in Ca^{2+} loss from the ER, but only 3 of these had a marked response. The other 6/12 oocytes did not show an increase in cytoplasmic Ca^{2+}, suggesting the effect of PA is perhaps not instantaneous, or higher concentrations are required for an immediate response.

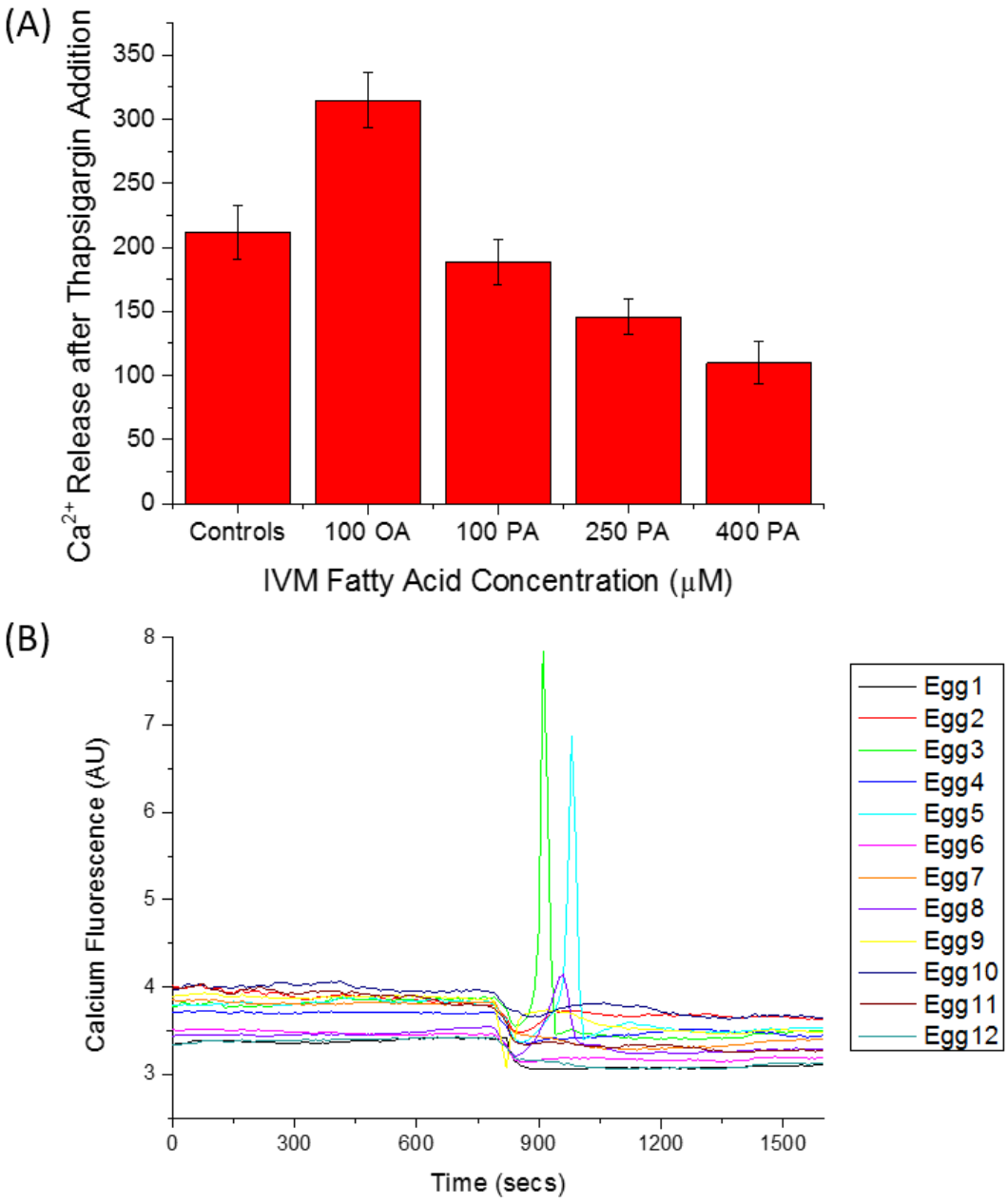

Fig.7.5.1. Effects of Feeding Mouse Eggs with Fatty Acids on Ca^{2+} Release from the Endoplasmic Reticulum

(A) Bar chart displaying the effects of incubation of eggs during IVM in 100μM oleic acid (n=31), or 100μM (n=24), 250μM (n=18), 400μM (n=12), or 700μM (n=12) palmitic acid on release of Ca^{2+} from ER SERCA pumps in response to thapsigargin addition, compared to controls (n=22). Data obtained from integrating areas under graphs of the change in fluorescence signal (ratio of Alexa/OGBD dyes) in response to thapsigargin. Mean values per population with SEM bars shown. (B) The instantaneous effect of 400μM PA addition on resting Ca^{2+} levels in GV oocytes (n=12).

In order to see the effect of FA metabolism inhibition on Ca^{2+} release from the ER, etomoxir was added to eggs (100µM final concentration) that had been injected with Ca^{2+} dye, Rhod Dextran. FAD autofluorescence was also measured alongside Ca^{2+} fluorescence. An increase in Ca^{2+} is seen with etomoxir addition (Fig.7.5.2. (A)). However, after addition of Ca^{2+} ionophore, ionomycin, it is clear that this increase is negligible (Fig.7.5.2. (B)) and probably as a consequence of other etomoxir effects such as the ATP decrease seen in (Fig.7.4.1. (A)).

FAD oscillations are normally seen to accompany Ca^{2+} transients at fertilisation, and these are stopped by Ca^{2+} chelator, BAPTA (Dumollard *et al.* 2004). However, etomoxir was found to have very little effect on the Ca^{2+} oscillations seen during egg activation, despite dampening FAD oscillations. Eggs were injected with Rhod Dextran and sperm factor PLCζ protein. They were imaged for FAD autofluorescence and Ca^{2+} fluorescence, and their response to etomoxir addition was recorded. Inhibition of β-oxidation had a normal effect on the FAD trace, lowering the signal, but no effect on the transient spikes of Ca^{2+} typically seen in response to PLCζ (Fig.7.5.2. (C)).

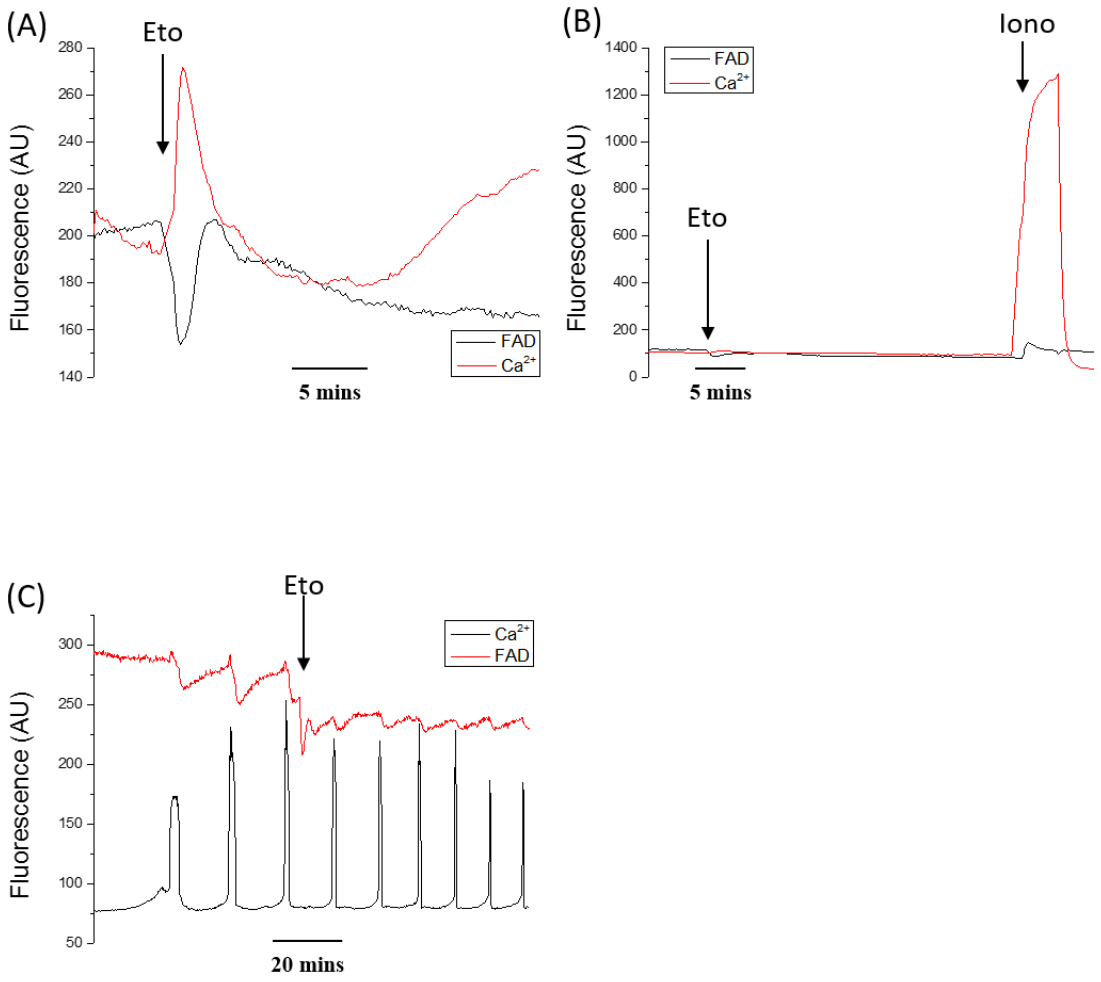

Fig.7.5.2. Effects of Alteration of Fatty Acid Metabolism on Ca^{2+} Release from the Endoplasmic Reticulum

Fluorescence imaging of (A) Effect of etomoxir on Ca^{2+} release from the ER (n=3), and (B) the effect of etomoxir on Ca^{2+} release from the ER in comparison to the effect of ionomycin on Ca^{2+} release from the ER (n=6), demonstrating negligibility of etomoxir effect. (C) Also negligible effect of etomoxir on Ca^{2+} release from the ER in response to PLCζ protein (sperm factor) injection (n=10). FAD responses measured in accompaniment to Rhod Dex response to show etomoxir addition.

7.6. Lipid Droplet Conformation after Feeding/Starvation

CARS imaging has also been used to gain evidence of lipid metabolism in the mammalian egg. CARS stacks were performed on MII eggs under conditions of pyruvate starvation (in HKSOM devoid of pyruvate or lactate) where only lipid may be used as a substrate for metabolism, or inhibition of lipid metabolism (addition of etomoxir) where only pyruvate can be used. In eggs with inhibited lipid metabolism, there seemed to be very little difference in LD distribution compared to control MII eggs (Fig.7.6.1. (G)), as aggregates are seen. Conversely, LDs in pyruvate-starved eggs appear to be smaller and notably less aggregated than control MII eggs, dispersed throughout the whole cytoplasm (Fig.7.6.1. (F)), as would be expected if LD distribution pattern reflects metabolism of lipids as a substrate. Quantitative analysis of the LD spatial distribution further supports this hypothesis, as MII eggs starved of pyruvate and thus requiring lipid metabolism have aggregates mostly consisting of a small number of droplets (Fig.7.6.2. (A)), with a higher percentage (>70%) of isolated LDs than even seen in GV oocytes (Fig.3.2.4.). Simple t-test analysis demonstrates the extent of this difference (P= 0.00007). MII inhibition of lipid metabolism by addition of etomoxir yields a distribution of aggregates containing many droplets, and only ~40% isolated LDs, as previously seen in untreated MII eggs (Fig.7.6.2. (B)). This population of eggs, however, is found to have a significant difference in LD aggregation, as distinguished by a simple t-test (P= 0.003).

The effect of lipid content of the surrounding media on intracellular LD characteristics was assessed by maturing GV oocytes to MII stage overnight in MEM medium containing either fatty acid-free BSA or FCS (with an abundance of fatty acids) and taking subsequent CARS images of eggs with a polar body. In fatty acid-free (FAF) media, the LDs appear to be well distributed (Fig.7.6.1. (H)), similar to that seen in pyruvate-free media. This is confirmed with aggregate analysis where 71% of droplets are seen to be isolated (Fig.7.6.2. (C)), a significant difference demonstrated by a t-test (P= 0.016). Meanwhile, CARS images of serum-supplemented eggs do not look different to normal MII eggs (Fig.7.6.1. (I)). However, quantitative analysis reveals a higher number of droplets is seen in serum-

supplemented eggs, but not a significant increase in clusters (Fig.7.6.2. (D)) (*P* = 0.229).

Addition of L-carnitine appeared to have no effect on LD distribution (7.6.1. (J)). CARS images of MII eggs supplemented with carnitine have a similar LD distribution as normal MII eggs seen in Fig.3.2.1., and quantitative analysis reveals a similar aggregation pattern (Fig.7.6.2. (E)), with no significant differences (*P*= 0.09).

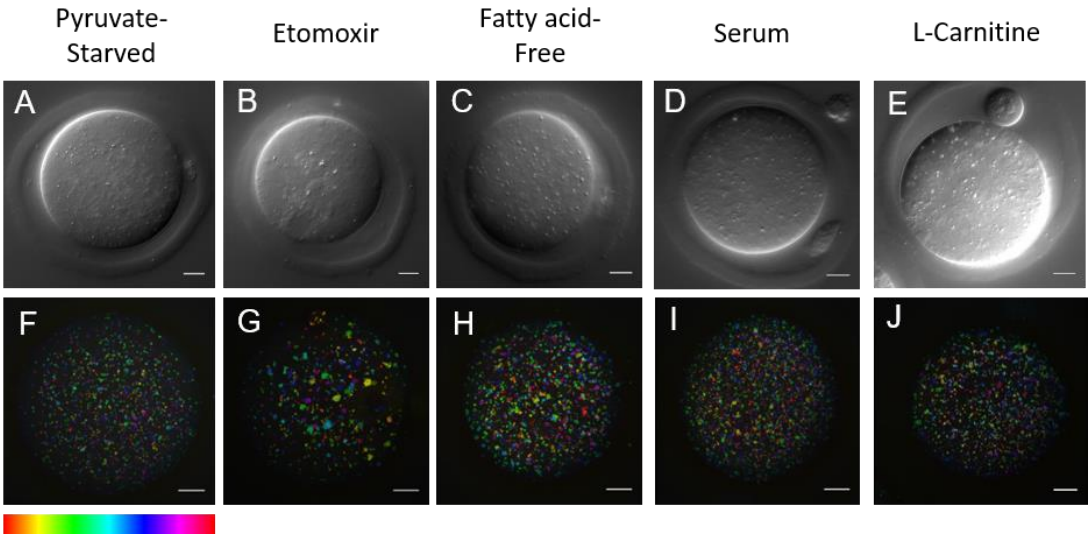

Fig.7.6.1. DIC and CARS Imaging of Mouse Eggs after Alteration of Fatty Acid Metabolism

(A-E) Single-plane (approximately equatorial) DIC images using a 1.27 NA water objective and a 1.4 NA oil condenser, and (F-J) Depth colour-coded images of CARS z-stacks at wavenumber 2850cm^{-1} through the same MII eggs, showing LDs in representative (A and F) pyruvate-starved eggs (n=8), (B and G) β-oxidation-inhibited eggs (100μM etomoxir) (n=6), (C and H) β-oxidation-limited eggs (fatty-acid free media) (n=16), (D and I) high-fat-supplemented eggs (serum-containing media) (n=5), and (E and J) β-oxidation-promoted eggs (1mM L-carnitine) (n=7). 0.1x0.1μm xy pixel size; 0.5μm z-step; 0.01ms pixel dwell time; ~14mW (~9mW) Pump (Stokes) power at the sample. Scale bars represent 10μm; colour bar shows depth colour-coding from -25μm-25μm of 101 z-stacks (0μm being the approximately equatorial plane of the egg), the brightness of each colour is the maximum intensity at each corresponding z-plane. Data from ≥2 trials, using 1-3 mice each.

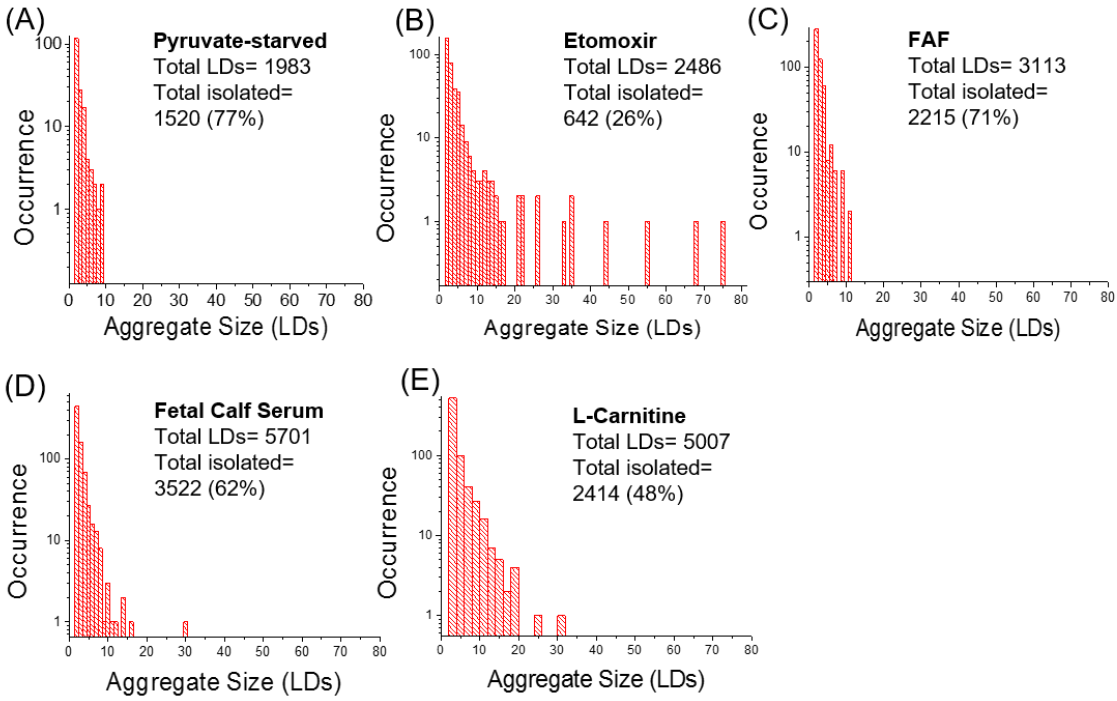

Fig.7.6.2. Histograms of Lipid Droplet Aggregation in Mouse Eggs after Alteration of Fatty Acid Metabolism

Histograms of the number of LDs making up clusters in MII eggs representative of (A) a pyruvate-starved egg (n=8), (B) a β-oxidation-inhibited egg (etomoxir addition) (n=6), (C) a β-oxidation-limited egg (fatty-acid free media) (n=16), (D) a high-fat-supplemented egg (serum-containing media) (n=5), and (E) a β-oxidation-promoted egg (L-carnitine addition) (n=7), demonstrating the difference seen in LD distribution under certain conditions. Total number of LDs and total number of un-clustered LDs are also indicated.

Feeding cells with OA and PA revealed slight differences in LD distribution (Fig.7.6.3.). OA is said to be involved in TAG and LD formation, while PA has negative effects on cells, and is more likely to be metabolised than promote formation of LDs (Das *et al.* 2010). CARS images suggest an increase in LD formation with OA incubation, as generally more droplets are seen to fill the cytoplasm than in control conditions (Fig.7.6.3. (D)). PA addition appears to have no effect on LD distribution (Fig.7.6.3. (E) and (F)), but effects are likely to be at a more molecular level, like the effect on the ER shown in section 7.5. Unfortunately, no quantitative analysis of FA-supplemented oocytes was possible due to time constraints.

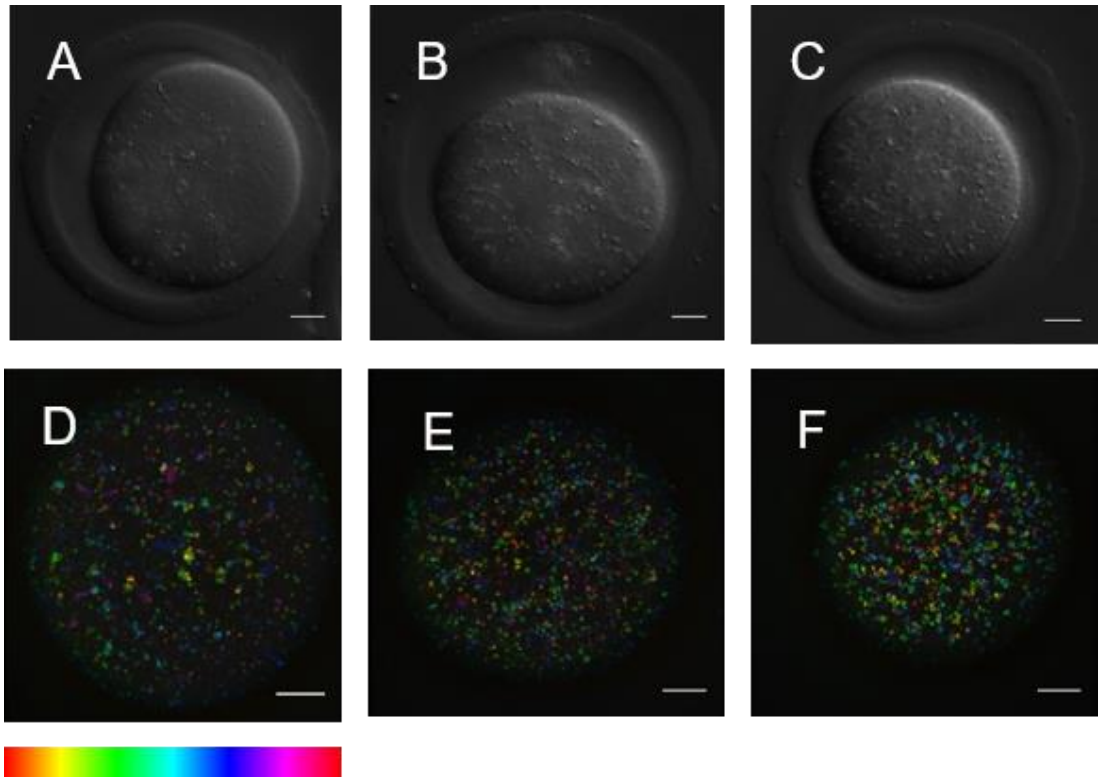

Fig.7.6.3. DIC and CARS Imaging of Mouse Eggs after Fatty Acid Feeding

(A-C) Single-plane (approximately equatorial) DIC images using a 1.27 NA water objective and a 1.4 NA oil condenser, and (D-F) Depth colour-coded images of CARS z-stacks at wavenumber 2850cm^{-1} through the same MII eggs, showing LDs in representative (A and D) 100µM oleic acid-supplemented eggs (n=8), (B and E) 100µM palmitic acid-supplemented eggs (n=23), and (C and F) 250µM palmitic acid-supplemented eggs (n=28). 0.1x0.1µm xy pixel size; 0.5µm z-step; 0.01ms pixel dwell time; ~14mW (~9mW) Pump (Stokes) power at the sample. Scale bars represent 10µm; colour bar shows depth colour-coding from -25µm-25µm of 101 z-stacks (0µm being the approximately equatorial plane of the egg), the brightness of each colour is the maximum intensity at each corresponding z-plane. Data from ≥2 trials, using 1-3 mice each.

Comparison of $\sqrt{\langle s^2 \rangle}$ of GV (black square) and MII (red circle) eggs with supplemented or starved eggs gave more quantitative information as to the effect on LD distribution (Fig.7.6.4.). Pyruvate starvation (green triangle) demonstrates a low number of LDs, which are very dispersed, but not as isolated as in the random case (violet, yellow, and points), whereas inhibition of lipid metabolism with addition of etomoxir (dark blue triangle) causes the most aggregated LD distribution. Incubation

of eggs with fatty-acid laden serum (magenta triangle) yields a LD distribution which is less aggregated, more like GV oocytes. This serum-supplemented population also tend to have a higher total number of LDs, which is consistent with the observation of increased LD number with increased time in culture. FAF media (orange triangle) also caused a more 'GV-like' aggregation pattern, but compared to serum-supplemented eggs, these showed a 'normal' total number of LDs similar to that of GV oocytes. L-carnitine supplementation of MII eggs (cyan diamond) was expected to see an increased dispersion of LDs, instead displaying more LD aggregation than MII eggs, but these are still within SDs.

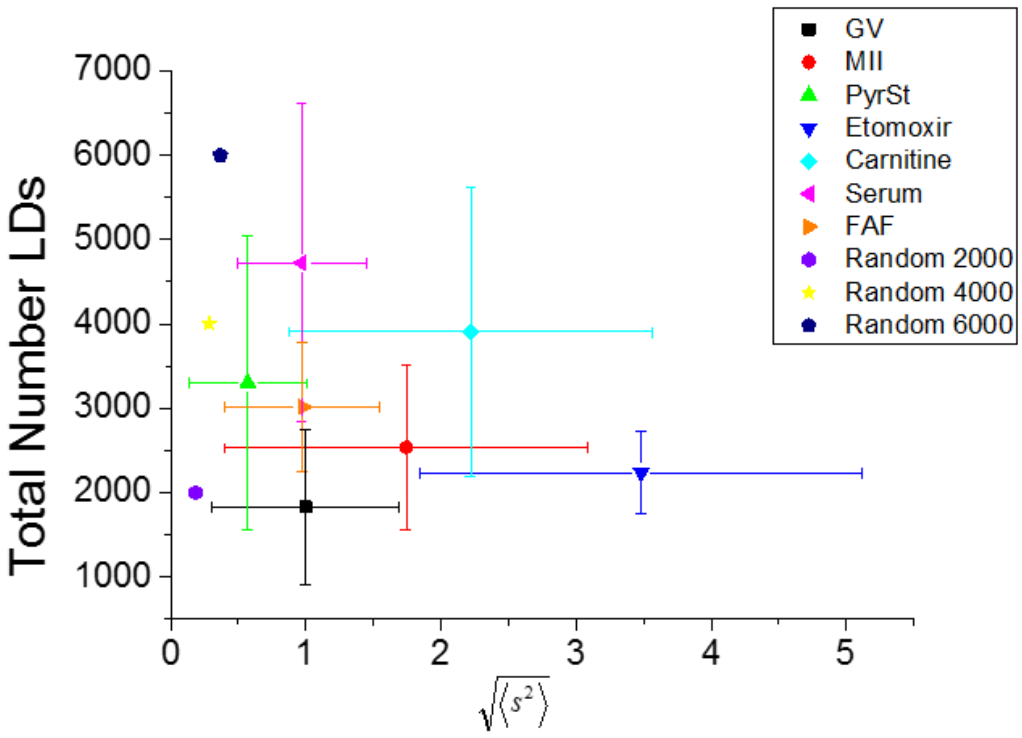

Fig.7.6.4. Scatter plot of the Extent of Lipid Droplet Aggregation ($\sqrt{\langle s^2 \rangle}$) in Mouse Eggs after Alteration of Fatty Acid Metabolism

Scatter plot of the square root of the mean squared aggregate size ($\sqrt{\langle s^2 \rangle}$) against the total number of LDs, in ensembles of GV oocytes (n=33), MII eggs (n=30), MII eggs that were pyruvate-starved (PyrSt) (n=8), MII eggs with β-oxidation-inhibition (100μM etomoxir) (n=6), MII eggs high-fat-supplemented eggs (FCS-containing media) (n=16), and MII eggs with limited β-oxidation (fatty acid-free media) (n=5). The distribution of each

variable in the corresponding ensemble is shown as an average (symbol) and standard deviation (bar).

Mean LD diameter does not appear to differ greatly between conditions (Fig.7.6.5. (A)). LDs of eggs under conditions inducing larger amounts of lipid metabolism do not seem significantly smaller than those in normal or supplemented conditions. Furthermore, comparing the total lipid amount per LD ($\langle\frac{TL}{LD}\rangle$) of supplemented or starved eggs with GV (black square) and MII (red circle) eggs shows that under most conditions, less lipid is seen per LD (Fig.7.6.5. (B)), apart from those in FAF media (orange triangle) which appears to have slightly more. However, all are within SDs of both GV and MII eggs, so are likely to be insignificant.

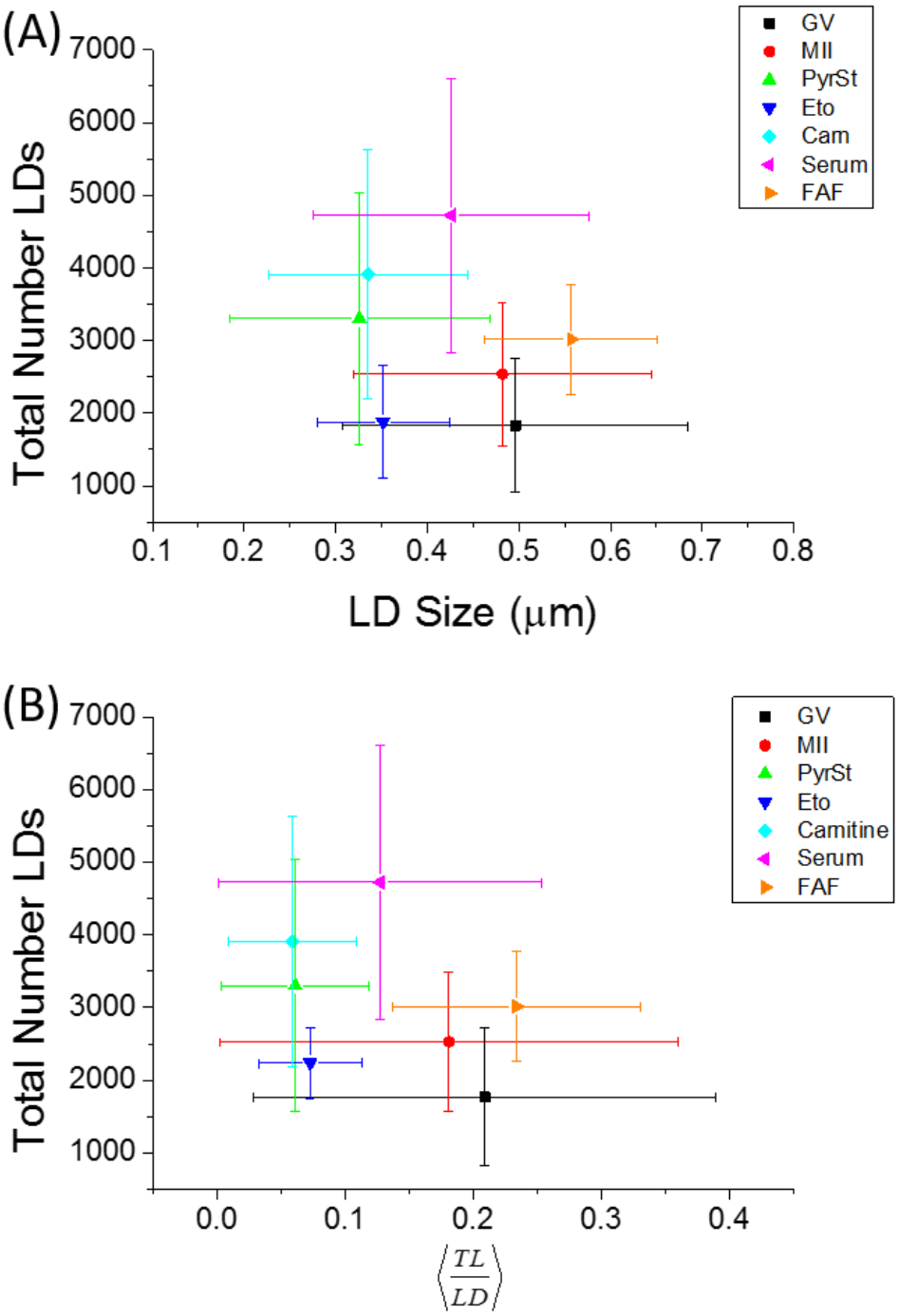

Fig.7.6.5. Scatter plots of LD Size and Total Lipid Content per LD ($\langle\frac{TL}{LD}\rangle$) of Mouse Eggs after Alteration of Fatty Acid Metabolism

(A) Scatter plots of the LD size and (B) total lipid content per LD ($\langle\frac{TL}{LD}\rangle$) in populations of GV oocytes (n=33), MII eggs (=30), MII eggs starved of pyruvate (pyruvate-free media) (n=8), MII eggs with inhibited lipid metabolism (etomoxir addition) (n=6), MII eggs with promoted lipid metabolism (L-carnitine addition) (n=5), MII eggs matured with high fat supplementation (serum-containing media) (n=5), and MII eggs matured with limited lipid metabolism (fatty acid-free media) (n=16). The distribution of each variable in the corresponding ensemble is shown as a mean (symbol) and standard deviation (bar).

7.7. Discussion

Mammalian oocytes, eggs and cleavage stage embryos rely almost exclusively upon the metabolism of pyruvate and FAs by their mitochondria for generating energy in the form of ATP (Acton *et al*. 2004; Dumollard *et al.* 2008). As described in Chapter 1, FAs stored as TAGs in LDs must be liberated in order to undergo metabolism by mitochondria, however the co-localisation of mitochondria and LDs is rather inconclusive. CARS and TPF images appear not to show direct correlation as channels do not appear to overlap with each other. However, it does seem to be made more apparent by running through a complete z-stack as shown in Fig.7.2.2.- that the two structures are somewhat associated. It is likely that LDs must be located fairly near to mitochondria, but that direct contact is not required. The action of lipases and carnitine, liberating and transporting fatty acids, occurs in the cytoplasm and it is likely that fatty acids from one LD are metabolised in multiple mitochondria within the surrounding vicinity. Mitochondrial and LD colocalisation has been described previously by fluorescence analysis, showing the organelles reside within 10nm of each other (Sturmey *et al.* 2006; Cui *et al.* 2009). Niu *et al.* (2014) describe loss of mitochondria with delipation of porcine oocytes, also suggesting colocalisation. However, Ambruosi *et al.* (2009) argue that LD position is not related to mitochondrial location, but to factors involved in cumulus expansion. Further work is required to investigate correlation of mitochondrial distributions associated with increased or decreased developmental competence such as that seen by Nagai *et al.* (2006), with LD spatial position. CARS and TPF images here show that not all LDs or mitochondria are associated with each other in both GV and MII eggs. This is likely to reflect the fact that oxidative phosphorylation is occurring, but not to an excessive extent, concurrent with Leese's proposition of a quiet metabolism (2002; 2007).

The idea that the LD distribution reflects the amount of metabolic activity within the cell is supported by comparison of the CARS images and the extent of LD aggregation ($\sqrt{\langle s^2 \rangle}$) seen under different conditions of altered metabolism. Starving eggs of any external source of pyruvate or lipid, with media devoid of these supplements, forces the use of the internal lipid stores for ATP production. Under

these conditions, the LDs are seen to disperse, resulting in minimal clusters, and suggesting that this dispersion is in order to make lipid stores more available for fatty acid liberation and metabolism by mitochondria. It would be of interest to measure TPF of MitoGFP alongside starvation experiments, in order to investigate whether localisation of LDs correlates more with that of mitochondria in cases such as these.

Conversely, inhibition of fatty acid metabolism from the internal lipid stores using etomoxir results in increased LD clustering. This observation supports the notion that LD clustering coincides with a reduced capacity for lipid metabolism, and further inhibition may lead to LD aggregate fusion, and larger LDs such as those seen in glycolytic blastocyst stage.

L-carnitine works to increase the amount of fatty acid metabolism of internal stores, however there was no effect on LD distribution: normal amounts of clustering for MII stage eggs and no dispersion was seen. It is possible that while able to promote development by improving fatty acid uptake into mitochondria (Dunning and Robker, 2012; Dunning *et al*. 2010; 2011), it is not involved in the increased liberation of fatty acids from LDs.

Supplementation of media with excess fatty acids increased the lipid stores externally available, meaning eggs were able to use internal fatty acids already stored, along with fatty acids taken up from the external environment for metabolism. No more clustering of LDs was seen with serum supplementation, but LD formation appeared to increase, with an increase in total LD number, concurrent with recent studies (Kim *et al.* 2001; Yang *et al.* 2010). This gives an interesting insight into the descriptions of LD formation, suggesting that further mechanisms of LD biogenesis are possible.

Previous studies show that the amount of lipid in LDs decreases with increased lipid metabolism (Ghanem *et al*. 2014). While this is likely to be the case, the results shown here demonstrate that no significant changes in LD diameter or lipid amount are seen with the experimental conditions used. No decrease in LD size is seen in starved conditions, and no LD diameter increase is noted with supplemented conditions, only an increase in total LD number is observed in the serum-supplemented population. Although giving a reasonable idea as to the content of

eggs, the $\langle \frac{TL}{LD} \rangle$ is only able to measure those contained in LDs as TAGs, giving off a detectable CARS signal. Discrepancies in lipid content may be due to the unseen or unmeasurable amounts of free fatty acids in the cytoplasm.

A decrease in mitochondrial oxidation products is expected to correlate with a more positive MMP and thus an increase in fluorescence signal from the positively-charged mitochondrial dye, TMRE. Inhibition of β-oxidation affected MMP at both GV and MII stages, showing an oscillatory response to loss of a metabolic substrate. There is a temporary hyperpolarisation of MMP which is eventually settled back to a resting MMP. Again, it is possible that this is reflective of an over-compensatory pyruvate uptake. The effect of etomoxir appeared to be larger at MII than at GV stage, and the MMP does not quite resume its previous level of polarisation. This may be indicative of a difference in the amount of fatty acid metabolism occurring at each meiotic stage, or may give an idea of the contribution of β-oxidation to the redox state of these cells. Although oxidative phosphorylation predominates at both stages, there is likely to be a difference, if only slight, between metabolic capacity of GV and MII eggs, due to the different responsibilities that face each developmental stage.

The contribution of lipid metabolism to mouse egg mitochondrial redox state and ATP production is thus far unknown. Results here show that this contribution is substantial, however, mechanisms exist to compensate for loss of fatty acids as a substrate. Advantage was taken of the FAD/NADH autofluorescence as a measure of mitochondrial redox state (Dumollard *et al.* 2004, 2007; Igosheva *et al.* 2010), and was used to provide evidence for, and determine the contribution and significance of lipid metabolism occurring during mouse egg and embryo development. Addition of etomoxir to eggs and embryos of all developmental stages had a significant effect on FAD autofluorescence. The very fact that etomoxir changes FAD signals shows, for the first time, that β-oxidation is making a significant contribution to mitochondrial metabolism in mouse oocytes. Calibration of the FAD autofluorescence was performed by addition of CN^- and FCCP to maximally reduce and oxidise mitochondria, respectively. This enabled the resting redox state of GV and MII eggs to be visualised and calculated (~60%), and addition of etomoxir displayed the considerable contribution of fatty acid metabolism to this resting potential (~30-

40%). There may be other minor substrate contributions that aren't addressed here, such as amino acid metabolism, hence it is impossible to calculate the exact contributions of substrates to redox state. It still appears that the majority of redox potential is provided by the oxidation of pyruvate, as the addition of rotenone, calibrated by CN^- addition, caused a majority decrease in FAD autofluorescence. However, Hinke *et al.* (2007) describe a mechanism through which succinate (a 4-carbon intermediate of the TCA cycle) bypasses metformin-induced Complex I inhibition in order to restore the ETC by transfer of e^- directly to Complex II. Metformin is a reversible inhibitor of Complex I, whereas rotenone action is irreversible and they act at different sites, so further investigation is required (Wheaton *et al.* 2014).

Although calibration could not be performed at all stages of development, it seems β-oxidation is lower in some stages than others, due to the lesser response to etomoxir. These differences most likely reflect the amount of ß-oxidation occurring at different stages of development. In the GV, a larger relative change is seen while the MII response is smaller and slower to settle back to the new 'resting' redox potential. A less marked response is seen with etomoxir addition to embryo stages, possibly indicating that metabolism in general is quieter at these stages, or it may mean that these stages have a lower capacity for lipid metabolism. Indeed, Sturmey and Leese, (2003) show that ATP production is lower during cleavage stages, and increases at blastocyst stage, though increased ATP generation at blastocyst stage may be due to initiation of glycolysis. Harris *et al.* (2009) describe how pyruvate and O_2 consumption increases as embryonic development continues, likely coupled with a decline in lipid metabolism.

Although a loss of fatty acid metabolism is expected to result in a decreased $FADH_2$ production (and increase in FAD^{++}), a rapid decrease in FAD autofluorescence signal is instead seen. This result is suggestive of an immediate increase in uptake of an alternative substrate in order to compensate for the loss of fatty acid as a source of metabolic energy. The response seen is rapid, but viable, as metabolic transitions occur very quickly; Romashko *et al.* (1998) noted redox oscillations in cardiac cells as a result absence of metabolic substrate, occurring in less than 6 seconds. Although L-carnitine had no effect on FAD autofluorescence or ATP production, this could

mean that a longer incubation is required to see the beneficial effects of this β-oxidation promoter. Previous studies have used long incubations and L-carnitine supplementation during IVM (Dunning *et al.* 2011, 2010; Somfai *et al.* 2011; You *et al.* 2012). Inhibition of β-oxidation, however, also results in a decrease in mitochondrial ATP production. This effect is not lasting, and the resting rate of ATP is soon resumed, appearing to continue to increase past the usual resting level. This result also suggests a compensation mechanism of substrate uptake in order to maintain a viable level of ATP production. This may also support the finding that the ATP bursts seen during IVM are not under the influence of fatty acid oxidation, as addition of etomoxir has no effect. Due to the changes occurring over a long time, the instantaneous effect of loss of lipid metabolism may be lost, compensatory mechanisms allowing usual IVM events to take place. Although, it was found that 90% of these eggs did not mature to MII stage in the time-frame usually allowed for maturation, suggesting a lack of β-oxidation slows maturation. This was indeed noted by Downs *et al.* (2009).

It was shown that, if pyruvate uptake inhibitor CIN is added to cells prior to etomoxir addition, there was no resumption of resting ATP level; CIN caused a decrease in mitochondrial ATP production, and etomoxir caused an even further reduction. It is likely that pyruvate uptake is increased when cells are faced with loss of fatty acid oxidation contribution to mitochondrial metabolism, in order to maintain cell viability, but cell cycle timing may be compromised. This compensatory pyruvate uptake would explain the rapid response seen in FAD signals at all stages of development. Despite later developmental stages appearing to have a lesser response to loss of β-oxidation, and at no stage is the previous resting redox potential regained, there is an oscillatory FAD response seen in all traces, suggesting the initial resultant pyruvate uptake may be over-compensatory.

Bryson *et al.* (1996) demonstrated that etomoxir inhibition of ß-oxidation causes an increase in PDH complex activity in different tissues in mouse, showing present results as concurrent with effects seen in differing cell systems. Interestingly, previous studies also show how inhibition of ETC Complex I, which accepts electrons from pyruvate oxidation-derived NADH, causes an increase in ß-oxidation and mobilisation of TAGs from storage, in skeletal muscle and hepatocytes, respectively (Collier *et al.* 2006; Owen *et al.* 2000). O_2 consumption is

also seen to continue in the absence of pyruvate as a substrate (Butcher *et al.* 1998). This points to a balance between pyruvate and fatty acid metabolism for optimal ATP production in various tissues, although we don't see a recovery to resting ATP level after CIN addition in the mouse egg. It could be postulated that fatty acid uptake into the mitochondria is less rapid than that of pyruvate, in which case a recovery increase in luminescence signal may be seen if measured for longer. Although mouse eggs have a comparatively low lipid content to other species, oxidation of fatty acid yields a large amount of ATP (106 ATP molecules, compared to ~30 with pyruvate oxidation), providing an effective source of energy when necessary, and a small lipid store may suffice (Dunning *et al.* 2014b). On the other hand, it could be possible that metabolism of FAs is not essential for ATP production- we see that with inhibition of β-oxidation, the production of ATP is not compromised- resting ATP level is resumed, even to a higher level, assumed to be due to increased oxidation of pyruvate. As described, it is also noted that the resting ATP level is not regained after CIN addition, perhaps indicating that there is no compensatory uptake of FAs. This is a reasonable theory as it does not seem that either pyruvate or fatty acid alone can maintain the viability of mouse eggs and embryos. Previously-described long-term effects of ß-oxidation inhibition, while supporting the hypothesis that lipid metabolism is in fact occurring in the mouse oocyte and egg, prove that metabolism of pyruvate alone does not allow production of viable, healthy embryos to develop, so a balance between pyruvate and lipid metabolism may well be present (Dunning *et al.* 2010; Downs *et al.* 2009; Merrill *et al.* 2002). Excess pyruvate sees no increase in ATP (Dumollard *et al.* 2009), but leads to ROS production, alongside a build-up of acetyl coA and cytosolic reactions producing lactate, both of which generate ketone bodies detrimental to cell viability (Wu *et al.* 2000).

Pig oocytes have been shown to survive on lipid alone, and bovine embryos cultured without pyruvate but with L-carnitine develop further than those simply without pyruvate (Sutton-McDowall *et al.* 2011). However, mouse eggs and embryos can also not survive on lipid only as a metabolic substrate. Pyruvate starvation of MII eggs leads to conversion of lactate to pyruvate, but lactate-derived pyruvate is not taken up into mitochondria and cannot contribute to ATP generation, and rather can be converted into ketone bodies (Dumollard *et al.* 2007, 2008, 2009; Collado-

Fernandez *et al.* 2012). Starving eggs of pyruvate also causes inhibition of the egg-activating Ca^{2+} oscillations which occur at fertilisation, and a decrease in ATP production, both of which can be rescued by excess pyruvate addition (Dumollard *et al.* 2004).

The TCA isn't fuelled by acetyl CoA alone. Intermediates of the TCA e.g. citrate, are transported out of the mitochondria into the cytosol, and pyruvate is also converted to oxaloacetate via pyruvate carboxylase, in order to maintain the cycle (Sugden and Holness, 2011). Metabolism of lipid alone would result in a dramatic reduction of oxaloacetate generation, leading to a build-up of acetyl CoA, again resulting ketone bodies.

Detrimental effects of excess lipid metabolism in eggs and embryos has previously been described (see Chapter 5). Briefly, culture media supplemented with high free fatty acid concentrations reduces egg or embryo developmental competence (Van Hoeck *et al.* 2011; Kruip and Kemp, 1999). Obese mothers or those with a high fat diet tend to produce eggs or embryos with reduced potential, developmental effects, or live offspring with severe birth defects (Igosheva *et al.* 2010; Dunning *et al.* 2014; Turner and Robker, 2014; Wu *et al*. 2010; Van Hoeck *et al.* 2011; Robker *et al.* 2009; Jungheim *et al.* 2011a, 2011b). This is likely to be due to the production of ROS as a result of lipotoxicity, inducing organelle damage and apoptotic pathways.

It is clear that a balance between the two primary substrates is best for ATP generation and subsequent development. Turner *et al.* (1994) describe how an intermediate level of pyruvate is best for development. Negative effects upon egg and embryo development are also seen with both low and high concentrations of fatty acids (Grazul-Bilska *et al.* 2012; Kubandova et al 2014; Van Hoeck *et al.* 2011). It is likely that both NADH derived from pyruvate oxidation, and $FADH_2$ from β-oxidation are required for generation of TCA intermediates for and proper ETC function. An intermediate level of both pyruvate and fatty acid metabolism is in agreement with the quiet embryo hypothesis, which suggests that an optimal threshold of metabolism is associated with maximal developmental competence (Leese, 2007, 2002).

It is largely unknown why the mammalian egg or embryo doesn't metabolise glucose in the initial stages of development. Glucose is present in the follicular fluid, and

glycolysis is performed in the cumulus cells, but it seems there are feedback mechanisms inhibiting the oocyte from performing glycolysis itself. Chatot *et al.* (1989) describe how glucose is inhibitory to mouse egg development. Methylglyoxal is a bi-product of glycolysis which is detrimental to embryo and oocyte development (Chang and Chan, 2010), so it is likely that glycolysis contributes to the decreased developmental quality of eggs or embryos with reduced fatty acid metabolism.

MacDonald *et al.* (2003) describe how high citrate levels inhibit glycolysis through the inhibition of glycolytic intermediate phosphofructokinase (PFK). β-oxidation and pyruvate dehydrogenation lead to production of citrate. However, citrate is converted to malonyl coA which would usually inhibit CPT transport of fatty acids into the mitochondria, reducing the amount of fatty acid metabolism occurring. Mechanisms preventing this conversion of citrate to malonyl CoA must be switched off in oocytes and eggs, maintaining β-oxidation, but also maintaining a glycolysis block (Barbehenn *et al.* 1974; Weitlauf and Nieder, 1984). Hardie and Pan (2002) indeed describe the mechanisms of PRKA (AMP-activated protein kinase, formally known as AMPK), which phosphorylates and subsequently inactivates acetyl coA carboxylase (ACAC), which works to convert acetyl coA to malonyl coA. While citrate is shown to activate ACAC, PRKA prevents malonyl coA production, and thus is shown to lead to an increase in FA oxidation in immature mouse oocytes (Valsangkar and Downs, 2015; Hardie and Pan, 2002).

MacDonald *et al.* (2003) also demonstrate citrate oscillations in β-cells, stating that the citrate profile parallels that of ATP production, and that the ATP/ADP and NAD/NADH ratios control citrate oscillations. Production of oxaloacetate for citrate synthesis is dependent on pyruvate carboxylase activation, enhanced by increased acetyl coA production, so it may be possible that oscillations in FAD seen in response to etomoxir reflect the oscillations of citrate in response to fluctuations of acetyl coA production (Sugden and Holness, 2011).

Many previous studies have described a shift in glucose metabolism seen in response to inhibited β-oxidation (Sturmey and Leese, 2008; Hewitson and Leese, 1993; Merrill *et al.* 2002), suggesting an increase in alterative substrate metabolism for energy generation, or perhaps a lift in the block of glycolysis by reduction of citrate formation. This is an example of what is known as the Randle cycle, which describes a balance between lipid and glucose metabolism where β-oxidation governs

inhibition of glycolysis (Hue and Taegtmeyer, 2009; Randle *et al.* 1963). This glucose-fatty acid cycle may come into effect with inhibition of FA oxidation, and may explain mechanisms induced at the blastocyst stage, where glycolysis block is alleviated, but may also explain the balance in pyruvate and fatty acid metabolism observed.

Glycolysis is initiated at blastocyst stage, but it is possible that the Warburg effect comes into play before blastocyst stage is reached. The Warburg effect is often seen in highly proliferative cells e.g. cancerous cells, when pyruvate is directed away from the TCA cycle in order to produce lactate, in order to support an elevation in glycolytic mechanisms. Fatty acid oxidation remains to maintain ATP generation from oxidative phosphorylation, 'freeing up' pyruvate for use elsewhere (Krisher and Prather, 2012). This could explain the increased response of blastocyst FAD autofluorescence to inhibited β-oxidation, but obviously more investigation into this area is required.

While Dumollard *et al.* (2004) explain that Ca^{2+} transients cause FAD oscillations, the dependence does not lie in both directions. There was no effect of inhibition of β-oxidation on Ca^{2+} transients seen during egg activation by PLCζ. ATP is required for IP_3 receptor Ca^{2+} release at fertilisation, but as previously shown, the decrease in ATP in response to etomoxir is only temporary, presumably because of a collateral increase in pyruvate uptake. Ca^{2+} oscillations at egg activation occur over a long period of time, so the initial effect of etomoxir on Ca^{2+} is likely lost, while the dampened effect on FAD signal remains. It is shown that the effect of etomoxir on Ca^{2+} release from the ER is manifested in a very small increase, which is negligible compared to the larger effects of ionomycin. This small increase is potentially due to the temporary decrease of ATP production seen, but visible effects are not lasting.

Despite the fact that there appears to be no effect of inhibiting FA metabolism on the normal ER functions and Ca^{2+} levels of the egg, there is found to be an effect seen with too much of the *wrong* type of FA. As previously described in Chapter 5, saturated FAs such as PA have negative effects on egg and embryo development (Nonogaki *et al.* 1994; Van Hoeck *et al.* 2011; 2013; Borradaille *et al.* 2006; Jungheim et al. 2011a; Valckx *et al.* 2014; Wu *et al.* 2012), whereas unsaturated FAs are predictive of increased developmental potential (Haggarty *et al.* 2006; Matorras

et al. 1998). OA in particular is described to reverse the negative effects of PA by stopping certain transcription responses to palmitate (Rutkowski *et al.* 2006; Das *et al.* 2010) and promoting TAG production and LD formation, decreasing lipotoxicity effects (Aardema *et al.* 2011, 2013; Cnop *et al.* 2001; Valckx *et al.* 2014). This increase in LD number was seen by CARS imaging of oocytes supplemented with OA during maturation. While no quantitative analysis was possible the time-frame in order to support this, there is certainly a potential to investigate this further. Addition of PA during IVM had no visible effects on LD distribution, but it is likely that the associated effects are on a more molecular level.

Large doses of PA are known to cause a full ER stress response (Rutkowski *et al.* 2006; Das *et al.* 2010), likely to lead to various other damage to the egg or embryo, henceforth reducing rates of fertilisation and blastocyst development (Sutton-McDowall *et al.* 2016; Wu *et al.* 2012). Here, it is shown that feeding eggs with detrimental concentrations of PA has a negative effect on IP_3 receptor Ca^{2+} release, this effect exaggerating with increasing concentrations of exposure, as would be seen in overweight or obese women. Whereas, feeding eggs with OA during IVM has a positive effect on IP_3 receptor Ca^{2+} release, releasing more Ca^{2+} than in control eggs. Certain negative effects of excess fatty acid exposure, such as embryonic arrest, can be rescued by antioxidants, suggesting lipid peroxidation and ROS to blame. However, effects of PA cannot simply be rescued by antioxidant addition, indicating that PA uses a different mechanism to induce embryonic arrest (Nonogaki *et al.* 1994). Zhang *et al.* (2012) show that BAPTA used to chelate Ca^{2+} in ER stress situations, significantly reduced PA-induced cell death. In the present study, it is suggested that this is likely to be due to the inhibition of SERCA pumps in the ER membrane, promoting Ca^{2+} release through IP_3 receptors and preventing re-uptake of Ca^{2+} into the ER. This would also support findings of the instantaneous response of Ca^{2+} release from the ER with PA addition, although results here were inconsistent and require further investigation.

It would be interesting to investigate this notion further. CARS has been previously used to image deuterium-labelled isotopic analogues of FAs where hydrogens are replaced with radioactive deuterium. The C-D bond has a vibrational resonance with a distinct CARS peak detectable independent of CH_2 (Schie *et al.* 2013). CARS imaging of deuterium-labelled OA and PA would be interesting to demonstrate the

loss of lipid from LDs as well as the incorporation of FAs into LDs under different metabolic conditions. DiO is a fluorescent membrane dye known to stain continuous membranes within the cytoplasm such as the ER. Simultaneous CARS and TPF imaging of LDs and ER, respectively, alongside FA incubation would give more insight into the formation of LDs and the differences occurring with FA exposure. CARS imaging of newly-formed LDs may be resolution-limited, as these are likely to be small.

In this chapter, it was found that FA metabolism contributes a substantial amount to the resting redox level in mammalian eggs and embryos. It appears that this metabolism is in balance with pyruvate as an alternative substrate, yet appears less significant in later embryo stages, when glycolysis becomes the main provider of ATP. LD distribution appears to reflect the level of FA metabolism occurring in the egg or embryo, with dispersion of LDs indicating an increased capacity for β-oxidation, while an increase in LD clustering reflects a decrease in FA metabolism. The negative effects of PA previously described appear to be due to action at the ER SERCA pumps, affecting the Ca^{2+} storage of the cell, and hence promoting damage to other organelles.

Chapter 8. General Discussion

8.1. Summary of Findings

The view of this thesis was to establish CARS microscopy as a non-invasive technique of oocyte and embryo imaging, with chemically-specific and 3D imaging capabilities. The motivation behind this work is the requirement for clinical techniques of oocyte and embryo quality assessment that are more effective than current methods, and can be done in a way that does not harm the subsequent development of the egg or embryo. Also considered was the lack of in-depth investigation into the content of fatty acids as a vital metabolic substrate in mouse and human oocytes and embryos, and to what extent lipid metabolism is occurring in the mouse egg.

8.1.1. CARS Microscopy as a Non-Invasive Tool for Oocyte, Egg and Embryo Assessment

In Chapter 3, it was shown that CARS microscopy can be used as an effective tool to specifically assess the presence and distribution of LDs in cells across all stages of oocyte and pre-implantation embryo development. CARS was able to resolve individual droplets in live oocytes and embryos, unlike previous efforts of assessment also using multiphoton techniques (Watanabe *et al.* 2010). With the ability to visually assess CARS images, and quantitatively analyse the size, number and proximity of LDs, it was found that LD distribution changes significantly as the egg and embryo continues development. At the prophase-arrested GV stage, oocyte LDs are homogeneously dispersed throughout the cytoplasm, save for the GV itself. LDs at the MII stage, however, showed an increase in LD clustering. Although LD movement is known to occur, mainly dependent on the action of microtubules, the mechanisms and reasoning behind this phenomenon of LD aggregation was at first unclear. CARS images of mouse embryos after fertilisation demonstrated that after the 8Cell stage was reached, large, singular LDs became more apparent, and LDs of

the morula and blastocyst stages were much fewer and larger than the uniformly-small LDs previously imaged. It was therefore postulated that this LD clustering occurs as a precursor to LD fusion. While LD fusion events are rare, it seems a likely explanation for the patterns seen in LD distribution and size. It would further understanding if the total volume of LDs in earlier embryo stages, then the total volume of LDs present in the blastocyst were analysed, to observe how much lipid is conserved or lost, or to examine whether fusion is likely. It would also be of interest to inhibit LD fusion by inhibition of Fsp27, or SNARE proteins in order to monitor how this affects morula and blastocyst LDs.

It was found that the distribution and characteristics of LDs is somewhat reflective of the oocyte or embryo's metabolic activity. It is known that glycolysis commences in the mouse embryo at blastocyst stage, and the fusion of LDs may be indicative of a decreased requirement for fatty acid metabolism at this stage of embryonic development. This idea was certainly supported by findings presented in Chapter 7, when starvation of MII eggs of pyruvate as a metabolic substrate caused a significant dispersion of LDs. Forcing the egg to metabolise its fatty acid stores for energy production appeared to require an increase in available LD surface area for FA liberation, suggesting a wide dispersion of LDs is an indication of prevalent β-oxidation. Furthermore, inhibiting FA metabolism with the FA uptake inhibitor, etomoxir, caused a significant increase in LD clustering. It was apparent that when LDs are not supplying FAs for mitochondrial metabolism, LD aggregation is enforced. It would be interesting to investigate the surface area of aggregates compared to dispersed individual droplets in order to determine how much LD surface area is available, or conversely, unavailable, to mitochondria under such conditions. While this explanation for LD clustering and fusion is logical and likely, there is still some ambiguity as to the mechanisms responsible for clustering at the MII stage. Oxidative phosphorylation dominates metabolism at both GV and MII stages, however, the arrest at different stages of the meiotic cycle may require different metabolic processes. It is likely that further investigation is required.

We were also able to show in Chapter 4 that this assessment of mouse egg and embryo LDs was in fact compatible with continued egg and embryonic development. Label-free imaging of oocytes with CARS before allowing them to mature *in vitro*

produced MII eggs, and imaging of freshly-fertilised zygotes allows continued development to the blastocyst stage. Despite the fact that CARS imaging of embryos at the 2Cell stage halted their development, this was attributed to the particular vulnerability of mouse embryos at this stage, where zygotic genome transcription is activated. Imaging embryos at the 4Cell stage allowed continued development. In humans, ZGA occurs at the 4Cell stage, so it is likely that CARS assessment of the earlier 2Cell stage is both more practical and more desirable. It is clear that further experiments are required to confirm the viability of these CARS-imaged eggs and embryos. Firstly, MII eggs which have undergone CARS assessment before or after maturation must have the ability to be fertilised and undergo embryonic development. Secondly, blastocysts derived from zygotes imaged with CARS must be implanted into surrogate mothers and develop to full term before CARS microscopy can be considered as a completely viable technique for *in vitro* egg or embryo assessment.

In order for CARS to be used as a prospective tool of egg or embryo quality assessment, we must first distinguish which parameters or indicators of developmental potential can be assessed using CARS. Thus, it would be of interest to correlate parameters already available, such as total LD number, size and aggregation, as well as further parameters measurable, with existing measures of egg or embryo quality. It has been established that whilst a great deal of information can be obtained from scanning a full egg or embryo, this prior knowledge means that a quick CARS scan through a small portion of the egg or embryo can provide enough qualitative and quantitative information for an informed assessment to be made to the trained eye.

8.1.2. CARS Microscopy as a Chemically-Specific Method of Oocyte, Egg and Embryo Assessment

Further to the assessment of LD distribution, we have shown that CARS microscopy can be used as a chemically-specific tool to measure the amount and type of lipids present in mouse egg and embryo LDs. In Chapters 3 and 7, it was shown that the proportional relationship between the CARS signal at 2850cm^{-1} and the number of CH_2 bonds in the focal volume allowed the calculation of the total amount of lipid

per LD present in different egg and embryo populations. Very little difference was seen between populations and conditions, giving interesting insight into the metabolic processes occurring at different developmental stages, or under different metabolic conditions. Even under circumstances where fatty acid metabolism was enforced e.g. under pyruvate-starved conditions, the smaller about of lipid measured per LD was an insignificant change. It could be postulated that the broad dispersion of LDs in this case means mobilisation of fewer FAs from each LD, as they are easily accessed by mitochondria throughout the cytoplasmic volume. Meanwhile, it may be possible that in cases where lipid metabolism is inhibited, there is no increased storage of FAs into LDs to accompany the LD clustering observed.

In Chapter 5 it was demonstrated that CARS can also be used to investigate the chemical lipid content of LDs in developing eggs and embryos. Whereas previous studies into the lipid content of mammalian eggs has used destructive techniques which require a large number of cells (McEvoy *et al.* 2000), hyperspectral imaging allows the extraction of Raman spectra from different spatial positions within individual imaged eggs or embryos, allowing visualisation of the types of FAs making up the TAGs contained in LDs in a non-invasive yet chemically-specific manner.

It was found that GV and MII eggs, 2Cell and morula-stage embryos all possessed LDs which contained a cocktail of poly-unsaturated FAs, distinguished by the peaks in their Raman spectra indicating a larger amount of chain disorder ($2930cm^{-1}$) and double bonds ($3010cm^{-1}$). This was compatible with the previous findings that unsaturated FAs are better for egg and embryo development (Aardema *et al.* 2011; Haggarty *et al.* 2006), and thus are more likely to be found in the developing egg/embryo. However, it was found that LDs of blastocyst embryos had differing FA content- some LDs gave a more PUFA Raman profile, whereas others gave profiles more indicative of saturated FAs. This was an interesting phenomenon, and while spatial positioning of LDs with differing composition did not appear to be of importance, it is possible that they are assigned different cellular responsibilities. Due to very low n numbers, it would be of interest to examine multiple LDs from multiple blastocyst embryos. Haggarty *et al.* (2006) describe that embryos with higher amounts of saturated FAs have a lesser capability of reaching blastocyst stage, thus hyperspectral CARS may be an effective method of non-invasively

assessing the chemical content of eggs and embryos, in order to give an indication of developmental potential.

Also shown in Chapter 5 and Chapter 7 are the effects of feeding oocytes and embryos with unsaturated and saturated FAs. It is known that the presence of FFAs in the follicular fluid reflect diet, and that specific FAs e.g. saturated PA and unsaturated OA, are taken up into the ovary. Less is known about the FA accumulation of oocytes themselves, but it is clear that uptake occurs during maturation, and this is largely influenced by their environment (Leroy *et al.* 2014; Fair, 2003). It is known that PA in particular is a saturated FA which causes developmental harm to mammalian eggs and embryos, whereas OA is a mono-unsaturated FA with positive effects on lipid storage and PA-induced cellular stress (Aardema *et al.* 2011). It was found in the present study that feeding oocytes with OA or PA was able to change their LD composition in the direction of MUFAs or saturated FAs, respectively. Eggs from women with a known high fat diet or obesity will have been exposed to detrimental high concentrations of FAs. It is potentially viable that eggs from such patients may be assessed for their actual lipid content using hyperspectral CARS, and subsequently may be exposed to tailored culture conditions which may improve the developmental potential of these oocytes.

Another advantage of non-invasive lipid assessment is the potential to correlate lipid content with cryosurvival. Many ART clinics offer egg or embryo freezing in cases where embryo transfer is not immediately required. This cryopreservation is less effective in oocytes and embryos of species with higher lipid content, i.e. domestic animals, the higher lipid content conveying a lower tolerance to freezing (Wirtu *et al.* 2013; Takahashi *et al.* 2013). It is therefore possible that an assessment of cryosurvival could also be performed using CARS once effective parameters have been established, as a tool for optimising ART cycles.

In Chapter 6 we were able to expose CARS microscopy as a superior method of chemical identification in oocytes and embryos. Fluorescent lipophilic stains conventionally used to investigate LD biology demonstrate many shortcomings that can be overcome by CARS imaging. Through the use of simultaneous CARS and TPF imaging of fluorescent dye-stained LDs, it was possible to investigate the lack of specificity and unpredictable staining patterns when using such dyes. It was found

that some of the LDs identified by CARS were not stained by the dyes, and other structures emitting fluorescence did not produce a CARS signal and were thus not LDs. We can be certain that CARS microscopy at the 2850cm^{-1} vibrational resonance will only image lipids present in the imaged cells, and thus we can trust that the lack of correlation between CARS and TPF signals can be attributed to the lack of fluorescent dye specificity and their inconsistent staining pattern. Furthermore, CARS imaging uses NIR wavelengths of light which is less damaging to cells than high intensity excitation wavelengths used in conventional fluorescence techniques. An additional benefit of CARS compared to fluorescence microscopy, certainly in ART applications, is its compatibility with live cell imaging, allowing continued development after imaging. Fluorescent techniques often require fixation of cells, and even those which can maintain cell viability cannot be used in clinical applications due to their invasive nature.

8.1.3. Contribution of Lipid Metabolism to Mitochondrial Redox State in the Mouse Egg and Embryo

In Chapter 7, the extent of lipid metabolism within the mouse egg and embryo was investigated, and the effects of altering lipid metabolism on ER and mitochondrial function was assessed through various assays. It is known that lipid metabolism is occurring in the mitochondria of the mouse egg and embryo, and that both increases (e.g. high fat diets and obesity) and decreases (e.g. chemical inhibition) in β-oxidation are associated with a decline in developmental success, but the significance of this metabolic pathway was yet to be elucidated.

While Dunning *et al.* (2010) demonstrated that they could measure FA oxidation in mouse eggs and embryos, they were not able to determine how much it contributes to overall FADH or ATP production. Taking advantage of the autofluorescence of FAD^{++} and NADH allowed investigation of the effects of FA oxidation inhibition on mitochondrial redox state throughout development and also enabled the contribution of FA metabolism to resting redox state to be measured in mouse oocytes for the first time. It was found that in GV and MII eggs, the metabolism of lipids is responsible for ~40% of the mitochondrial FAD^{++}/FADH redox state, the other ~60% through

pyruvate oxidation and any other, minor metabolic substrates. Inhibiting this metabolism at various developmental stages and seeing the effect on the FAD^{++}/FADH redox state gave insight into the level of FA metabolism occurring throughout embryonic development. At the GV and MII stages, an oscillatory response of FAD autofluorescence is seen with etomoxir addition, suggesting an over-compensatory uptake of pyruvate to account for the loss of FA as a substrate. This oscillation and pyruvate compensation suggests a balance between FA oxidation and pyruvate metabolism for maintenance of ATP level. Luminescence assays of ATP certainly showed that removal of FA as a substrate had a temporary effect on ATP production, a resting level shortly regained higher than the initial resting ATP. Again, this points towards an over-compensation of pyruvate uptake, supported by the fact that the previous ATP level was not regained after pyruvate uptake inhibition. Measurement of this effect on MMP shows that inhibition of FA oxidation leads to hyperpolarised (more negative) MMP, again in agreement that with increased substrate uptake i.e. pyruvate, the MMP is increased. The oscillations seen are indicative of the cyclical regulation of pyruvate and FA metabolism as discussed in Chapter 7. β-oxidation inhibition during embryonic stages, however, appeared to maintain this increased uptake of pyruvate, but lost the oscillation in FAD response, signifying a change in the level of metabolism occurring as development continues. This is suggestive of a decreased reliance on FA metabolism as a source of metabolic energy, as the embryo moves towards the glycolytic switch at blastocyst stage and corresponds to the LD aggregation and fusion patterns observed with CARS imaging at these developmental stages. This switch in metabolism is likely to see the decreased inhibition of glucose metabolism, in association with the lowered FA oxidation, as described by mechanisms in the Randle cycle (Hue and Taegtmeyer, 2009; Randle *et al.* 1963).

Also investigated was the mechanisms of PA-induced ER stress. PA is known to cause a stress response in the ER, which in turn causes altered mitochondrial activity and production of ROS. This process is extremely detrimental to cellular organelles and processes, leading to apoptosis and decreased developmental success in oocytes and embryos (Sutton-McDowall *et al.* 2016; Wu *et al.* 2012), however, the mechanism through which PA induces this ER stress is as yet unclear. IVM of

oocytes with high concentrations of PA simulated the physiological levels of PA estimated by Wu *et al.* (2012) to reside in the follicular fluid of obese women, and concentrations known to cause altered metabolism and apoptosis in mammalian embryos (Wu *et al.* 2012; Jungheim *et al.* 2011). It is estimated that physiological follicular fluid PA concentrations of ~115μM exist in women of a moderate weight, while eggs of obese women may be exposed to up to 660μM PA (Wu *et al.* 2012), whereas Jungheim *et al.* (2011) found that exposure of embryos to PA concentrations of 250μM caused altered metabolism and long-term growth defects, both in the foetus and post-birth. In the current study, incubation of oocytes with 100-400μM PA greatly reduced the Ca^{2+} release in response to SERCA pump inhibitor thapsigargin, providing understanding that the negative effects of PA are active through SERCA pump inhibition. This inhibition prevents the re-uptake of Ca^{2+} into the ER, thus the thapsigargin-induced Ca^{2+} release is lower, due to an emptier intracellular Ca^{2+} store. SERCA pump inhibition also elevates cytosolic Ca^{2+} concentrations, which enters the mitochondria, increasing production of ROS and uncoupling oxidative phosphorylation (Wu *et al.* 2012).

The relative spatial distribution of mitochondria and LDs was investigated using simultaneous CARS imaging of LDs and TPF imaging of mitochondria stained with a GFP. Although this method did not fully clarify the co-localisation of LDs and mitochondria, it did suggest that LDs are spatially available for mitochondrial metabolism of their liberated FAs. It has been previously shown that mitochondria and LDs within the pig oocyte reside within 10nm of each other (Sturmey *et al.*, 2006), and the LD protein perilipin 5 has been found to provide a mechanical linkage between LDs and mitochondria, though further investigation is required (Wang *et al.* 2011a).

8.1.4. Comparison of Mammalian Species

The amount of lipid content and extent of lipid metabolism differs greatly between mammalian species, and study of these species leads to increased understanding of the processes occurring and how and why they differ. Domestic animals such as pigs, sheep and cows are often studied in order to optimise animal breeding programmes, required in farming technologies. Oocytes of rodents can be used as a

suitable model for human oocytes, as their cellular processes and development draw many parallels. This is particularly useful for the investigation into improving reproductive technologies such as IVF, without the ethical and legal issues arising with use of human tissue. Studies into the clinical success of ART using various experimental parameters allow the investigation into the competence of existing techniques, and variables which may affect achievement of subsequent pregnancy and live birth, such as the composition of follicular fluid or spent culture media. However human eggs, although the best species for investigation of ART success, are not readily available in large numbers or good quality- studies in human eggs are often performed on failed-fertilisation oocytes, which clearly have existing developmental difficulties.

In this study, we were able to examine bovine eggs with CARS in the same way as mouse oocytes. Hyperspectral CARS imaging showed that, like in the mouse egg, bovine oocyte LDs are composed of mainly PUFAs. This suggests that these types of FAs are the most beneficial to the developing egg, and possibly indicating that PUFAs are more readily esterified into TAGs for storage in LDs. This supports the notion that saturated FFAs are more detrimental to the egg due to their presence in the cytoplasm, allowing accumulation of long-chain acyl-coAs, diacylglyerides (DAGs) and ceramides which activate alternative pathways and alter metabolic processes (Nolan and Larter, 2009; Turner and Robker, 2014).

However, in contrast to mouse eggs, CARS images revealed bovine MII LDs to be larger than those observed in mouse oocytes (>1μm), varying in size, and spatially isolated with no obvious clustering. It appears that these differences signify the variations previously observed between mouse and bovine lipid metabolism. It is thought that those species whose eggs contain a larger amount of lipid, such as pigs and dogs, tend to rely further on FAs as a metabolic substrate. While this idea makes logical sense, it is unclear why eggs and embryos of these different species contain and use varying amounts of lipid. It is not, for example, solely eggs and embryos of ruminants which contain large droplets and large amounts of lipid metabolism. Rodents and humans are considerably different organisms, however their egg and embryo biology is comparatively similar.

One of several considered factors responsible for this difference in mammalian reproductive cells is the litter size. For example, pig and dog oocytes which have

dark cytoplasms containing lots of lipid are polytocous (producing more than one offspring per birth). However, horse and minke whale oocytes also contain large amounts of lipid and are monotocous like the human. The mouse is also polytocous, and its oocytes have a clear cytoplasm containing fewer smaller LDs, like the human (Prates *et al.* 2014). Phylogenetic connections have also been suggested (Prates *et al.* 2014), as both horse and pig are ungulates; however, cows, sheep, rodents and humans all belong to the chordate phylum and differences are still notable. It also doesn't appear that oestrous cycles are responsible, for dogs are mono-oestrous, pigs and mice are poly-oestrous, and sheep and cattle show seasonal oestrous cycles. It could be that the amount of lipid metabolism and lipid content are purely species-specific.

Rates of embryonic development to blastocyst and the processes that occur during this time frame are relatively similar between species, but the events surrounding embryonic implantation into the uterine wall has also been suggested as a responsible motive for large lipid stores. The varying methods of embryo implantation are described by Lee and DeMayo (2004): dogs, pigs, cows and sheep undergo what is known as centric implantation, where the blastocyst fuses with the uterine wall without penetrating it; rodents exhibit eccentric implantation, where the uterine epithelium surrounds the embryo, while, humans undergo interstitial implantation, involving blastocyst invasion of the endometrial lining. While these variations are marked, it is unlikely that this has an effect on the metabolic processes prior to implantation. Regardless of the method of implantation, the blastocyst of all species will reach the maternal blood supply and thus their internal lipid reservoir is of lesser metabolic importance.

The timing of embryonic implantation is a valid suggestion put forward. Bovine embryos do not implant until ~day 30 post-fertilisation, compared with attachment of dog and sheep blastocysts ~21-22 days, cats ~day 13, porcine embryos ~day 11, ~day 6 in the human and ~day 4 in mouse (Prates *et al.* 2014; Lee and DeMayo, 2004; Concannon *et al.* 2001; Giminez and Rodning, 2007; Schatten and Constantinescu, 2008; Tsutsui and Stabenfeldt, 1993). Incredibly, goat blastocysts do not implant until ~52 days post-fertilisation but their lipid content is thought to be intermediate, similar to that of sheep (Giminez and Rodning, 2007). It is possible that this prolonged pre-attachment time means that a higher amount of internal

metabolic substrate is required, in order for the embryo to survive a number of days before access to maternal sustenance. However, it is arguable that because glycolysis is switched on at blastocyst development, the lipid stores are required to a lesser capacity past this stage.

Once implantation has occurred, there are further differences recorded, such as the fact that porcine embryos maintain their ICM for ~6-7 days after implantation, compared to ~1-3 days in mouse and human embryos (Oestrup *et al.* 2009). It is clear that the investigation into the differences between species metabolism must be furthered.

It is possible that a balance of pyruvate and FA metabolism occurs in oocytes and embryos of other species. For example, pyruvate is included at 0.2mM in culture media for mouse and human eggs, whilst culture media for pig oocytes may contain 2-5mM (Dumollard *et al.* 2009; Kikuchi *et al.* 2002). This appears to reflect the amount of lipid metabolism occurring in these species, and neither pyruvate concentration is compatible with the egg survival of the other species: 2-5mM is far too high for mouse or human egg survival, while 0.2mM pyruvate is insufficient for continued porcine egg development. The increased pyruvate metabolism appears to reflect the increased lipid metabolism, possibly to reduce the production of ROS if they were to solely rely on FAs as a source of ATP.

It would therefore be of further interest to image eggs and embryos of multiple alternative mammalian species with CARS in order to improve understanding of lipid storage and metabolism. It would be interesting to compare the LD distribution of other cell types, and eggs or embryos of other species with known variations in lipid metabolism, with the information obtained in this study about the LD spatial patterning and the level of lipid metabolism present in the mouse egg or embryo. Ultimately, examination of human eggs with CARS microscopy would be invaluable for investigation into LD lipid composition and distribution, and perhaps the correlation of this information gained through CARS with increased or decreased development, or failed fertilisation.

8.2. Future Directions

8.2.1. Limitations of this study

The most notable limitation of this study is the limited quantification of lipids allowed by CARS. Although CARS is able to provide vast amounts of information as to the number of LDs, their aggregation patterns, and the amount and type of lipids present, it is not without its weaknesses. Calculation of $\langle\frac{TL}{LD}\rangle$ allows us to estimate the 'amount of lipid per LD' but we are not able to directly quantify the exact amount of lipid present in each LD. While the CARS signal is proportional to the number of chemical bonds present in the focal volume, no absolute number of CH_2 bonds or indeed FAs are given. It is also not currently possible to specifically identify individual FAs present in LDs, as we are not able to delineate either chain length or location of double bonds within unsaturated chains. Furthermore, while it is assumed that lipids present in LDs are TAGs, this is not discernible, and it is thus far impossible to image the lipid monolayer surrounding LDs, the lipid bilayer comprising the cell membrane, or individual FAs within the cell cytoplasm.

In the present study it was not possible to verify the concentrations of palmitic and oleic acid-BSA conjugates, and thus the amounts added to IVM environments. This may prove useful to further measure the effects of FA supplementation to eggs or embryos, before high fat diets are introduced. An additional limitation is the observation that thus far, there has been no quantification of later embryo-stage LDs, thus no direct comparison or statistical relevance can be determined. Only a portion of the egg or embryo was imaged throughout this study, which, while giving excellent insight into the LD number and distributions at different developmental stages, does not give a beneficial representation of the whole egg or embryo. Low n numbers in some experiments must also be increased in order to verify certain results observed in this study.

There are also suggested weaknesses of mice as model organism. While eggs and embryos of the particular species used in this study mimic those of humans in multiple ways, use of an alternative species is often criticised.

8.2.2. Further investigations

As already mentioned, the results of this project lend themselves to many further investigations into the use of CARS as a diagnostic tool for egg and embryo developmental potential. First, quantitative analysis of embryos must be optimised in order to investigate their lipid biology in the same capacity as the previous developmental stages. Information obtained using CARS must be correlated with embryo implantation and development to live birth. It must also be correlated with the multiple known markers of egg and embryo quality e.g. GV chromosome alignment, MII cytoplasm granularity, and embryonic cell apoptosis. It would be interesting to observe CARS imaging of oocytes from older women, which are proven to have chromosomal and mitochondrial abnormalities, likely impacting on their metabolic processes (Eichenlaub-Ritter *et al.* 2003, 2011; Wilding *et al.* 2001; Nagai *et al.* 2004). Mitochondrial transfer or nuclear transfer to a cytoplasm of a better quality oocyte are proven to improve developmental success, and aged eggs often have higher amounts of ROS and peroxidised FAs so assessment of their lipid metabolism would be of interest (Nagai *et al.* 2004; Craven *et al.* 2010; Bogliolo *et al.* 2013; Gioacchini et al 2014).

As described, further comparison of mammalian oocytes and embryos are required to decipher the differences in lipid content and metabolism seen in such similar cellular models. Also required is the further investigation into how the ER, LDs and mitochondria interact, in order to shed light on LD formation and degradation. It is not clear whether Brownian motion of LDs may obscure results, thus it would be interesting to test whether the movement of LDs is facilitated passive, and whether there is an effect of temperature on their number or distribution. It is postulated that methods of LD regulation in mammalian oocytes and embryos, including autophagy- the degradation of intracellular vesicles through the action of lysosomes- may be upregulated in situations of cellular stress-response. Thus, in addition, a detailed study into how the oocyte or embryo regulates their lipid stores, and copes with stress would be valuable to increasing our understanding of these dynamic organelles.

8.2.3. The use of CARS Microscopy to Improve Human ART

There is the potential for the use of CARS microscopy to improve current ART outcomes. The knowledge gained from investigating mouse embryos with CARS has greatly improved the understanding of lipid metabolism in a model species, and promises to broaden this knowledge with further investigation.

Fertility problems frequently occur in obese women or those with a high fat diet, likely due to the metabolic alterations that occur with increased exposure of oocytes to excess FAs within the ovarian follicles (Leary *et al.* 2015). While factors such as body mass index (BMI) and follicular fluid FA composition can be indicators of an altered metabolism, BMI may not be a sufficient measure of a woman's diet or body fat percentage. Follicular fluid gives a better indication of the conditions in which an oocyte has matured, but CARS can be used to look at the oocytes or embryos themselves, enabling informed quantitative analyses to be made on an individual egg or embryo basis. This also addresses the issues of analysis of metabolism as an embryo selection method. It is well-documented that an increased metabolism of FAs correlates with a decreased oocyte or embryo developmental competence (Wu *et al.* 2010; Jungheim *et al.* 2010; Igosheva *et al.* 2010; Van Hoeck *et al.* 2013). However, it is likely that eggs from individual women have variations within their own population, signifying that a method of analysis of individual oocytes is more necessary than analysis of the follicular fluid.

It is certainly true that if CARS was to be used as a tool for improvement of ART, a set of parameters, i.e. not solely an analysis of their lipid content, must be established in order to identify oocytes or embryos of an increased developmental potential. Additional parameters revealed by this study to be identifiable through CARS, such as the LD distribution, size, number, composition, along with other measurable quantities, may allow an informed egg or embryo selection. While CARS may currently prove an expensive tool for such methods, it is possible that informed decisions may be made using only DIC, based on knowledge gained from further investigation into CARS and its applications in human embryo imaging.

With lipid analysis of individual oocytes or embryos, there is the capacity to further improve the developmental success of cells deemed to have a lower quality, with specifically-tailored culture media. Suppression of β-oxidation in oocytes previously exposed to excess FA concentrations has been shown to restore their developmental

competence, likely through the reduction of ROS production (Van Hoeck *et al.* 2013). Meanwhile, addition of L-carnitine has been shown to increase quality of oocytes from non-obese women (Dunning and Robker, 2012). Alternatively, as stated previously, the addition of PUFAs in embryo culture media may improve the quality of those exposed to damaging concentrations of saturated FAs. Thus, CARS may be able to identify multiple factors comprising the quality of an egg or embryo, allowing a system of specifically-designed culture media to benefit their further development.

8.2.4. Concluding Remarks

The increased understanding of oocyte and embryo cellular processes that promote or compromise the growth and development of the mammalian oocyte or embryo are vital in the improvement of ART. The expansion of such knowledge and the improved assessment of oocyte and embryo quality relies on the development of a more effective, non-invasive technique. This thesis brings to light some of the exciting capabilities of CARS microscopy as an imaging tool for label-free, and chemically-specific quantitative assessment of major metabolic processes within the mammalian egg or embryo. It provides an insight into the metabolic mechanisms occurring throughout mouse egg and embryo development, and promises the potential for CARS to expand upon this knowledge. There is an optimistic aspiration that CARS microscopy could have eventual successful application as a non-invasive, highly-quantitative method of egg and embryo quality assessment.

References

Aardema, H., Vos, P., Lolicato, F., Roelen, B., Knijn, H.M., Vaandrager, A.B., Helms, J.B. and Gadella, B.M. 2011 Oleic Acid Prevents Detrimental Effects of Saturated Fatty Acids On Bovine Oocyte Developmental Competence *Biol Reprod* **85** 62–69

Aardema, H., Lolicato, F., Van De Lest, C.., Brouwers, J.F. Vaandrager, A.B., Van Tol, H., Roelen, B., Vos, P. J., Helms, B and Gadella, B.M. 2013 Bovine Cumulus Cells Protect Maturing Oocytes from increased Fatty Acid Levels by Massive Intracellular Lipid Storage *Biol Reprod* **88**(6):164 1-15

Abe, H., Yamashita, S., Satoh, T. and Hoshi, H. 2002 Accumulation of Cytoplasmic Lipid Droplets in Bovine Embryos and Cryotolerance of Embryos Developed in Different Culture Systems using Serum-Free or Serum-Containing Media *Mol Reprod Dev* **61** 57-66

Acton, B.M., Jurisicova, A., Jurisica, I. and Casper, R.F. 2004 Alterations in Mitochondrial Membrane Potential During Preimplantation Stages of Mouse and Human Embryo Development *Mol Hum Reprod* **10**(1) 23-32

Adamiak, S.J., Powell, K., Rooke, J.A., Webb, R. and Sinclair, K.D. 2006 Body Composition, Dietary Carbohydrates and Fatty Acids Determine Post-Fertilisation Development of Bovine Oocyte *in vitro Reprod* **131** 247-258

Ajduk, A. and Zernicka-Goetz, M. 2012 Advances in Embryo Selection Methods *F1000 Biol Rep* **4**:11

Ambruosi, B., Lacalandra, G.M., Iorga, A.I., De Santis, T., Mugnier, S., Matarrese, R., Goudet, G., and Dell'Aquila, M.E. 2009 Cytoplasmic Lipid Droplets and Mitochondrial Distribution in Equine Oocytes: Implications On Oocyte Maturation, Fertilisation and Developmental Competence After ICSI *Theriogenology* **71** 1093-1104

Anderson, S., Bankier, A.T., Barrell, B.G., De Bruijn, M.H.L., Coulson, A.R., Drouin, J., Eperon, I.C., Nierlich, D.P., Roe, B.A., Sanger, F., Schreier, P.H., Smith, A.J.H., Staden, R. and Young, I.G. 1981 Sequence and Organisation of the Human Mitochondrial Genome *Nature* **290** 457-465

Apparicio, M., Ferreira, C.R., Tata, A., Santos, V.G., Alves, A.E., Mostachio, G.Q., Pires-Butler, E.A., Motheo, T.F., Padilha, L.C., Pilau, E.J., Gozzo, F.C., Eberlin, M.N., Lo Turco, E.G., Luvoni, G.C. and Vicente, W.R.R. 2012 Chemical Composition of Lipids Present in Cat and Dog Oocyte by Matrix-Assisted Desorption Ionization Mass Spectrometry (MALDI-MS) *Reprod Dom Anim* **47**(6) 113-117

Bakos, H.W., Henshaw, R.C., Mitchell, M. and Lane, M. 2010 Paternal Body Mass index Is Associated with Decreased Blastocyst Development and Reduced Live Birth Rates Following Assisted Reproductive Technology *Fertil Steril* **95**(5) 1700-1704

Barbehenn, E.K., Wales, R.G., and Lowry, O.H. 1974 the Explanation for the Blockade of Glycolysis in Early Mouse Embryos *Proc Nat Acad Sci USA* **71** 1056-1060

Barcelo-Fimbres, M. and Seidel Jnr., G.E. Cross-Validation of Techniques for Measuring Lipid Content of Bovine Oocytes and Blastocysts 2011 *Theriogenology* **75** 434-444

Bavister, B.D. and Squirrell, J.M. 2000 Mitochondrial Distribution and Function in Oocytes and Early Embryos *Hum Reprod,* **15** (Suppl. 2) 189-198

Bellone, M., Zuccotti, M., Redi, C.M. and Garagna, S. 2009 the Position of the Germinal Vesicle and the Chromatin Organization Together Provide a Marker of the Developmental Competence of Mouse Antral Oocytes *Reprod* **138** 639–643

Bettencourt, EM.V., Bettencourt, C.M.V., Chagas E Silva, J.N., Ferreira, P., Oliveira, E., Romao, R., Rocha, A. and Sousa, M. 2015 Ultrastructural Characterisation of *in vivo*-Produced Ovine Morulae and Blastocysts *Zygote* **23**(4) 583-593

Bianchi, E., Doe, B., Goulding, D., Sanger Mouse Genetics Project, and Wright, G.J. 2014 Juno is the Egg Izumo Receptor and is Essential for Mammalian Fertilisation *Nature* **508**(7497) 483-497

Biggers, J.D., Whittingham, D.G. and Donahue, R.P. 1967 the Pattern of Energy Metabolism in the Mouse Oocyte and Zygote *Zoology* **58** 560-567

Bilodeau-Goeseels, S. and Panich, P. 2002 Effects of Oocyte Quality On Development and Transcriptional Activity in Early Bovine Embryos *Anim Reprod Sci* **71** 143-155

Bogliolo, L., Ledda, S., innocenzi, P., Arui, F., Bebbere, D., Rosati, I., Leoni, G.G. and Piccinini, M. 2012 Raman Microspectroscopy as a Non-invasive tool to Assess the Vitrification-Induced Changes of Ovine Oocyte Zona Pellucida *Cryobiology* **64** 267-272

Bogliolo, L., Murrone, O., Di Emidio, G., Piccinini, M., Arui, F., Ledda, S. and Tatone, C. 2013 Raman Spectroscopy-Based Approach to Detect Aging-Related Oxidative Damage in the Mouse Oocyte *J Assist Reprod Genet* **30** 877-882

Boone, W.R., Higdon, H.L. and Johnson, J.E. 2010 Quality Management Issues in the Assisted Reproduction Laboratory *J Reprod Stem Cell Biotechnol* **1**(1) 30-107

Borradaille, N.M., Han, X., Harp, J.D., Gale, S.E., ory, D.S. and Schaffer, J.E. 2006 Disruption of Endoplasmic Reticulum Structure and Integrity in Lipotoxic Cell Death *J Lipid Res* **47** 2726-2737

Bostrom, P., Rutberg, M., Ericsson, J., Holmdahl, P., andersson, L., Frohman, M.A., Boren, J. and Olofsson, S. 2005 Cytosolic Lipid Droplets increase in Size by Microtubule-Dependent Complex Formation *Ateriosclerosis Thromb Vasc Biol* **25** 1945-1951

Bostrom, P., andersson, L., Rutberg, M., Perman, J., Lidberg, U., Johansson, B.R., Fernandez-Rodriguez, J., Ericson, J., Nilsson, T., Boren, J. and Olofsson, S. 2007 SNARE Proteins Mediate Fusion Between Cytosolic Lipid Droplets and Are Implicated in Insulin Sensitivity *Nature Cell Biol* **9**(11) 1286-1293

Bouniol-Baly, C., Hamaroui, L., Guibert, J., Beaujean, N., Szollosi, M.S. and Debey, P. 1999 Different Transcriptional Activity Associated with Chromatin Configuration in Fully Grown Mouse Germinal Vesicle Oocytes *Biol Reprod* **60** 580-587

Brewer, C.J., and Balen, A.H. 2010 The Adverse Effects of Obesity on Conception and Implantation *Reprod* **140** 347–364

Brison, D.R., Houghton, F.D., Falconer, D., Roberts, S.A., Hawkhead, J., Humpherson, P.G., Lieberman, B.A. and Leese, H.J. 2004 Identification of Viable Embryos in IVF by Non-invasive Measurement of Amino Acid Turnover *Hum Reprod* **19**(10) 2319-2324

Brunet, S., and Maro, B. 2007 Germinal Vesicle Position and Meiotic Maturation in Mouse Oocyte *Reprod* **133** 1069–1072

Bryson, J.M., Cooney, G.J., Wensley, V.R., Phuyal, J.L., and Caterson, I.D. 1996 the Effects of the Inhibition of Fatty Acid Oxidation On Pyruvate Dehydrogenase Complex Activity in Tissues of Lean and Obese Mice *Int J Obes Relat Metab Disord* **20** 738-744

Butcher, L., Coates, A., Martin, K.L., Rutherford, A.J., and Leese, H.J. 1998 Metabolism of Pyruvate in the Early Human Embryo *Biol Reprod* **58** 1054-1056

Campbell, K., and Swann, K. 2006 Ca^{2+} Oscillations Stimulate an ATP Increase During Fertilization of Mouse Eggs *Dev Biol* **298** 225-233

Chang, Y. and Chan, W. 2010 Methylglyoxal Has Injurious Effects On Maturation of Mouse Oocytes, Fertilisation and Fetal Development, via Apoptosis T*oxicol Lett* **193** 217-223

Chatot, C.L., Ziomek, C.A., Bavister, B.D., Lewis, J.L. and Torres, I. 1989 An Improved Culture Medium Supports Development of Random-Bred 1-Cell Mouse Embryos *in vitro J Reprod Fert* **86** 679-688

Chen, H., Kui, C. and Chan, H.C. 2013 Ca^{2+} Mobilisation in Cumulus Cells: Role in Oocyte Maturation and Acrosome Reaction *Cell Calcium* **53**(1) 68-75

Chimento, P.F., Jurna, M., Bouwmans, H.S.P., Garbacik, E.T., Hartsuiker, L., Otto, C., Herek, J.L. and Offerhaus, H.L. 2009 High-Resolution Narrowband CARS Spectroscopy in the Spectral Fingerprint Region *J Raman Spectrosc* **40** 1229-1233

Christians, E., Boiani, M., Garagna, S., Dessy, C., Redi, C.A., Renard, J.P. and Zuccotti, M. 1999 Gene Expression and Chromatin Organisation During Mouse Oocyte Growth *Dev Biol* **207** 76-85

Cillo, F., Brevini, T.A.L., Antonini, S., Paffoni, A., Ragni, G., and Gandolfi, F. 2007 Association Between Human Oocyte Developmental Competence and Expression Levels of some Cumulus Genes *Reprod* **134** 645–650

Ciotti, P.M., Notarangelo, L., Morselli-Labate, A.M., Felletti, V., Porcu, E. and Venturoli, S. 2004 First Polar Body Morphology Before ICSI Is Not Related to Embryo Quality or Pregnancy Rate *Hum Reprod* **19** 2334-2339

Clark, A.M., Thornley, B., Tomlinson, L., Galletley, C. and Norman, R.J. 1998 Weight Loss in Obese Infertile Women Results in Improvement in Reproductive Outcome for All Forms of Fertility Treatment *Hum Reprod* **13**(6) 1502-1505

Cnop, M., Hannaert, J.C., Hoorens, A., Eizirik, D.L. and Pipeleers, D.G. 2001 Inverse Relationship Between Cytotoxicity of Free Fatty Acids in Pancreatic Islet Cells and Cellular Triglyceride Accumulation *Diabetes* **50** 1771-1777

Cohen, J., Edwards, R., Fehilly, C., Fishel, S., Hewitt, J., Purdy, J., Rowland, G., Steptoe, P. and Webster, J. 1985 *In vitro* Fertilisation: A Treatment for Male Infertility *Fertil Steril* **43**(3) 422-432

Collado-Fernandez, E., Picton, H. and Dumollard, R. 2012 Metabolism Throughout Follicle and Oocyte Development in Mammals *Int J Dev Biol* **56** 799-808

Collier, C.A., Bruce, C.R., Smith, A.C., Lopschuk, G., and Dyck, D.J. 2006 Metformin Counters the Insulin-Induced Suppression of Fatty Acid Oxidation and Stimulation of Triglycerol Storage in Rodent Skeletal Muscle *Am J Physiol. Endocrinol Metab* **291** 182-189

Conaghan, J., Handyside, A.H., Winston, R.M.L. and Leese, H.J. 1993 Effects of Pyruvate and Glucose on the Development of Human Preimplantation Embryos *in vitro J Reprod Fertil* **99** 87-95

Concannon, P., Tsutsui, T. and Shille, V. 2001 Embryo Development, Hormonal Requirements and Maternal Responses During Canine Pregnancy *J Reprod Fertil Suppl* **57** 169-179

Coull, G.D., Speake, B.K., Staines, M.E., Broadbent, P.J. and McEvoy, T.G. 1998 Lipid and Fatty Acid Composition of Zona-intact Sheep Oocytes *Theriogenology* **49** 179

Craven, L., Tuppen, H.A. Greggains, G.D., Harbottle, S.J., Murphy, J.L., Cree, L.M., Murdoch, A.P., Chinnery, P.F., Taylor, R.W., Lightowlers, R.N., Herbert, M. and Turnbull, D.M. 2010 Pronuclear Transfer in Human Embryos to Prevent Transmission of Mitochondrial DNA Disease *Nature* **465**(7294) 82-85

Crosier, A.E., Farin, P.W., Dykstra, M.J., Alexander, J.E. and Farin, C.E. 2000 Ultrastructural Morphometry of Bovine Compact Morulae Produced *in vivo* and *in vitro Biol Reprod* **62** 1459-1465

Cui, M.S., Fan, Y.P., Wu, Y., Hao, Z.D., Liu, S., Chen, X.J., and Zeng, S.M. 2009 Porcine Cumulus Cell Influences Ooplasmic Mitochondria-Lipid Distributions, GSH-ATP Contents and Calcium Release Pattern After Electro-Activation *Theriogenology* **71** 412-421

Cummins, J.M. 2000 Fertilisation and the Elimination of the Paternal Mitochondrial Genome *Hum Reprod* **15**(2) 92-101

Das, S.K. Chu, W.S., Mondal, A.K., Sharma, N.K., Kern, P.A., Rasouli, N. and Elbein, S.C. 2008 Effect of Pioglitazone Treatment on Endoplasmic Reticulum Stress Response in Human Adipose and in Palmitate-Induced Stress in Human Liver and Adipose Cell Lines *Am J Physiol Endocrinol Metab* **295** 393-400

Das, S.K., Mondal, A.K. and Elbein, S.C. 2010 Distinct Gene Expression Profiles Characterise Cellular Responses to Palmitate and Oleate *J Lipid Res* **51** 2121-2131

Davidson, B., Spears, N., Murray, A. and Elfick, A. 2012 The Changing Biochemical Composition and Organisation of the Murine Oocyte and Early Embryo as Revealed by Raman Spectroscopic Mapping *J Raman Spectrosc* **43** 24-31

Davidson, B., Murray, A.A., Elfick, A. and Spears, N. 2013 Raman Microspectroscopy Can Be Used to investigate the Developmental Stage of the Mouse Oocyte *PLoS One* **8**(7) 1-9

De La Fuente, R. and Eppig, J.J. 2001 Transcriptional Activity of the Mouse Oocyte Genome: Companion Granulosa Cells Modulate Transcription and Chromatin Remodelling *Dev Biol* **229**(1) 224-236

Del Collado, M., Saraiva, N.Z., Lopes, F.L., Gaspar, R.C., Padilha, L.C., Costa, R.R., Rossi, G.F., Vantini, R., Garcia, J.M. 2015 Influence of Bovine Serum Albumin and Fetal Bovine Serum Supplementation During *in vitro* Maturation on Lipid and Mitochondrial Behaviour in Oocytes and Lipid Accumulation in Bovine Embryos *Reprod Fertil Dev* (in Press)

Di Napoli, C., Pope, I., Masia, F., Watson, P., Langbein, W. and Borri, P. 2014a Hyperspectral and Differential CARS Microscopy for Quantitative Chemical Imaging in Human Adipocytes *Biomed Opt Express* **5**(5) 1378-1390

Di Napoli, C., Masia, F., Pope, I., Otto, C., Langbein, W. and Borri, P. 2014b Chemically-Specific Dual/Differential CARS Micro-Spectroscopy of Saturated and Unsaturated Lipid Droplets *J Biophotonics* **7**(1–2) 68–76

Dominko, T. and First, N.L. 1997 Timing of Meiotic Progression in Bovine Oocytes and Its Effect on Early Embryo Development *Mol Reprod Dev* **47** 456-467

Downes, A. and Elfick, A. 2010 Raman Spectroscopy and Related Techniques in Biomedicine *Sensors* **10** 1971-1889

Downs, S.M. 1989 Specificity of Epidermal Growth Factor Action On Maturation of the Murine Oocyte and Cumulus Oophorus *in vitro Biol Reprod* **41** 371-379

Downs, S.M. 1995 The influence of Glucose, Cumulus Cells and Metabolic Coupling On ATP Levels and Meiotic Control in the Isolated Mouse Oocyte *Dev Biol* **167** 502-512

Downs, S.M., Mosey, J.L., and Klinger, J. 2009 Fatty Acid Oxidation and Meiotic Resumption in Mouse Oocytes *Mol Reprod Dev* **76** 844–853

Downs, S.M. and Mastropolo, A.M. 1994 The Participation of Energy Substrates in the Control of Meiotic Maturation of Murine Oocytes *Dev Biol* **162** 154-168

Ducharme, N.A. and Bickel, P.E. 2008 Lipid Droplets in Lipogenesis and Lipolysis *Endocrinology* **149**(3) 942-949

Dumollard, R., Marangos, P., Fitzharris, G., Swann, K., Duchen, M., and Carroll, J. 2004 Sperm-Triggered [Ca^{2+}] Oscillations and Ca2+ Homeostasis in the Mouse Egg have an Absolute Requirement for Mitochondrial ATP Production *Dev* **131** 3057-3067

Dumollard, R., Duchen, M., and Sardet, C. 2006 Calcium Signals and Mitochondria at Fertilisation *Semin Cell Dev Biol* **17** 314–323

Dumollard, R., Ward, Z., Carroll, J., and Duchen, M. 2007 Regulation of Redox Metabolism in the Mouse Oocyte and Embryo *Dev* **134** 455-465

Dumollard, R., Campbell, K., Halet, G., Carroll, J., and Swann, K. 2008 Regulation of Cytosolic and Mitochondrial ATP Levels in Mouse Eggs and Zygotes *Dev Biol* **316** 431–440

Dumollard, R., Carroll, J., Duchen, M.R., Campbell, K., and Swann, K. 2009 Mitochondrial Function and Redox State in Mammalian Embryos *Semin Cell Dev Biol* **20** 346–353

Dumoulin, J.C.M., Coonen, E., Bras, M., Bergers-Janssen, J.M., Ignoul-Vanvuchelen, R.C.M. Van Wissen, L.C.P., Geraedts, J.P.M. and Evers, J.L.H. 2001 Embryo Development and Chromosomal Anomalies After ICSI: Effect of the Injection Procedure *Hum Reprod* **16**(2) 306-312

Dunning, K.R., Cashman, K., Russell, D.L., Thompson, J.G., Norman, R.J., and Robker, R.L. 2010 Beta-Oxidation is Essential for Mouse Oocyte Developmental Competence and Early Embryo Development *Biol Reprod* **83** 909–918

Dunning, K.R., Akison, L.K., Russell, D.L., Norman, R.J., and Robker, R.L. 2011 Increased Beta-Oxidation and Improved Oocyte Developmental Competence in Response to L-Carnitine During Ovarian *in vitro* Follicle Development in Mice *Biol Reprod* **85** 548–555

Dunning, K.R., and Robker, R.L. 2012 Promoting Lipid Utilization with L-Carnitine to Improve Oocyte Quality Animal Reproduction *Science* **134** 69– 75

Dunning, K.R., Anastasi, M.R., Zhang, V.J., Russell, D.L., and Robker, R.L. 2014a Regulation of Fatty Acid Oxidation in Mouse Cumulus-Oocyte-Complexes During Maturation and Modulation by PPAR Agonists *PloS ONE* **9**(2) E87327

Dunning, K.R., Russell, D.L., and Robker, R.L. 2014b Lipid and Oocyte Developmental Competence: The Role of Fatty Acids and B-Oxidation *Reprod* **148**(1) R15-27

Dutta, A. and Sinha, D.K. 2015 Turnover of the Actomyosin Complex in Zebrafish Embryos Directs Geometric Remodelling and the Recruitment of Lipid Droplets *Sci Rep* **5**:13915

Ebner, T., Yaman, C., Moser, M. Sommergruber, M., Jesacher, C. and Tews, G. 2001 A Prospective Study on Oocyte Survival Rate After ICSI: Influence of Injection Technique and Morphological Features *J Assist Reprod Genet* **18**(12) 623-628

Ebner, T. Moser, M., Sommergruber, M. and Tews, G. 2003 Selection Based On Morphological Assessment of Oocytes and Embryos at Different Stages of Preimplantation Development: A Review *Hum Reprod Update* **9**(3) 251-262

Edwards, R.G., Steptoe, P.C. and Purdy, J.M. 1980 Establishing Full-Term Human Pregnancies using Cleavage Embryos Grown *in vitro BJOG* **87**(9) 737-756

Eichenlaub-Ritter, U., Vogt, E., Yin, H. and Gosden, R. 2003 Spindles, Mitochondria and Redox Potential in Ageing Oocytes *Reprod Biomed Online* **8**(1) 45-58

Eichenlaub-Ritter, U., Wieczorek, M., Luke, S., and Seidel, T. 2011 Age Related Changes in Mitochondrial Function and New Approaches to Study Redox Regulation in Mammalian Oocytes in Response to Age or Maturation Conditions *Mitochondrion* **11** 783–796

Eppig, J.J., O'Brien, M.J., Wigglesworth, K., Nicholson, A., Zhang, W. and King, B.A. 2009 Effect of *in vitro* Maturation of Mouse Oocytes On the Health and Lifespan of Adult Offspring *Hum Reprod* **24**(4) 922-928

Evans, C.L., Potma, E.O. and Xie, X.S. 2004 Coherent Anti-Stokes Raman Scattering Spectral Interferometry: Determination of the Real and Imaginary Components of Nonlinear Susceptibility $\chi^{(3)}$ for Vibrational Microscopy *Opt Lett* **29**(24) 2923-2925

Evans, C.L., Potma, E.O., Puoris'haag, M., Cote, D., Lin, C.P. and Xie, X.S. 2005 Chemical Imaging of Tissue *in vivo* with Video-Rate Coherent Anti-Stokes Raman Scattering Microscopy *PNAS* **102**(46) 16807-16812

Evans, C.L. and Xie, X.S. 2008 Coherent Anti-Stokes Raman Scattering Microscopy: Chemical Imaging for Biology and Medicine *Annu Rev Anal Chem* **1** 883–909

Fair, T., Hyttel, P. and Greve, T. 1995 Bovine Oocyte Diameter in Relation to Maturational Competence and Transcriptional Activity *Mol Reprod Dev* **42** 437-442

Fair, T. 2003 Follicular Oocyte Growth and Acquisition of Developmental Competence *Anim Reprod Sci* **78** 203-216

Ferguson, E.M. and Leese, H.J. 1999 Triglyceride Content of Bovine Oocytes and Early Embryos *J Reprod Fertil* **116** 373-378

Ferreira, C.R., Saraiva, S.A., Catharino, R.R., Garcia, J.S., Gozzo, F.C., Sanvido, G.B., Santos, L.F., Lo Turco, E., Pontes, J.H., Basso, A.C., Bertolla, R.P., Sartori, R., Guardieiro, M.M., Perecin, F., Meirelles, F.V., Sangalli, J.R., Eberlin, M.N. 2010 Single Embryo and Oocyte Lipid Fingerprinting by Mass Spectrometry *J Lipid Res* **51** 1218-1227

Folick, A., Min, W. and Wang, M.C. 2011 Label-Free Imaging of Lipid Dynamics using Coherent Anti-Stokes Raman Scattering (CARS) and Stimulated Raman Scattering (SRS) Microscopy *Curr Opin Genet Dev* **21** 585-590

Fouladi-Nashta, A.A., Wonnacott, K.E., Gutierrez, C.G., Gong, J.G., Sinclair, K.D., Garnsworthy, P.C. and Webb, R. 2009 Oocyte Quality in Lactating Dairy Cows Fed on High Levels of n-3 and n-6 Fatty Acids *Reprod* **138** 771-781

Fujimoto, T. and Parton, R.G. 2011 Not Just Fat: The Structure and Function of the Lipid Droplet *Cold Spring Harb Prospect Biol* **3**(3)

Fukumoto, S. and Fujimoto, T. 2002 Deformation of Lipid Droplets in Fixed Samples *Histochem Cell Biol* **118**(5) 423-428

Fullston, T., Palmer, N.O., Owens, J.A., Mitchell, M., Bakos, H.W. and Lane, M. 2012 Diet-induced Paternal Obesity in the Absence of Diabetes Diminishes the Reproductive Health of Two Subsequent Generations of Mice *Hum Reprod* **27**(5) 1391-1400

Garcia, C.K., Goldstein, J.L., Pathak, R.K., Anderson, R.G.W., and Brown, M.S. 1994 Molecular Characterisation of a Membrane Transporter for Lactate, Pyruvate and Other Monocarboxylates: Implications for the Cori Cycle *Cell* **7**(11) 865-873

Gardner, D.K., Lane, M., Stevens, J., Schlenker, T. and Schoolcraft, W.B. 2000 Blastocyst Score Affects Implantation and Pregnancy Outcome: Towards a Single Blastocyst Transfer *Fertil Steril* **73**(6) 1155-1158

Genicot, G., Leroy, J.L.M.R., Van Soom, A., and Donnay, I. 2005 The Use of Fluorescent Dye, Nile Red, to Evaluate the Lipid Content of Single Mammalian Oocytes *Theriogenology* **63** 1181-1194

Ghanem, N., Ha, A., Fakruzzaman, M., Bang, J., Lee, S. and Kong, I. 2014 Differential Expression of Selected Candidate Genes in Bovine Embryos Produced *in vitro* and Cultured with Chemicals Modulating Lipid Metabolism *Theriogenology*

Gilchrist, R.B., Lane, M. and Thompson, J.G. 2008 Oocyte-Secreted Factors: Regulators of Cumulus Cell Function and Oocyte Quality *Hum Reprod Update* **14**(2) 159-177

Gilchrist, R.B. and Thompson, J.G. 2007 Oocyte Maturation: Emerging Concepts and Technologies to Improve Developmental Potential *in vitro Theriogenology* **67** 6-15

Gioacchini, G., Giorgini, E., Vaccari, L., Ferraris, P., Sabbatini, S., Bianchi, V., Borini, A., and Carnevali, O. 2014 A New Approach to Evaluate Aging Effects on Human Oocytes: Fourier Transform Infrared Imaging Spectroscopic Study *Fertil Steril* **101** 120-127

Giminez, D. and Rodning, S. 2007 Reproductive Management of Sheep and Goats *Alabama Cooperative Extension System* **ANR**-1316

Gocze, P.M. and Freeman, D.A. 1994 Factors Underlying the Variability of Lipid Droplet Fluorescence in MA-10 Leydig Tumor Cells *Cytometry* **17** 151-158

Gong, J., Sun, Z., Wu, L., Xu, W., Schieber, N., Xu, D., Shui, G., Yang, H., Parton, R.G. and Li, P. 2011 Fsp27 Promotes Lipid Droplet Growth by Lipid Exchange and Transfer at Lipid Droplet Contact Sites *J Cell Biol* **195**(6) 953-963

Gonzalez-Garcia, J.R., Bradley, J., Nomikos, M., Paul, L., Machaty, Z., Lai, F.A. and Swann, K. 2014 the Dynamics of MAPK Inactivation at Fertilisation in Mouse Eggs *J Cell Sci* **127**(12) 2749-2760

Grazul-Bilska, A.T., Borowczyk, E., Bilski, J.J., Reynolds, L.P., Redmer, D.A., Caton, J.S. and Vonnahme, K.A. 2012 Overfeeding and Underfeeding have Detrimental Effects on Oocyte Quality Measured by *in vitro* Fertilisation and Early Embryonic Development in Sheep *Dom Anim Endocrinol* **43** 289-298

Griffin, J., Emery, B.R., Huang, I., Peterson, C.M. and Carrell, D.T. 2006 Comparative Analysis of Follicle Morphology and Oocyte Diameter in Four Mammalian Species (Mouse, Hamster, Pig and Human) *J Exp Clin Assist Reprod* **3**:2

Gwiazda, K.S., Yang, T.B., Lin, Y. and Johnson, J.D. 2009 Effects of Palmitate On ER and Cytosolic Ca^{2+} Homeostasis in B-Cells *Am J Physiol Endocrinol Metab* **296** 690-701

Haggarty, P., Wood, M., Ferguson, E., Hoad, G., Srikantharajah, A., Milne, E., Hamilton, M. and Bhattacharya, S. 2006 Fatty Acid Metabolism in Human Preimplantation Embryos *Hum Reprod* **21**(3) 766-773

Hammiche, F., Vujkovic, M., Wijburg, W., de Vries, J.H.M., Macklon, N.S., Laven, J.S.E. and Steegers-Theunissen, R.P.M. 2011 Increased Preconception Omega-3 Polyunsaturated Fatty Acid Intake Improves Embryo Morphology *Fertil Steril* **95** 1820-1823

Hansen, P.J. 2002 Embryonic Mortality in Cattle from the Embryo's Perspective *J Anim Sci* **80** 22-44

Hardarson, T., Hanson, C., Sjogren, A. and Lundin, K. 2001 Human Embryos with Unevenly Sized Blastomeres Have Lower Pregnancy and Implantation Rates: Indications for Aneuploidy and Multinucleation *Hum Reprod* **16**(2) 313-318

Hardie, D.G. and Pan, D.A. 2002 Regulation of Fatty Acid Synthesis and Oxidation by the AMP-Activated Protein Kinase *Biochem Soc Trans* **30**(6) 1064-1070

Harris, S.E., Leese, H.J., Gosden, R.G. and Picton, H.M. 2009 Pyruvate and Oxygen Consumption Throughout the Growth and Development of Murine Oocytes *Mol Reprod Dev* **76** 231-238

Harris, L.L.S., Skinner, J.R. and Wolins, N.E. 2013 Imaging of Neutral Lipid Associated Proteins *Methods Cell Biol* **116**

Hellerer, T., Axang, C., Brackmann, C. Hillertz, P., Pilon, M. and Enejder, A. 2007 Monitoring of Lipid Storage in *Caenorhabditis elegans* using Coherent Anti-Stokes Raman Scattering (CARS) Microscopy *Proc Nat Acad Sci* **104**(37) 14658-14663

Helmchen, F., and Denk, W. 2005 Deep Tissue Two-Photon Microscopy *Nat Methods* **2**(12) 932-940

Hewitson, L.C. and Leese, H.J. 1993 Energy Metabolism of the Trophectoderm and Inner Cell Mass of the Mouse Blastocyst *J Exp Zool* **267** 337-343

Hinke, S.A., Martens, G.A., Cai, Y., Finsi, J., Heimberg, H., Pipeleers, D. and Van de Casteele, M. 2007 Methyl Succinate Antagonises Biguanide-Induced AMPK-activation and Death of Pancreatic β-cells Through Restoration of Mitochondrial Electron Transfer *Brit J Pharmacol* **150** 1031-1043

Hishinuma, M., Nakata, H., Urano, K., Takahashi, Y. and Kanagawa, H. 1985 Histochemical Observations of Lipid Droplets and Glycogen in Mouse Eggs with Abnormal Development *Jpn J Vet Res* **33** 145-149

Homa, S.T., Racowsky, C. and McGaughey, R.W. 1986 Lipid Analysis of Immature Pig Oocytes *J Reprod Fert* **77** 425-434

Houghton, F.D. 2006 Energy Metabolism of the Inner Cell Mass and Trophectoderm of the Mouse Blastocyst *Differentiation* **74** 11-18

Hsieh, C., Chen, S., Lee, Y., Yang, Y. and Sun, C. 2008 Higher Harmonic Generation Microscopy of *in vitro* Cultured Mammal Oocytes and Embryos *Opt Express* **16**(15) 11574-11588

Hue, L. and Taegtmeyer, H. 2009 Randle Cycle Revisited: A new Head for an Old Hat *Am J Physiol Endocrinol Metab* **297** 578-591

Hunter, M.G. 2000 Oocyte Maturation and Ovum Quality in Pigs *Rev Reprod* **5** 122-130

Igosheva, N., Abramov, A.Y., Poston, L., Eckert, J.J., Fleming, T.P., Duchen, M., and McConnell, J. 2010 Maternal Diet-Induced Obesity Alters Mitochondrial Activity and Redox Status in Mouse Oocytes and Zygotes *PloS ONE* **5**(4) E10074

Inoue, A., Nakajima, R., Nagata, M. and Aoki, F. 2008 Contribution of the Oocyte Nucleus and Cytoplasm to the Determination of Meiotic and Developmental Competence in Mice *Hum Reprod* **23**(6) 1377-1384

Jeong, W.J., Cho, S.J., Lee, H.S., Deb, G.K., Lee, Y.S., Kwon, T.H. and Kong, I.K. 2009 Effect of Cytoplasmic Lipid Content On *in vitro* Developmental Efficiency of Bovine IVP Embryos *Theriogenology* **72** 584-589

Johnson, M.H. and Day, M.L. 2000 Egg Timers: How is the Developmental Time Measured in the Early Vertebrate Embryo? *Bioessays* **22** 57-63

Johnston, L.A., O'Brien, S.J. and Wildt, D.E. 1989 *In vitro* Maturation and Fertilisation of Domestic Cat Follicular Oocytes *Gamete Res* **24**(3) 343-356

Jungheim, E.S., Schoeller, E.L., Marquard, K.L., Louden, E.D., Schaffer, J.E. and Moley, K.H. 2010 Diet-Induced Obesity Model: Abnormal Oocytes and Persistent Growth Abnormalities in the Offspring *Endocrinology* **151** 4039-4046

Jungheim, E.S., Louden, E.D., Chi, M.M., Frolova, A.I., Riley, J.K. and Moley, K.H. 2011a Preimplantation Exposure of Mouse Embryos to Palmitic Acid Results in Fetal Growth Restriction Followed by Catch-Up Growth in the Offspring *Biol Reprod* **85** 678-683

Jungheim, E.S., Macones, G.A., Odem, R.R., Patterson, B.W., Lazendorf, S.E., Ratts, V.S. and Moley, K.H. 2011b Associations Between Free Fatty Acids, Cumulus Oocyte Complex Morphology and Ovarian Function During *in vitro* Fertilisation *Fertil Steril* **95**(6) 1970-1974

Jungheim, E.S., Frolova, A.I., Jiang, H. and Riley, J.K. 2013 Relationship Between Serum Polyunsaturated Fatty Acids and Pregnancy in Women Undergoing *in vitro* Fertilisation *J Clin Endocrinol Metab* **98**(8) 1364-1368

Kamjoo, M., Brison, D.R. and Kimber, S.J. 2002 Apoptosis in the Preimplantation Mouse Embryo: Effect of Strain Difference and *in vitro* Culture *Mol Reprod Dev* **61** 67-77

Khandoker, M.A.M.Y., Tsujii, H. and Karasawa, D. 1997 Fatty Acid Composition of Oocytes, Follicular, Oviductal and Uterine Fluids of Pig and Cow *AJAS* **10**(5) 523-527

Kikuchi, K., Ekwall, H., Tienthai, P., Kawai, Y., Noguchi, J., Kaneko, H., and Rodriguez-Martinez, H. 2002 Morphological Features of Lipid Droplet Transition During Porcine Oocyte Fertilisation and Early Embryonic Development to Blastocyst *in vivo* and *in vitro Zygote* **10** 355-366

Kim, J.Y., Kinoshita, M., Ohnishi, M., and Fukui, Y. 2001 Lipid and Fatty Acid Analysis of Fresh and Frozen-Thawed Immature and *in vitro* Matured Bovine Oocytes *Reprod* **122** 131-138

Kim, K., Park, S. and Roh, S. 2012 Lipid-Rich Blastomeres in the Two-Cell Stage of Porcine Parthenotes Show Bias Toward Contributing to the Embryonic Part *Anim Reprod Sci* **130** 91-98

Klapper, M., Ehmke, M., Palgunow, D., Bohme, M., Matthaus, C., Bergner, G., Dietzek, B., Popp, J., and Doring, F. 2011 Fluorescence-Based Fixative and Vital Staining of Lipid Droplets in *C. elegans* Reveal Fat Stores using Microscopy and Flow Cytometry Approaches *J Lipid Res* **52** 1281-1293

Kohlwein, S.D., Veenhuis, M. and Van der Klei, I.J. 2013 Lipid Droplets and Peroxisomes: Key Players in Cellular Lipid Homeostasis or A Matter of Fat—Store 'Em Up or Burn 'Em Down *Genetics* **193** 1-50

Krisher, R.L. & Bavister, B.D. 1998 Responses of Oocytes and Embryos to the Culture Environment *Theriogenology* **49**(1) 103-114

Krisher, R.L. and Prather, R.S. 2012 A Role for the Warburg Effect in Preimplantation Embryo Development: Metabolic Modification to Support Rapid Cell Proliferation *Mol Reprod Dev* **79** 311-320

Kruip, T.A. and Kemp, B. 1999 Nutrition and Fertility in Agricultural Domestic Animals *Tijdschr Diergeneeskd* **124**(16) 462-467

Kubandova, J., Cikos, S., Burkus, J., Czikkova, Koppel, J. and Fabian, D. 2014 Amount of Maternal Body Fat Significantly Affected the Quality of Isolated Mouse Preimplantation Embryos and Slowed Down Their Development *Theriogenology* **81** 187-195

Land, J.A. and Evers, J.L.H. 2003 Risks and Complications in Assisted Reproduction Techniques: Report of an ESHRE Consensus Meeting *Hum Reprod* **18**(2) 455-457

Lam, A.K., Silva, P.N., Altamentov, S.M., and Rocheleau, J.V. 2012 Quantitative Imaging of Electron Transfer Flavoprotein Autofluorescence Reveals the Dynamics of Lipid Partitioning in Living Pancreatic Islets *Integr Biol* **4** 838–846

Le, T.T., Langohr, I.M., Locker, M.J. Sturek, M. and Cheng, J. 2007 Label-Free Molecular Imaging of Atherosclerotic Lesions using Multimodal Nonlinear Optical Microscopy *J Biomed Opt* **12**(5): 054007

Le, T.T., Yue, S., and Cheng, J. 2010 Shedding New Light on Lipid Biology with CARS Microscopy *J Lipid Res* **51** 3091-3102

Leary, C., Leese, H.J. and Sturmey, R.G. 2015 Human Embryos from Overweight and Obese Women Display Phenotypic and Metabolic Abnormalities *Hum Reprod* **30**(1) 122-132

Lee, K.Y. and DeMayo, F.J. 2004 Animal Models of Implantation *Reprod* **128** 679-695

Leese, H. 2002 Quiet Please, Do Not Disturb: A Hypothesis of Embryo Metabolism and Viability *Bioessays* **24** 845-849

Leese, H.J., Sturmey, R.G., Baumann, C.G., and McEvoy, T.G. 2007 Embryo Viability and Metabolism: Obeying the Quiet Rules *Hum Reprod* **22**(12) 3047-3050

Leroy, J.L.M.R., Genicot, G., Donnay, I., and Van Soom, A. 2005 Evaluation of the Lipid Content in Bovine Oocytes and Embryos with Nile Red: A Practical Approach *Reprod Domestic Anim* **40** 76-78

Leroy, J.L.M.R., Sturmey, R.G., Van Hoeck, V., De Bie, J., McKeegan, P.J. and Bols, P.E.J. 2014 Dietary Fat Supplementation and the Consequences for Oocyte and Embryo Quality: Hype or Significant Benefit for Dairy Cow Reproduction? *Reprod Dom Anim* **49** 353-361

Li, M., Zhao, Y., Zhao, C.H., Yan, J., Yan, Y.L., Rong, L., Liu, P., Feng, H., Yu, Y. and Qiao, J. 2013 High FSH Decreases the Developmental Potential of Mouse Oocytes and Resulting Fertilized Embryos, but Does Not influence offspring Physiology and Behavior *in vitro* or *in vivo Hum Reprod* **28**(5) 1309-1323

Lin, J., Lu, F., Zheng, W., Xu, S., Tai, D., Yu, H. and Huang, Z. 2011 Assessment of Liver Steatosis and Fibrosis in Rats using Integrated Coherent Anti-

Stokes Raman Scattering and Multiphoton Imaging Technique *J Biomed Optics* **16**(11): 116024

Loewenstein, J.E. and Cohen, A.I. 1964 Dry Mass, Lipid Content and Protein Content of the Intact and Zona-Free Mouse Ovum *J Embryol Exp Morph***12**(1) P.113-121

Loutradis, D., Kiapekou, E., Zapanti, E., and Antsaklis, A. 2006 Oocyte Maturation in Assisted Reproductive Techniques *Ann NY Acad Sci* **1092** 235–246

Luke, B., Brown, M.B., Stern, J.E., Missmer, S.A., Fujimoto, V.Y. and Leach, R. 2011 Female Obesity Adversely Affects Assisted Reproductive Technology (ART) Pregnancy and Live Birth Rates *Hum Reprod* **26**(1) 245-252

Luzzo, K.M., Wang, Q., Purcell, S.H., Chi, M., Jiminez, P.T., Grindler, N., Schedl, T. and Moley, K.H. 2012 High Fat Diet Induced Developmental Defects in the Mouse: Oocyte Meiotic Aneuploidy and Fetal Growth Retardation/Brain Defects *PLoS One* **7**(11) e49217

Macdonald, M.J., Fahien, L.A., Buss, J.D., Hasan, N.M., Fallon, M.J. and Kendrick, M.A. 2003 Citrate Oscillates in Liver and Pancreatic Beta Cell Mitochondria and in INS-1 Insulinoma Cells *J Biol Chem* **278** 51894-51900

Matorras, R., Ruiz, J.I., Mendoza, R., Ruiz, N., Sanjurjo, P. and Rodriguez-Escudero, F.J. 1998 Fatty Acid Composition of Fertilisation-Failed Human Oocytes *Hum Reprod* **13**(8) 2227-2230

Marcinkiewicz, A., Gauther, D., Garcia, A. and Brasaemle, D.L. 2006 the Phosphorylation of Serine 492 of Perilipin A Directs Lipid Droplet Formation and Dispersion *J Biol Chem* **281**(17) 11901-11909

Martin, K.L. and Leese, H.J 1999 Role of Developmental Factors in the Switch from Pyruvate to Glucose as the Major Exogenous Energy Substrate in the Preimplantation Mouse Embryo *Reprod Fertil Dev* **11** 425-433

Martin, S. and Parton, R.G. 2006 Lipid Droplets: A Unified View of a Dynamic organelle *Nat Rev Mol Cell Biol* **7**(5) 373-378

Masia, F., Karuna, A., Borri, P. and Langbein, W. 2015 Hyperspectral Image Analysis for CARS, SRS and Raman Data *J Raman Spectrosc* **46**(8) 727-734

Masia, F., Glen, A., Stephens, P., Borri, P. and Langbein, W. 2013 Quantitative Chemical Imaging and Unsupervised Analysis using Hyperspectral Coherent Anti-Stokes Raman Scattering Microscopy *Anal Chem* **85**(22) 10820-10828

McEvoy, T.G., Coull, G.D., Broadbent, P.J., Hutchinson, J.S.M., and Speake, B.K. 2000 Fatty Acid Composition of Lipids in Immature Cattle, Pig and Sheep Oocytes with Intact Zona Pellucida *J Reprod Fertil* **118** 163-170

McPhee, C.I., Zoriniants, G., Langbein, W., and Borri, P. 2013 Measuring the Lamellarity of Giant Lipid Vesicles with Differential Interference Contrast Microscopy *Biophys J* **105**(6) 1414-1420

Meldrum, R.A., Botchway, S.W., Wharton, C.W. and Hirst, G., J. 2 003 Nanoscale Spatial Induction of Ultraviolet Photoproducts in Cellular DNA by Three-Photon Near-Infrared Absorption *EMBO Rep* **4**(12) 1144-1149

Merrill, C.L., Ni, H., Yoon, L.W., Tirmenstein, M.A., Narayanan, P., Benavides, G.R., Easton, M.J., Creech, D.R., Hu, C.X., McFarland, D.C., Hahn, L.M., Thomas, H.C. and Morgan, K.T. 2002 Etomoxir-Induced Oxidative Stress in HepG2 Cells Detected by Differential Gene Expression is Confirmed Biochemically *Toxicol Sci* **68** 93-101

Min, W., Freudiger, C.W., Lu, S. and Xie, X.S. 2011 Coherent Nonlinear Optical Imaging: Beyond Fluorescence Microscopy *Annu Rev Phys Chem* **62** 507-530

Murphy, S., Martin, S. and Parton, R.G. 2010 Quantitative Analysis of Lipid Droplet Fusion: Inefficient Steady State Fusion but Rapid Stimulation by Chemical Fusogens *PLoS One* **5**(12): 15030

Nagai, S., Mabuchi, T., Hirata, S., Shoda, T., Kasai, T., Yokota, S., Shitara, H., Yonekawa, H. and Hoshi, K. 2004 Oocyte Mitochondria: Strategies to Improve Embryogenesis *Hum Cell* **17**(4) 195-201

Nagai, S., Mabuchi, T., Hirata, S., Shoda, T., Kasai, T., Yokota, S., Shitara, H., Yonekawa, H. and Hoshi, K. 2006 Correlation of Abnormal Mitochondrial Distribution in Mouse Oocytes with Reduced Developmental Competence *Tohoku J Exp Med* **210** 137-144

Nan, X., Cheng, J. and Xie, X.S. 2003 Vibrational Imaging of Lipid Droplets in Live Fibroblast Cells with Coherent Anti-Stokes Raman Scattering Microscopy *J Lipid Res* **44** 2202-2208

Niakan, K.K., Han, J., Pedersen, R.A., Simon, C. and Reijo Pera, R.A. 2012 Human Pre-Implantation Embryo Development *Dev* **139** 829-841

Niu, Y., Wang, C., Xiong, Q., Yang, X., Chi, D., Li, P., Liu, H. and Huang, R. 2014 Distribution and Content of Lipid Droplets and Mitochondria in Pig

Parthenogenetically Activated Embryos After Delipation *Theriogenology* **83**(1) 131-138

Nolan, C.J. and Larter, C.Z. 2009 Lipotoxicity: Why do Saturated Fatty Acids Cause and Monounsaturates Protect Against It? *J Gastroenterol Hepatol* **24** 830-840

Nonogaki, T., Noda, Y., Goto, Y., Kishi, J. and Mori, T. 1994 Developmental Blockage of Mouse Embryos Caused by Fatty Acids *J Assist Reprod Genet* **11**(9) 482-488

O'Gorman, A.O., Wallace, M., Cottell, E., Gibney, M.J., McAuliffe, F.M., Wingfield, M. and Brennen, L. 2013 Metabolic Profiling of Human Follicular Fluid Identifies Potential Biomarkers of Oocyte Developmental Competence *Reprod* **146** 389-395

Ohsaki, Y., Shinohara, Y., Suzuki, M. and Fujimoto, T. 2010 A Pitfall in using BODIPY Dyes to Label Lipid Droplets for Fluorescence Microscopy *Histochem Cell Biol* **133** 477-480

Ordonez-Leon, E.A., Merchant, H., Medrano, A., Kjelland, M. and Romo, S. 2014 Lipid Droplet Analysis using *in vitro* Bovine Oocytes and Embryos *Reprod Dom Anim* **49**(2) 306-314

O'Rourke, E.J., Soukas, A.A., Carr, C.E. and Ruvkun, G. 2009 *C. elegans* Major Fats Are Stored in Vesicles Distinct from Lysosome-Related Organelles *Cell Metab* **10**(5) 430-435

Otto, D.A. 1984 Relationship of the ATP/ADP Ratio to the Site of Octanoate Activation *J Biol Chem* **259** 5490-5494

Ottosen, L.D.M., Hindkjaer, J. and ingerslev, J. 2007 Light Exposure of the Ovum and Preimplantation Embryo During ART Procedures *J Assist Reprod Genet* **24** 99-103

Owen, M.R., Doran, E., and Halestrap, P. 2000 Evidence That Metformin Exerts Its Anti-Diabetic Effects Through Inhibition of Complex I of the Mitochondrial Respiratory Chain *Biochem. J* **348** 607-614

Parekh, S.H., Lee, Y.J., Aamer, K.A. and Cicerone, M.T. 2010 Label-Free Cellular Imaging by Broadband Coherent Anti-Stokes Raman Scattering Microscopy *Biophys J* **99** 2695-2704

Perry, S.W., Norman, J.P., Barbieri, J., Brown, E.B. and Gelbard, H.A. 2011 Mitochondrial Membrane Potential Probes and the Proton Gradient: A Practical Usage Guide *Biotechniques* **50**(2) 98-115

Pike, L.S., Smift, A.L., Croteau, N.J., Ferrick, D.A. and Wu, M. 2011 Inhibition of Fatty Acid Oxidation by Etomoxir Impairs NADPH Production and increases Reactive Oxygen Species Resulting in ATP Depletion and Cell Death in Human Glioblastoma Cells *BBA* **1807** 726-734

Pomeroy, K.O. and Reed, M.L. 2013 The Effect of Light On Embryos and Embryo Culture *J Reprod Stem Cell Biotechnol* **3**(2) 46-54

Pope, I., Langbein, W., Borri, P., and Watson, P. 2012 Live Cell Imaging with Chemical Specificity using Dual Frequency CARS *Method Enzymol* **504** 273-291

Pope, I., Langbein, W., Watson, P. and Borri, P. 2013. Simultaneous Hyperspectral Differential-CARS, TPF, and SHG Microscopy with a Single 5fs Ti:Sa Laser *Opt Express* **21**(6) 7096-7106

Potma, E.O. and Xie, X.S. 2004 CARS Microscopy for Biology and Medicine *Opt Photonics News* **15**(11) 40-45

Potma, E.O. and Xie, X.S. 2005 Direct Visualisation of Lipid Phase Segregation in Single Lipid Bilayers with Coherent Anti-Stokes Raman Scattering Microscopy *Chem Phys Chem* **6** 77-79

Purcell, S.H., and Moley, K.H. 2011 The Impact of Obesity On Egg Quality *J Assist Reprod Gen* **28** 517–524

Prates, E.G., Marques, C.C., Baptista, M.C., Vasques, M.I., Carolino, N., Horta, A.E.M., Charneca, R., Nunes, J.T. and Pereira, R.M. 2012 Fat Area and Lipid Droplet Morphology of Porcine Oocytes During *in vitro* Maturation with *Trans*-10, *Cis*-12 Conjugated Linoleic Acid and Forskolin *Animal* **7**(4) 602-609

Prates, E.G., Nunes, J.T., and Pereira, R.M. 2014 A Role of Lipid Metabolism During Cumulus-Oocyte Complex Maturation: Impact of Lipid Modulators to Improve Embryo Production *Mediat inflamm* **2014** 11 Pages

Pratt, H.P.M. and George, M.A. 1989 Organisation and Assembly of the Surface Membrane During Early Cleavage of the Mouse Embryo *Roux's Arch Dev Biol* **198** 170-178

Preis, K.A., Seidel Jnr, G.E. and Gardner, D.K. 2007 Reduced Oxygen Concentration Improves the Developmental Competence of Mouse Oocytes Following *in vitro* Maturation *Mol Reprod Dev* **74** 893-903

Qui, J.J., Zhang, W.W., Wu, Z.L., Wang, Y.H., Qian, M., and Li, Y.P. 2003 Delay of ZGA initiation Occurred in 2-Cell Blocked Mouse Embryos *Cell Res* **13**(3) 179-185

Randle, P.J., Hales, C.N., Garland, P.B. and Newsholme, E.A. 1963 The Glucose Fatty-Acid Cycle: Its Role in Insulin Sensitivity and the Metabolic Disturbances of Diabetes Mellitus *Lancet* **1**(7285) 785-789

Revelli, A., Delle Piane, L., Casano, S., Molinari, E., Massobrio, M. and Rinaudo, P. 2009 Follicular Fluid Content and Oocyte Quality: From Single Biochemical Markers to Metabolomics *Reprod Biol Endocrinol* **7**:40

Richani, D., Sutton-McDowall, M.L., Frank, L.A., Gilchrist, R.B. and Thompson, J.G. 2014 Effect of Epidermal Growth Factor-Like Peptides on the Metabolism of *in vitro*-Matured Mouse Oocytes and Cumulus Cells *Biol Reprod* **90**(3) 49

Rieger, D. 1992 Relationships Between Energy Metabolism and Development of Early Mammalian Embryos *Theriogeniology* **37**(1) 75-93

Rinia, H.A., Burger, K.N.J., Bonn, M., and Muller, M. 2008 Quantitative Label-Free Imaging of Lipid Composition and Packing of Individual Cellular Lipid Droplets using Multiplex CARS Microscopy *Biophys J* **95**(10) 4908-4914

Rizos, D., Ward, F., Duffy, P., Boland, M.P. and Lonergan, P. 2002 Consequences of Bovine Oocyte Maturation, Fertilization or Early Embryo Development *in vitro* Versus *in vivo*: Implications for Blastocyst Yield and Blastocyst Quality *Mol Reprod Dev* **61** 234-248

Robker, R.L., Akison, L.K., Bennett, B.D., Thrupp, P.N., Chura, L.R., Russell, D.L., Lane, M. and Norman, R.J. 2009 Obese Women Exhibit Differences in Ovarian Metabolites, Hormones, and Gene Expression Compared with Moderate-Weight Women *J Clin Endocrinol Metab* **94(**5) 1533–1540

Romashko, D.N., Marban, E., and O'Rourke, B. 1998 Subcellular Metabolic Transients and Mitochondrial Redox Waves in Heart Cells *Proc Nat Acad Sci USA* **95** 1618–1623

Romek, M., Gajda, B., Krzysztofowicz, E. and Smorag, Z. 2009 Lipid Content of Non-Cultured and Cultured Pig Embryo *Reprod Dom Anim* **44** 24-32

Romek, M., Gajda, B., Krzysztofowicz, E. and Smorag, Z. 2011 New Technique to Quantify the Lipid Composition of Lipid Droplets in Porcine Oocyte and Pre-Implantation Embryos using Nile Red Fluorescent Probe *Theriogenology* **75** 42-54

Rose, B.I. and Laky, D. 2013 Polar Body Fragmentation in IVM Oocytes is Associated with Impaired Fertilization and Embryo Development *J Assist Reprod Genet* **30** 379-682

Rutkowski, D.T., Arnold, S.M., Miller, C.N., Wu, J., Li, J., Gunnison, K.M., Mori, K., Sadighi Akha, A.A., Raden, D. and Kaufman, R.J. 2006 Adaptation to ER Stress is Mediated by Differential Stabilities of Pro-Survival and Pro-Apoptotic mRNAs and Proteins *PloS Biol* **4**(11): 374

Sata, R., Tsuji, H., Abe, H., Yamashita, S. and Hoshi, H. 1999 Fatty Acid Composition of Bovine Embryo Cultured in Serum-Free and Serum-Containing Medium during Early Embryonic Development *J Reprod Dev* **45**(1) 97-103

Sadler, T.W. 2004 Langman's Medical Embryology 9th Ed. *Lippincott Williams and Wilkins* Chapters 1-2

Sananthan, A.H. and Gunasheela, S. 2007 Human Oocyte and Embryo Assessment for ART. In: Cohen, J. and Elder, K. 2007 *Human Preimplantation Embryo Selection* CRC Press

Sananthan, A.H. and Trouson, A.O. 2000 Mitochondrial Morphology During Preimplantational Human Embryogenesis *Hum Reprod* **15**(2) 148-159

Saunders, C.M., Larman, M.G., Parrington, J., Cox, L.J., Royse, J., Blayney, L.M., Swann, K. and Lai, F.A. 2002 PLCζ: A Sperm-Specific Trigger of Ca^{2+} Oscillations in Eggs and Embryo Development *Dev* **129** 3533-3544

Schatten, H. and Constantinescu, G.M. 2008 Comparative Reproductive Biology *John Wiley & Sons* p.128

Schell, J.C. and Rutter, J. 2013 The Long and Winding Road to the Mitochondrial Pyruvate Carrier *Cancer Metab* **1**:6

Schie, I.W., Nolte, L., Pedersen, T.L., Smith, Z., Wu, J., Yahiatene, I., Newman, J.W. and Huser, T. 2013 Direct Comparison of Fatty Acid Ratios in Single Cellular Lipid Droplets as Determined by Comparative Raman Spectroscopy and Gas Chromatography *Analyst* **138** 6662-6670

Schon, E.A. 2000 Mitochondrial Genetics and Disease *Trends Biochem Sci* **25** 555–560

Shaaker, M., Rahimipour, A., Nouri, M., Khanaki, K., Darabi, M., Farzadi, L., Shahnazi, V. and Mehdizadeh, A. 2012 Fatty Acid Composition of Human Follicular Fluid Phospholipids and Fertilization Rate in Assisted Reproductive Techniques *Iran Biomed J* **16**(3) 162-168

Shirazi, A. and Sadeghi, N. 2007 The Effect of Ovine Oocyte Diameter On Nuclear Maturation *Small Ruminant Res* **69(**1-3) 103-107

Sirard, M.A., Florman, H.M., Liebfried-Rutledge, M.L., Barnes, F.L., Sims, M.L. and First, N.L. 1989 Timing of Nuclear Progression and Protein Synthesis Necessary for Meiotic Maturation of Bovine Oocytes *Biol Reprod* **40** 1257-1263

Somfai, T., Kaneda, M., Akagi, S., Watanabe, S., Haraguchi, S., Mizutani, E., Dang-Nguyen, T.Q., Geshi, M., Kikuchi, K. and Nagai, T. 2011 Enhancement of Lipid Metabolism with L-Carnitine During *in vitro* Maturation Improves Nuclear Maturation and Cleavage Ability of Follicular Porcine Oocytes *Reprod Fertil Dev* **23**(7) 912-920

Squirrell, J.M, Wokosin, D.L., White, J.G., and Bavister, B.D. 1999 Long-Term Two-Photon Fluorescence Imaging of Mammalian Embryos without Compromising Viability *Nat Biotechnol* **17** 763-767

Stojkovic, M. Machado, S.A., Stojkovic, P., Zakhartchenko, V., Hutzler, P., Goncalves, P.B., and Wolf, E. 2001 Mitochondrial Distribution and Adenosine Triphosphate Content of Bovine Oocytes Before and After *in vitro* Maturation: Correlation with Morphological Criteria and Developmental Capacity After *in vitro* Fertilization and Culture *Biol Reprod* **64** 904–909

Sturmey, R.G. and Leese, H.J. 2003 Energy Metabolism in Pig Oocytes and Early Embryos *Reprod* **126** 197-204

Sturmey, R.G., O'toole, P.J., and Leese, H.J. 2006 Fluorescence Resonance Energy Transfer Analysis of Mitochondrial:Lipid Association in the Porcine Oocyte *Reprod* **132** 829–837

Sturmey, R.G., Reis, A., Leese, H.J., and McEvoy, T.G. 2009 Role of Fatty Acids in Energy Provision During Oocyte Maturation and Early Embryo Development *Reprod Dom Anim* **44** (Suppl. 3) 50–58

Sudiman, J., Ritter, L.J., Feil, D.K., Wang, X., Chan, K., Mottershed, D.G., Robertson, D.M., Thompson, J.G., Gilchrist, R.B. 2014 Effects of Differing Oocyte-Secreted Factors During Mouse *in vitro* Maturation On Subsequent Embryo and Fetal Development *J Assist Reprod Genet* **31**(3) 295-306

Sugden, M.C. and Holness, M.J. 2011 The Pyruvate Carboxylase-Pyruvate Dehydrogenase Axis in Islet Pyruvate Metabolism: Going Round in Circles? *Islets* **3**(6) 302-319

Sun, Q.Y., Wu, G.M., Lai, L., Park, W., Cabot, R., Cheong, H.T., Day, B.N., Prather, R.S., and Schatten, H. 2001 Translocation of Active Mitochondria During Pig Oocyte Maturation, Fertilization and Early Embryo Development *in vitro Reprod* **122** 155–163

Sun, T.T., Chung, C.M., Chan, H.C. 2011 Acrosome Reaction in the Cumulus Oophorus Revisited: Involvement of a Novel Sperm-Released Factor NYD-SP8 *Protein Cell* **2**(2) 92-98

Sutovsky, P., Moreno, R.D., Ramalho-Santos, J., Dominiko, T., Simerly, C. and Schatten, G. 1999 Development: Ubiquitin Tag for Sperm Mitochondria *Nature* **402** 371-372

Sutton-McDowall, M.L., Gilchrist, R.B., and Thompson, J.G. 2010 The Pivotal Role of Glucose Metabolism in Determining Oocyte Developmental Competence *Reprod* **139** 685–695

Sutton-McDowall, M.L., Feil, D., Robker, R.L., Thompson, J.G. and Dunning, K.R. 2012 Utilization of Endogenous Fatty Acid Stores for Energy Production in Bovine Preimplantation Embryos *Theriogenology* **77**(8) 1632-1641

Sutton-McDowall, M.L., Wu, L.L., Purdey, M., Abell, A.D., Goldys, E.M., MacMillan, K.L., Thompson, J.G. and Robker, R.L. 2016 Nonesterified Fatty Acid-Induced Endoplasmic Reticulum Stress in Cattle Cumulus Oocyte Complexes Alters Cell Metabolism and Developmental Competence *Biol Reprod* **94**(1):23

Swann, K., Larman, M., Saunders, C.M. and Lai, F.A. 2004 The Cytosolic Sperm Factor That Triggers Ca^{2+} Oscillations and Egg Activation in Mammals is a Novel Phospholipase C: PLCζ *Reprod* **127** 431-439

Takahashi, M., Saka, N., Takahashi, H., Kanai, Y., Schultz, R.M. and Okano, A. 1999 Assessment of DNA Damage in Individual Hamster Embryos by Comet Assay *Mol Reprod Dev* **54** 1-7

Takahashi, T., Inaba, Y., Somfai, T., Kaneda, M, Geshi, M., Nagai, T. and Manabe, N. 2013 Supplementation of Culture Medium with L-Carnitine Improves Development and Cryotolerance of Bocine Embryos Produced *in vitro Reprod Fert Dev* **25** 589-599

Takenaka, M., Horiuchi, T. and Yanagimachi, R. Effects of Light On Development of Mammalian Zygotes 2007 *Proc Nat Acad Sci* **104**(36) 14289-14293

Thayil, A., Watanabe, T., Jesacher, A., Wilson, T., Srinivas, S. and Booth, M. 2011 Long-Term Imaging of Mouse Embryos using Adaptive Harmonic Generation Microscopy *J Biomed Opt* **16**(4): 046018

Thiam, A.R., Farese Jnr, R.V. and Walther, T.C. 2013 The Biophysics and Cell Biology of Lipid Droplets *Nature Rev Mol Cell Biol* **14** 775-786

Thiele, C. and Spandl, J. 2008 Cell Biology of Lipid Droplets *Curr Opin Cell Biol* **20** 378-385

Tsutsui, T. and Stabenfeldt, G.H. 1993 Biology of Ovarian Cycles, Pregnancy and Pseudopregnancy in the Domestic Cat *J Reprod Fertil Suppl* **47** 29-35

Turner, N. and Robker, R.L. 2014 Developmental Programming of Obesity and Insulin Resistance: Does Mitochondrial Dysfunction in Oocytes Play a Role? *Mol Hum Reprod* **21**(1) 23-30

Valckx, S.D.M., Arias-Alvarez, M., De Pauw, I., Fievez, V., Vlaeminck, B., Fransen, E., Bols, P.E.J. and Leroy, J.L.M.R. 2014 Fatty Acid Composition of the Follicular Fluid of Normal Weight, Overweight and Obese Women Undergoing Assisted Reproductive Treatment: A Descriptive Cross-Sectional Study *Reprod Biol Endocrinol* **12**:13

Valsangkar, D.S. and Downs, S.M. 2015 Acetyl CoA Carboxylase Inactivation and Meiotic Maturation in Mouse Oocytes *Mol Reprod Dev* **82** 679-693

Van Blerkom, J., Davis, P.W., and Lee, L. 1995 ATP Content of Human Oocytes and Developmental Potential and Outcome After *in-vitro* Fertilization and Embryo Transfer *Hum Reprod* **10** (2) 415-424

Van Blerkom, J., Antczak, M. and Schrader, R. 1997 The Developmental Potential of the Human Oocyte is Related to the Dissolved Oxygen Content of Follicular Fluid: Association with Vascular Endothelial Growth Factor Levels and Perifollicular Blood Flow Characteristics *Hum Reprod* **12**(5) 1047-1055

Van Blerkom, J., Davis, P. and Alexander, S. 2001 A Microscopic and Biochemical Study of Fragmentation Phenotypes in Stage-Appropriate Human Embryos *Hum Reprod* **16**(4) 719-729

Van Blerkom, J., Davis, P. and Alexander, S. 2003 Inner Mitochondrial Membrane Potential ($\Delta\Psi m$), Cytoplasmic ATP Content and Free Ca^{2+} Levels in Metaphase II Mouse Oocytes *Hum Reprod* **18**(11) 2429-2440

Van Blerkom, J. 2004 Mitochondria in Human Oogenesis and Preimplantation Embryogenesis: Engines of Metabolism, Ionic Regulation and Developmental Competence *Reprod* **128** 269-280

Van Hoeck, V., Sturmey, R.G., Bermejo-Alvarez, P., Rizos, D., Gutierrez-Adan, A., Leese, H.J., Bols, P.E.J. and Leroy, J.L.M.R. 2011 Elevated Non-Esterified Fatty Acid Concentrations During Bovine Oocyte Maturation Compromise Early Embryo Physiology *PLoS One* **6**(8): 23183

Van Hoeck, V., Leroy, J.L., Arias-Alvarez, M., Rizos, D., Gutierrez-Adan, A., Schnorbusch, K., Bols, PE., Leese, H.J. and Sturmey, R.G. 2013 Oocyte Developmental Failure in Response to Elevated Nonesterified Fatty Acid Concentrations: Mechanistic Insights *Reprod* **145**(1) 33-44

Vartiainen, E., Rinia, H.A., Muller, M. and Bonn, M. 2006 Direct Extraction of Raman Line-Shapes from Congested CARS Spectra *Opt Express* **14**(8) 3622-3631

Vauthey, E. Introduction to Nonlinear Optical Spectroscopic Techniques for Investigating Ultrafast Processes *Lectures of Virtual European University On Lasers*

Verlinsky, Y., Lerner, S., Illkevitch, N., Kuznetsov, V., Kutznetsov, I., Cieslak, J. and Kuliev, A. 2003 Is there Any Predictive Value of First Polar Body Morphology for Embryo Genotype or Developmental Potential? *Reprod Biomed Online* **7**(3) 336-341

Voronina, E. and Wessel, G.M. 2003 The Regulation of Oocyte Maturation *Curr topics Reprod Biol* **58** 53-110

Walter, A., Erdmann, S., Bocklitz, T., Jung, E., Vogler, N., Akimov, D., Dietzek, B., Rosch, P., Kothe, E. and Popp, J. 2010 Analysis of the Cytochrome Distribution via Linear and Nonlinear Raman Spectroscopy *Analyst* **135** 908-917

Walther, T.C. and Ferese Jr., R.V. 2012 Lipid Droplets and Cellular Lipid Metabolism *Annu Rev Biochem* **81** 687-714

Watanabe, T., Thayil, A., Jesacher, A., Grieve, K., Debarre, D., Wilson, T., Booth, M., and Srinivas, S. 2010 Characterisation of the Dynamic Behaviour of Lipid Droplets in the Early Mouse Embryo using Adaptive Harmonic Generation Microscopy *BMC Cell Biol* **11**(38)

Wang, G., Tsujii, H. and Khandoker, M.Y. 1998 Fatty Acid Compositions of Mouse Embryo, Oviduct and Uterine Fluid *Anim Sci Technol* **69**(10) 923-928

Wang, H., Fu, Y., Zickmund, P., Shi, R. and Cheng, J. 2005 Coherent Anti-Stokes Raman Scattering Imaging of Axonal Myelin in Live Spinal Tissues *Biophys J* **89** 581-591

Wang, L., Wang, D., Zou, X. and Xu, C. 2009 Mitochondrial Functions On Oocytes and Preimplantation Embryos *J Zhejiang Univ Sci B* **10**(7) 483-492

Wang, H., Sreenivasan, U., Hu, H., Saladino, A., Polster, B.M., Lund, L.M., Gong, D., Stanley, W.C. and Sztalryd, C. 2011a Perilipin 5, a Lipid Droplet-Associated Protein, Provides Physical and Metabolic Linkage to Mitochondria *J Lipid Res* **52** 2159-2168

Wang, M.C., Min, W., Freudiger, C.W., Ruvkun, G. and Xie, X.S. 2011b RNAi Screening for Fat Regulatory Genes with SRS Microscopy *Nat Methods* **8**(2) 135-138

Weitlauf, H.M. and Nieder, G.L. 1984 Metabolism in Preimplantation Mouse Embryos *J Biosci* **6**(2) 33-42

Welte, M.A. 2009 Fat On the Move: Intracellular Motion of Lipid Droplets *Biochem Soc Trans* **37** 991-996

Wheaton, W.W., Weinberg, S.E., Hamanaka, R.B., Soberanes, S., Sullivan, L.B., Anso, E., Glasauer, A., Dufour, E., Mutlu, G.M., Budigner, G.R.S. and Chandel, N.S. 2014 Metformin Inhibits Mitochondrial Complex I of Cancer Cells to Reduce Tumorigenesis *eLife* **3**: 02242

Wilding, M., Dale, B., Marino, M., Di Matteo, L., Alviggi, C., Pisaturo, M.L., Lombardi, L. and De Placido, G. 2001 Mitochondrial Aggregation Patterns and Activity in Human Oocytes and Preimplantation Embryos *Hum Reprod* **16**(5) 909-917

Wilding, M., Coppola, G., Dale, B. and Di Matteo, L. 2009 Mitochondria and Human Preimplantation Embryo Development *Reprod* **137** 619-624

Wilfling, F., Haas, J.T., Walther, T.C., and Farese Jr., R.V. 2014 Lipid Droplet Biogenesis *Curr Opin Cell Biol* **29** 39-45

Wirtu, G., McGill, J., Crawford, L., Williams, A., Reddy, G., Bergen, W.G. and Simon, L. 2013 Targeting Lipid Metabolism to Improve Oocyte Cryopreservation (OCP) in Domestic Animals *Trans Clin Bio* **1**(1) 15-20

Wong, C.C., Loewke, K.E., Bossert, N.L., Behr, B., De Jonge, C.J., Baer, T.M. and Reijo Pera, R.A. 2010 Non-Invasive Imaging of Human Embryos Before Embryonic Genome Activation Predicts Development to the Blastocyst Stage *Nature Biotechnol* **28**(10) 1115-1124

Wood, B.R., Chernenko, T., Matthaus, C., Diem, M., Chong, C., Bernhard, U., Jene, C., Brandli, A. A., Mcnaughton, D., Tobin, M.J., Trounson, A. and Lacham-Kaplan, O. 2008 Shedding New Light On the Molecular Architecture of Oocytes using a Combination of Synchrotron Fourier Transform-infrared and Raman Spectroscopic Microscopy *Anal Chem* **80**(23) 9065-9072

Wu, P., Blair, P.V., Sato, J., Jaskiewicz, J., Popov, K.M. and Harris, R.A. 2000 Starvation Increases the Amount of Pyruvate Dehydrogenase Kinase in Several Mammalian Tissues *Arch Biochem Biophys* **381**(1) 1-7

Wu, L.L., Dunning, K.R., Yang, X., Russell, D.L., Lane, M., Norman, R.J., and Robker, R.L. 2010 High-Fat Diet Causes Lipotoxicity Responses in Cumulus–Oocyte Complexes and Decreased Fertilization Rates *Endocrinology* **151** 5438–5445

Wu, L.L., Russell, D.L., Norman, R.J. and Robker, R.L. 2012 Endoplasmic Reticulum (ER) Stress in Cumulus-Oocyte Complexes Impairs Pentraxin-3 Secretion, Mitochondrial Membrane Potential (ΔΨm), and Embryo Development *Mol Endocrinol* **26**(4) 562-573

Wu, L.L., Russell, D.L., Wong, S.L., Chen, M., Tsai, T., St John, J.C., Norman, R.J., Febbraio, M.A., Carroll, J. and Robker, R.L. 2015 Mitochondrial Dysfunction in Oocytes of Obese Mothers: Transmission to Offspring and Reversal by Pharmacological Endoplasmic Reticulum Stress Inhibitors *Dev* **142** 681-691

Xia, P. 1997 Intracytoplasmic Sperm Injection: Correlation of Oocyte Grade Based On Polar Body, Perivitelline Space and Cytoplasmic Inclusions with Fertilization Rate and Embryo Quality *Hum Reprod* **12**(8) 1750-1755

Xie, X.S., Yu, J., and Yang, W. 2006 Living Cells as Test Tubes *Science* **312** 228-230

Yang, X., Dunning, K.R., Wu, L.L., Hickey, T.E., Norman, R.J., Russell, D.L., Liang, X., Robker, R.L. 2010 Identification of Perilipin-2 as a Lipid Droplet Protein Regulated in Oocytes During Maturation *Reprod Fertil Dev* **22**(8) 1262-1271

Yang, H., Galea, A., Sytnyk, V. and Crossley, M. 2012 Controlling the Size of Lipid Droplets: Lipid and Protein Factors *Curr Opin Cell Biol* **24** 509-516

Yen, K., Le, T.T., Bansal, A., Devi Narasimhan, S., Cheng, J., Tissenbau, H.A. 2010 A Comparative Study of Fat Storage Quantitation in Nematode *Caenorhabditis elegans* using Label and Label-Free Methods *PLoS One* **5**(9): 12810

Yoshida, N. and Perry, A.C.F. 2007 Piezo-Actuated Mouse intracytoplasmic Sperm Injection (ICSI) *Nature Protocols* **2** 296-304

You, J., Lee, J., Hyun, S. and Lee, E. 2012 L-Carnitine Treatment During Oocyte Maturation Improves *in vitro* Development of Cloned Pig Embryos by Influencing Intracellular Glutathione Synthesis and Embryonic Gene Expression *Theriogenology* **78** 235-243

Yu, Y., Dumollard, R., Rossbach, A., Lai, A., and Swann, K. 2010 Redistribution of Mitochondria Leads to Bursts of ATP Production During Spontaneous Mouse Oocyte Maturation *J Cell Physio* **224** 672–680

Yu, Y., Nomikos, M., theodoridou, M., Nounesis, G., Lai, A., and Swann, K. 2012 PLCζ Causes Ca2+ Oscillations in Mouse Eggs by Targeting Intracellular and not Plasma Membrane PI(4,5)P2 *Mol Biol Cell* **23** 1-12

Zachut, M., Dekel, I., Lehrer, H., Arieli, A., Arav, A., Livshitz, L., Yakoby, S. and Moallem, U. 2010 Effects of dietary fats differing in n-6:n-3 ratio fed to high-

yielding dairy cows on fatty acid composition of ovarian compartments, follicular status, and oocyte quality *J Dairy Sci* **93**(2) 529-545

Zhang, Y., Xue, R., Zhang, Z., Yang, X. and Shi, H. 2012 Palmitic and Linoleic Acids induce ER Stress and Apoptosis in Hepatoma Cells *Lipids Health Dis* **11**:1

Zipfel, W.R., Williams, R.M. and Webb, W.W. 2003 Nonlinear Magic: Multiphoton Microscopy in the Biosciences *Naure Biotechnol* **21**(11) 1369-1377

Zuccotti, M., Ponce, R.H., Boiani, M., Guizzardi, S., Govoni, P., Scandroglio, R., Garagna, S., and Redi, C.A. 2002 The Analysis of Chromatin Organisation Allows Selection of Mouse Antral Oocytes Competent for Development to Blastocyst *Zygote* **10**(1) 73-78

Zumbusch, A., Langbein, W. W. and Borri, P. 2013 Nonlinear Vibrational Microscopy Applied to Lipid Biology *Prog Lipid Res* **52**(4) 615-632

Appendices

1. *M199 (1L)*

14.7g	M199 Powder (Sigma)
2.2g	Sodium Bicarbonate (Sigma)
0.006g	Benzylpenicillin
0.05g	Streptomycin Sulphate
Up to 1L	Sterile water (Sigma)

For oocyte collection, add:

2.38g (10mM)	HEPES

For maturation (Chung *et al.* 1999), add:

10%	FCS (Sigma)
0.05U/μL	FSH (Sigma)
1mg/ml	Estradiol in DMSO

2. *T6 (1L)*

1 vial (7.31g)	Tyrode's Salts
0.06g	Benzylpenicillin
0.05g	Streptomycin Sulphate
0.055g	Sodium Pyruvate (Sigma)
2.106g	Sodium Bicarbonate (Sigma)
3.5ml	Sodium Lactate syrup (Sigma)
Up to 1L	Sterile water

3. *MEM (1L)*

1 litre	MEM liquid (Sigma) **or**
1 vial	MEM powder (Sigma)
0.026g (0.23mM)	Sodium Pyruvate (Sigma)
0.35ml	Sodium Lactate syrup (Sigma)
0.06g	Benzylpenicillin
0.05g	Streptomycin Sulphate
2.2g	Sodium Bicarbonate (if required) (Sigma)
3mg/ml	BSA (Sigma) **or**
5mg/ml	FCS
up to 1L	Sterile water

4. *HKSOM 10x Stock (500ml)*

27.75g	Sodium Chloride
0.925g	Potassium Chloride
0.238g	Monopotassium Phosphate
0.11g	Sodium Pyruvate (Sigma)
0.73g	L-Glutamine
0.25g	Streptomycin Sulphate
0.315g	Benzylpenicillin
0.019g	EDTA
0.2465g	Magnesium Sulphate
7.37ml	Sodium Lactate syrup (Sigma)
1.68g	Sodium Bicarbonate (Sigma)
0.05g	Phenol red
23.8g	HEPES
Up to 500ml	Sterile water (Sigma)

For use:

7ml	Sterile water (Sigma)
1ml	HKSOM 10x stock (Sigma)
10µl (1.7M)	Calcium Chloride
10µl (0.2M)	Glucose
10-30µl	Sodium Hydroxide (Sigma)

5. *Program code used for Aggregate Analysis, calculating and plotting aggregate size and occurrence in a 3D volume*

```
// This script assigns a group index to points arranged within given distance from XYZ coordinates

RL=0.3; // set the lateral resolution in um
RA=0.6; // set the axial resolution in um

L=1.5*sqrt(3); // set the distance value in resolution units

worksheet -c gindex; //creates a column called gindex

for (i=1;i<=%H!wks.nrows;i+=1){

%H_gindex[i]=0;

};


for (i=1;i<=%H!wks.nrows;i+=1){

for (j=1;j<=%H!wks.nrows;j+=1){

dij=sqrt((((%H_X[i]-%H_X[j])/RL)^2)+(((%H_Y[i]-%H_Y[j])/RL)^2)+(((%H_Z[i]-
%H_Z[j])/RA)^2)) ; // calculate pair distances in resolution units

if (dij>0 && dij<L){

indexi=%H_gindex[i];
indexj=%H_gindex[j];

if (indexi==0 && indexj==0){
%H_gindex[i]=i ;
%H_gindex[j]=i ;
};

else {
if (indexi!=0 && indexj==0) %H_gindex[j]=indexi ;
else {
if (indexj!=0 && indexi==0) %H_gindex[i]=indexj ;
else {
if (indexi!=indexj){

for (k=1;k<=%H!wks.nrows;k+=1){

if (%H_gindex[k]==indexj) %H_gindex[k]=indexi;

};
};
};
};
};
};

};

};
```

6. *Program code used for generating Random Distributions of 2000, 4000 or 6000 'droplets' in a 50x50µm cube*

```
// this script creates a randon distribution of XYZ coordinates
// over a given range and for a given number of points

worksheet -c X; //creates a column called X;
worksheet -c Y; //creates a column called Y;
worksheet -c Z; //creates a column called Z;

range=50;
Npoints=2000 or 4000 or 6000

for (i=1;i<=Npoints;i+=1){

%H_X[i]=rnd(0)*range;

%H_Y[i]=rnd(0)*range;

%H_Z[i]=rnd(0)*range;

};
```

7. *Examples of @5000cm^{-1} images*

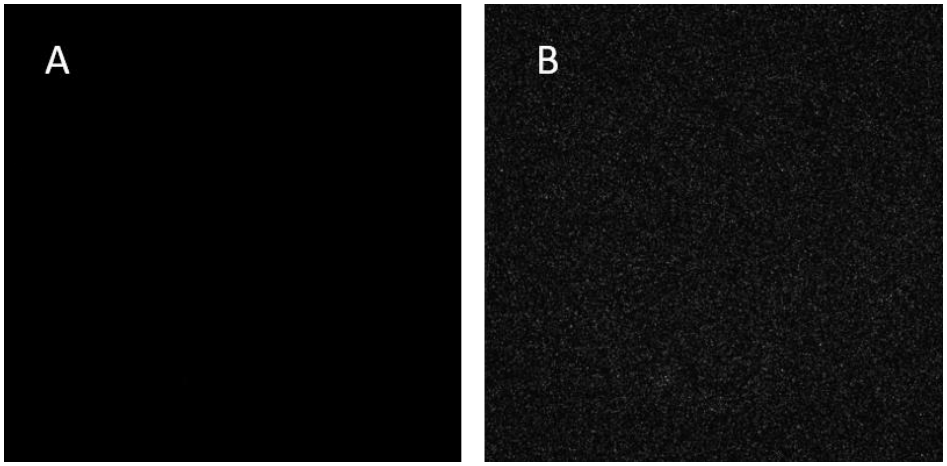

An image taken where there is no overlap of pump and Stokes beams (A) scaled to the CARS intensity, and (B) unscaled.

Manuscripts

Josephine Bradley, Iestyn Pope, Francesco Masia, Randa Sanusi, Wolfgang Langbein, Karl Swann, and Paola Borri “Quantitative imaging of lipids in living mouse oocytes and early embryos using CARS microscopy” (2016) *Development* **143** 2238-2247